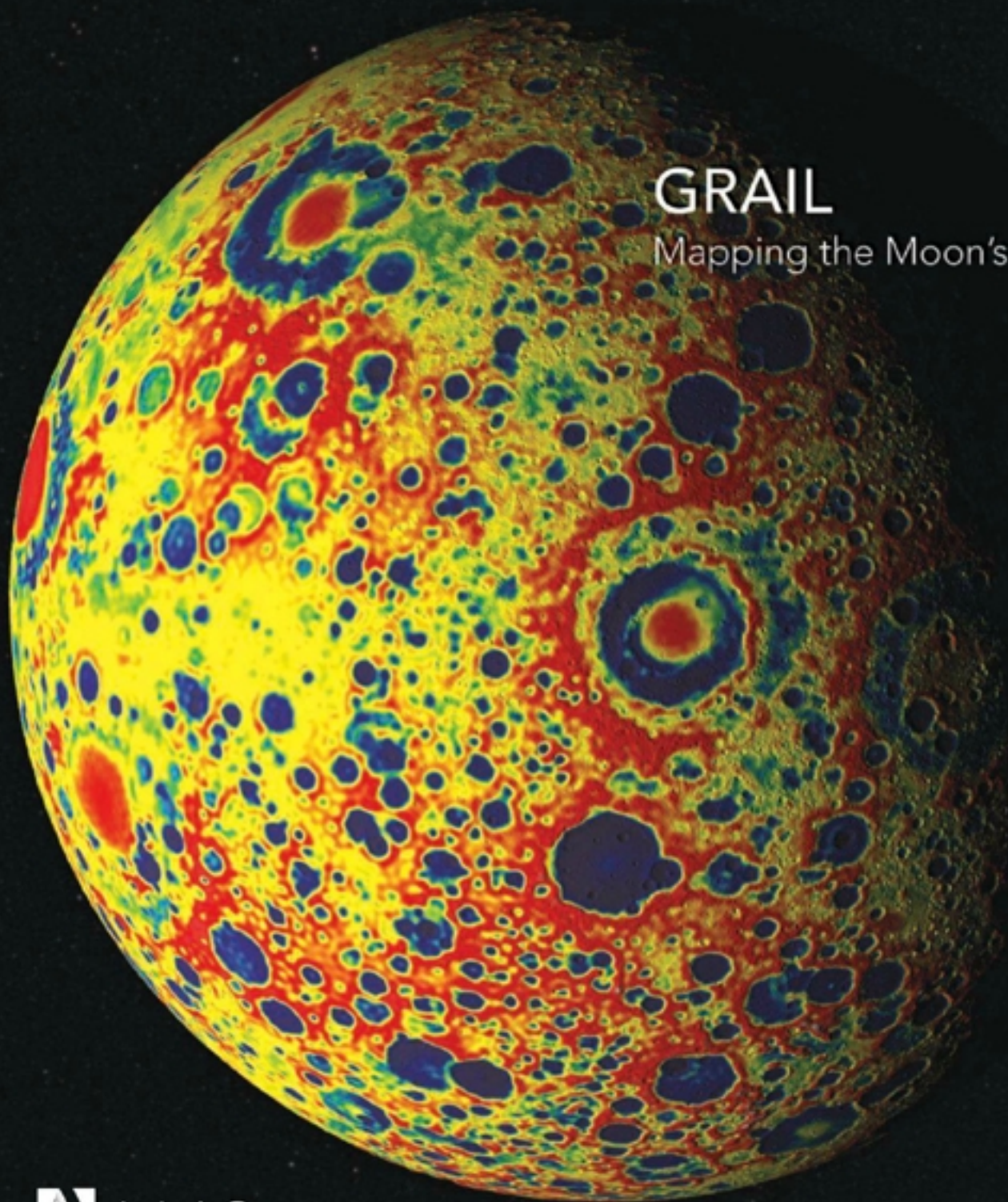


8 February 2013 | \$10

Science

GRAIL

Mapping the Moon's Interior



EDITORIAL

- 627 Investing in Distant Rewards
William H. Press

NEWS OF THE WEEK

- 632 A roundup of the week's top stories

NEWS & ANALYSIS

- 635 Chu's Legacy at DOE: Some Fields Gain, Others Falter
- 636 BP Research Dollars Yield Signs of Cautious Hope
- 638 Forecasting Regional Climate Change Flunks Its First Test
- 639 Supreme Court to Review the Scope of Monsanto's Seed Patents

NEWS FOCUS

- 640 Giant Marine Reserves Pose Vast Challenges
- 642 Archaeologist Hammers Away at 'Modern' Behavior
- 644 Losing Arable Land, China Faces Stark Choice: Adapt or Go Hungry
>> Science Podcast

LETTERS

- 646 Physical Laws Shape Biology
K. Selvarajoo and M. Tomita
- Biodiversity Despite Selective Logging
D. P. Edwards and W. F. Laurance
- Legal Limits to Data Re-Identification
S. Wilson
- 647 NextGenVOICES
- 647 TECHNICAL COMMENT ABSTRACTS

BOOKS ET AL.

- 648 The Annotated and Illustrated Double Helix
J. D. Watson. A. Gann and J. Witkowski, Eds., reviewed by N. Comfort
- 649 A Cultural History of Heredity
S. Müller-Wille and H.-J. Rheinberger, reviewed by H. Landecker

POLICY FORUM

- 650 Is Europe Evolving Toward an Integrated Research Area?
A. Chessa et al.

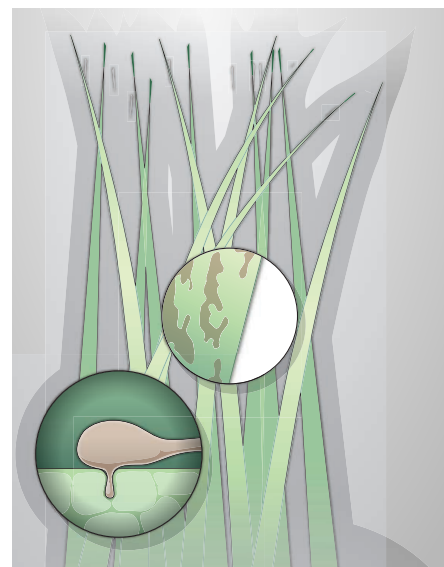
PERSPECTIVES

- 652 Shielding Broken DNA for a Quick Fix
J. Lukas and C. Lukas
>> Reports pp. 700 and 711
- 653 Pollution, Politics, and Vultures
A. Balmford
>> Science Podcast
- 654 Metamaterials with Quantum Gain
O. Hess and K. L. Tsakmakidis
- 655 Impact and Extinction
H. Pälke
>> Report p. 684
- 656 Fossils Versus Clocks
A. D. Yoder
>> Research Article p. 662
- 658 Copying Biology's Ways with Hydrogen
F. A. Armstrong
>> Report p. 682
- 659 Jack of All Trades, Master of Flowering
J. Á. H. Danielson and W. B. Frommer
>> Report p. 704
- 661 Retrospective: Carl R. Woese (1928–2012)
N. Goldenfeld and N. R. Pace

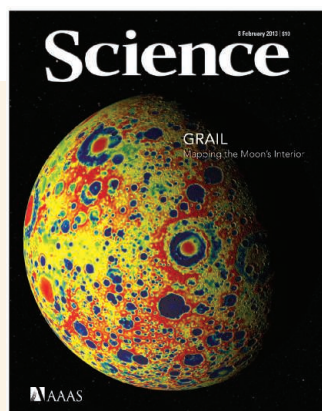
CONTENTS continued >>



page 640



pages 659 & 704



COVER

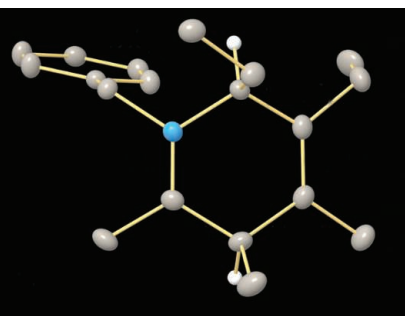
Rendering from the Gravity Recovery and Interior Laboratory (GRAIL) mission showing free-air gravity anomalies of the Moon's farside. Here, red corresponds to mass excesses and blue to mass deficits. This map resolves spatial scales as fine as 13 kilometers and reveals impact basins, complex craters, and simple craters. For more results from the GRAIL mission, see the Reports on pages 668, 671, and 675.

Image: NASA/Massachusetts Institute of Technology/Jet Propulsion Laboratory/Goddard Space Flight Center/Scientific Visualization Studio

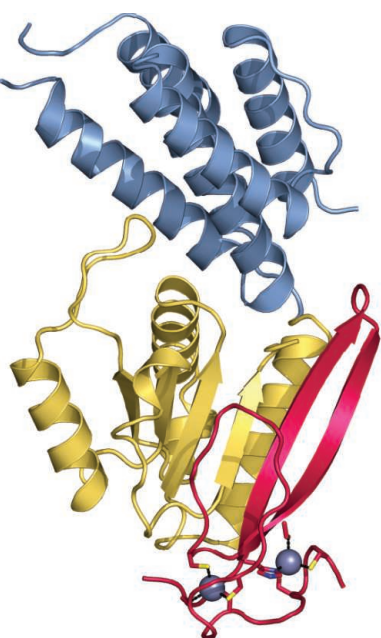
Explore our rich online offerings, including multimedia, news, *Science Careers*, and our two research journals—*Science Signaling* and *Science Translational Medicine*—at www.sciencemag.org

DEPARTMENTS

- 625 This Week in *Science*
- 628 Editors' Choice
- 630 *Science* Staff
- 716 Information for Authors
- 718 New Products
- 719 *Science Careers*



page 678



page 690

RESEARCH ARTICLE

- 662** The Placental Mammal Ancestor and the Post-K-Pg Radiation of Placentals
M. A. O'Leary et al.
Fossil and DNA phylogenies suggest that placental mammals diversified in the Cenozoic and reconstruct the ancestral form.
>> *Perspective p. 656*

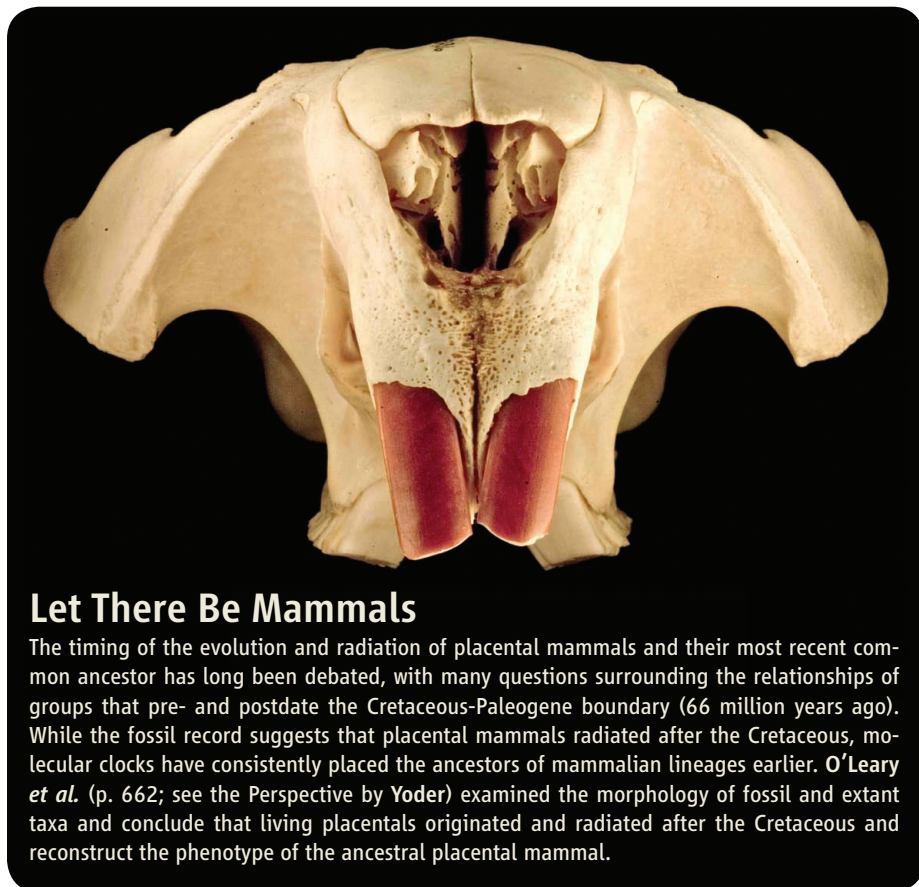
REPORTS

- 668** Gravity Field of the Moon from the Gravity Recovery and Interior Laboratory (GRAIL) Mission
M. T. Zuber et al.
The Moon's gravity field reveals that impacts have homogenized the density of the crust and fractured it extensively.
- 671** The Crust of the Moon as Seen by GRAIL
M. A. Wieczorek et al.
The Moon's gravity field shows that the lunar crust is less dense and more porous than was thought.
- 675** Ancient Igneous Intrusions and Early Expansion of the Moon Revealed by GRAIL Gravity Gradiometry
J. C. Andrews-Hanna et al.
The Moon's gravity map shows that the crust is cut by extensive magmatic dikes, perhaps implying a period of early expansion.
- 678** Proton Donor Acidity Controls Selectivity in Nonaromatic Nitrogen Heterocycle Synthesis
S. Duttwyler et al.
Acids of different strengths propel a common intermediate to a diverse array of compounds sought in pharmaceutical research.
- 682** A Functional [NiFe]Hydrogenase Mimic That Catalyzes Electron and Hydride Transfer from H₂
S. Ogo et al.
A bimetallic complex mimics a widely studied enzyme class of particular interest in renewable energy research.
>> *Perspective p. 658*
- 684** Time Scales of Critical Events Around the Cretaceous-Paleogene Boundary
P. R. Renne et al.
Radiometric dating establishes the mass extinction that killed the dinosaurs as synchronous with a large asteroid impact.
>> *Perspective p. 655*

- 687** Stress State in the Largest Displacement Area of the 2011 Tohoku-Oki Earthquake
W. Lin et al.
Borehole stress measurements indicate a nearly total stress drop in the region of largest slip.
- 690** Paramyxovirus V Proteins Disrupt the Fold of the RNA Sensor MDA5 to Inhibit Antiviral Signaling
C. Motz et al.
The crystal structure of a viral protein core complex reveals how paramyxoviruses inhibit the innate immune response.
- 694** Structural Basis for Hijacking of Cellular LxxLL Motifs by Papillomavirus E6 Oncoproteins
K. Zanier et al.
Crystal structures show how a key oncoprotein in human papillomavirus binds host proteins.
- 698** A Histone Mutant Reproduces the Phenotype Caused by Loss of Histone-Modifying Factor Polycomb
A. R. Pengelly et al.
Histone genetics provides functional evidence for the importance of histone modifications in gene regulation.
- 700** 53BP1 Regulates DSB Repair Using Rif1 to Control 5' End Resection
M. Zimmermann et al.
In mammalian cells, Rap1-interacting factor 1 protects DNA ends against resection.
>> *Perspective p. 652; Report p. 711*
- 704** Regulation of Flowering by Trehalose-6-Phosphate Signaling in *Arabidopsis thaliana*
V. Wahl et al.
Specific sugar signals integrate carbohydrate status with day length and developmental age to regulate flowering.
>> *Perspective p. 659*
- 708** Host-Derived Nitrate Boosts Growth of *E. coli* in the Inflamed Gut
S. E. Winter et al.
During inflammation, *Escherichia coli* uses nitrate respiration to gain a growth advantage over other gut bacteria.
- 711** Rif1 Prevents Resection of DNA Breaks and Promotes Immunoglobulin Class Switching
M. Di Virgilio et al.
In mammalian cells, Rap1-interacting factor 1 protects DNA ends against resection.
>> *Perspective p. 652; Report p. 700*

SCIENCE (ISSN 0036-8075) is published weekly on Friday, except the last week in December, by the American Association for the Advancement of Science, 1200 New York Avenue, NW, Washington, DC 20005. Periodicals Mail postage (publication No. 484460) paid at Washington, DC, and additional mailing offices. Copyright © 2013 by the American Association for the Advancement of Science. The title SCIENCE is a registered trademark of the AAAS. Domestic individual membership and subscription (51 issues): \$149 (\$74 allocated to subscription). Domestic institutional subscription (51 issues): \$990; Foreign postage extra: Mexico, Caribbean (surface mail) \$55; other countries (air assist delivery) \$85. First class, airmail, student, and emeritus rates on request. Canadian rates with GST available upon request, GST #1254 88122. Publications Mail Agreement Number 1069624. Printed in the U.S.A.

Change of address: Allow 4 weeks, giving old and new addresses and 8-digit account number. Postmaster: Send change of address to AAAS, P.O. Box 96178, Washington, DC 20090-6178. Single-copy sales: \$10.00 current issue, \$15.00 back issue prepaid includes surface postage; bulk rates on request. Authorization to photocopy material for internal or personal use under circumstances not falling within the fair use provisions of the Copyright Act is granted by AAAS to libraries and other users registered with the Copyright Clearance Center (CCC) Transactional Reporting Service, provided that \$30.00 per article is paid directly to CCC, 222 Rosewood Drive, Danvers, MA 01923. The identification code for Science is 0036-8075. Science is indexed in the Reader's Guide to Periodical Literature and in several specialized indexes.



Let There Be Mammals

The timing of the evolution and radiation of placental mammals and their most recent common ancestor has long been debated, with many questions surrounding the relationships of groups that pre- and postdate the Cretaceous-Paleogene boundary (66 million years ago). While the fossil record suggests that placental mammals radiated after the Cretaceous, molecular clocks have consistently placed the ancestors of mammalian lineages earlier. **O'Leary *et al.*** (p. 662; see the Perspective by **Yoder**) examined the morphology of fossil and extant taxa and conclude that living placentals originated and radiated after the Cretaceous and reconstruct the phenotype of the ancestral placental mammal.

The Holy GRail?

The gravity field of a planet provides a view of its interior and thermal history by revealing areas of different density. GRail, a pair of satellites that act as a highly sensitive gravimeter, began mapping the Moon's gravity in early 2012. Three papers highlight some of the results from the primary mission. **Zuber *et al.*** (p. 668, published online 6 December) discuss the overall gravity field, which reveals several new tectonic and geologic features of the Moon. Impacts have worked to homogenize the density structure of the Moon's upper crust while fracturing it extensively. **Wieczorek *et al.*** (p. 671, published online 6 December) show that the upper crust is 35 to 40 kilometers thick and less dense—and thus more porous—than previously thought. Finally, **Andrews-Hanna *et al.*** (p. 675, published online 6 December) show that the crust is cut by widespread magmatic dikes that may reflect a period of expansion early in the Moon's history.

Fixing Broken DNA

Some physiological processes, such as immunoglobulin class switching and telomere attrition, result in double-stranded DNA breaks. The DNA damage repair protein, 53BP1, prevents nucleolytic processing of these breaks, but the proteins

it partners with to do this are unknown (see the Perspective by **Lukas and Lukas**). **Di Virgilio *et al.*** (p. 711, published online 10 January), using mass spectroscopy-based methods, and **Zimmermann *et al.*** (p. 700, published online 10 January), using a telomere-based assay, identify Rif1 as a 53BP1 phosphorylation- and DNA damage-dependent interaction partner. Mice with a B cell-specific deletion in Rif1 showed impaired immunoglobulin class switching. Rif1-deficient cells exhibited extensive 5'-3' resection at DNA ends, with enhanced genetic instability. Thus, Rif1 partners with 53BP1 to promote the proper repair of double-stranded DNA breaks.

E. coli kNOws How to Win

The harmonious existence among the various microbial inhabitants of the gut is critical for good health. However, inflammation from injury or inflammatory bowel disease, can disrupt this balance and lead to the outgrowth of particular bacteria. The outgrowth of members of the Enterobacteriaceae family, which includes *Escherichia coli*, is often observed. Because *E. coli* are facultative rather than obligate anaerobes, **Winter *et al.*** (p. 708) postulated that they may be able to use by-products of reactive oxygen and nitrogen species, which are produced during inflammation, for anaerobic respiration, thereby edging out other fermenting

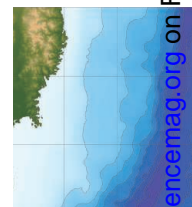
bacteria. Indeed, in two mouse models of colitis and in a model of intestinal injury, various *E. coli* strains were able to use host-derived nitrate as an energy source and outcompete mutant strains unable to do this.

Mimicking Hydrogenase

Hydrogenase enzymes possess unusual bimetallic active sites that cleave H₂. The enzymes make use of abundant metals (iron and sometimes nickel), in contrast to the often expensive synthetic catalysts that rely on rarer elements such as ruthenium or platinum. **Ogo *et al.*** (p. 682; see the Perspective by **Armstrong**) now report a bimetallic coordination compound of iron and nickel that can catalyze electron and hydride transfers from H₂ in a manner analogous to the corresponding enzyme and characterize the structure of an intermediate with bound hydride.

Stressed Out

Large seismic events such as the 2011 magnitude 9.0 Tohoku-Oki earthquake can have profound effects not just on the severity of ground motion and tsunami generation, but also on the overall state of the crust in the surrounding regions. **Lin *et al.*** (p. 687) analyzed the stress 1 year after the Tohoku-Oki earthquake and compared it with the estimated stress state before the earthquake. In situ resistivity images were analyzed from three boreholes drilled into the crust across the plate interface where the earthquake occurred. Stress values indicate a nearly complete drop in stress following the earthquake such that the type of faulting above the plate boundary has changed substantially. These findings are consistent with observations that the sea floor moved nearly 50 meters during the earthquake.



Targeting HPV

Papillomaviruses infect mammalian epithelial cells and induce cancers, including cervical cancer in humans. Vaccines against human papillomavirus (HPV) can prevent, but not cure, infection. A key viral oncoprotein, E6, acts by binding and inactivating many host proteins. **Zanier *et al.*** (p. 694) determined high-resolution crystal structures of bovine papillomavirus bound to a peptide from the focal adhesion protein, paxillin, and of HPV bound to a peptide from the ubiquitin ligase E6AP. The structures show that the peptide binds in a pocket formed by two zinc domains and a linker helix, which represents a promising target for therapeutics.

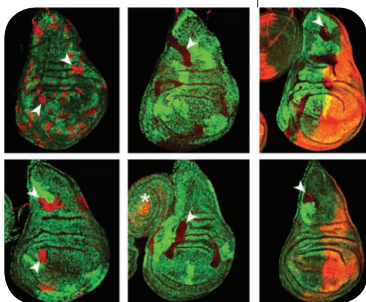
Additional summaries

Genetic Epigenetics

Posttranslational modifications of histone proteins have been implicated in the regulation of gene transcription in organisms ranging from yeast to humans. However, epigenetic regulators can modify multiple proteins. By mutating specific histone sites in *Drosophila*, **Pengelly et al.** (p. 698) demonstrate that mutation of lysine 27 of histone H3

causes the same transcriptional defects as those observed in mutants lacking the methyltransferase PRC2 that modifies this H3 residue. These results demonstrate the functional importance of H3-K27

methylation in Polycomb repression. Furthermore, this genetic approach may be applied to investigating numerous other metazoan-specific histone modifications.



Acid-Derived Diversity

Compounds with nitrogen-bearing rings have proven rather promising in pharmaceutical research, spurring the need for improved synthetic methods to access structurally diverse variants of this motif. **Duttwyler et al.** (p. 678) show that applying acids of different strengths to a dihydropyridine intermediate leads to selective protonation at either of two sites, depending on whether the reaction proceeds under kinetic or thermodynamic (that is, equilibrated) control. The protonations in turn activate the rings for addition of various carbon nucleophiles to the periphery, thereby affording multiple different substitution patterns for use in screening studies.

Impact Dating

The large mass extinction of terrestrial and marine life—most notably, non-avian dinosaurs—occurred around 66 million years ago, at the boundary between the Cretaceous and Paleogene periods. But attributing the cause to a large asteroid impact depends on precisely dating material from the impact with indicators

of ecological stress and environmental change in the rock record.

Renne et al. (p. 684; see the Perspective by **Pälike**) acquired high-precision radiometric dates of stratigraphic layers surrounding the boundary, demonstrating that the impact occurred within 33,000 years of the mass extinction. The data also constrain the length of time in which the atmospheric carbon cycle was severely disrupted to less than 5000 years. Because the climate in the late Cretaceous was becoming unstable, the large-impact event appears to have triggered a state-shift in an already stressed global ecosystem.

Parainfluenza 5 and MDA5

Our immune system and the viruses that infect us are in a constant arms race, with one side always trying to outwit the other. One example is the inhibition of host protein MDA5, a member of the retinoic acid-inducible gene 1 (RIG-I)-like receptor (RLR) family of innate immune sensors, by the V protein expressed by parainfluenza virus 5 (PIV5). To better understand how this inhibition is accomplished, **Motz et al.** (p. 690, published online 17 January) solved the crystal structure of PIV5 V protein bound to the adenosine triphosphatase (ATPase) domain of porcine MDA5.

This analysis, together with mutational studies using mouse and human versions of MDA5, revealed that the V protein unfolds the ATPase domain of MDA5 and replaces two strands of this domain's structural core. These changes disrupt the ATPase hydrolysis site and prevent the formation of filaments by MDA5, which are important for transmitting downstream signals that activate antiviral immunity. Mutation of just two amino acids in RLR family member RIG-I also rendered this receptor susceptible to V protein-mediated inhibition.

Sweet Enough to Flower

In making the developmental switch from vegetative growth to flowering, plants integrate diverse information, including photoperiod, hormone signals, and carbohydrate status. **Wahl et al.** (p. 704; see the Perspective by **Danielson and Frommer**) analyzed the physiology of the signaling sugar trehalose-6-phosphate (T6P) in *Arabidopsis*. Quantities of T6P cycle in daily rhythms that peak toward the end of the day. T6P levels in the shoot apical meristem mirrored sucrose levels. Disruption of T6P production also disrupted expression of the *FLOWERING LOCUS T* gene, which responds in leaves to day length and generates signals that direct the meristem to initiate flowering programs. T6P production also affected the signaling pathway that links the age of the plant to flowering. By incorporating requirements for T6P signaling in the flowering induction pathways, the plant ensures that adequate carbohydrate reserves have been accumulated. Thus, T6P regulates the shift to flowering by linking carbohydrate status to day length in the leaves and to developmental age in the shoot apical meristem.



William H. Press is the president of the American Association for the Advancement of Science and the Warren J. and Viola M. Raymer Professor in Computer Science and in Integrative Biology at the University of Texas, Austin, TX, USA. E-mail: wpress@cs.utexas.edu.

Investing in Distant Rewards

WOULD YOU SPEND MONEY TODAY TO MAKE THE WORLD A SUBSTANTIALLY BETTER PLACE FOR YOUR children and grandchildren? Most of us would. But what if the benefit would accrue only to your great-great-great-great-grandchildren, not born until the 22nd century? That's an awfully distant time horizon for most people. Many would probably spend today's resources on more immediate concerns.

Economists model this preference as a "social discount rate," a form of reverse compound interest that assesses future benefits or catastrophes as exponentially less important than immediate ones. Mathematical arguments favor this model over several alternatives. But when applied to the question "How much should we spend today on basic science research?" the model often gives the answer "Not much!" This is because the returns from basic research, although possibly large, can be quite distant. Reverse compound interest thus knocks out the returns. But, I argue here, exponential discounting is both mathematically and practically inappropriate when applied to basic science. Also, importantly, the public appears to know instinctively why it does not apply.

In its broad range, from useful incremental advances to world-changing discoveries, scientific research exhibits what statisticians call a "heavy-tailed" probability distribution. Such distributions have the property that more important events are only mildly less probable, a so-called power law. A consequence is that rare events can have truly huge magnitudes, in comparison to typical ones. The discovery of penicillin was no typical incremental advance, and the confluence of fundamental discoveries in quantum mechanics and atomic structure that led to modern electronics was surely world-changing. Yet both occurred in a single century. Science's heavy tail allows us to expect even greater future discoveries, even though we can't predict when they will occur. (Less grand but more easily quantified surrogate statistics such as research publication or patent citation frequencies are also heavy-tailed.)

How should the rational investor think about investing in a heavy-tailed opportunity? It is mathematically unlike any conventional investment with a knowable annual return on investment. Formally, the return is divergent in that the longer you make continuous investments, the greater will be your effective return. Invest long enough, and your return will eventually overtake any doubter's exponential discount, thus justifying your patient investment. The mathematical opposite of "gambler's ruin"—losing everything on a run of bad luck—heavy-tailed investments exhibit "patient investor's bounty," in which one stays in the game to reap large, rare returns.

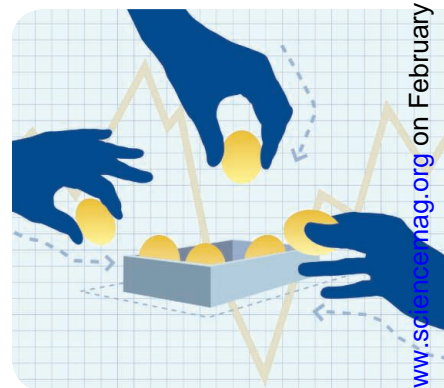
The U.S. public appears to understand this concept intuitively, without needing the formalism of mathematical arguments. The evidence is indirect but convincing. Polls show that in the United States, the public ranks science as one of the most prestigious occupations, along with firefighters, doctors, nurses, teachers, and military officers.* Thus, science is in the company of professions whose benefit to people is immediate. Yet, when I ask nonscientists about the benefits of science, few give answers that imply the short time horizons that motivate most economic activity. They like science because, among other things, it can lead to longer, healthier lives; protect the planet and feed humanity; and channel and empower the natural idealism of young people; and it satisfies a basic human need to understand the world.

The public recognizes science as having long-term, often idealistic, goals, yet accords scientists a level of respect otherwise reserved for "immediate helper" occupations. The combination suggests an instinctive understanding of heavy-tailed distributions and the patient investor's bounty. Put differently, the public realizes that the beauty and benefits of science are inseparable as a single long-term enterprise. Elected public officials worldwide would do well to listen to this particular wisdom of crowds.

— William H. Press

10.1126/science.1235227

*www.harrisinteractive.com/vault/Harris-Interactive-Poll-Research-Pres-Occupations-2009-08.pdf.

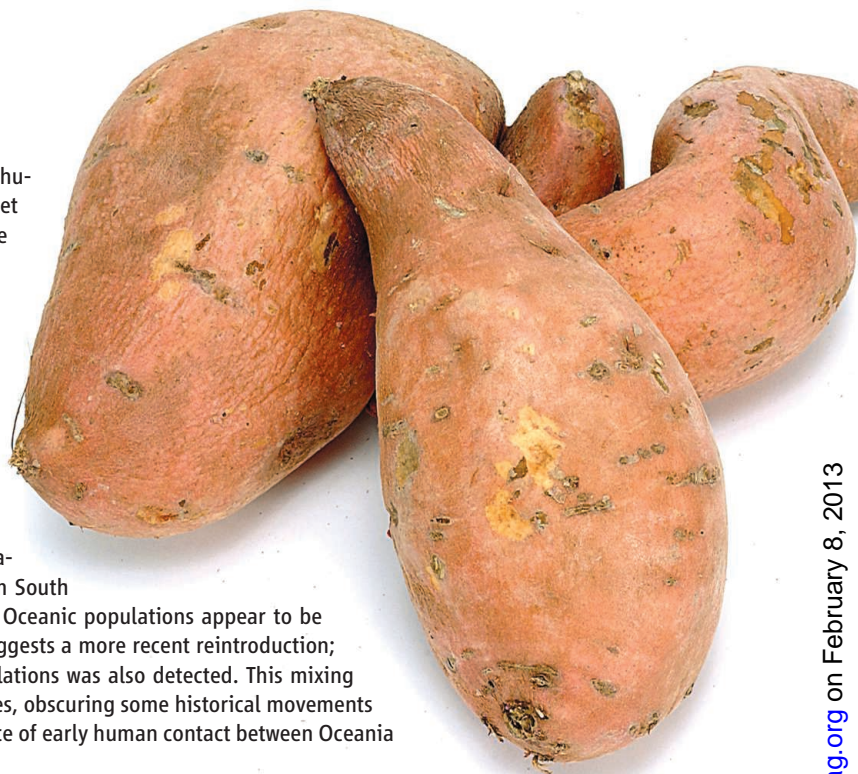


EVOLUTION

Sweet Potatoes Get Around

The origins of the sweet potato and its movement with humans have long been debated. This is because the sweet potato originated in South and Central America, but some evidence suggests that it was found in Polynesia during pre-Columbian times, indicative of contact between these human populations at this early time. Roulier *et al.* have used genetic markers in modern and herbarium specimens to infer the movements of this crop across the world. Two distinct gene pools were discovered in the northern and southern regions of the neotropics; in addition, recent interbreeding and movement between these two distinct gene pools could be detected. On the basis of herbarium specimens collected across the globe, there was evidence that the majority of lineages in Polynesia were initially derived from South America during pre-Columbian times. However, modern Oceanic populations appear to be primarily from the northern region population, which suggests a more recent reintroduction; although evidence of mixing with South American populations was also detected. This mixing has led to the generation of local varieties and phenotypes, obscuring some historical movements of plant germplasm, and provides more definitive evidence of early human contact between Oceania and South America. — LMZ

Proc. Natl. Acad. Sci. U.S.A. **110**, 10.1073/pnas.1211049110 (2013).



BIOMEDICINE

Doxorubicin Revisited

Doxorubicin (Dox) is a chemotherapeutic drug with efficacy in many cancers, yet after 40 years of clinical use, there are lingering mysteries about its mechanism of action. The prevailing hypothesis is that Dox forms a complex with topoisomerase II, a DNA-unwinding enzyme, and this leads to DNA strand breaks that induce cell cycle arrest. Although much evidence supports this model, not all data are consistent with it. New insights into Dox's cellular effects could help optimize its antitumor activity, reduce its adverse side effects, and/or help oncologists identify which patients are most likely to respond to the drug.

Denard *et al.* propose that the membrane-associated transcription factor CREB3L1 plays a key role in Dox's antitumor activity. In cultured cells, Dox increased synthesis of the lipid ceramide, which in turn caused proteolytic activation of CREB3L1 and its entry into the nucleus, where it increased transcription of cell cycle-inhibitory genes. When CREB3L1 levels were experimentally suppressed, cancer cells became resistant to Dox. These results suggest that CREB3L1 may be a biomarker of Dox-responsive cancer cells or even a druggable target itself. — PAK
eLife **1**, e00090 (2012).

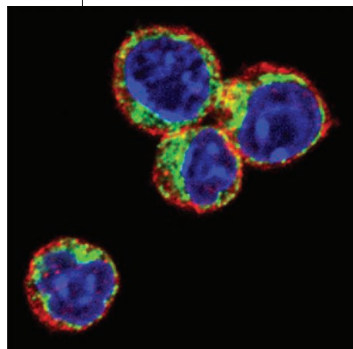
IMMUNOLOGY

T Cells Stay FIT During Flu

Immunological memory is critical for keeping us from getting sick from many pathogens for a second time. For example, infection with chicken pox usually confers lifelong immunity. Tissue-resident memory CD8⁺ T cells are a key population that is responsible for this protection. By being poised at sites of pathogen entry, such as the lung, they can quickly kill virus-infected cells. But what protects these cells from virus-induced cell death so that they can carry out their duties? Wakim *et al.* revealed that during influenza infection in mice, the antiviral protein IFITM3 affords such protection to lung, CD8⁺ memory T cells. IFITM3 is expressed specifically by resident CD8⁺ memory T cells in the lung, and cells deficient in IFITM3 did not survive well in response to secondary infection with influenza as compared to controls. Moreover, mice whose lung-resident CD8⁺ memory T cells were deficient in

IFITM3 were more susceptible to infection with influenza. These results suggest that the selective expression of an antiviral factor in memory T cells allows the host to protect itself against subsequent viral infection. — KLM

Nat. Immunol. **14**, 10.1038/ni.2525 (2013).



PHYSICS

Hastatic Order

Phase transitions are usually associated with the breaking of symmetry; the colder phase is generally more ordered than the hotter one. Normally, it is easy to deduce which symmetry is broken. A rare exception to that rule is the heavy fermion compound URu₂Si₂, which forms a mysterious phase below 17.5 K, known as "hidden order," that is yet to reveal its true nature in spite of intense experimental and theoretical efforts. Inspired by recent experimental findings, Chandra *et al.* propose that the exotic state breaks not only the time reversal symmetry (as is the case in magnetism), but also the doubly applied time reversal symmetry. This hastatic order is achieved through the hybridization of conduction electrons with the f-orbital states of uranium, which leads to the mixing of states of integer and half-integer spin, the latter ones causing the peculiar behavior. The theory makes testable predictions, and whether or not future experiments confirm that this is the correct

description of the hidden order in URu_2Si_2 , it describes an attractive mechanism that may be at work in other similar compounds. — JS

Nature **493**, 621 (2013).

EVOLUTION

Getting a Big Head

Brain size correlates roughly with intelligence. So, assuming that more intelligence gives a selective advantage, what limits the size of our heads? To see if bigger brains are better and what the tradeoffs might be, Kotschal *et al.* experimentally addressed the effects of selection for brain size in guppies (*Poecilia reticulata*). After only two generations of selection, the authors obtained populations of fish whose brains were larger or smaller than normal and differed from one another by about 10%. The big-brained female fish (but not the males, for some unknown reason) were better than those with smaller brains at a task where the fish associated the number of symbols (two or four) with a food reward. The cost of the increased brain power was a decrease in the size of the gut and a decrease in reproductive function. The brain is very active metabolically, and thus its growth must be balanced against the cost of maintaining other processes in the organism. The offsetting effect on reproductive function is consistent with interspecies comparisons in which more intelligent mammals, such as humans, whales, and dolphins, have decreased fertility. — LBR

Curr. Biol. **23**, 168 (2013).

EDUCATION

Stats for Scientists

Most science students receive their math instruction through the math department. Not surprisingly, math professors teach the math itself, without describing how it could be applied in a scientific setting. What would happen if instead, science departments began teaching core math skills in the context of science curriculums? Schlotter suggests that in chemistry, this question can be evaluated once a statistics curriculum addressing the specific needs of chemistry majors has been established. The main challenge in developing such a curriculum is to truly keep topics to a core minimum; a difficult task considering that the availability of computers and software has not only increased the amount

and frequency of routine statistical tests, but has also put a larger emphasis on students needing to understand how, and when, to apply statistical concepts appropriately. Although a tradeoff exists in removing chemistry topics from the curriculum to make room for statistics instruction, Schlotter argues that without it students will have little more understanding of statistical tests than where to find the buttons on their calculators. A draft version of a statistics curriculum for chemists is presented, and Schlotter welcomes comments from the science community. — MM

J. Chem. Educ. **90**, 51 (2013).

ASTRONOMY

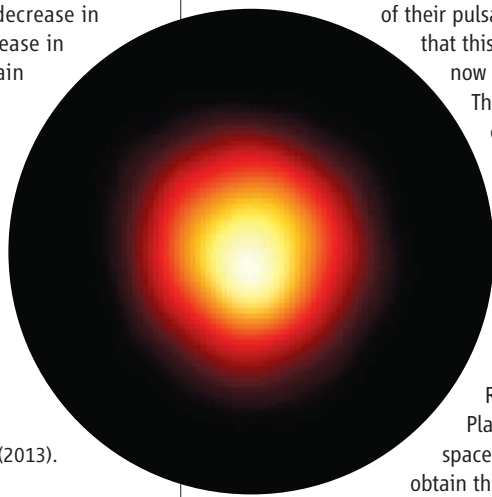
Pulsing with History

Understanding the history of our galaxy depends on having precise measurements of the properties of its stars. This has only been possible for stars that are within around 300 light-years from Earth, but as Miglio *et al.* demonstrate, advances in asteroseismology—the study of the interior structure of stars through the analysis of their pulsations—mean that this limitation can now be overcome.

The authors combined color measurements from the Two Micron All Sky Survey with pulsation data from the CoRoT (Convection Rotation and Planetary Transits) space telescope to obtain the radii, masses, distances, and ages of a

sample of just over 2000 red giant stars. These are stars that do not burn hydrogen in their cores any more and that, as a result, have expanded and cooled down; the Sun is expected to become a red giant star in about 5 billion years. The analysis shows that the stars in the sample spread across nearly 50,000 light-years over two separate regions in the disc of our galaxy and that their ages range from 0.3 to 12 billion years, spanning the entire history of the Milky Way. The two regions show significantly different mass distributions. The region higher below the galactic plane has a larger fraction of low-mass and hence older stars, supporting the idea that dynamical processes in the disc increase the velocity dispersion of stars over time. — MJC

Mon. Not. R. Astron. Soc. **429**, 423 (2013).



AAAS Travels

Wild & Prehistoric FRANCE



May 17-30, 2013
 including Lascaux II & Rouffignac
 Discover wild areas and prehistoric sites in Haute Provence, the Massif Central, and the Dordogne. See spectacular gorge country and images of the great cave paintings at Lascaux II and Rouffignac of mammoths. Visit the Vézère Valley, Font de Gaume, Arles, and Les Baux. \$3,695 + air.

For a detailed brochure, please call (800) 252-4910
 All prices are per person twin share + air


BETCHART EXPEDITIONS inc.
 17050 Montebello Rd, Cupertino, CA 95014
 Email: AAASInfo@betchartexpeditions.com
 www.betchartexpeditions.com



Join the Conversation!

Twitter is a great way to connect with AAAS members and staff about the issues that matter to you most. Be a part of the discussion while staying up-to-date on the latest news and information about your personal member benefits.

Follow us @AAASmember
 and join the conversation
 with #AAAS



MemberCentral.aaas.org

1200 New York Avenue, NW
Washington, DC 20005

Editorial: 202-326-6550, FAX 202-289-7562
News: 202-326-6591, FAX 202-371-9227

Bateman House, 82-88 Hills Road
Cambridge, UK CB2 1LQ

+44 (0) 1223 326500, FAX +44 (0) 1223 326501

SUBSCRIPTION SERVICES For change of address, missing issues, new orders and renewals, and payment questions: 866-434-AAAS (2227) or 202-326-6417, FAX 202-842-1065. Mailing addresses: AAAS, P.O. Box 96178, Washington, DC 20090-6178 or AAAS Member Services, 1200 New York Avenue, NW, Washington, DC 20005

INSTITUTIONAL SITE LICENSES please call 202-326-6755 for any questions or information

REPRINTS: Author Inquiries 800-635-7181

Commercial Inquiries 803-359-4578

PERMISSIONS 202-326-7074, FAX 202-682-0816

MEMBER BENEFITS AAAS Travels: Betchart Expeditions 800-252-4910; Apple Store www.store.apple.com/us/go/epstore/aaas; NASA Federal, 1-888-NASA-FCU (1-888-627-2328) or www.nasafcu.com; Cold Spring Harbor Laboratory Press Publications www.cshlpress.com/affiliates/aaas.htm; GEICO Auto Insurance www.geico.com/landingpage/go51.htm?logo=17624; Hertz 800-654-2200 CDP#343457; Office Depot <https://bbs.officepoint.com/portalLogin.do>; Seabury & Smith Life Insurance 800-424-9883; Subaru VIP Program 202-326-6417; VIP Moving Services www.vipmayflower.com/domestic/index.html; Other Benefits: AAAS Member Services 202-326-6417 or www.aaasmember.org.

science_editors@aaas.org (for general editorial queries)
science_letters@aaas.org (for queries about letters)
science_reviews@aaas.org (for returning manuscript reviews)
science_bookrevs@aaas.org (for book review queries)

Published by the American Association for the Advancement of Science (AAAS), *Science* serves its readers as a forum for the presentation and discussion of important issues related to the advancement of science, including the presentation of minority or conflicting points of view, rather than by publishing only material on which a consensus has been reached. Accordingly, all articles published in *Science*—including editorials, news and comment, and book reviews—are signed and reflect the individual views of the authors and not official points of view adopted by AAAS or the institutions with which the authors are affiliated.

AAAS was founded in 1848 and incorporated in 1874. Its mission is to advance science, engineering, and innovation throughout the world for the benefit of all people. The goals of the association are to: enhance communication among scientists, engineers, and the public; promote and defend the integrity of science and its use; strengthen support for the science and technology enterprise; provide a voice for science on societal issues; promote the responsible use of science in public policy; strengthen and diversify the science and technology workforce; foster education in science and technology for everyone; increase public engagement with science and technology; and advance international cooperation in science.

INFORMATION FOR AUTHORS

See pages 716 and 717 of the 8 February 2013 issue or access www.sciencemag.org/about/authors

SENIOR EDITORIAL BOARD

A. Paul Alivisatos, Lawrence Berkeley Nat'l. Laboratory
Cori Bargmann, The Rockefeller Univ.
Ernst Fehr, Univ. of Zurich
Erin O'Shea, Harvard Univ.
Michael S. Turner, University of Chicago

BOARD OF REVIEWING EDITORS

Adriano Aguzzi, Univ. Hospital Zürich
Takuzo Aida, Univ. of Tokyo
Leslie Aiello, Wenner-Gren Foundation
Sonia Altizer, Univ. of Georgia
Sebastian Amigorena, Institut Curie
Angelika Amon, MIT
Kathryn Anderson, Memorial Sloan-Kettering Cancer Center
Siv G. E. Andersson, Uppsala Univ.
Peter Andolfatto, Princeton Univ.
Meinrat O. Andreae, Max Planck Inst., Mainz
Paola Ariotti, Harvard Univ.
Johan Auwerka, EPFL
David Auschalom, Univ. of California Santa Barbara
Ben Barres, Stanford Medical School
Jordi Bascompte, Estación Biológica de Doñana, CSIC
Facundo Batista, London Research Inst.
Ray H. Baughman, Univ. of Texas, Dallas
David Baum, Univ. of Wisconsin
Mark Bear, Massachusetts Inst. of Technology
Yasmine Belkaid, NIH
Philip Benfey, Duke Univ.
Stephen J. Benkovic, Penn State Univ.
Christophe Bernard, Aix-Marseille Univ.
Gregory C. Berzosa, Stanford Univ.
Gabriele Bergers, Univ. of California, San Francisco
Peter Bork, EMBL
Bernard Bourdon, Ecole Normale Supérieure de Lyon
Chris Bowler, Ecole Normale Supérieure
Ian Boyd, Univ. of St. Andrews
Christian Büchel, Universität Hamburg-Eppendorf
Joseph A. Burns, Cornell Univ.
William P. Butz, Population Reference Bureau
Gyorgy Buzsáki, New York Univ., School of Medicine
Mats Carlsson, Univ. of Oslo
Mildred Cho, Stanford Univ.
David Clapham, Children's Hospital, Boston
David Clary, Univ. of Oxford
Jonathan D. Cohen, Princeton Univ.
Robert Cook-Deegan, Duke Univ.
James Collins, Boston Univ.
Alan Cowman, Walter & Eliza Hall Inst.
Robert H. Crabtree, Yale Univ.
Wolfgang Cramer, Mediterranean Inst. of Biodiversity and Ecology
Jeff L. Dangl, Univ. of North Carolina
Tom Daniel, Univ. of Washington

Frans de Waal, Emory Univ.
Stanislav Dehaene, Collège de France
Robert Desimone, MIT
Claude Desplan, New York Univ.
Ap Dijksterhuis, Radboud Univ. of Nijmegen
Dennis Discher, Univ. of Pennsylvania
Gerald W. Dorn II, Washington Univ. School of Medicine
Jennifer A. Doudna, Univ. of California, Berkeley
Julian Downward, Cancer Research UK
Bruce Dunn, Univ. of California, Los Angeles
Christopher Dye, WHO
David Ehrhardt, Carnegie Inst. of Washington
Tim Elston, Univ. of North Carolina at Chapel Hill
Gerhard Ertl, Fritz-Haber-Institut, Berlin
Barry Everitt, Univ. of Cambridge
Paul G. Falkowski, Rutgers Univ.
Ernst Fehr, Univ. of Zurich
Tom Fenchel, Univ. of Copenhagen
Michael Feuer, The George Washington Univ.
Alain Fischer, INSERM
Susan Fiske, Princeton Univ.
Anne C. Ferguson-Smith, Univ. of Cambridge
Peter Fratzl, Max Planck Inst.
Elaïne Fuchs, Rockefeller Univ.
Wulfram Gerstner, EPFL Lausanne
Andrew Gewirth, Univ. of Illinois
Karl-Heinz Glassmeier, TU Braunschweig
Elizabeth Grove, Univ. of Chicago
Kip Guy, St. Jude's Children's Research Hospital
Tejapraj Ha, Univ. of Illinois at Urbana-Champaign
Christian Haass, Ludwig Maximilians Univ.
Steven Hahn, Fred Hutchinson Cancer Research Center
Gregory J. Hannon, Cold Spring Harbor Lab.
David Held, Univ. of Cambridge
Yka Helariutta, Univ. of Finland
Isaac Held, NOAA
James A. Hendler, Rensselaer Polytechnic Inst.
Janet G. Hering, Swiss Fed. Inst. of Aquatic Science & Technology
Ray Hilborn, Univ. of Washington
Michael E. Himmel, National Renewable Energy Lab.
Kai-Uwe Hinrichs, Univ. of Bremen
Kei Hirose, Tokyo Inst. of Technology
David Holdell, Univ. of Cambridge
David Holdren, Imperial College
Lora Hooper, UT Southwestern Medical Ctr at Dallas
Jeffrey A. Hubbell, EPFL Lausanne
Thomas Hudson, Ontario Inst. for Cancer Research
Ray Huey, Univ. of California, Los Angeles
Steven Jacobsen, Univ. of California, Los Angeles
Kai Johnsson, EPFL Lausanne
Peter Jonas, Universität Freiburg
Matt Kaebert, Univ. of Washington
William Kaelin Jr., Dana-Farber Cancer Inst.

Daniel Kahne, Harvard Univ.
Daniel Kamm, Univ. of California, Berkeley
Joel Kingsolver, Univ. of North Carolina at Chapel Hill
Robert Kingston, Harvard Medical School
Roberto Kolter, Harvard Medical School
Alberto R. Kornblith, Univ. of Buenos Aires
Leonid Kruglyak, Princeton Univ.
Thomas Langer, Univ. of Cologne
Mitchell A. Lazar, Univ. of Pennsylvania
Bruce Lazer, Harvard Univ.
Virginia Lee, Univ. of Pennsylvania
Ottoline Leyser, Cambridge Univ.
Marcia C. Linn, Univ. of California, Berkeley
Junguo Liu, Michigan State Univ.
Luis Liz-Marzán, CIC bioGUNE
Jonathan Losos, Harvard Univ.
Ke Lu, Chinese Acad. of Sciences
Christian Lüscher, Univ. of Geneva
Laura Machesky, CRUK Beatson Inst. for Cancer Research
Anne Magurran, Univ. of St. Andrews
Oscar Marin, CSIC & Univ. Miguel Hernández
Charles Marshall, Univ. of California, Berkeley
Chris Marshall, Inst. of Cancer Research
Martin M. Matzuk, Baylor College of Medicine
C. Robertson McClung, Dartmouth College
Graham Medley, Univ. of Warwick
Yasushi Miyashita, Univ. of Tokyo
Richard Morris, Univ. of Edinburgh
Edward Mosser, Norwegian Univ. of Science and Technology
Sean Munro, MRC Lab. of Molecular Biology
Thomas Murray, The Hastings Center
Naoto Nagaosa, Univ. of Tokyo
James Nelson, Stanford Univ. School of Med.
Daniel Neftci, Univ. of Minnesota
Stuart Newman, New York Medical College
Timothy W. Nilsen, Case Western Reserve Univ.
Pär Nordlund, Karolinska Inst.
Helga Nowotny, European Research Advisory Board
Luk O'Neill, Univ. of Virginia
Stuart Newman, New York Medical College
N. Phuan Ong, Princeton Univ.
Joe Orenstein, Univ. of California, Berkeley & Lawrence Berkeley National Lab
Harry Orr, Univ. of Minnesota
Andrew Oswald, Univ. of Warwick
Steve Palumbi, Stanford Univ.
Jane Parker, Max-Planck Inst. of Plant Breeding Research
Donald R. Paul, Univ. of Texas at Austin
David Pearsall, Univ. of California, Berkeley
John H. J. Petrij, Memorial Sloan-Kettering Cancer Center
Simon Philpott, Univ. of Florida
Joshua Plotkin, Univ. of Pennsylvania
Philippe Poulin, CNRS
Colin Renfrew, Univ. of Cambridge

Trevor Robbins, Univ. of Cambridge
Jim Roberts, Fred Hutchinson Cancer Research Ctr.
Barbara A. Romanowicz, Univ. of California, Berkeley
Kjell Rostrop-Nielsen, Haldor Jørgsen
Mike Ryan, Univ. of Texas, Austin
Shimon Sakaguchi, Kyoto Univ.
Miguel Salmeron, Lawrence Berkeley National Lab
Jürgen Sandkühler, Medical Univ. of Vienna
Alexander Schier, Harvard Univ.
Randy Seeley, Univ. of Cincinnati
Vladimir Shalaev, Purdue Univ.
Joseph Silk, Institut d'Astrophysique de Paris
Denis Simon, Arizona State Univ.
Alison Smith, John Innes Centre
Davor Solter, Inst. of Medical Biology, Singapore
Peter Sorger, Harvard Medical School
John Speakman, Univ. of Aberdeen
Allan C. Spradling, Carnegie Institution of Washington
Jonathan Sprent, Garvan Inst. of Medical Research
Paula Stephan, Georgia State Univ. and National Bureau of Economic Research
Elisbeth Stern, ETH Zürich
V. S. Subrahmanian, Univ. of Maryland
Ira Tabas, Columbia Univ.
Yoshiko Takahashi, Kyoto University
Sarah Teichmann, Cambridge Univ.
John Thomas, Duke Univ.
Herbert Virsik, Washington Univ.
Bert Vogelstein, Johns Hopkins Univ.
Cynthia Volkert, Univ. of Göttingen
Bruce D. Walker, Harvard Medical School
Douglas Wallace, Dalhousie Univ.
Ian Walmsley, Univ. of Oxford
David A. Wardle, Swedish Univ. of Agric Sciences
David Waxman, Fudan Univ.
Jonathan Weissman, Univ. of California, San Francisco
Kathy Willis, Oxford Univ.
Ian A. Wilson, The Scripps Res. Inst.
Timothy D. Wilson, Univ. of Illinois
Rosemary Wyse, Johns Hopkins Univ.
Jan Zaenen, Leiden Univ.
Kenneth Zaret, Univ. of Penn. School of Medicine
Jonathan Zehr, Univ. of California, Santa Cruz
Maria Zuber, MIT

BOOK REVIEW BOARD

John Aldrich, Duke Univ.
David Bloom, Harvard Univ.
Angela C. Davis, Princeton Univ.
Richard Shwede, Univ. of Chicago
Ed Wasserman, DuPont
Lewis Wolpert, Univ. College London

EDITOR-IN-CHIEF Bruce Alberts

EXECUTIVE EDITOR

Monica M. Bradford

Colin Norman

MANAGING EDITOR, RESEARCH JOURNALS Katrina L. Kelnar

DEPUTY EDITORS R. Brooks Hanson, Barbara R. Jasny, Andrew M. Sugden, Valda J. Vinson

EDITORIAL SENIOR EDITORS/COMMENTARY Lisa D. Chong, Brad Wible; SENIOR EDITORS Gilbert J. Chin, Pamela J. Hines, Paula A. Kiberstis (Boston), Marc S. Lavine (Toronto), Beverly A. Purnell, L. Bryan Ray, Guy Riddihough, H. Jesse Smith, Phillip D. Szurovi (Tennessee), Jake S. Yeston, Laura M. Zahn (San Diego); ASSOCIATE EDITORS Melissa R. McCartney (Education Projects), Kristen L. Mueller, Jelena Stajic, Sacha Vignieri (Oregon), Nicholas S. Wigginton; BOOK REVIEW EDITOR Sherman J. Suter; ASSOCIATE LETTERS EDITOR Jennifer Ellis; EDITORIAL MANAGER Cara Tate; SENIOR COPY EDITORS Jeffrey E. Cook, Cynthia Howe, Harry Jach, Lauren Kmeck, Barbara P. Ordway, Trista Wagoner; COPY EDITOR Chris Filiatreau; SENIOR EDITORIAL COORDINATORS Carolyn Kyle, Beverly Shields; EDITORIAL COORDINATORS Joi S. Granger, Anita Wynn; PUBLICATIONS ASSISTANTS Ramatoulaye Diop, Anerea Dobbins, Jeffrey Hearn, Lisa Johnson, Dona Mathieu, Le-Toya Mayne Flood, Shannon McMahon, Scott Miller, Jerry Richardson, Teresa R. Sakon, Brian White; EDITORIAL ASSISTANT Patricia M. Moore; EXECUTIVE EDITORIAL ASSISTANT Yolanda O'Bannon (San Francisco); EXECUTIVE ASSISTANT Alison Crawford; ADMINISTRATIVE SUPPORT Maryrose Madrid

EDITORIAL DIRECTOR, WEB AND NEW MEDIA Stewart Wills; SENIOR WEB EDITOR Sarah Crespi; WEB EDITOR Kerry Klein; WEB DEVELOPMENT MANAGER Martyn Green; WEB DEVELOPER Corinna Cohn

NEWS DEPUTY NEWS EDITORS Robert Coontz, Elizabeth Culotta, David Grimm (Online), Eliot Marshall, Jeffrey Mervis, Leslie Roberts, Richard Stone, John Travis; CONTRIBUTING EDITOR Polly Shulman; NEWS WRITERS Yudhiht Bhattacharjee, Adrian Cho, Jennifer Couzin-Frankel, Carolyn Gramling, Jocelyn Kaiser, Richard A. Kerr, David Malachuk, Elizabeth Pennisi, Robert F. Service (Pacific NW), Erik Stokstad, Emily Underwood; WEB DEVELOPER Daniel Berger; SOCIAL MEDIA STRATEGIST Meghna Sachdev; INTERN Lizzie Wade; CONTRIBUTING CORRESPONDENTS John Bohannon, John Cohen (San Diego, CA), Ann Gibbons, Sam Kean, Eli Kintisch, Andrew Lawler, Mitch Leslie, Charles C. Mann, Virginia Morell, Gary Taubes; COPY EDITORS Melissa Raimondi, Kara Estelle; ADMINISTRATIVE SUPPORT Sherina Mack; BUREAU: San Diego, CA: 760-942-3252, FAX 760-942-4979; Pacific Northwest: 503-963-1940

PRODUCTION DIRECTOR Wendy K. Shank; ASSISTANT MANAGER Rebecca Doshi; SENIOR SPECIALISTS Steve Forrester, Christopher Redwood, Anthony Rosen; PREFLIGHT DIRECTOR David M. Tompkins; MANAGER Marcus Spiegel; SPECIALISTS Jan Hillman, Tara Kelly

ART DIRECTOR Yael Fitzpatrick; ASSOCIATE ART DIRECTOR Laura Creveling; SENIOR ILLUSTRATORS Chris Bickel, Katharine Suttifit; ILLUSTRATOR Yana Hammond; SENIOR ART ASSOCIATES Holly Bishop, Preston Huey; ART ASSOCIATES Kay Engman, Garvin Grullón, Chrystal Smith; PHOTO EDITOR Leslie Blizard

SCIENCE INTERNATIONAL

EUROPE (science@science-int.co.uk) EDITORIAL: INTERNATIONAL MANAGING EDITOR Andrew M. Sugden; SENIOR EDITOR/COMMENTARY Julia Fahrenkamp-Uppenbrink; SENIOR EDITORS Caroline Ash, Stella M. Hurlley, Ian S. Osborne, Peter Stern; ASSOCIATE EDITOR Maria Cruz; CONTRIBUTING EDITOR Helen Pickersgill; EDITORIAL SUPPORT Rachel Roberts, Alice Whaley; ADMINISTRATIVE SUPPORT Janet Clements, Jenny Hinson, John Wood; NEWS: DEPUTY NEWS EDITOR, U.K. Daniel Clery; CONTRIBUTING EDITOR, EUROPE Martin Enserink; CONTRIBUTING CORRESPONDENTS Michael Balter (Paris), Kai Kupferschmidt (Berlin), Gretchen Vogel (Berlin)

ASIA Japan Office: Ascia Corporation, Tomoko Furusawa, Rustic Bldg. 7F, 77 Tenjin-cho, Shinjuku-ku, Tokyo 162-0808, Japan; +81 3 6802 4616, FAX +81 3 6802 4615, inquiry@sciencemag.jp; CONTRIBUTING EDITOR, ASIA Mara Hivestendahl [China: mvhivest@aaas.org]; CONTRIBUTING CORRESPONDENTS Dennis Normile [Japan: +81 (0) 333910630, FAX +81 (0) 3 5936 3531; dnormile@gol.com]; Hao Xin [China: cindyhao@gmail.com]; Pallava Bagla [South Asia: +91 (0) 11 2271 2896; pbagla@vsnl.com]

EXECUTIVE PUBLISHER Alan I. Leshner

PUBLISHER Beth Rosner

FULFILLMENT SYSTEMS AND OPERATIONS (membership@aaas.org); CUSTOMER SERVICE SUPERVISOR Pat Butler; SPECIALISTS Latoya Casteel, Michelle Oforidire, April Marshall; MANAGER, DATA ENTRY Mickie Napoleoni; DATA ENTRY SPECIALISTS JJ Regan, Jaimee Wise, Fiona Gildin

BUSINESS OPERATIONS AND ADMINISTRATION DIRECTOR Deborah Rivera-Wienhold; BUSINESS SYSTEMS AND FINANCIAL ANALYSIS DIRECTOR Randy Yi; MANAGER, FULFILLMENT SYSTEMS Frits Buningh; SYSTEMS ANALYST Nicole Mehmedovich; MANAGER, BUSINESS ANALYSIS Eric Knott; MANAGER, BUSINESS OPERATIONS Jessica Tierney; BUSINESS ANALYSTS Cory Lipman, Celeste Troxler; Christine Wehrli; FINANCIAL ANALYST Jeremy Clay; RIGHTS AND PERMISSIONS: ADMINISTRATOR Emilie David; ASSOCIATE Elizabeth Sandler; MARKETING DIRECTOR Ian King; MARKETING MANAGERS Alison Chandler, Julianne Wielga, Justin Sawyers; MARKETING ASSOCIATES Mary Ellen Crowley, Elizabeth Sattler, Rebecca Rifkin; SENIOR MARKETING EXECUTIVE Jennifer Reeves; DIRECTOR, SITE LICENSING Tom Ryan; DIRECTOR, CORPORATE RELATIONS Eileen Bernadette Moran; SENIOR PUBLISHER RELATIONS SPECIALIST Kiki Forsythe; PUBLISHER RELATIONS MANAGER Catherine Holland; PUBLISHER RELATIONS, EASTERN REGION Keith Layson; PUBLISHER RELATIONS, WESTERN REGION Ryan Rexroth; CUSTOMER RELATIONS MANAGER Iquo Edim; MARKETING MANAGER Christina Schlechter; MARKETING ASSOCIATES Paulina Curto, Mitchell Edmund; CUSTOMER RELATIONS ANALYSTS Simon Chong, Lana Gu; ELECTRONIC MEDIA: DIRECTOR Elizabeth Harman; ASSISTANT MANAGER Lisa Stanford; PRODUCTION SPECIALISTS Antoinette Hodal, Michele Johnston, Lori Murphy, Kimberly Oster; WEB AND NEW MEDIA: SENIOR PROJECT MANAGER Trista Smith, PROJECT LEADER Luke Johnson COMPUTER SPECIALISTS Walter Jones, Kai Zhang, WEB DEVELOPER Chris Coleman; PROGRAM DIRECTOR, AAAS MEMBER CENTRAL Peggy Mihelich

DIRECTOR, GLOBAL COLLABORATION, CUSTOM PUBLICATIONS, ADVERTISING Bill Moran

EDITOR, CUSTOM PUBLISHING Sean Sanders: 202-326-6430

ASSISTANT EDITOR, CUSTOM PUBLISHING Tianna Hicklin 202-326-6463

ASSOCIATE DIRECTOR, COLLABORATION, CUSTOM PUBLICATIONS/CHINA/TAIWAN/KOREA/ SINGAPORE Ruolei Wu +86-1367-101-5294

PRODUCT (science_advertising@aaas.org); MIDWEST Rick Bongiovanni: 330-405-7080, FAX 330-405-7081; EAST COAST/E. CANADA Laurie Faraday: 508-747-9395, FAX 617-507-8189; WEST COAST/W. CANADA Lynne Stickrod: 415-931-9782, FAX 415-520-6940; UK EUROPE/ ASIA Roger Gonçalves: TEL/FAX +41 43 243 1358; JAPAN, Makiko Hara: +81 (0) 3 6802 4616, FAX +81 (0) 3 6802 4615; ads@sciencemag.jp; CHINA/TAIWAN Ruolei Wu: +86 1367 1015 294 ruwu@aaas.org

WORLDWIDE ASSOCIATE DIRECTOR OF SCIENCE CAREERS Tracy Holmes: +44 (0) 1223 326525, FAX +44 (0) 1223 326532

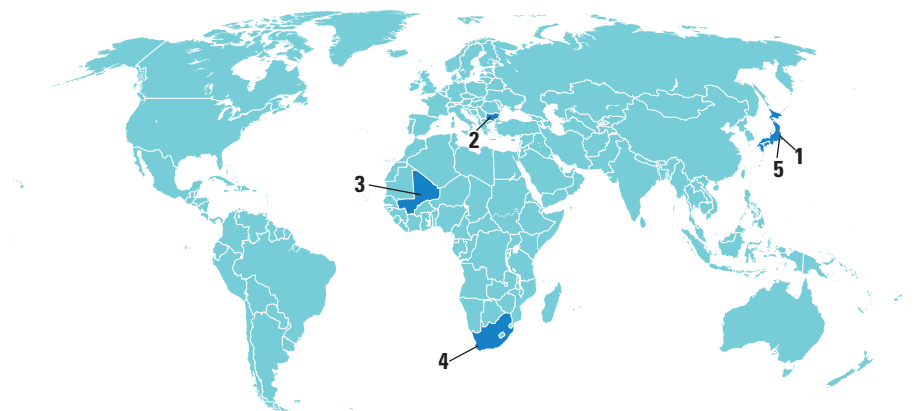
CLASSIFIED (advertise@sciencecareers.org); U.S.: EAST COAST/WEST COAST/SOUTH CENTRAL/SOUTH AMERICA Tina Burks: 202-326-6577; MIDWEST/CANADA/EUROPE Allyson Ross: 202-326-6578; SALES ADMINISTRATOR Marci Gallun; EUROPE/ROW SALES Lucy Nelson; SALES ASSISTANT Kelly Grace; JAPAN Yuri Kobayashi +81 (0)90-9110-1719; careerads@sciencemag.jp; CHINA/TAIWAN Ruolei Wu: +86 1367 1015 294 ruwu@aaas.org; ADVERTISING SUPPORT MANAGER Karen Foote: 202-326-6740; ADVERTISING PRODUCTION OPERATIONS MANAGER Deborah Tompkins; SENIOR PRODUCTION SPECIALIST/GRAPHIC DESIGNER Amy Hardcastle; PRODUCTION SPECIALIST Yuse Lajiminhup; SENIOR TRAFFIC ASSOCIATE Christine Hall; SALES COORDINATOR Shirley Young; MARKETING MANAGER Allison Pritchard; MARKETING ASSOCIATE Aimee Aponte

AAAS BOARD OF DIRECTORS RETIRING PRESIDENT, CHAIR Nina V. Fedoroff; PRESIDENT William H. Press; PRESIDENT-ELECT Phillip A. Sharp; TREASURER David E. Shaw; CHIEF EXECUTIVE OFFICER Alan I. Leshner; BOARD MAY R. Berenbaum, Bonnie L. Bassler, Stephen L. Mayo, Raymond Orbach, Julia M. Phillips, Sue V. Rosser, David D. Sabatini, Inder M. Verma



ADVANCING SCIENCE. SERVING SOCIETY

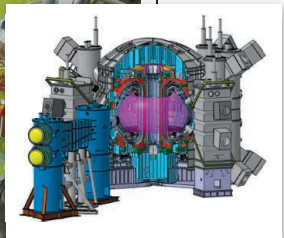
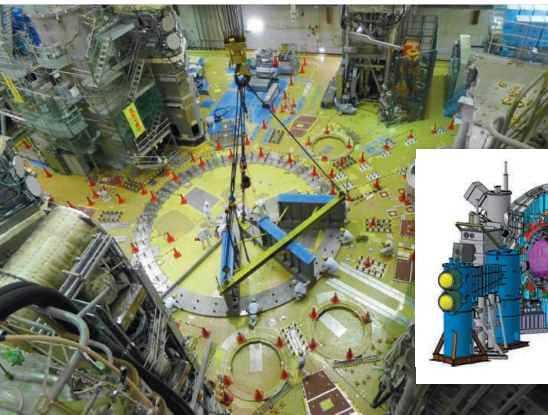
AROUND THE WORLD



Naka, Japan 1

Assembly Starts on the JT-60SA Fusion Reactor

Japan and the European Union last week started assembling the JT-60SA, an experimental nuclear fusion device. JT-60SA will supplement research using ITER, the international fusion reactor now under construction in France that will hopefully demonstrate the feasibility of producing more energy from fusion than is used to produce



it. The new machine's predecessor, JT-60, had been the workhorse of Japan's fusion research since the mid-1980s. Upgrading it became an international project under the E.U.-Japan Broader Approach, part of the deal that sent ITER to Europe. JT-60SA features superconducting coils that will magnetically confine the superhot plasma needed for fusion for up to 100 seconds, generating data and experience useful for optimizing ITER operations, says Yutaka Kamada, a plasma physicist with the Japan Atomic Energy Agency. The first assembly step was placing the components of a 12-meter-diameter, 250-tonne base that

were fabricated in Spain. Originally scheduled to come online in 2016, the \$450 million reactor faced a redesign to reduce costs and then was further delayed by procurement problems and the March 2011 Tohoku earthquake. Kamada says they now aim to start operations in 2019.

Sofia 2

Reshuffle in Science Leadership

After months of protests by scientists and a government report that found corruption and mismanagement of funds, Bulgaria's Prime Minister Boyko Borissov has shaken up leadership at the country's ministry of research and education, sacking research minister Sergei Ignatov and Hristo Petrov, the head of the Bulgarian National Science Fund (BNSF). Hundreds of scientists had protested BNSF's latest round of funding decisions in November and December. After a government probe confirmed long-running accusations that

the ministry had hired people lacking the required qualifications and that the grant review process was prone to corruption, Borissov asked for and received the officials' resignations on 28 January. A few days later, he nominated the president of the Bulgarian Academy of Sciences, Stefan Vodenicharov, to replace Ignatov. Emil Horozov, a mathematician at Sofia University who helped organize the protests, says that the departures are "a very good sign," but says the law governing the ministry also needs to be overhauled to prevent future corruption. As *Science* went to press, the parliament was expected to vote on Vodenicharov's appointment on 6 February.



Timbuktu, Mali 3

Manuscripts Escaped Burning

Thousands of historical manuscripts, initially thought destroyed when Islamic fundamentalists fled Timbuktu as French and Malian troops retook the city on 28 January after 9 months of occupation, have in fact survived. Islamic militants burned down Timbuktu's Ahmed Baba Institute of Higher Learning and Islamic Research, which opened in 2009, and burned what they could find, according to reports from journalists and researchers within the country. But that amounted to only about 5% of the library's original collection of 30,000 manuscripts—many had already been hidden away by archivists who earlier fled to Mali's capital, Bamako, while a cache was stored within an older building on the other side of town, says Susana Molins-Lliteras, a historian at the University of Cape Town in South Africa and a researcher at the Cape Town-based Tombouctou Manuscripts Project, which helped construct the library building. <http://scim.ag/timbukman>

Cape Town 4

New TB Vaccine Fails in Large Infant Study

Hopes that the experimental tuberculosis vaccine MVA85A would boost the benefits of a partially effective 90-year-old TB vaccine known as BCG have been met with disappointment. BCG offers some protection to infants against serious forms of the disease, but it has a checkered success in preventing infection with *Mycobacterium tuberculosis* and the common lung ailments it causes. A study, published online on 4 February in *The Lancet*, of nearly 3000 infants who live in a rural area near Cape Town reveals that those who received both vaccines had roughly the same amount of new infections and disease as infants in a control group who received only BCG. On the upside, the investigators noted that MVA85A was safe, and that adults have a stronger immune response to the vaccine than do infants, holding out the prospect that it may work in older populations. This was the first efficacy trial of a TB vaccine in

infants in more than 45 years. Now, groups such as the nonprofit Aeras (based in Rockville, Maryland) and the Wellcome Trust—both of which funded the study—have teamed up with academia and industry to aggressively address BCG's shortcomings.

Tokyo, 5

Research Loses—And Wins

At first glance, the Japanese ministry of education's 2013 science and technology budget, approved on 29 January, looks grim for scientists, with a decline in research spending of 3.3% to \$13.2 billion. But two-thirds of the reduction reflects the transfer of nuclear safety research to a new regulatory agency. And a stimulus package adopted last month also more than makes up for cuts in some programs. For example, the budget includes a \$42 million cut for large research facilities such as the K supercomputer and the SPring-8 synchrotron, but those facilities will receive \$299 million in stimulus spending.

The new budget showers money on a few programs that received hefty chunks of money from the stimulus, too, such as the commercialization of regenerative medicine, including the use of induced pluripotent stem cells, and drug discovery—in line with the new government's goals of supporting innovative research that will have an economic payoff and spending on hardware to immediately boost the economy. Support for investigator-driven research is holding steady, with funding for grants to individual scientists and small groups up a mere 0.5% to \$2.5 billion.

NEWSMAKERS

NSF Director Named President Of Carnegie Mellon University

The director of the National Science Foundation is leaving the \$7-billion agency to become president of Carnegie Mellon University. **Subra Suresh**, an engineer and materials scientist, told NSF staff members this week that he will depart at the end of March and take up his post at the Pittsburgh, Pennsylvania, institution on 1 July. He will have served less than half of a 6-year term that began in October 2010.

As has become standard practice for Obama appointees, Suresh announced his departure in a lengthy letter that listed



Suresh



Honoring the Best and Brightest

Twelve researchers and 11 inventors gathered in the East Room of the White House on 1 February to receive the U.S. federal government's highest honor for researchers: the National Medal of Science and the National Medal of Technology and Innovation. Pictured here are Medal of Science winners (left to right) physicist Sidney Drell of Stanford University; biologist Leroy Hood of the Institute for Systems Biology; astronomer Sandra Faber of the University of California, Santa Cruz; chemist M. Frederick Hawthorne of the University of Missouri; physicist Sylvester James Gates Jr. of the University of Maryland, College Park; mathematician Solomon Golomb of the University of Southern California; and physicist John Goodenough of the University of Texas (UT), Austin. The five other Medal of Science winners are chemist Allen Bard of UT Austin, biologist Sallie Chisholm of the Massachusetts Institute of Technology, mathematician Barry Mazur of Harvard University, biologist Lucy Shapiro of Stanford University, and psychologist Anne Treisman of Princeton University. Technology and Innovation Medal winners ranged from an inventor studying astronomical phenomena in the ultraviolet to the retina surgeon who invented LASIK eye surgery. President Barack Obama praised the group, noting that "it's clearer than ever that our future as a nation depends on keeping that spirit of curiosity and innovation alive in our time."

his many accomplishments. He has paid particular attention to expanding NSF's international footprint, integrating research and education across the foundation, and encouraging NSF-funded scientists to think harder about the commercial potential of their discoveries. As one of three agencies targeted for major increases as part of a proposed 10-year doubling of federal support for the physical sciences, NSF has benefited from bipartisan support from Congress despite increasing pressure to trim overall spending.

Lubchenco Earns Spanish Research Prize

Marine scientist **Jane Lubchenco** has won the €400,000 Frontiers of Knowledge Award in Ecology and Conservation Biology, bestowed on 5 February by the Madrid-based BBVA Foundation. Lubchenco, who will head the U.S. National Oceanic and

Atmospheric Administration until the end of this month, was distinguished for work that advanced "understanding of coastal ecosystems and laid the scientific groundwork for the design of marine reserves."

Lubchenco joins six other 2012 winners announced earlier this year. Atmospheric chemist **Susan Solomon** of the Massachusetts Institute of Technology (MIT) received an award for contributing to "the safeguarding of our planet." Electrical engineer **Lotfi A. Zadeh** of the University of California, Berkeley, was distinguished for inventing fuzzy logic. Mathematicians **Ingrid Daubechies** of Duke University and **David Mumford** of Brown University were jointly rewarded for contributions to data compression and pattern recognition. Chemist **Douglas Coleman** of The Jackson Laboratory in Maine and physician **Jeffrey Friedman** of The Rockefeller University in New York City shared an award for furthering our understanding of obesity.

FINDINGS

Comb Your Antennae

Counterintuitively, perhaps, cockroaches are quite fastidious, especially when it comes to their antennae, which the insects clean often, grabbing one with a front leg and drawing it through their mouths. Now, at last, we know why: When restrained or prevented from grooming, American cockroaches develop a shiny, waxy buildup on the antennae that clogs the tiny pores that lead to odor-sensing cells. Measurements of the electrical activity in those cells in response to sex-attractant and food odors showed that the gunk interferes with the roach's sense of smell, the



team reported online on 4 February in the *Proceedings of the National Academy of Sciences*. The insects appear to produce wax continuously, likely to keep from drying out, and grooming helps remove the excess wax as well as dust and other foreign chemicals that land on the antennae and get trapped in the gunk. When they can't groom, carpenter ants, houseflies, and German cockroaches also suffer from gunk overload, suggesting that fastidiousness is widespread.

Science LIVE

Next week, *Science* will be reporting from the AAAS Annual Meeting in Boston. Visit http://scim.ag/aaas_2013 for breaking news, podcasts, and live video chats.

BY THE NUMBERS

93 Number of recently published micro-RNA articles, out of 127, that did not comply with data-sharing guidelines, according to an analysis published this month in *Clinical Chemistry*.

\$100 million Amount of funding provided by the National Football League players union for a 10-year research project at Harvard Medical School to reduce the impact of on-the-field injuries and improve the long-term health of players.

1,000,000 Number of Twitter followers of astrophysicist Neil deGrasse Tyson, who *Time* called one of the world's most influential tweeters in 2011 and 2012.

Random Sample

A Kingdom for a Hearse?

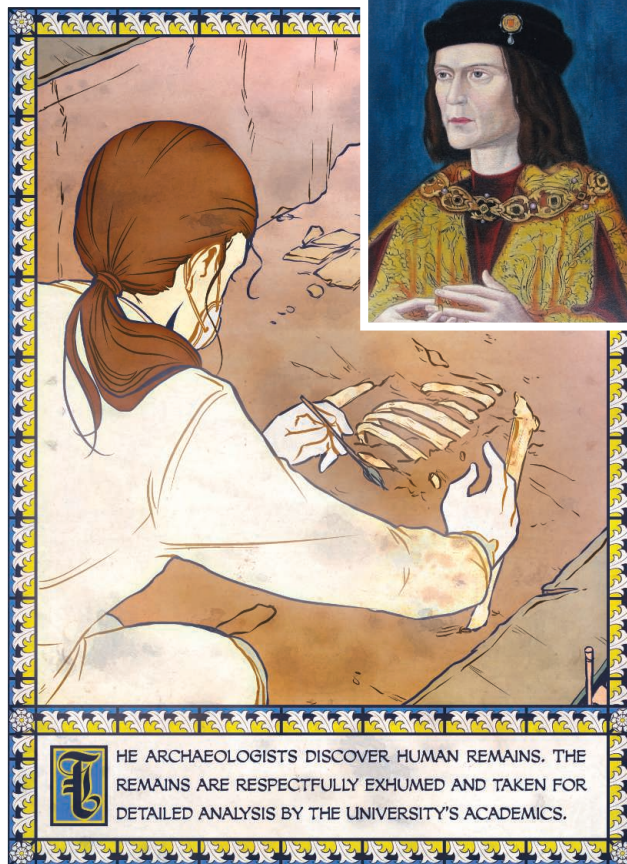
Where a medieval Franciscan monastery once stood in Leicester, U.K., there is now a humble parking lot—which concealed a historical treasure. Human remains found there are “beyond reasonable doubt” those of England's much-maligned monarch Richard III, scientists announced on 4 February at a press conference.

Richard III (inset) died at age 32 at the Battle of Bosworth Field, a battle that ended the bloody civil war known as the Wars of the Roses and established the House of Tudor as the next English dynasty. Last summer, archaeologists excavating the monastery, demolished in the 16th century and long rumored to be Richard III's final resting place, dug up a skeleton in a small grave. The individual was male, in his late 20s to late 30s, and had a feminine build, squaring with historical sources, osteoarchaeologist Jo Appleby of the University of Leicester said at the press conference.

Scientists extracted DNA from the teeth and a thigh bone and compared it to mitochondrial DNA from two known living relatives of the king, both descendants of his sister, Anne of York. It was a match, said geneticist Turi King of the University of Leicester at the press conference.

It's “a spectacular find and a great bit of research,” says battle archaeologist Tony Pollard of the University of Glasgow in the United Kingdom. But, says Ross Barnett, an expert on ancient DNA at the Centre for GeoGenetics at the Natural History Museum of Denmark in Copenhagen, “my preference would have been for this to have occurred in tandem with publication of a peer-reviewed paper.”

Richard III will be reinterred at Leicester Cathedral probably early next year, the mayor of Leicester said. <http://scim.ag/richiii>





ENERGY RESEARCH

Chu's Legacy at DOE: Some Fields Gain, Others Falter

Steven Chu, the first Nobel-winning scientist to lead the sprawling U.S. Department of Energy (DOE), has rarely been at a loss for words during his 4 years in office. So it wasn't surprising that his 3800-word letter of resignation last week contained a sweeping description of the department's accomplishments and a look ahead.

"The Department has made significant progress in breaking down the walls between our basic science and applied science programs," Chu wrote in a letter touting a major effort to expand research programs aimed at developing new, cleaner energy technologies. And that demolition is likely to stand as one of Chu's major achievements, department watchers say. "You've got to give him credit for a nimbler, more forward leaning organization that is trying to respond to some of the big hairy problems out there," says William Madia, vice president at Stanford University for DOE's SLAC National Accelerator Laboratory in Menlo Park, California.

That shift, which includes the successful launch of DOE's Advanced Research Projects Agency-Energy (ARPA-E), also reflects the priorities of President Barack Obama. "Without a doubt, the secretary has been in synch with the administration on energy," remarks James Decker, a lobbyist in Washington, D.C., who was principal deputy director of the Office of Science from 1985 to 2006. "He's done his best to support basic research related to energy.

And then there are programs that don't necessarily support that as directly. In tough budget times, those become tough choices."

At the same time, Chu gets mixed grades for his political skills. Observers say his professorial style sometimes played poorly in fights with Congress over the administration's plans to kill a national nuclear waste dump in Nevada and the bankruptcy of DOE-backed green energy companies. "It hasn't been an easy time," says Paul Alivisatos, director of DOE's Lawrence Berkeley National Laboratory in California, which Chu ran before coming to DOE. "The issue of energy has been a political football."

Chu's letter asks that his tenure be judged "not by the money we direct ... but by the character of our decisions." Notwithstanding that request, many scientists will rate him on his stewardship of the nation's single biggest funder of the physical sciences, DOE's \$4.9 billion Office of Science. And the record suggests he was largely unsuccessful in preventing flat budgets that are forcing painful retreats in several fields that have been DOE strengths.

Chu arrived in Washington as the new Obama administration was cobbling together its response to the 2008 global financial meltdown. And the \$787 billion stimulus package approved in February 2009 gave DOE an unprecedented \$37 billion windfall.

Although most of the money was ear-

Visionary? Chu, seen here trying out a three-dimensional visualization display, set DOE research on a new course.

marked for industry subsidies, there was also \$1.6 billion for projects at DOE's national labs and \$400 million for ARPA-E. That money was seen as part of a bipartisan promise for a 10-year doubling of federal funding for the physical sciences.

After Republicans reclaimed the majority in the House of Representatives after the 2010 elections, however, their top priority was to clamp down on federal spending in hopes of reducing the trillion-dollar annual deficits. As a result, DOE spending on basic research has remained essentially flat during Chu's tenure, rising 1.2% to \$4.87 billion.

That stagnation has forced some painful tradeoffs. Budgets in DOE's particle physics, nuclear physics, and fusion research programs have flat-lined, and major facilities in those fields are under threat. DOE officials have called for closing a fusion experiment at the Massachusetts Institute of Technology in Cambridge, for instance, to help pay for the United States' 2013 contribution to the \$23 billion international fusion experiment ITER, in Cadarache, France (*Science*, 30 March 2012, p. 1553). Nuclear physicists, meanwhile, are facing the possible closure of the last U.S. particle collider, at Brookhaven National Laboratory in Upton, New York (*Science*, 1 February, p. 498).

In contrast, budgets have grown—sometimes by 10% or more—in those basic research programs with close links to developing things like new biofuels, advanced materials, or high-performance computing. Those shifts had begun before Chu arrived, but observers credit him for accentuating and accelerating the changes.

These changes of direction within the Office of Science were accompanied by new initiatives elsewhere. In 2009, he obtained the department's first funding for ARPA-E, which Congress created in 2007 to jump-start work on risky but commercially promising energy technologies. Despite bipartisan support in Congress, however, ARPA-E's annual budget of \$275 million falls far short of Chu's dream of a billion-dollar agency.

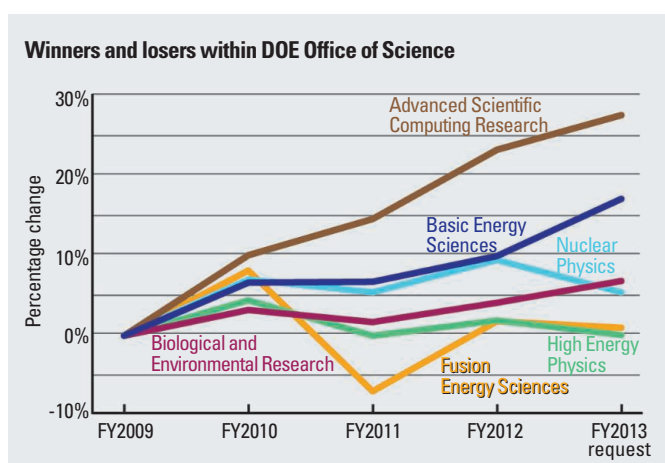
Chu also started a suite of "Energy Innovation Hubs" to allow researchers from many fields to focus in on key issues in energy research, such as producing fuels from sunlight or building more energy-efficient buildings. Chu has won approval for five centers, at \$120 million each over 5 years, although the

number of hubs and their funding levels are less than he had aimed for.

Some lawmakers have been critical of another DOE effort to speed new energy technologies into the marketplace by having the government guarantee the repayment of private loans to companies. When several firms heavily backed by DOE went bankrupt—most notably a solar panel maker named Solyndra—Republicans in Congress accused Chu of having wasted public money by trying to pick “winners and losers.” His defense of the program was seen as weak, even by some allies.

Some members of Congress have also complained about the administration’s decision to kill the long-planned Yucca Mountain repository in Nevada for nuclear waste from commercial reactors. Critics of the 2010 decision—including governors who fear their states will now be asked to take the waste—have sued to overturn the decision. But Chu has steadfastly said there is no going back, and last month DOE released a plan that calls for creating two temporary storage sites by 2025 and a permanent facility by 2048.

In his letter, Chu claims to have made “historic progress” on another waste issue—



Growth curves. Energy-related research and computing flourished during Chu’s tenure, while fusion, nuclear, and high-energy physics stagnated.

members of Congress, says Tom Carpenter, director of the Hanford Challenge, a local citizen’s group. “And he did so by forming a secret panel of scientists that operated behind closed doors.”

At the same time, Carpenter and other environmentalists give Chu kudos for his efforts to defend climate change science and his hands-on approach to finding a fix for the 2010 *Deepwater Horizon* oil spill in the Gulf of Mexico.

In his letter of resignation, Chu wrote that “I would like to return to an academic life of teaching and research.” It is unlikely it will be as tumultuous as his tenure in Washington.

—ADRIAN CHO AND DAVID MALAKOFF

With reporting by Robert F. Service.

GULF OIL SPILL

BP Research Dollars Yield Signs of Cautious Hope

NEW ORLEANS, LOUISIANA—Here’s an unfamiliar group of victims hard hit by the 2010 *Deepwater Horizon* oil spill tragedy: insects and spiders. When the scope of the Gulf of Mexico blowout became clear, ecologist Linda Hooper-Bui of Louisiana State University (LSU) in Baton Rouge and her graduate student Xuan Chen raced to add sites to their study of coastal wetlands. Kick-started by a rapid grant from the National Science Foundation, they discovered that insects and spiders were few and far between in the oiled marshes. “I would call it devastation,” Hooper-Bui says. The experiments have also shown—to her surprise—that insects continued to die in unusually high numbers even a year later, perhaps due to vapors from the oil.

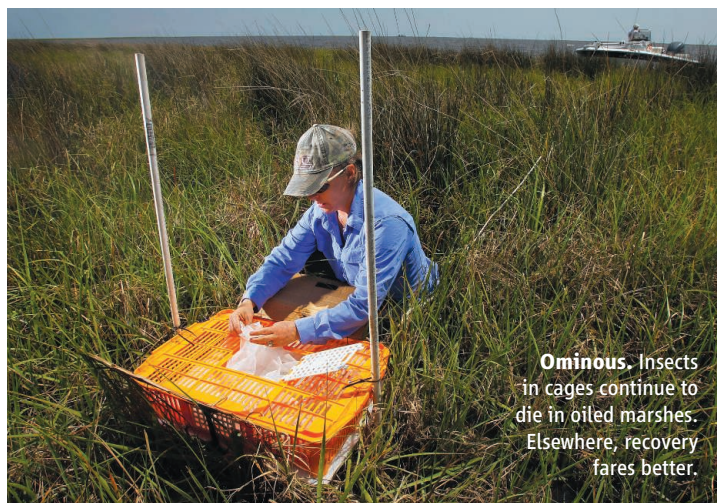
That unexpected toll was just one of the new results described at an unusual interdisciplinary conference held here late last month. The event was the first public meeting of Gulf of Mex-

ico Research Initiative (GOMRI), a nonprofit organization that is disbursing \$500 million donated by oil giant BP to scientists over 10 years. The peer-reviewed grants cover a broad range of areas, such as the modeling of ocean currents, the chemistry of oil dispersants, and the biological impact of petroleum. “GOMRI money is stimulating a huge pool of scientists to study oil spills in the

Gulf,” says geochemist Christopher Reddy of the Woods Hole Oceanographic Institution (WHOI) in Massachusetts.

Many of the researchers got their grants from GOMRI just a year ago, so results were often preliminary. But, in general, the findings sketched a picture of ecosystems beginning to recover from one of the world’s largest marine releases of hydrocarbons.

“The scars are diminishing,” says Charles “Chuck” Wilson, GOMRI’s chief scientific officer. In large part, he explains, that is thanks to microbes that evolved in the Gulf to break down the oil and gas that emerge from natural seeps in the gulf; they feasted when the broken wellhead spewed almost 5 million barrels of crude and untold amounts of methane into the sea. But scientists emphasized that much remains to be learned. It’s still unclear, for instance, “what the long term impacts of the oil in the deep-water Gulf will be,”



Ominous. Insects in cages continue to die in oiled marshes. Elsewhere, recovery fares better.

notes Scott Eustis of the nonprofit Gulf Restoration Network in New Orleans.

A major emphasis is figuring out the details of where the oil went—a full one-quarter of the estimated release is still unaccounted for—where it remains, and the toxicity of these residues. LSU ecologist Eugene Turner reported that sediments in coastal marshes still contain 1000 times the background level of aromatic hydrocarbons, although levels are decreasing very slowly. “There is a lot still out there,” he says.

One hope is that new instruments will reveal previously undetected components of weathered oil. Several presentations discussed the use of a relatively new technique called Fourier transform ion cyclotron resonance mass spectrometry. Christoph Aepli, a postdoc at WHOI, used it to identify so-called recalcitrant oxygenated hydrocarbons in tarballs collected from beaches. Traditional methods would have missed more than one-half of the compounds, says Reddy, who predicts that, “with time, you are going to see the field of oil spill science be completely changed” by such methods.

More oil is probably contained in a chocolate-brown layer on the seafloor. This fluffy gunk can be several centimeters thick and might have been deposited in what some researchers call a “dirty blizzard” of marine snow (dead microorganisms or plankton that accrete into large globs and sink). In recent lab experiments, a team led by biological oceanographer Uta Passow of the University of California, Santa Barbara, showed that, in the presence of oil, bacteria can create this snow solely with their own secretions and without larger particles from other organisms. “This is a totally new mechanism,” she said at the meeting.

Although some corals were coated with the oily snow, the broader impact on seafloor organisms isn’t clear. But if the blizzard was composed of bacteria that were feeding on hydrocarbons from the blowout, the sticky microbes could have helped clean the water column of oil droplets and fine sediment as they sank. Passow’s experiments also showed that low concentrations of the oil dispersant Corexit—which was used to break up the spill—inhibited bacterial formation of marine snow. “That’s huge,” says biogeochemist Samantha Joye of the University of Georgia in Athens, because it means the dispersant may

have made things worse by impeding the Gulf microbes’ natural ability to break down oil. Passow, who hadn’t studied oil spills before 2010, says: “I was really shocked about how little we know about oil in the system.”

To help create more effective dispersants, GOMRI is funding other projects to better understand how they work at a molecular level. Courtney Ober, a Ph.D. student in chemical engineering at Auburn University in Alabama described research on developing “smart” particles of dispersant coated with water-insoluble polystyrene that dissolves in oil. Such a formulation might reduce the amounts of dispersants needed to break up a spill and reduce the chemicals’ impacts on organisms.

Slick. Hundreds of small drifters have traced currents in the Gulf of Mexico, helping to improve computer models of how oil spills may spread.



Other GOMRI researchers want to be able to do a better job of predicting where currents will push oil slicks. During the Gulf spill, responders lacked good data on currents and so had trouble figuring out where best to locate booms to prevent oil from reaching marshes and beaches. To improve computer models, a project called the Consortium for Advanced Research on Transport of Hydrocarbon in the Environment, directed by the University of Miami’s Tamay Özgökmen, designed inexpensive GPS-enabled drifters to track so-called subscale currents, on the scale of 100 meters to 10 kilometers. Last August, researchers released a dense array of 317 drifters, the most ever released in a single deployment,

and gathered months of data.

Another big concern is the spill’s long-term impact on wildlife and the ecosystems. Much of this research is being done to inform the federal government’s effort to put a price tag on the damage caused by the spill, and it will remain confidential until a settlement or judgment is reached with BP and the other companies responsible for the spill. “Until the data are released, we’re only seeing a bit of the elephant,” says Edward Overton of LSU. “The amount of knowledge is going to explode.”

Meanwhile, researchers are getting pieces of the picture from studies such as Hooper-Bui’s look at wetland insects and surveys of various marine communities. Geochemist Isabel Romero of the University of South Florida (USF), St. Petersburg reported that total levels of polycyclic aromatic hydrocarbons in deeper-water fishes, such as hatchetfish, increased 10-fold from 2007 to 2011. The levels continued to rise in 2011 and haven’t declined yet. “There is still oil in the system and it is still affecting the fish,” she says.

A brighter note came from Steven Murawski of USF St. Petersburg who reported that skin ulcers and lesions declined significantly in shallower-water fish in the northern Gulf of Mexico in 2012. But it has been difficult to sort out how the spill may have affected overall fish populations. One major confounding factor is that officials closed many commercial fisheries during the spill—perhaps helping stressed populations to rebound. A study of blue crab numbers, for example, found no decline in 2010 and a big increase in 2011.

That “really surprised” study leader Joseph Neigel, a population geneticist at the University of Louisiana, Lafayette. Survey data showed similar increases for six species of fish and a decrease for just one. “It’s hard to draw a lot of firm conclusions, because marine populations are notoriously stochastic,” he says.

Researchers have 8 more years of GOMRI funding to help answer questions, along with other, longer-term payouts related to the spill that BP and other firms are making to the U.S. National Academies and other groups (*Science*, 30 November 2012, p. 1137). “It was a terrible accident,” says Margaret Leinen of Florida Atlantic University. But it has provided “a once in a lifetime opportunity to look at the Gulf.”

—ERIK STOKSTAD

GLOBAL CHANGE

Forecasting Regional Climate Change Flunks Its First Test

The strengthening greenhouse is warming the world, but what about your backyard, or at least your region? It's hard to say, climate researchers concede. Modelers have sharpened their tools enough to project declining grape yields in a warmer, drier California wine country and to forecast that the Mediterranean region will be getting drier in coming decades. But just how reliable such localized projections might be remains unclear.

Now, a group of global, rather than regional, modelers has tested a widely used regional model by simulating climate change, not just static past climate. That's how these researchers say all regional models should be tested, but aren't. Preliminary results show that the model improved little if at all on the

provide detailed, reliable climate projections for, say, West Texas versus East Texas. So modelers began embedding a detailed, higher resolution climate model spanning, for example, much of North America, in a global climate model. The global model would calculate broad changes and feed them into the embedded regional model, which would then compute more-detailed (and, presumably, more-accurate) simulations of smaller atmospheric features, such as storms and fronts, as well as better rendering of the atmospheric effects of surface features such as coastlines and mountains.

But was regional modeling doing any better than global modeling at making regional predictions? Pavan Racherla, Drew Shindell,

and Gregory Faluvegi, all of GISS, tackled the question while doing regional modeling for a climate impacts study. "The first thing we wanted to do was evaluate the [model] output," Shindell says. "That's what we do with [global] models." But they found that regional modelers were checking model performance only when simulating climatology, the average climate for a given period of time. "That was strange," Shindell says. "The key thing we look at is climate change. That hasn't been the standard in regional climate modeling."

WRF did not shine. "Skill capturing climatology does not translate into skill capturing climate change," Shindell concludes, echoing the group's paper of late last year in the *Journal of Geophysical Research: Atmospheres*. "There is modest improvement over the [global] model, but it's not so large." And most of that improvement came only when the global model was periodically allowed to "nudge" the wandering regional model back toward a more realistic broad-scale pattern of climate.

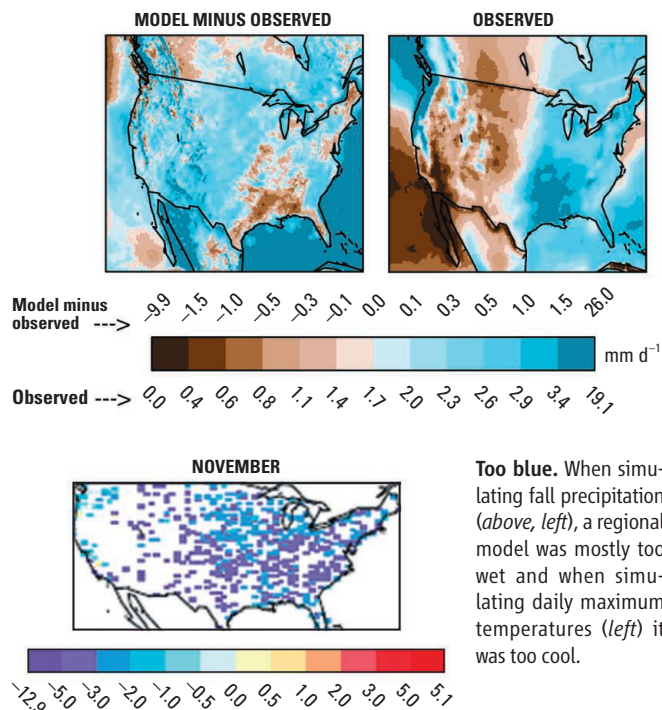
The GISS group does not identify why WRF failed to improve significantly on their global model, but Shindell suspects it has something to do with what the two kinds of models are best at. Climatology is determined mainly by the interplay of the land, sea, and topography with the atmosphere, which is regional models' forte, he says, but those aren't changing. Climate change, on the other hand, progresses by changes in physical properties such as the migration of jet streams, changes in cloud cover, and shifts in precipitation patterns, which a global model handles pretty well on its own.

Other researchers say the GISS group has tackled a problem that has too long been neglected. "It's an intriguing, very thought-provoking paper," says climate scientist Robert Wilby of Loughborough University in the United Kingdom. "It's a first step that's to be applauded." But it's far from a knockout punch to regional modeling. Instead, "it really highlights how tricky it is to show the value added" by regional modeling, Wilby says.

Regional modeler Lai-Yung Ruby Leung of Pacific Northwest National Laboratory in Richland, Washington, agrees. "The questions they ask are the right questions, but it would be much better if done in a multimodel experiment," she says: Different models in different combinations could identify model strengths to be exploited and weaknesses to be avoided.

Leung is a co-principal investigator of the North American Regional Climate Change Assessment Program (NARCCAP), which ran six regional models in 12 possible combinations with four global models. But the climate changes of recent decades were so small and the natural variations of climate so large, NARCCAP models were not tested against past climate change as the GISS team did. That, Leung says, is really a job for a larger, more international program.

—RICHARD A. KERR



fuzzy view of future climate provided by a globe-spanning model. More such testing "is something that the [regional modeling] community needs to do to get its act together," says global climate modeler Gavin Schmidt of NASA's Goddard Institute for Space Studies (GISS) in New York City who was not involved in the work.

Regional modeling was the natural next step for climate modelers. To predict next week's weather, much less the next century's climate, models have to take in the whole planet. But after several decades of development, those planet-scale models still couldn't

does a better job simulating climatology, the three wondered, will it also do a better job forecasting climate change? To at least begin to find out, they considered a widely used regional model—the Weather Research and Forecasting (WRF) model—embedded in the global GISS-ModelE2 over the continental United States. They simulated the climate of two periods, 1968 through 1978 and 1995 through 2005, to see how WRF did at simulating climatology. Then they subtracted the earlier period from the later one to see how WRF handled climate change.



INTELLECTUAL PROPERTY

Supreme Court to Review the Scope Of Monsanto's Seed Patents

Vernon Hugh Bowman, a 75-year-old farmer from Indiana, is heading to the U.S. Supreme Court this month to challenge the agribusiness giant Monsanto over its "Roundup Ready" soybeans, one of the biggest selling products of agricultural biotechnology. The fight centers on the company's patented genes, which enable plants to grow even after being treated with the widely used weed killer Roundup (glyphosate). The key issue is where DNA patents end: Do they apply to the seeds' entire progeny, or just to seeds sold under license? Bowman argues that patents don't apply to unlabeled seeds he got from a grain elevator. Monsanto says they do.

Two lower courts have sided with Monsanto. The U.S. government agreed, asking the Supreme Court last year not to hear this case. But the justices took it up anyway, scheduling oral arguments for 19 February. Bowman and his supporters argue that accepting Monsanto's view would effectively give the company a monopoly on all U.S. soybean planting, make every farmer a potential patent infringer, and raise food costs. Monsanto counters that if it cannot control planting of any seeds containing its patented genes, it would lose patent rights (and revenues) as soon as a new product is introduced. Monsanto believes that a decision to support Bowman would "devastate innovation in biotechnology."

At this writing, 23 amicus briefs have been filed. Patent law groups have lined up behind Monsanto, as have farm organizations, agriculture research groups, and the Biotechnology Industry Organization. Five briefs opposing the company include those

from long-time adversaries of Monsanto and genetic engineering—the Center for Food Safety in Washington, D.C., and the Berlin-based Save Our Seeds. The nonprofit Public Patent Foundation of New York City, which will argue for a ban on human gene patents in a case before the Supreme Court in April, also backs Bowman.

As Bowman tells it, he got into this fight because of his "dumb tightwad" method of farming. He grows wheat and soybeans in Knox County, Indiana, on more than 240 hectares that belong to his family. In 1999 he tried an experiment. After the first harvest, he often plants a second crop, but he doesn't like to invest a lot of money in it, he says, because heat, drought, and floods are more likely in late summer. To get a good second crop, you need to plant twice as many seeds. For his first planting, Bowman bought Monsanto-licensed seeds and followed all the rules, which permit planting for a single harvest. For the second planting, he bought cheap "commodity seeds"—generally sold for industrial use or animal feed—from a grain elevator. Such "junk seeds," Bowman figures, are less than one-fifth the cost of licensed seeds. It is "illegal" under federal and Indiana laws to sell unlabeled seeds for planting, Bowman admits. But he argues that nothing forbids a farmer from planting them.

When Bowman's second crop came up in 1999, he treated it with glyphosate, just like the first crop. This chemical kills plants by blocking an enzyme needed for growth. Bowman's second crop flourished because most of the seeds from the elevator contained Roundup Ready genes, which produce a

Monopoly beans? Nearly all U.S. soybeans carry patented genes, but a farmer says he shouldn't need permission to plant them.

growth enzyme that isn't blocked by glyphosate. This technology is so popular that nearly all soybeans grown in the United States contain Roundup Ready genes. Bowman sold some of his second-crop seeds back to the elevator and kept some for planting.

Bowman claims that he wrote to Monsanto and its licensee, Pioneer Hi-Bred, several times. But he says they never told him not to plant commodity seeds. He adds: "In all the literature that Monsanto put out, there was never one word about getting seed from an elevator." Monsanto sued him for patent infringement in 2007. A U.S. federal court ruled against Bowman in 2009, assessing damages of \$84,456.30 plus costs. An appeals court affirmed the decision in 2010. Bowman appealed to the Supreme Court.

In its brief to the Supreme Court, Monsanto claims that Bowman knew exactly what he was doing when he sprayed glyphosate on his second crop—he was selecting for Roundup Ready plants. Although the company maintains a large staff to find cheating farmers, it says it does not sue those who "inadvertently" plant Roundup Ready seeds, for instance, through accidental cross pollination or mixing of seeds. It is illegal to deliberately "make" a patented technology without a license, the company says. Bowman argues that nature made the plants.

The brief by the Center for Food Safety and Save Our Seeds argues that Monsanto is trying to dominate the seed industry by expanding the reach of its patents. It also alleges that by prohibiting experimental planting of its seeds, it has "suppressed independent scientific research on the potential impacts of transgenic crops." Innovation will suffer, it argues.

On the contrary, argues the brief of a nonprofit bioindustry group in New York City, called BayhDole25: Innovation would suffer if the court does not uphold Monsanto's claims on commodity seeds. And revenues from patent licenses would dry up without such patent protection, reducing support for continued research and development. The BayhDole25 group dismisses as "disingenuous" Bowman's argument that Monsanto's rules apply only to his first crop. And it suggests that he was using the grain elevator as a way to "launder" violations of the patent agreement.

Bowman plans to file a final response brief in the case this week; the court is expected to deliver a decision by June.

—ELIOT MARSHALL



Giant Marine Reserves Pose Vast Challenges

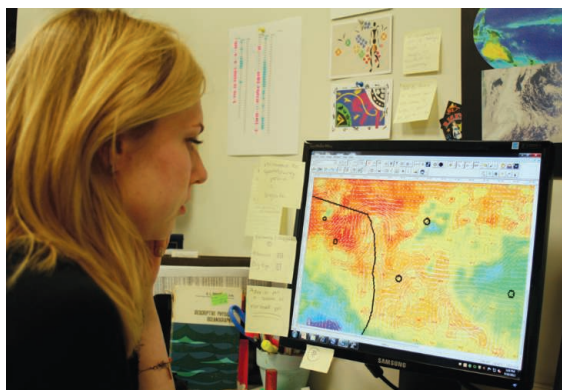
Huge no-fishing zones might save widely traveled tuna and other species, but monitoring their effectiveness—and enforcing catch bans—will require new approaches

HERNDON, VIRGINIA—On a typical workday, Alyson Kauffman pores over oceanographic data streaming into her computer from all over the world, including maps of plankton concentrations and water temperatures. Then, the analyst at GeoEye, a satellite company headquartered in this Washington, D.C., suburb, sends reports to her clients, who are fishing vessel captains at sea. Each report highlights otherwise invisible “hot spots” where they might find concentrations of valuable species such as tuna and swordfish. “Our job is to make fishing vessels more efficient,” she says.

A growing number of those hot spots, however, are becoming off-limits to such high-tech fish killers. Over the past 6 years, the United States, Australia, and the United Kingdom have created huge marine reserves that have banned fishing in more than 1.9 million square kilometers of ocean—an area equivalent to the size of Mexico. And more “megareserves” are on the way, with nations seriously considering plans to ban fishing in an additional 3.6 million square kilometers of marine habitat over the next few years (see map).

Unlike an older generation of preserves that mostly focused on small patches of coral or coastal fish stocks, these vast new sanctuaries are designed to protect high-seas ecosystems that include fish and other animals that routinely wander over huge territories.

The trend delights conservation scientists who are worried about overexploitation of the world’s oceans. The reserves “are a real game-changer,” says fisheries scientist Daniel Pauly of the University of British Columbia, Vancouver, in Canada. Fishing fleets now have technology that allows them to penetrate even remote, deep waters that once “served as refuges for a lot of fish,” he



Eye in the sky. Satellite images designed to help fishermen could also be used to spot poachers.

No go. New reserves are off-limits to commercial fishing boats, such as this tuna seiner in Micronesia.

notes. “There’s an urgent need to replace them with big, manmade protected areas.”

Giant reserves are also posing unprecedented challenges to scientists and policymakers, however. Researchers are struggling to design and fund studies that will enable them to monitor changes over vast areas and determine whether the reserves are actually helping to rebuild marine populations. And managers are trying to figure out how they can affordably enforce fishing bans in remote waters. Some environmentalists, meanwhile, fear that the push to create megareserves could become a charade if nations are allowed to take credit for conservation without actually giving the new sanctuaries real protection.

The big three

Three giant reserves have so far attracted most of the attention. In 2006, then-President George W. Bush designated some 362,000 square kilometers around the Northwestern Hawaiian Islands as a U.S. Marine National Monument in which all exploitation would be banned. The United Kingdom followed in 2010 by creating a much bigger reserve around the Chagos Islands in the Indian Ocean. Last year, Australia banned all fishing in much of the Coral Sea—at 989,842 square kilometers, the biggest no-take zone in the world.

Of the trio, only the Chagos Islands reserve had been heavily fished—primarily for tuna. Most of those stocks are now depleted, and conservationists hope the sanctuary will help restore them. But commercial fishers—who largely opposed the creation of the reserve—have their doubts. Speedy tuna can travel great distances, notes Julio Moron of OPAGAC, the Spanish tuna fleet association headquartered in Madrid, so even a megareserve will have “have negligible effects on the pelagic [open-ocean] ecosystem,” he predicts.

Mainstream marine biologists are more optimistic. Studies in the nearby Pacific have found that tuna there don’t necessarily swim vast distances, so some scientists believe that some Chagos tuna could spend their entire lives inside the nearly 1000-kilometer-wide preserve. “Tuna don’t migrate randomly,” says Heather Koldewey, a geneticist at the Zoological Society of London. “They stay near seamounts, islands, upwellings, and good feeding grounds—and the Chagos provide all these.” Bruce Collette, a senior scientist at the Smithsonian Institution’s National

Museum of Natural History in Washington, D.C., predicts that Chagos stocks could “reach a density not seen on Earth in many decades.” And tuna won’t be the reserve’s only beneficiaries, adds marine ecologist Charles Sheppard of the University of Warwick in Coventry, U.K. “The tuna ban also stops the loss of sharks, billfish, seabirds, and turtles” that tuna fishers once killed unintentionally.

A monitoring challenge

Proving that the reserve is helping tuna and other species, however, could be difficult. Prior to the ban, researchers relied largely on catch data to make population estimates. Now, with fishing boats banned there, they are exploring alternatives.

On a cruise through the Chagos reserve late last year, for example, researchers tested some electronic eyes that can count creatures without killing them. Jessica Meeuwig, a quantitative ecologist at the University of Western Australia in Perth, suspended in midocean a crosslike device with two cameras pointed at a bag of bait designed to attract fish. The cameras record for 3 hours, enabling the researchers to “determine what species are present, their relative abundance, and their size,” she says. And by returning to study sites repeatedly over time, researchers should ultimately be able to determine if the populations are, in fact, increasing.

Biological oceanographer Andrew Brierley of the University of St. Andrews in the United Kingdom has taken a complementary approach, using a state-of-the-art echo sounder to survey the waters around Meeuwig’s cameras for fish and other animals. The sonar data “will tell us how representative the pictures are of that part of the ocean,” he says.

Sanctuary managers, meanwhile, are trying to get their arms around how best to prevent poaching within their vast domains, which can take days to cross in ships. One option, using satellite imagery and data to spot poachers, is getting a close look in studies funded by the Pew Environment Group of Washington, D.C. “Satellite sensing is not cheap, but it’s a lot cheaper than sending [an airplane] to patrol a big area,” says John Amos, president of SkyTruth, a nonprofit organization based in Shepherdstown, West Virginia, that is exploring the idea. He believes companies like GeoEye that help fishers find

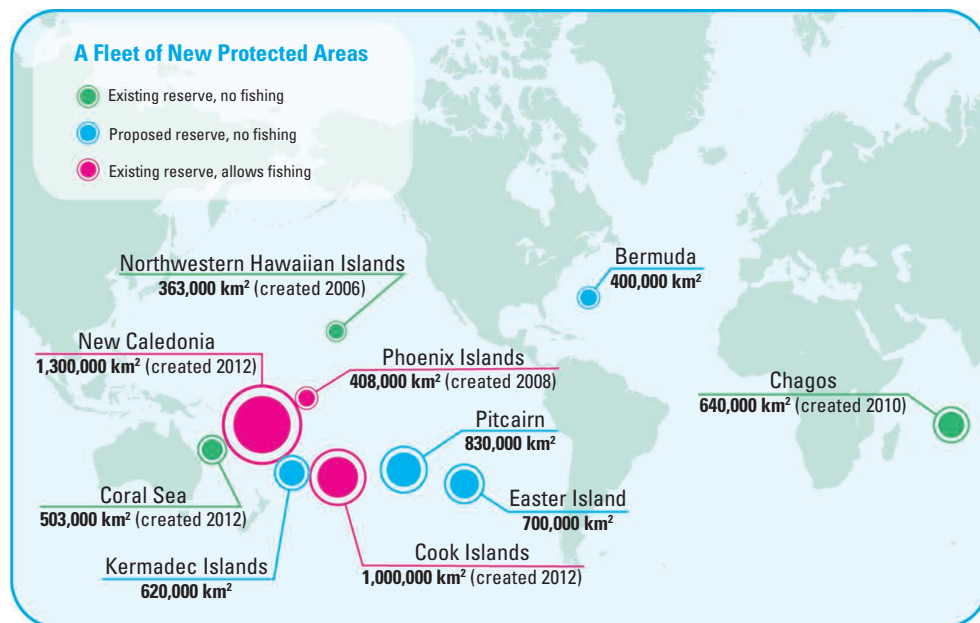
their catches now produce imagery that is detailed enough to help identify vessels that are breaking the law. (GeoEye officials say they would be ready to help.)

Mega-expansion

The enforcement challenge could soon get bigger. Five more giant no-take reserves are now on the drawing boards, notes Jay Nelson, director of Pew’s Global Ocean Legacy program, which has played a major role in promoting the idea. They include efforts to protect the United Kingdom’s Pitcairn Islands and Bermuda, the Kermadec Islands of New Zealand, and Chile’s Easter Island. “The time to create large, well-protected marine reserves is before they’re targeted by the industrial fishing fleets,” Nelson says. “Ten years from now will be too late.”

to the administrators of the Hillary Institute of International Leadership awards in New Zealand and the U.S. Peter Benchley Ocean Awards, who said that they thought the whole reserve was fully protected when they gave awards to Tong last year. Current plans, developed with the assistance of the nonprofit Conservation International in Arlington, Virginia, call for increasing the total no-take area to 25% of the Phoenix reserve in 2014. “Because of its strategic location, it could play an important role conserving tuna if all of it became a no-take area,” Pauly says.

Similar fine print accompanies some other recent announcements of megareserves. This past summer, the Cook Islands announced that it would create the world’s biggest marine park, covering



Still, the public and the press may need to carefully scrutinize any new grand marine conservation claims to avoid misunderstandings. For instance, President Anote Tong of the Pacific island nation of Kiribati won several environmental prizes after he created the 408,000-square-kilometer Phoenix Islands Protected Area in 2008. He has repeatedly called it “a fully protected marine park, ... off limits to fishing and other extractive uses.” But, in fact, fishing is forbidden in just 3% of the reserve, which is located in the Central Pacific, home to the world’s last major tuna stocks. In the rest of the reserve, just as in the rest of the Central Pacific, fishing by foreign fleets has continued at a pace that regional fisheries scientists have warned is excessive. This was news

1 million square kilometers of the southern Pacific. New Caledonia quickly trumped that with the announcement of a 1.4-million-square-kilometer preserve. Neither, however, plans to restrict fishing.

Still, conservationists are pleased that nations are thinking big. If nothing else, megareserves that ban fishing can be cost-effective, notes Ashley Strub, a fisheries economist at the University of British Columbia, Vancouver. Her research has found that a small reserve can cost 100 times more per square kilometer to set up and administer than a giant one. But big reserves don’t necessarily replace small ones, she adds. “Coastal and small-island reserves protect different species than open-ocean ones,” she says. “You need both.”

—CHRISTOPHER PALA

PROFILE: JOHN SHEA

Archaeologist Hammers Away At 'Modern' Behavior

Stone tools suggest that the earliest modern humans were as smart as we are—they just had different problems to solve, an archaeologist argues

STONY BROOK, NEW YORK—One day in the late 1980s, an alarmed secretary at Harvard University called campus police. An apparently crazed young man had cornered a deer in the courtyard of the university's Peabody Museum and was hurling spears at it. Once on the scene, however, the police established that the deer was dead when it arrived on campus, and that archaeology graduate student John Shea was simply doing research: He was trying to understand how striking a large mammal damaged stone points.

That episode, says then-fellow Harvard grad student Daniel Lieberman, was a prime example of "John Shea being John Shea." It demonstrates Shea's hands-on, take no prisoners approach to prehistory, says Lieberman, who is now a paleoanthropologist at Harvard. "John is always a little on the edge. ... He doesn't just sit back in the lab and ponder the Paleolithic, he tries to understand it on its own terms."

Shea, now at New York's Stony Brook University, has remained on archaeology's cutting edge despite his reputation for occasional outrageousness. His stone tool studies have helped archaeologists identify how stone points were used, and he has documented the sophisticated toolmaking skills of the oldest known *Homo sapiens*. More recently, Shea has been doing his best to shake up human origins research with a radical proposal: That the idea of "behavioral modernity"—a term long used by scientists to describe behaviors such as the use of symbolism, art, and elaborate tools—should be thrown into the scrap heap.

Shea argues that the first *H. sapiens* about 200,000 years ago had cognition fully equal to ours today. Instead of studying how our species gradually acquired "modernity," he urges

analyzing our "behavioral variability," or the number of different ways we adapted to changing conditions. "The concept of modernity has been like a security blanket," Shea says. "But it's a 19th century model, the idea that evolution is directional and ends with us modern humans. It's an embarrassment, and we don't need it anymore."

Although many researchers agree that the concept of modernity has lost much of its usefulness, many are less eager to embrace Shea's proposed alternative. "The traditional concept of behavioral modernity does need to be replaced," says archaeologist Curtis Marean of Arizona State University, Tempe,

who calls Shea "a major figure" in the field. But "I am unconvinced that John's behavioral variability is the correct replacement."

A wild child

The young man who brought a woodland creature to a Harvard courtyard was himself a child of the forest. Shea grew up in eastern Massachusetts, the oldest of three sons born to working class parents of Irish and French ancestry, and spent his early years hiking and fishing in nearby woods. "Mom and Dad would have been perfectly happy if I worked in a factory," says Shea, whose stocky body seems ready-made for manual labor. But a local biology teacher, seeing his love of nature, encouraged him to go to college.

In high school, Shea became interested in flint knapping, and while an undergraduate at Boston University, he perfected his technique so that he could fashion a hand ax in a matter of minutes. "It was instant gratification, and you can do it outdoors."

Shea's proficiency at making stone tools spurred his success as an archaeologist, says his Stony Brook colleague John Fleagle. "He has a deep appreciation of the effort that goes into the creation of different kinds of tools, and he is less bound by abstract typology and closer to the perceptions of the prehistoric people who made them."

Indeed, it was in part his flint-knapping talents, Shea says, that won him a spot as a graduate student at Harvard. Yet Shea feels that he never really fit in there. "Academia requires you to think before you talk, whereas I talk before I think."

Shea's self-critique is shared by many colleagues, although not all view it negatively. "He often comes up with outlandish ideas and just blurts them out," says Harold Dibble, an archaeologist at the University of Pennsylvania. Dibble recalls one conference where graduate student Shea "shocked most of the

archaeologists in the room" by arguing that impact fractures on a common type of stone artifact showed that they had been used as projectile points. That idea is now widely accepted. "This is a trait of some very



Making his point. John Shea thinks modern humans were cognitively advanced long before they etched this piece of ochre (inset) 77,000 years ago.

CREDITS: SARAH PILLIARD; (INSET) CHRISTOPHER HENSHILWOOD

Downloaded from www.sciencemag.org on February 8, 2013

intelligent people,” Dibble says. “They are not afraid to be wrong and enjoy throwing out ideas and seeing what happens.”

The road from modernity

The turning point in Shea’s thinking about modernity came around 2002, when he, Fleagle, and others reopened excavations at Omo Kibish in Ethiopia. Back in the 1960s, Richard Leakey’s team had found *H. sapiens* fossils at this site, and the new team redated those fossils to 195,000 years ago, making them the oldest known modern humans.

Many researchers had long perceived an apparent gap between when humans started to look modern in anatomy and when they started acting modern, as shown by their stone tools and other artifacts. But Shea was sitting at the site one day, looking at stone points the team had found, when he had an epiphany. The points “were very well made, nothing primitive about them at all—they were like what I would make to show off,” he recalls. “Suddenly it hit me right in the head. These were people just like me. They just had different challenges to face.” There was no sense trying to track these humans’ progression to modernity, Shea says, because they already were modern.

To test this insight, Shea undertook a broad study of African stone tools. In a 2011 paper in *Current Anthropology*, entitled “*Homo sapiens* Is as *Homo sapiens* Was,” Shea analyzed stone tools from 10 sites in Africa associated with either *H. sapiens* or its immediate ancestors, dated from 284,000 to less than 7000 years ago. If the modernity concept was correct, Shea argued, there should be significant behavioral differences over time, with younger sites having more types of stone tools—showing specific and flexible adaptations to the environment—as well as more sophisticated tools overall.

Instead, Shea found that with just one exception, the oldest modern humans in Africa used just as wide a variety of stone tools as later humans of the early Upper Paleolithic period—long considered the time when modern behavior began to flourish—whose tools fell into four widely accepted types.

Shea concluded that early *H. sapiens* were as cognitively advanced as those today. Differences in the most ancient artifacts did not reflect a different level of cognition in their makers, but simply the need to create objects to suit different environmental and social conditions. Indeed, fully modern people haven’t always used “sophisticated” tools. For example, 40,000 years ago the first Australians used relatively simple tools

compared with the spectacular artifacts of the European Upper Paleolithic (EUP) of the same time.

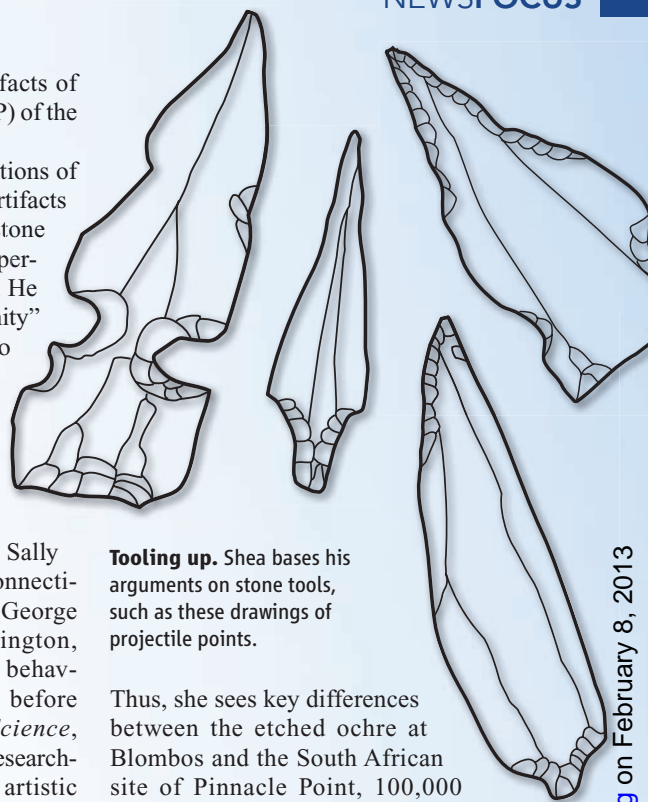
Shea noted that traditional definitions of “modernity” were biased by lists of artifacts characteristic of the EUP, such as stone blades, tools made of carved bone, personal ornaments, and cave paintings. He decided that the concept of “modernity” could no longer be used as a guide to understanding modern humans, who first emerged in Africa more than 150,000 years earlier.

Indeed, a decade before Shea’s article, an influential paper had warned against defining “modernity” with EUP behaviors. In 2000, Sally McBrearty of the University of Connecticut, Storrs, and Alison Brooks of George Washington University in Washington, D.C., argued that modern human behavior had deep roots in Africa long before *H. sapiens* colonized Europe (*Science*, 15 February 2002, p. 1219). Other researchers have noted that symbolic and artistic behaviors flicker in and out of the record tens of thousands of years before becoming permanently established, perhaps because of demographic rather than cognitive factors (*Science*, 9 April 2010, p. 164).

But Shea’s critique “is probably the most comprehensive to date,” says archaeologist James O’Connell of the University of Utah in Salt Lake City. Shea argues that no one set of behaviors—such as art—proves advanced cognition. Thus, he remains unimpressed by discoveries that some others see as milestones of “modern” behavior, such as 77,000-year-old pieces of ochre with etched patterns from Blombos Cave in South Africa, sometimes heralded as the earliest art (*Science*, 11 January 2002, p. 247). Shea thinks the Blombos people created those etchings because that was their style, not because they suddenly had become able to think abstractly for the first time. “What, were the Blombos people retarded?” Shea asks rhetorically. “That’s a pretty pessimistic view of early humans, that scratching a rock with a tic-tac-toe pattern is some kind of threshold of cognition.”

Shea seems confident that his assault on behavioral modernity will end up killing off what he sees as a fatally flawed concept. “Sally and Alison led the way,” he says of McBrearty and Brooks. “They wounded the beast; I’m cutting off its head and putting it on a stick.”

But Brooks says that the concept still has advantages: “It implies an evolutionary trajectory, which variability does not.”



Tooling up. Shea bases his arguments on stone tools, such as these drawings of projectile points.

Thus, she sees key differences between the etched ochre at Blombos and the South African site of Pinnacle Point, 100,000 years earlier, which has ochre but no etchings.

Other researchers are giving Shea’s new ideas qualified praise. “Unlike modernity, the concept of behavioral variability is quantifiable and amenable to statistical analysis,” says archaeologist Metin Eren of the University of Kent in the United Kingdom. All the same, O’Connell says, the research community “will need to hear more before buying in.” Dibble agrees: “The problem is how to test” Shea’s idea.

Some testing has already begun. In a paper published last month in the *Journal of Archaeological Science*, Eren’s team analyzed variability in the use of a specialized technique for producing stone flakes—placing a stone core on an anvil and striking it with a hammer instead of performing this task in midair—at the Mumba Rockshelter in Tanzania. The team found that the use of this technique came and went over time, and that it was more likely to have correlated with changing climate and demographic factors than any cognitive “revolutions.”

Shea and Fleagle are planning more tests: They have just received grants to return to Omo Kibish to compare behavioral variability between older and younger archaeological layers, and hope to start next year. “We’re focusing on the actual properties of the archaeological record,” Shea says, rather than searching for elusive signs of modernity, “which is just a metaphorical construct.”

—MICHAEL BALTER

Losing Arable Land, China Faces Stark Choice: Adapt or Go Hungry

To ensure food security, China is racing to develop new cultivars of staple grains that thrive in a warmer world

YUCHENG, CHINA—Hou Ruixing weaves his way through plots of winter wheat, stopping beneath an infrared heater suspended from wooden crossbars. The make-shift lamp and others arranged at 15-meter intervals at Yucheng Integrated Agricultural Experimental Station are simulating climate change by nudging up the thermometer an extra 1.6°C—the average annual temperature increase that models predict

as flood control, drought, wind erosion, and soil alkalinity. To this list of concerns, researchers have now added climate change and its potential impact on grain yields. “We want to know how crops will reflect global warming,” says Tao Fulu, an agricultural meteorologist at the Institute of Geographic Sciences and Natural Resources Research of the Chinese Academy of Sciences in Beijing.



Hard row to hoe. Warming is expected to trigger more episodes of heat stress that can sterilize the pollen of China's most important staple grain: rice.

will take hold here by 2030. Hou, a graduate student who lives 8 months a year on station grounds, points at two rows of wheat, explaining how traditional hand tilling and machine tilling trap different amounts of heat and water in the soil. “There are many experiments in the lab,” Hou says. But nothing beats testing how new cultivars perform in the field.

Online
sciencemag.org

Podcast interview
with author
Christina Larson (http://scim.ag/pod_6120).

For half a century, Chinese scientists have been flocking to this spot on the eastern rim of the North China Plain, China's breadbasket, to probe pressing agricultural questions. The region just north of the Yellow River is ground zero for tackling food-security challenges such

Across the globe, scientists and policymakers are studying how climate change will affect agriculture. But in China, the question is especially urgent. The country has roughly 20% of the world's population but only 7% of its arable land—a share that is shrinking in the face of rapid urbanization. From 1998 to 2006, more than 860,000 hectares of arable land were swallowed up by cities each year on average, according to data from China's Ministry of Land and Resources. Changing dietary habits, meanwhile, are fueling a rapid rise in food consumption. Accompanying the expansion of China's middle class is a growing appetite for meat, which heaps more pressure on land and water resources. In 1978, China's total meat consumption was 8 million tons, but by 2012 it had ballooned to 71 million tons,

according to the Earth Policy Institute, a think tank in Washington, D.C. In 2011, one-third of China's total grain harvest was converted to feed for livestock and aquaculture.

Climate change could exacerbate the fallout. According to the Chinese government's Second National Assessment Report on Climate Change in 2011, rising sea levels are likely to threaten China's eastern rice-growing regions by 2050, about the time that eight provinces in the north expect to face severe water shortages.

Already, annual mean temperatures near Yucheng rose 0.8°C between 1955 and 2011, according to China Meteorological Administration (CMA) records. The uptick is felt most in winter and spring—coinciding with the growing season for winter wheat, the region's most important staple crop. Charting how warming affects various plant growth stages, from seed maturation to flowering to maturity, is “very important to understanding the impact of climate change,” Tao says.

His group has discovered that contrary to conventional wisdom, rising temperatures in China's heartland are translating into shorter overall growing periods. Although warming accelerates the early stages of wheat growth, the length of the reproductive period—the phase spanning flowering and maturity—remains roughly the same for cultivars now commonly grown in the region. Tao and others are trying to tease out what that means for future yields, which are determined by grain number multiplied by the weight of each grain. “The number of grains is determined in the middle of the season, while the weight of each grain is determined during the reproductive phase,” explains David Lobell, an agricultural scientist at Stanford University's Center on Food Security and the Environment in Palo Alto, California. At Yucheng, Lobell suggests, faster growth may mean fewer grains, spelling lower yields. Unless, that is, researchers develop cultivars better suited to the changing conditions, Tao notes.

By comparing records compiled by CMA and provincial agricultural departments between 1980 and 2008, Tao has attempted to tease out the climate signal from other factors affecting yield, such as crop management and fertilizer use. In a paper published online last October in *Climate Research*, Tao linked changes across China in temperature, precipitation, and solar radiation over those 3 decades with 1.3% and 1.7% reductions in projected wheat and maize yields, respectively. That translates to hundreds of thousands of tons

of lost harvest. A team at the Chinese Academy of Agricultural Sciences in Beijing and the International Food Policy Research Institute in Washington, D.C., has also identified a significant impact from climate change. They reported in *Agricultural and Forest Meteorology* in 2009 that warming caused a 4.5% decline in growth of wheat yields across China from 1979 to 2000.

Regional variation complicates the picture. In frigid northern China, where annual mean temperatures have risen faster than the national average, warming has extended arable land northward. But the potential agricultural benefits may be hard to reap, Tao warns, as climate change is expected to increase the frequency of drought and extreme weather events in an already water-stressed region.

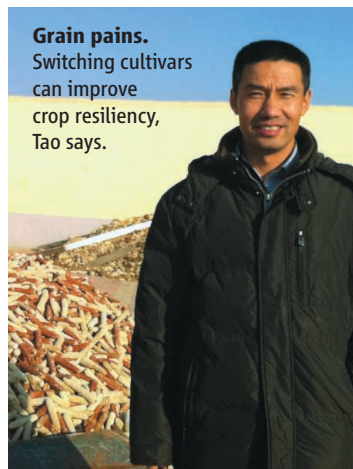
Much of northern China is dry, making agriculture dependent upon irrigation from the Yellow River and the northern China aquifer. But pollution has degraded the quality of China's "Mother River" and growing cities are siphoning off water for urban uses. Some 120 billion cubic meters more water were pumped from the aquifer than were replaced by rainfall over the last 4 decades, resulting in a steadily retreating water table (*Science*, 18 June 2010, p. 1462). "The main

have been equipped with ultrasonic wave sensors to measure water levels; data are fed in real time to a local water-use association. On the experimental station's grounds, farmers can check their water usage data at a computer terminal set incongruously next to a mound of dried corn kernels.

In rice-growing south-eastern China, warming may boost yields in the short term, but it is also likely to heighten damage from heat stress. "The increasing frequency of high temperature days is a risk factor," Tao says. Timing is critical: If rice is subjected to temperatures greater than approximately 37°C during pollination—as happened during a particularly roasting stretch during the summer of 2003—the pollen may be sterilized. "Even a brief exposure to high temperatures can lead to extremely reduced yields," says Jerry L. Hatfield, an agricultural scientist at the U.S. Department of Agriculture's Agricultural Research Service in Ames, Iowa.

Faced with such threats, China is mull-

Grain pains.
Switching cultivars
can improve
crop resiliency,
Tao says.



from Chinese research bodies. Among the trends he has noted so far is an upward spike in the frequency of weather-related disasters, including drought and wild temperature extremes.

Potential adaptation strategies for food security include altering sowing and harvesting dates, adjusting irrigation schemes, and selecting or developing cultivars equipped to thrive in new climate

conditions. Research from other parts of Asia could prove useful in China. At the Los Baños, Philippines-based International Rice Research Institute (IRRI), scientists are working to identify cultivars that release pollen during the early morning hours, before temperatures climb too high. The institute has also developed cultivars with greater flood and drought tolerance that are now in pilot trials in eastern India, where rice harvests largely depend on variable rainfall. "We are cautiously optimistic that we can develop rice varieties that will tolerate much of what climate change has to throw at us," says IRRI Director Robert Zeigler.

Back here in Yucheng, some locals are not waiting for a scientific verdict on how to adapt. Zhao Xiazhen, a 47-year-old farmer sporting a bright orange headscarf, says that in recent years, temperatures have been creeping up in late October, the sowing season for winter wheat. About 5 years ago, her family noticed that their wheat was growing more rapidly than before. If it were to mature too quickly, they would risk losing part of their harvest to frost damage; here, fast-maturing wheat plants are more fragile. To avert crop losses, they began delaying sowing by 5 or 6 days. Their harvests have held steady. Other farmers who have stuck with what has worked in the past haven't been so lucky, Zhao says: "Their crop was damaged."

Translating such observations into policy will ultimately require more research into shifting temperatures and precipitation patterns, says Li Yunsheng of the Institute of Geographic Sciences and Natural Resources Research. Employing a standard refrain for adapting any system to China's circumstances, Li says: "We are studying climate change with Chinese characteristics."

—CHRISTINA LARSON

Christina Larson writes on science in China.

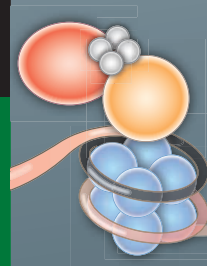
Food security frontlines. Rapid plant maturation and water shortages are threatening wheat in the north; heat stress and rising sea levels are the big worries in rice-growing areas in the south and east.



problem in this region is water," Tao says.

In a pilot project launched in Yucheng in 2009, farmers are charged for the actual amount of water they draw from irrigation networks, rather than according to their acreage. Old concrete irrigation channels

ing adaptation strategies. "The government doesn't yet have a very clear idea" of how to design adaptation policies, but it wants to understand the whole situation," says CMA scientist Zhou Guangsheng, who is compiling data on climate change and agriculture



LETTERS

edited by Jennifer Sills

Physical Laws Shape Biology

IN THE PERSPECTIVE “A DYNAMICAL-SYSTEMS VIEW OF STEM CELL biology” (12 October 2012, p. 215), C. Furusawa and K. Kaneko discuss the relevance of dynamic systems biology approaches and the concept of “attractors” to understand cell differentiation and proliferation. We share their excitement in using computational models that apply physical laws to cell fate decision.

Because there are still naysayers who question whether simple physical laws operate in living systems, we want to emphasize the existence of numerous examples in which the laws of physics have been used to provide mechanistic insights on complex behaviors of living organisms. In the past two decades, numerous works in biology



Laws of physics come to life. Patterns in zebrafish can be reproduced by Alan Turing’s reaction-diffusion model.

have integrated computational models with experimental verifications. Leibler and colleagues showed, using a simple mass-action model, that bacterial chemotaxis is highly robust to biochemical parameter variations (1, 2). Complex pattern

formation in seashells and zebrafish can be reproduced by Alan Turing’s simple reaction-diffusion model (3). For immune-related Toll-like receptor signaling, a linear response model utilizing the physical law of mass conservation was sufficient to show the enhancement of an alternative TRIF-dependent pathway in MyD88 mutant murine macrophages (4, 5). Similar biological flux redistribution in gain-of-function mutation was also observed for the energy metabolic pathways in *Escherichia coli* (6).

With further integration of the latest experimental innovations, such as in vivo tracking of individual molecules in single cells, with computational models applying physical laws at different scales (quantum or classical), the future looks optimistic for a leap in understanding the origins of biological decisions. We hope schools and colleges will inspire students to learn multidisciplinary concepts.

KUMAR SELVARAJOO* AND MASARU TOMITA

Institute for Advanced Biosciences and Systems Biology Program, Graduate School of Media and Governance, Keio University, Japan.

*To whom correspondence should be addressed. E-mail: kumar@ttck.keio.ac.jp

References

1. N. Barkai, S. Leibler, *Nature* **387**, 913 (1997).
2. U. Alon, M. G. Surette, N. Barkai, S. Leibler, *Nature* **397**, 168 (1999).
3. S. Kondo, T. Miura, *Science* **329**, 1616 (2010).
4. K. Selvarajoo et al., *PLoS One* **3**, e3430 (2008).
5. K. Selvarajoo, *Cell Commun. Signal.* **9**, 9 (2011).
6. N. Ishii et al., *Science* **316**, 593 (2007).

Biodiversity Despite
Selective Logging

PRIMARY TROPICAL FORESTS ARE POWERHOUSES of biodiversity (1) but are rapidly declining in extent and are threatened even within some protected areas (2). As a result, non-primary forests, especially those that have been selectively logged, are becoming more important to conservation efforts.

In the tropics, logging is almost always selective, targeting only certain commercially valuable tree species above a minimum size and leaving other species unharvested. More than 400 million hectares of tropical forest are now in permanent timber estates (3), and at least 20% of all tropical forests were logged from 2000 to 2005 (4).

Biologists have often emphasized the del-

eterious impacts of selective logging for disturbance-sensitive wildlife [e.g., (5, 6)], but recent evidence suggests that logged forests can have surprisingly high conservation values. In a meta-analysis across four tropical regions, selectively logged forests were by far the most biologically similar to primary forests, compared with agricultural and agroforestry systems (1). Even after repeated, intensive logging, the biodiversity of native forests in Borneo is roughly comparable to that after the first cut (7). Logged forests also store considerable carbon (8) and maintain most hydrological functions of primary forests. Hence, while they cannot replace primary forests, logged forests have great potential to enhance conservation at landscape and regional scales, act as buffer zones around protected areas, and help maintain forest con-

nectivity for wildlife.

Unfortunately, logged forests are more likely than primary forests to be cleared or burned in some (9) but not all (10) nations. For this reason, we do not advocate an expansion of logging—although this will surely continue in many regions. Rather, we assert that logged forests are too vast, vulnerable,

Letters to the Editor

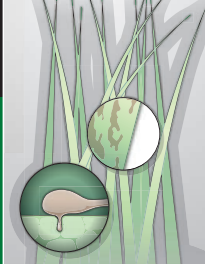
Letters (~300 words) discuss material published in *Science* in the past 3 months or matters of general interest. Letters are not acknowledged upon receipt. Whether published in full or in part, Letters are subject to editing for clarity and space. Letters submitted, published, or posted elsewhere, in print or online, will be disqualified. To submit a Letter, go to www.submit2science.org.

CREDIT: WIKIMEDIA COMMONS



Asian vulture
recovery?

653



Sugar for
flowers

659

TECHNICAL COMMENT ABSTRACTS

Comment on "Large Volcanic Aerosol Load in the Stratosphere Linked to Asian Monsoon Transport"

Michael Fromm, Gerald Nedoluha, Zdenek Charvát

Bourassa *et al.* (Reports, 6 July 2012, p. 78) report on the 13 June 2011 eruption of the Nabro volcano and satellite observations of stratospheric aerosol that they attribute to troposphere to stratosphere ascent via the Asian monsoon. They claim (citing another source) that the 13 June top injection height was well below the tropopause. We will show that the 13 June Nabro eruption plume was clearly stratospheric and contained both volcanic gases and aerosols. Moreover, we will show height-resolved stratospheric sulfur dioxide and volcanic aerosol enhancements 1 to 3 days old, unaffected by the Asian monsoon, precisely connected to the volcano. The observed stratospheric aerosols and gases are fully explained by the 13 June eruption and do not require a monsoon vehicle.

Full text at <http://dx.doi.org/10.1126/science.1228605>

Comment on "Large Volcanic Aerosol Load in the Stratosphere Linked to Asian Monsoon Transport"

J.-P. Vernier, L. W. Thomason, T. D. Fairlie, P. Minnis, R. Palikonda, K. M. Bedka

Bourassa *et al.* (Reports, 6 July 2012, p. 78) have suggested that deep convection associated with the Asian monsoon played a critical role in transporting sulfur dioxide associated with the Nabro volcanic eruption (13 June 2011) from the upper troposphere (9 to 14 kilometers) into the lower stratosphere. An analysis of the CALIPSO lidar data indicates, however, that the main part of the Nabro volcanic plume was injected directly into the lower stratosphere during the initial eruption well before reaching the Asian monsoon deep convective region.

Full text at <http://dx.doi.org/10.1126/science.1227817>

Response to Comments on "Large Volcanic Aerosol Load in the Stratosphere Linked to Asian Monsoon Transport"

Adam E. Bourassa, Alan Robock, William J. Randel, Terry Deshler, Landon A. Rieger, Nicholas D. Lloyd, E. J. Llewellyn, Douglas A. Degenstein

Fromm *et al.* and Vernier *et al.* suggest that their analyses of satellite measurements indicate that the main part of the Nabro volcanic plume from the eruption on 13 June 2011 was directly injected into the stratosphere. We address these analyses and, in addition, show that both wind trajectories and height-resolved profiles of sulfur dioxide indicate that although the eruption column may have extended higher than the Smithsonian report we highlighted, it was overwhelmingly tropospheric. Additionally, the height-resolved sulfur dioxide profiles provide further convincing evidence for convective transport of volcanic gas to the stratosphere from deep convection associated with the Asian monsoon.

Full text at <http://dx.doi.org/10.1126/science.1227961>

and important to ignore, given their large conservation potential. We should strive to retain and better manage them.

DAVID P. EDWARDS* AND WILLIAM F. LAURANCE

Centre for Tropical Environmental and Sustainability Science and School of Marine and Tropical Biology, James Cook University, Cairns, QLD 4878, Australia.

*To whom correspondence should be addressed. E-mail: dave.edwards@jcu.edu.au

References

1. Gibson *et al.*, *Nature* **478**, 378 (2011).
2. W. F. Laurance *et al.*, *Nature* **489**, 290 (2012).
3. J. Blaser, A. Sarre, D. Poore, S. Johnson, *Status of Tropical Forest Management* (International Tropical Timber Organization, Japan, 2011).
4. G. P. Asner, T. K. Rudel, T. M. Aide, R. S. DeFries, R. Emerson, *Conserv. Biol.* **23**, 1386 (2009).
5. W. F. Laurance, S. G. Laurance, *Biotropica* **28**, 310 (1996).
6. I. A. Bowles, R. E. Rice, R. A. Mittermeier, G. A. B. Fonseca, *Science* **280**, 1899 (1998).
7. D. P. Edwards *et al.*, *Proc. R. Soc. London Ser. B* **278**, 82 (2011).
8. F. E. Putz *et al.*, *Conserv. Lett.* **5**, 296 (2012).
9. G. P. Asner *et al.*, *Proc. Nat. Acad. Sci. U.S.A.* **103**, 12947 (2006).
10. D. L. A. Gaveau *et al.*, *Conserv. Lett.* **5**, 142 (2012).

Legal Limits to Data Re-Identification

YANIV ERLICH AT THE WHITEHEAD INSTITUTE for Biomedical Research used his hacking skills to decipher the names of anonymous DNA donors ("Genealogy databases enable naming of anonymous DNA donors," J. Bohannon, News and Analysis, 18 January, p. 262). A little-known legal technicality in international data privacy laws could curb the privacy threats of reverse identification from genomes. "Personal information" is usually defined as any data relating to an

individual whose identity is readily apparent from the data. The OECD Privacy Principles are enacted in over 80 countries worldwide (<http://oecdprivacy.org>). Privacy Principle No. 1 states: "There should be limits to the collection of personal data and any such data should be obtained by lawful and fair means and, where appropriate, with the knowledge or consent of the data subject." The principle is neutral regarding the manner of collection. Personal information may be collected directly from an individual or indirectly from third parties, or it may be synthesized from other sources, as with "data mining."

Computer scientists and engineers often don't know that recording a person's name against erstwhile anonymous data is technically an act of collection. Even if the consent form signed at the time of the original collection includes a disclaimer that absolute anonymity cannot be guaranteed, re-identifying the information later signifies a new collection. The new collection of personal information requires its own consent; the original disclaimer does not apply when third parties take data and process it beyond the original purpose for collection. Educating those with this capability about the legal meaning of collection should restrain the misuse of DNA data, at least in those jurisdictions that strive to enforce the OECD principles. It also implies that bioinformaticians working "with little more than the Internet" to attach names to samples may need ethics approval, just as they would if they were taking fresh samples from the people concerned. STEPHEN WILSON

Lockstep Consulting Pty Ltd, Five Dock (Sydney) NSW 2046, Australia. E-mail: swilson@lockstep.com.au

NextGenVOICES

Science Communication's Future: Last Call

You have one more week to respond to the NextGen VOICES survey!
Share your thoughts about this question:

Ideally, how will scientists share their results with each other and the public in 50 years?

To submit, go to <http://scim.ag/NextGen6>.

Deadline for submissions is 15 February. A selection of the best responses will be published in the 5 April issue of *Science*. Submissions should be 250 words or less. Anonymous submissions will not be considered. Please submit only once.

HISTORY OF SCIENCE

“Novel features of considerable interest”

Nathaniel Comfort

“I do not think you realize what others will see in it,” Crick wrote, scoldingly, to Watson in 1967. He was referring to *Base Pairs*—previously *Honest Jim*—Watson’s account of their solution of the structure of DNA; ultimately, of course, the book was called *The Double Helix* (1). The first title was the best; the last, the worst. Whereas *The Double Helix* promises a history, the original title’s pun on Kingsley Amis’s *Lucky Jim* suggests a farce. The Watson character is anything but honest; he is the quintessential unreliable narrator. Crick never understood this. Furious about the book’s factual licenses, he could not see that it is a sardonic, platonic, shoulder-chucking love letter from his partner. Nor did he grasp that, independent of its historical accuracy, *The Dou-*

ble Helix is profoundly true. Watson blasted the stuffy, gentlemanly heroism of popular stereotype, making laboratory life seem playful, naughty, and, well, cool. This infuriated and puzzled Crick, as well as Maurice Wilkins (who shared with Watson and Crick the 1962 Nobel Prize in Physiology or Medicine). Others did understand. The book has sold more than a million copies, been translated into 20 languages, lured generations of students into science, and provoked coveys of clucking academics into debate. The impossibility of predicting what others would see in it is what makes the book literature: its meaning grows and shifts with our culture. *The Double Helix* is the most important—and most fun—popular science book of the 20th century.

But do we need another version of it? Yes, it turns out. This edition, annotated by Alex Gann and Jan Witkowski (both at Cold Spring Harbor Laboratory), is, like the original, idiosyncratic and self-conscious. Richly annotated and almost obsessively illustrated with snapshots, scanned documents, and reprints of previously published material, the book invites a slower, perhaps more reflective reading of Watson’s page-turner. The best of the marginalia make Watson’s narrative even

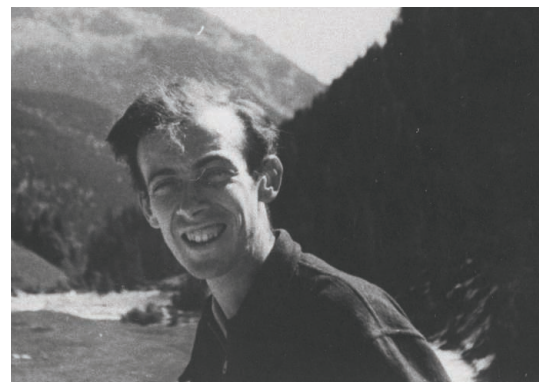
more vivid and clarify both the story and the science. Cookbook-shaped, with wide margins for the annotations, the volume is designed for a coffee table, yet it also belongs on the shelf of serious Watsonologists.

Many of the photos and notes are like scrapbook pages from one of the rippingest trips in modern science history, as compiled by an omniscient-compulsive observer: a postcard from the Italian Alps; candids of Watson’s friends, acquaintances, and nemeses; the Eagle pub; the Green Door; Matthews’ wine merchants; newspaper headlines reputedly read by John Kendrew and by Crick on 30 October and 22 November 1951, respectively; Rosalind Franklin’s research notes; an ecstatic Hedy Lamarr; a depiction of Watson’s “cozy corners”; a train crash; Crick

lounging on the roof of University College London. If reading *The Double Helix* is, as Horace Judson once said (3), like bouncing in a jeep over ploughed fields, the annotated edition is an air-conditioned safari bus, with a knowledgeable if slightly overenthusiastic tour guide at the microphone, pointing out both the lions and the lichens.

The book also contributes to the small but burgeoning scholarship in what we might call DNA studies. Though it contains no quantum revelations, a number of new details come to light. For example, the side-by-side reproduction of two letters written back-to-back by Wilkins—one formal and meant for public eyes, the other private and intended for Crick alone—following the marvelous false climax halfway through the book, when Watson and Crick flamboyantly show off the incorrect DNA structure, complicate our picture of the allegiances of the principals. Rosalind Franklin’s main adversary wasn’t Watson but Wilkins; in this respect, Watson’s character is really a mouthpiece for Maurice.

Following Watson’s text, five appendices document new findings of scholarly interest. Two letters—one from Crick to his 13-year-old son, the other from Watson to his mentor Max Delbrück—are the earliest known written descriptions of the double helix. The editors draw on another series of letters in a descriptive-analytical essay on the ker-



Holiday snapshot. Watson on vacation in the Italian Alps, August 1952.

fuffle over Watson’s leaving Copenhagen for Cambridge, in violation of his postdoctoral fellowship from the Merck Fellowship Board. Another appendix deepens our understanding of the controversy surrounding the publication of *Honest Jim/Base Pairs/The Double Helix*. The story of how Harvard University Press dropped what would have certainly been the most profitable book in its history and how the upstart trade press Atheneum picked up the manuscript is well known, as is the disapproval of Crick and others. The new material—which includes the quotation with which I began—tracks Crick’s attitude cooling from tepid to icy, both toward Watson’s manuscript and, to Jim’s sadness, toward Watson himself. And one appendix presents a digressive chapter from the middle of *The Double Helix* that Watson had relegated to the wastebasket. Watson was wise to cut that account of his trip to the Italian Alps in the summer of 1952—it adds nothing of substance to the narrative and slows the pace. But it ends with the germ of the book’s superb last line: “I was twenty-five and too old to be unusual.” Watson recycled that for a rainy, lonely night in Paris, on his birthday in 1953.

These and other small revelations are both pleasurable and valuable. In such ways, the archives help us understand the artful construction and tone of Watson’s off-handed, uneven masterpiece. If this annotated edition wavers over whether to treat the text as history or literature, it is because *The Double Helix* is both. Sorting out how fact, fiction, and interpretation intertwine should keep us reading more into the book for years yet.

References and Notes

1. J. D. Watson, *The Double Helix: A Personal Account of the Discovery of the Structure of DNA* (Atheneum, New York, 1968); reviewed in (2).
2. E. Chargaff, *Science* **159**, 1448 (1968); reprinted in the book.
3. H. F. Judson, *Nature* **413**, 775 (2001).

The reviewer is at the Institute of the History of Medicine, Johns Hopkins University, 1900 East Monument Street, Baltimore, MD 21205, USA. E-mail: comfort@jhmi.edu

10.1126/science.1233356

CREDIT: COURTESY JAMES D. WATSON COLLECTION, COLD SPRING HARBOR LABORATORY ARCHIVES

Downloaded from www.sciencemag.org on February 8, 2013

HISTORY OF SCIENCE

Heredity—The Very Long View

Hannah Landecker

We have all experienced, in one form or another, the history of a scientific concept reduced to a slide at the beginning of a talk or lecture that shows a stern-faced individual from another era, who gets to be the “father” of the topic at hand. Francis Galton gets to be the father of eugenics, while Gregor Mendel gets to be the father of genetics. The stories of such individuals, like wheel ruts established in soft ground that has since hardened, have become narrow and hard to escape from. Staffan Müller-Wille and Hans-Jörg Rheinberger’s *Cultural History of Heredity*, with its sustained attention to what happened to ideas and practices of heredity over centuries, is the antidote to such caricatures. It resets well-known figures and events back in the fabric of the development of scientific thought on inheritance, sometimes with delicious detail. For example, Francis Galton (who at the end of the 19th century provided one of the first and clearest articulations of a biological theory of heredity) is quoted disdainfully dismissing his French contemporary Adolphe Quetelet’s interest in the “average man”: “Some thorough-going democrats may look with complacency on a mob of mediocrities, but to most other persons they are the reverse of attractive.”

Galton likened heredity to a post office and ova and their contents to mailbags with piles of letters in them (biologists were, in this analogy, only able to gaze in the windows of the post office). People did not start to speak about heredity in a biological sense until the end of the 18th century; indeed, the word heredity itself was not systematically used in its modern sense until around 1830. Even then, it took the next century or so for heredity to become tangible in a set of specific research objects, such as peas and flies, in which it could be both explored and manipulated. Moreover, heredity has never

been a concept with a definite meaning that persists—not then and not now. The curious reader will find much reward in the authors’ careful exploration of what people did think and talk about before the modern genetic sense of heredity—particularly given that new findings in genetics, RNA biology, epigenetics, development, and evolution are destabilizing the modern genetic definition of heredity as articulated in the late 20th century.

There is some magic in taking a familiar concept from one’s own time, realizing that it has only existed for a relatively short spell, and getting inside a completely different way, from another historical moment, of looking at the world. To really understand the logic of another time (or another culture or language), one needs a good guide; otherwise it just seems unfathomable—or irrational. The authors note, “What contemporary biology identifies as an essential feature of all living systems—namely, their ability to reproduce themselves more or less identically through nutri-

tion, pregnancy, birth, and weaning contributed to the work of forming the individual in question.

Facing the paradox of giving a history of a concept before it exists, the book characterizes transformations in ideas about generation, reproduction, and transmission from this early period forward. The authors depict scattered thoughts and practices in property law, racial anthropology, plant hybridization, philosophy, and medicine gradually consolidating into a set of shared questions and eventually into a set of

shared research objects. In the 20th century, heredity came to be understood as a material thing, which could be manipulated and changed. Only here, as the book moves into modern genetics and describes the transformation to ideas of heredity wrought by molecular biology, does the ground begin to feel much more familiar.

This is an auspicious time to be laying open the concept of heredity to such detailed historical examination, showing it to be a capacious domain of scientific and cultural intermingling. One could complain that the “culture” part of the history is rather thin on the ground in parts, particularly as the book moves into the present. But the work of producing a readable, detailed narrative from a vast landscape of hundreds of years of European history must be recognized. The book results from a long-running project at the Max Planck Institute for the History of Science, in Berlin, to document the history of heredity in all its cultural complexity and in the *longue durée*—a historical approach emphasizing structures over the long term rather than discrete events. Several previously published edited volumes

from the project provide a kind of patchwork view of the story of heredity in Western culture, with each participating scholar contributing a piece from their particular specialty or research focus. Synthesizing a great mass of scholarship, Müller-Wille and Rheinberger attempt to really give the long view and to give it in depth. Their account provides an important point of reference for going forward and a timely contribution to thinking about the cultural and scientific meaning of heredity today.

A Cultural History of Heredity

by Staffan Müller-Wille and Hans-Jörg Rheinberger

University of Chicago Press, Chicago, 2012. 337 pp. \$45, £29. ISBN 9780226545707.



A bizarre union. Woodcut of the so-called Scythian lamb, from Claude Duret’s *Histoire Admirable des Plantes* (Nicolas Buon, Paris, 1605).

tion, growth, and propagation—... seems to have escaped the attention of natural philosophers and physicians prior to the eighteenth century.” Through a series of examples and thinkers—from the Scythian lamb (a sheep-plant hybrid that grew out of the ground on a trunk) to William Harvey chasing down the earliest moments of conception—the book demonstrates that premodern theories of propagation saw generation as an act of creation: Each organism’s generation was a singular, local event in which the surrounding circumstances of copulation, concep-

The reviewer is at the Institute for Society and Genetics and the Department of Sociology, University of California, Los Angeles, CA 90095–1551, USA. E-mail: landecker@soc.ucla.edu

Is Europe Evolving Toward an Integrated Research Area?

A. Chessa, A. Morescalchi, F. Pammolli,* O. Penner, A. M. Petersen, M. Riccaboni*

Efforts toward European research and development (R&D) integration have a long history, intensifying with the Fifth Framework Programme (FP) in 1998 (1–3) and the launch of the European Research Area (ERA) initiative at the Lisbon European Council in 2000. A key component of the European Union (EU) strategy for innovation and growth (4, 5), the ERA aims to overcome national borders through directed funding, increased mobility, and streamlined innovation policies.

To assess the rate of progress toward this ERA vision, we analyzed the evolution of geographical collaboration networks constructed from patent and scientific publication data. Although these data may not capture every facet of the ERA, they are widely accepted measures of R&D output, and the European Commission considers them crucial for the evaluation of the Horizon 2020 FP (6). All in all, we find no evidence since 2003 that EU innovation policies aimed at promoting an integrated research and innovation system have corresponded to intensified cross-border R&D activity in Europe vis-à-vis other Organization for Economic Cooperation and Development (OECD) countries.

We exploited the June 2012 release of the OECD REGPAT database (7) and analyzed all $\sim 2.4 \times 10^6$ patent applications filed with the European Patent Office (EPO) over the period 1986–2010. For comparison with scientific publications, we take a random sample of

$\sim 2.6 \times 10^5$ records from the Thomson ISI Web of Science over the period 1991–2009. We geographically coded each data set at the NUTS3 region level [see supplemental materials (SM)].

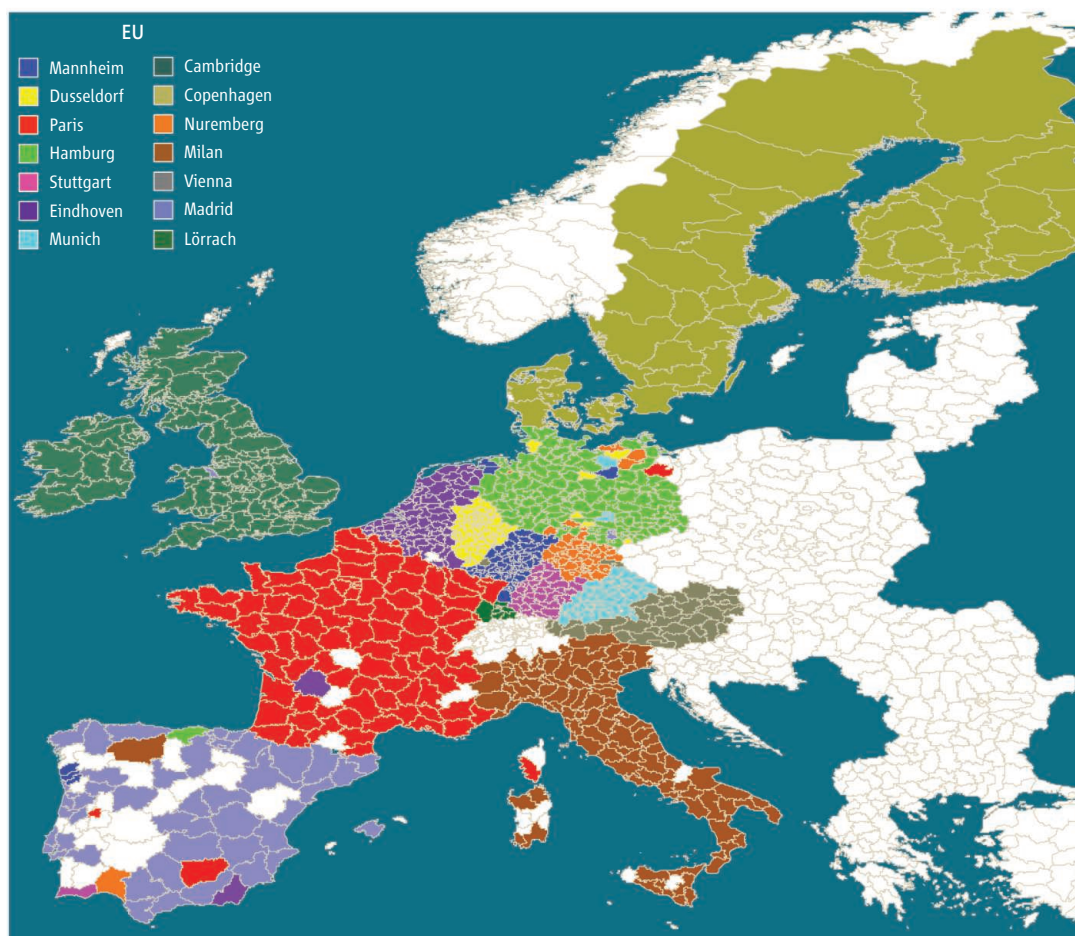
Using the data, we constructed five networks, which provide different perspectives into EU R&D integration. In our networks, nodes correspond to NUTS3 regions and links represent collaboration and/or mobility measures. Specifically, (i) the patent coinventor network and (ii) the publication coauthor network measure the intensity of interregional collaboration at the individual level; (iii) the coapplicant patent network measures the collaboration between institutions (“applicants”) located in different regions; (iv) the patent

Despite efforts to integrate across borders, Europe remains a collection of national innovation systems.



citation network indirectly measures scientific integration by following the flow of citations from patents in one region to patents in another; and (v) the patent mobility network measures the mobility of inventors from one region to another by tracking their location in subsequent patents.

We use a standard network-clustering algorithm to identify communities, i.e., subsets of nodes more strongly linked to one another than to nodes outside, to compare geopolitical borders and R&D networks. Regional integration is shown in the first figure in the purple community, centered on Eindhoven, which is composed of strongly



Community structure of the 2009 EU-15 coinventor network. Communities (color blocs) are labeled by their most-central region and were generated by iteratively aggregating them into clusters of increasing size (see SM). Blank regions, no ties in 2009.

IMT (Institutions, Markets, Technologies) Institute for Advanced Studies Lucca, 55100 Lucca, Italy.

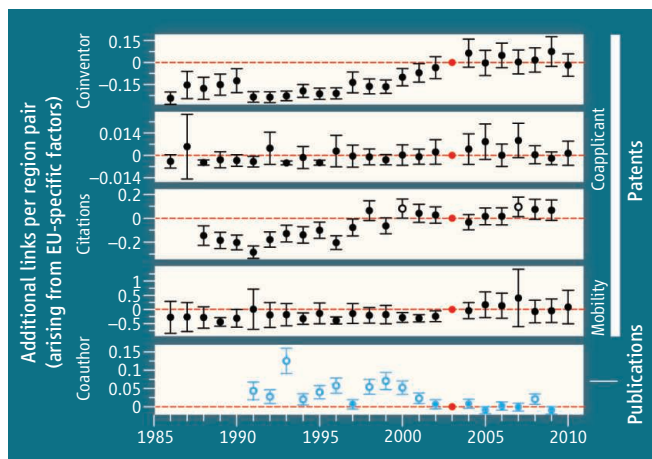
*Authors for correspondence. E-mail: f.pammolli@imtlucca.it (F.P.); m.riccaboni@imtlucca.it (R.M.)

collaborating regions in the Benelux, and in the international Nordic community with its center in Copenhagen. Despite these exceptions, coinventorship in Europe continues to be largely shaped by national borders, in contrast to the community structure of the highly dispersed “coast-to-coast” U.S. coinventor network (see SM for comparison) (8).

Europe is shown in the figure to be a collection of regional and national innovation communities. However, that does not necessarily mean that integration efforts have been unsuccessful. The more relevant question is at what rate is Europe evolving toward an integrated research system relative to the rate of cross-border R&D collaboration observed in non-EU OECD countries?

As shown elsewhere (3, 9–11), we observe a significant increase in the total number of cross-border research collaborations, both within and outside Europe (see fig. S1). To assess the role of EU-specific factors, we compared relative changes in cross-border collaboration between European countries (e.g., distinguishing German-French, from German-German and French-French collaborations) with changes in cross-border collaboration between non-European OECD countries. We did not analyze collaborations between EU and non-EU regions.

For each network, our econometric model performs three quantitative differences and controls for the size of regions, geographic distance, and time effects (see SM). First, the difference between cross-border and intra-border average number of links is computed, both for EU and non-EU OECD nations. Second, the difference between these two estimates isolates the impact of EU-specific factors on R&D integration. Finally, comparison with a baseline year yields the quantitative output of the model, i.e., the expected number of additional links between regions resulting from EU-specific factors. This quantity is shown in the second figure. Comparing data points from two different years, a higher y-axis value indicates a greater impact of EU-specific factors upon integration among EU nations. Choice of the baseline year does not alter our results. A positive (or negative)



Evolution of European integration in five R&D networks. The y axis reports the additional number of cross-border links for an average pair of regions (i) relative to within-border links, (ii) due to EU-specific factors as compared with non-EU OECD countries, and (iii) relative to 2003 baseline year. Error bars indicate 95% confidence intervals for four different patent networks (black circles) and a scientific publication network (green circles). Open circles indicate statistically significant (0.05 level) positive deviations from the baseline year. See SM.

slope indicates Europe is integrating faster (or slower) than non-EU OECD countries.

Since the late 1990s, signs of integration in European patent statistics are often seen. In the patent coinventor network, cross-border collaboration in Europe have increased vis-à-vis other OECD countries. This effect was relatively pronounced from 1998 to 2002 but stalled in 2003. Since then, additional links for an average pair of regions due to Europe-specific factors has never been significantly larger than zero. The patent coapplicant network exhibits no significant increase since 1996. The citation network shows a temporary bump in integration in the late '90s, then fluctuates around that level. Finally, the inventors' mobility network shows almost no progress in the last decade, confirming a slow pace of integration for the European high-skill labor market.

The scientific publication coauthorship network shows a negative trend since 1999, indicating that cross-border links among non-EU OECD countries grew faster than European cross-border links. These results are striking and deserve further investigation given the amount of resources the EU has committed to promote cross-border scientific collaboration through programs like FPs, European Cooperation in Science and Technology, Networks of Excellence, Marie Curie Actions, and so on.

In sum, our analysis of R&D patent and publication networks shows that Europe remains a collection of loosely coupled national innovation systems (12). Furthermore, since 2003, cross-border collaborations in Europe have developed no faster than in the

rest of the OECD countries.

Several ongoing initiatives seek to address general shortcomings that have affected previous integration efforts (5). The European Institute of Innovation and Technology's (EIT) Knowledge and Innovation Communities are long-term (7 to 15 years) collaboration networks spanning all aspects of the R&D ecosystem. To foster synergetic interaction between national funding bodies, Science Europe, an association of national research organizations, was founded in 2011 (14).

The European Research Council (ERC) has taken steps toward cross-border mobility by making grants competitive and portable. Likewise, a memorandum of understanding signed by the European Commission and the League of European Research Universities (13) pushes for pension unification and transparency in hiring and tenure decisions.

Despite these initiatives to increase competition within the system, monitoring and evaluation must drastically change if Europe is to accomplish its ambitious goals in science and technology. Evidence-based evaluation focused on output and impact is crucial, as recognized in the plans for the Horizon 2020 FP (6). Our methodology promotes this vision by combining interdisciplinary expertise with data relevant to impact analysis.

References and Notes

1. H. Delanghe, U. Muldur, L. Soete, *European Science and Technology Policy: Towards Integration or Fragmentation?* (Edward Elgar, Cheltenham, UK, 2009).
2. T. Scherngell, M. J. Barber, *Ann. Reg. Sci.* **46**, 247 (2011).
3. T. Scherngell, R. Lata, *Pap. Reg. Sci.* (2012). 10.1111/j.1435-5957.2012.00419.x
4. M. Nedeva, M. Stampfer, *Science* **336**, 982 (2012).
5. ERA, <http://ec.europa.eu/research/era>.
6. Commission Staff Working Paper, Impact Assessment; http://ec.europa.eu/research/horizon2020/pdf/proposals/horizon_2020_impact_assessment_report.pdf.
7. S. Maraut *et al.*, The OECD REGPAT Database: a Presentation (STI Working Paper 2008/2, OECD, Paris, 2008); www.oecd.org/science/innovation/sciencetechnologyandindustry/40794372.pdf.
8. J. Owen-Smith *et al.*, *Manage. Sci.* **48**, 24 (2002).
9. S. Breschi, L. Cusmano, *Int. J. Technol. Manag.* **27**, 747 (2004).
10. J. Hoekman *et al.*, *J. Econ. Geogr.* **13**, 23 (2013).
11. National Science Board, *Science and Engineering Indicators 2012* (NSB 12-01, National Science Foundation, Arlington, VA, 2012).
12. R. R. Nelson, *National Innovation Systems: A Comparative Analysis* (Oxford Univ. Press, New York, 1993).
13. Memorandum of Understanding on ERA, (July 2012); www.leru.org/files/publications/ERA_Final_MoU_LERU.pdf.

Acknowledgments: Authors acknowledge funding from the National Research Program of Italy (PNR) project “CRISIS Lab” and thank M. Buchanan and F. Cerina for comments. M.R. acknowledges funding from the Italian Ministry of Education, University, and Research (MIUR) [Progress in Research of Interest (PRIN) project 2009Z3E2BF] and the Research Foundation of Flanders (FWO) (G073013N). O.P. acknowledges funding from the Social Sciences and Humanities Research Council of Canada.

Supplementary Materials

www.sciencemag.org/cgi/content/full/339/6120/650/DC1

10.1126/science.1227970

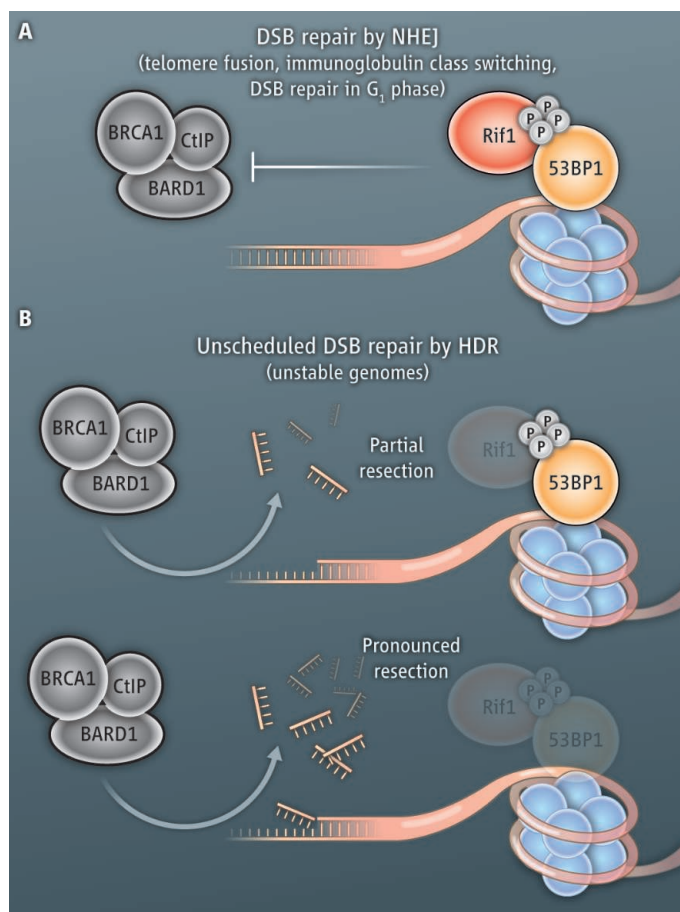
Shielding Broken DNA for a Quick Fix

Jiri Lukas and Claudia Lukas

DNA double-strand breaks are constantly generated throughout the cellular life span, making the genome vulnerable to mutation and irreversible damage. Cells are equipped to mend such breaks through two mechanisms, each with positive and negative aspects: homology-directed repair (HDR), which tends not to make mistakes, but requires that a cell wait until DNA replication generates homologous templates; or a faster process called nonhomologous end joining (NHEJ), which, though error-prone, can rapidly “glue” DNA breaks together (1). Making the right choice between HDR and NHEJ is vital for genome integrity. Recent studies (2, 3), including those on page 711 and 700 of this issue by Di Virgilio *et al.* (4) and Zimmermann *et al.* (5), respectively, show how the HDR pathway is blocked so that the alternate repair process can proceed.

In a number of physiological settings such as immunoglobulin diversification in blood cells, the natural erosion of telomeres (protective ends of chromosomes), or DNA breakage during G₁ phase of the cell division cycle, the HDR repair process must be actively suppressed to avoid genomic rearrangements. This is achieved by blocking the action of enzymes that create single-strand DNA at the break sites, in preparation for recombination. The barrier against excessive resection involves 53BP1, a large adaptor protein that interacts with the DNA scaffold made of histones and histone-binding proteins (6).

To elucidate how 53BP1 shields DNA ends, Di Virgilio *et al.* and Zimmermann *et al.* took advantage of the fact that for 53BP1



Protected ends. (A) At the site of a DNA double-strand break, Rif1 interacts with chromatin-bound and phosphorylated (P) 53BP1 to protect DNA ends against resection (executed in part by the BRCA1-CtIP complex). This allows DNA repair by the NHEJ mechanism. (B) In the absence of Rif1 (alone or with 53BP1), DNA ends undergo excessive resection, which may lead to unscheduled repair by HDR, and consequently to genomic instability. BARD1, BRCA1-associated RING domain protein 1.

to block DNA-end resection, it must be phosphorylated by the enzyme ataxia telangiectasia mutated (ATM) (7). Di Virgilio *et al.* performed a mass spectrometry screen for proteins that interact with phosphorylated 53BP1, whereas Zimmermann *et al.* extended their previous work on proteins that interact with phosphorylated 53BP1 at dysfunctional telomeres. Rewardingly, both groups identified Rap1-interacting factor 1 (Rif1) as a key suppressor of DNA-end resection that acts downstream of 53BP1 (see the figure). To demonstrate the physiological relevance

A fast-acting DNA repair mechanism involves a protein complex that blocks an alternative process that requires a cell to wait for repair.

of this finding, Di Virgilio *et al.* show that depletion of Rif1 in activated B lymphocytes triggered excessive 5' DNA-end resection, impaired immunoglobulin class switch recombination (a DNA rearrangement strictly dependent on NHEJ), and led to genetic instability including translocations at the immunoglobulin H (IgH) locus. Zimmermann *et al.* show that at telomeres deprived of the protective shelterin complex (and thus converted to DNA ends resembling double-strand breaks), depletion of Rif1 also enhanced 5' DNA-end resection, thereby rendering the DNA ends unsuitable for direct ligation and reducing the frequency of telomere fusions.

Most DNA repair reactions can be regarded as a double-edged sword. Although NHEJ is beneficial under physiological settings, it can turn against the genome under pathological conditions that arise during cellular transformation. One cytological manifestation of this is the formation of radial chromosomes, aberrant structures caused by toxic NHEJ reactions in tumor cells with compromised BRCA1 function (1). BRCA1 is a tumor suppressor protein that acts in the HDR repair pathway. Consistent with its role in promoting NHEJ, Zimmermann *et al.* show that Rif1 depletion in cultured mammalian

cells lowered the frequency of aberrant chromosomes under these conditions. However, this and all other phenotypes associated with Rif1 depletion were milder than in 53BP1-deficient cells, indicating that although Rif1 substantially contributes to DNA-end protection downstream of 53BP1, it cannot completely explain the entire spectrum of anti-resection cellular activities. To explain this, Zimmermann *et al.* suggest that the enhanced mobility of 53BP1-bound DNA ends (a function of 53BP1 that is Rif1-independent) increases their chance of finding each other,

Novo Nordisk Foundation Center for Protein Research, Faculty of Health and Medical Sciences, University of Copenhagen, Blegdamsvej 3b, 2200 Copenhagen, Denmark. E-mail: claudia.lukas@cpr.ku.dk; jiri.lukas@cpr.ku.dk

whereas the mass spectrometry screen of Di Virgilio *et al.* reveals additional proteins that interact with phosphorylated 53BP1, raising the possibility that some of them might join Rif1 in shielding DNA ends.

53BP1 has stood out as a molecular shield against 5' DNA-end resection at double-strand breaks without a clear mechanism attached to it. Adding Rif1 to the picture breaks this deadlock and provides the much-needed impetus to mechanistically explore DNA-end protection by addressing previously unforeseen questions. The recent studies by Escribano-Díaz *et al.* (2) and Ross Chapman *et al.* (3) provide an important lead by showing that during G₁ phase of the cell division cycle, Rif1 opposes the function of the complex involved in DNA-end resection, composed of BRCA1 and C-terminal binding protein-interacting protein (CtIP) (1). Conversely, after entry into S phase and activation of cyclin-dependent kinases, the phosphorylated BRCA1-CtIP complex prevails, unloads Rif1 from chromatin, and initiates DNA-end resection. This neatly explains how

periodicity of the cell cycle is linked to repair pathway choice, but additional mechanisms should not be discounted. For instance, Rif1 is a multifunctional protein that organizes higher-order chromatin structure at origins of DNA replication. It is possible that chromatin accessibility contributes to restraining DNA resection at double-strand breaks (8, 9).

Other unresolved issues include how Rif1 binds to phosphorylated 53BP1 and how the activated BRCA1-CtIP complex disrupts this interaction. The absence of a phospho-recognition motif in the Rif1 sequence indicates that enhanced interaction between 53BP1 and Rif1 after DNA damage is mediated by a hitherto unknown molecular linker. This is not merely an academic problem—mechanisms that influence DNA-end resection have a therapeutic potential in cancer (10), and if we are to expand the list of targets for more efficient synthetic treatments with modalities that involve DNA breakage (radiotherapy, many forms of chemotherapy), factors that enhance recognition of phosphorylated 53BP1 by Rif1 after DNA damage could be of crucial rele-

vance as targets for therapeutic interventions. Regardless, defining the role of Rif1 in human diseases associated with unstable genomes deserves attention, and the discovery of its function in DNA-end processing is an important milestone toward achieving this goal.

References and Notes

1. J. R. Chapman, M. R. Taylor, S. J. Boulton, *Mol. Cell* **47**, 497 (2012).
2. C. Escribano-Díaz *et al.*, *Mol. Cell.* 10.1016/j.molcel.2013.01.001 (2013).
3. J. Ross Chapman *et al.*, *Mol. Cell* 10.1016/j.molcel.2013.01.002 (2013).
4. M. Di Virgilio *et al.*, *Science* **339**, 711 (2013); 10.1126/science.1230624.
5. M. Zimmermann, F. Lotterberger, S. B. Buonomo, A. Sfeir, T. de Lange, *Science* **339**, 700 (2013); 10.1126/science.1231573.
6. J. Lukas, C. Lukas, J. Bartek, *Nat. Cell Biol.* **13**, 1161 (2011).
7. A. Bothmer *et al.*, *Mol. Cell* **42**, 319 (2011).
8. D. Cornacchia *et al.*, *EMBO J.* **31**, 3678 (2012).
9. S. Yamazaki *et al.*, *EMBO J.* **31**, 3667 (2012).
10. S. P. Jackson, J. Bartek, *Nature* **461**, 1071 (2009).

Acknowledgments: J.L. and C.L. are supported by Novo Nordisk Foundation, Danish Cancer Society, and Danish National Research Foundation.

10.1126/science.1234602

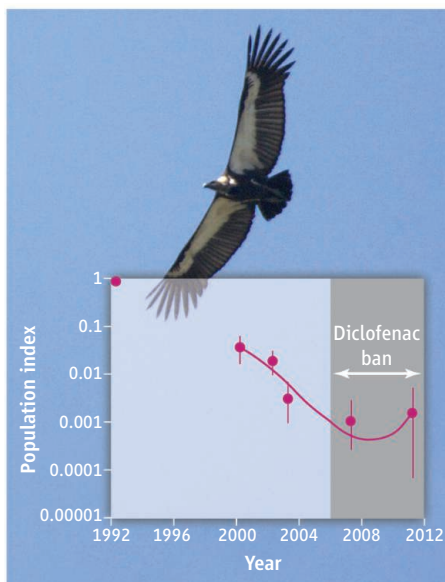
ECOLOGY

Pollution, Politics, and Vultures

Andrew Balmford

Fifty years after the publication of Rachel Carson's groundbreaking book *Silent Spring*, environmental pollutants, whose impacts are hard to diagnose and harder still to control, continue to cause grave damage to nontarget organisms. The range of substances of concern has expanded since Carson's day from nutrients, pesticides, and heavy metals and now includes pharmaceuticals. Although drug pollution problems have been particularly difficult to address (1), recent developments in south Asia offer some positive news on one of the best-known examples. Scientists and politicians are at last making progress in reversing the accidental but catastrophic poisoning of the region's vultures by a widespread veterinary drug.

Two decades ago, vulture populations across the Indian subcontinent began a collapse to just 1% of what they had been (2). As well as being a crisis for bird conservation, this was a serious problem for public health, because it ended the free disposal by



Turning a corner? Changes in population indices of the oriental white-backed vulture *Gyps bengalensis*, from 6 years of repeat surveys of a large number of road transects in India. Vertical lines show 95% confidence limits derived by bootstrapping; the curve shows the cubic log-linear trend for 2000 to 2011. The y axis has a logarithmic scale.

The catastrophic collapse of south Asia's vultures may at last be coming to an end, thanks to a ban on the veterinary drug responsible.

the birds of the region's vast annual tonnage of cattle carcasses (3). Ten years after the decline began, its cause was finally identified: The vultures were being poisoned by widespread use of the out-of-patent nonsteroidal anti-inflammatory drug diclofenac, which causes kidney failure when the birds feed on carcasses of recently treated cattle (4).

Based on evidence that deaths of vultures by diclofenac were widespread and frequent and that contamination of cattle carcasses was sufficient to account for the rapid decline (5), the governments of India, Pakistan, and Nepal banned the veterinary use of diclofenac in 2006. Bangladesh followed suit in 2010, and in May 2012 the four governments reached an unprecedented political agreement to further coordinate and improve actions to prevent adverse effects of veterinary drugs on vultures (6).

These responses were a considerable achievement for conservation science, but the diclofenac ban did not solve the vulture problem overnight. Surveillance of diclofenac contamination of cow carcasses in India soon after the ban showed little change (7), and test purchases in pharmacies found

diclofenac formulated for human use widely on sale for the treatment of cattle (8). These findings, coupled with coordinated efforts by nongovernmental organizations (NGOs) and governments, led to further restrictions and remedial efforts. By 2008, diclofenac contamination had fallen substantially (7), largely as a result of two factors: awareness-raising work by NGOs and government departments with the public, pharmaceutical industry, and veterinarians; and the identification and promotion of the alternative drug meloxicam, which is effective for treating cattle but does not harm vultures (9).

A suite of studies of the latest vulture population trends suggests that these efforts are working and that the vulture declines have slowed or even stopped. In India, all three critically endangered *Gyps* vultures did not decline between 2007 and 2011; one species, the oriental white-backed vulture, may have increased slightly (10). Population models indicate that these changes match predictions from the measured reduction in carcass contamination (7, 10). The oriental white-

backed vulture population in Nepal has also increased since the ban, and the decline of this species in Bangladesh has slowed since the more recent ban there. A long-billed vulture population in Pakistan, which was declining before the ban in 2006, has now increased substantially (11).

It seems that carefully targeted research—combined with political commitment and government-NGO cooperation—is making a real difference for the subcontinent's vultures. Yet, recovery will likely be partial and take decades. Continued monitoring of vultures and of veterinary drugs and their toxicity is necessary to measure the effectiveness of interventions and suggest modifications where necessary.

This need for vigilance and adaptive management is underscored by the increased use of several other veterinary drugs with unknown effects on vultures: aceclofenac, a precursor of diclofenac that is highly likely to be toxic (12), and ketoprofen, which was shown to be toxic to vultures 3 years ago (13) but is still permitted for veterinary use in India. The

governments of the vulture range states have moved much faster and more effectively than did western governments when responding to the environmental impacts of organochlorine pesticides identified by Rachel Carson, but sustained scientific scrutiny is vital, as is continued political resolve.

References

1. N. Gilbert, *Nature* **491**, 503 (2012).
2. V. Prakash *et al.*, *J. Bombay Nat. Hist. Soc.* **104**, 129 (2007).
3. A. Markandya, T. Taylor, A. Longoc, M. N. Murty, K. Dhav-alad, *Ecol. Econ.* **67**, 194 (2008).
4. J. L. Oaks *et al.*, *Nature* **427**, 630 (2004).
5. R. E. Green *et al.*, *PLoS ONE* **2**, e686 (2007).
6. Regional Declaration on the Conservation of South Asia's Critically Endangered Vulture Species, http://cmsdata.iucn.org/downloads/regional_declaration_on_vulture_conservation.pdf.
7. R. Cuthbert *et al.*, *PLoS ONE* **6**, e19069 (2011).
8. R. J. Cuthbert *et al.*, *Oryx* **45**, 420 (2011).
9. G. E. Swan *et al.*, *PLoS Biol.* **4**, e66 (2006).
10. V. Prakash *et al.*, *PLoS ONE* **7**, e49118 (2012).
11. M. J. I. Chaudhry *et al.*, *Bird Cons. Int.* **22**, 389 (2012).
12. P. Sharma, *J. Raptor Res.* **46**, 314 (2012).
13. V. Naidoo *et al.*, *Biol. Lett.* **6**, 339 (2010).

10.1126/science.1234193

APPLIED PHYSICS

Metamaterials with Quantum Gain

Ortwin Hess and Kosmas L. Tsakmakidis

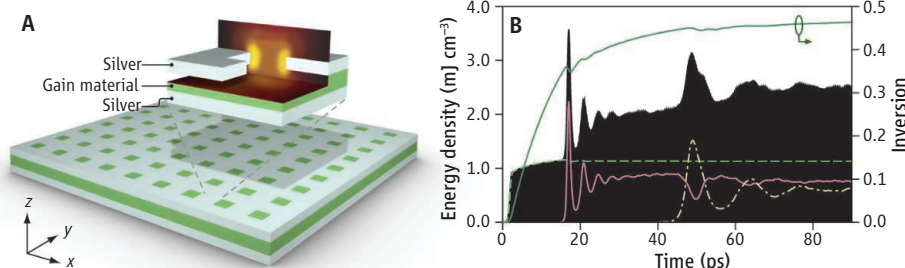
Optical metamaterials and nanoplasmonics offer extreme control and localization of light within volumes that can be smaller than a cubic light wavelength by more than three orders of magnitude, but they suffer from appreciable dissipative losses. This weakness is thought to constitute the prime impediment before many of the envisaged applications can succeed in practice. However, recent breakthroughs in the theoretical understanding and experimental fabrication of gain-enhanced metamaterials and nanoplasmonic heterostructures promise to overcome these hindrances, while allowing for new ways to control spontaneous and stimulated emission of light on the nanoscale (1, 2).

Resistive losses in nanoplasmonic metamaterials arise from the interaction of the incident photons with the quasi-free conduction electrons of the metals, thereby constituting an inherent feature of the response of metal-based nanodevices. For truly subwave-

length plasmonic structures, these losses follow universal laws; that is, they do not depend on the particular geometric configuration but only on the metal used (usually noble metals) (3). Meanwhile, there has been an increased emphasis on two-dimensional (2D) metasurfaces, which are much more convenient to fabricate than their full-3D metamaterial counterparts but can steer light in equally dramatic ways, well below the fundamental diffraction limit and over broad, flat areas (4).

Integrating amplifying media with metamaterials allows loss-free plasmonic operation and opens a route for controlling nanoscale quantum emitters.

In such a 2D nanostructure with laser dyes (gain medium) incorporated into its fabric (see the figure, panel A), the objective is to obtain optimum coupling of the plasmonic excitations to the gain molecules, so that maximum harnessing of the gain medium can be achieved—a requirement due to the high losses. When the pattern of the nano-holes periodically perforating the two silver nanofilms is engineered such that the desired plasmonic resonance coincides with



Playing for gain. (A) An illustration of the gain-enhanced optical metamaterial, with a magnified unit cell and an example of plasmonic field enhancement at two vertical planes inside the cell. (B) Energy and average inversion (green solid line, right axis) inside the lasing nanofishnet over time. The signals, time-averaged over 0.4 ps (black), are decomposed into the pump mode (green dashed line), the bright mode (red solid line), and the dark mode (yellow dash-dotted line).

Blackett Laboratory, Department of Physics, Imperial College London, London SW7 2AZ, UK. E-mail: o.hess@imperial.ac.uk

the emission wavelength of the dyes, full loss compensation and amplification can be achieved, even in the exotic negative refractive index regime (5–7). By extending the duration of the incident probe pulse such that the energy inside the nanostructure becomes constant with time, the quantum plasmonic amplifier can operate transiently and also in a steady-state mode (8).

If the gain supplied by the active medium is sufficient to overcome both dissipative and radiative losses, then the structure can function as a coherent emitter of surface plasmons over the ultrathin 2D area, deep below the diffraction limit for visible light (1, 9). Here, controlling the spontaneous emission rate is crucial (10) as both bright and dark plasmonic lasing states exist, giving rise to a strong, nonlinear competition. Which one eventually dominates can be controlled by the design and excitation of the metamaterial (see the figure, panel B). In this example, where bright plasmonic emission dominates, the bright-mode energy (red solid line) builds up initially, followed by picosecond-period relaxation oscillations and steady-state emission, interrupted (at ~50 ps) by an instability of the dark mode (yellow dash-dotted line) until again steady-state emission is reached.

These 2D active nanostructures can function as powerful on-chip light sources, either coherent (nanolasers) or incoherent (light-

emitting diodes, LEDs), delivering intense optical power. Although the typical plasmonic cavity Q factors are rather small (~50), the attained Purcell factors (a measure of the spontaneous emission rate enhancement that varies as Q/V_m) can be large because the mode volume V_m can be extremely small. A major goal in the field is to enhance the Purcell factor so as to accelerate spontaneous emission to the degree that it becomes faster than stimulated emission, so that ultrafast, low-energy LEDs can be attained and integrated within nanoscale circuits (11).

Large Purcell factors can also be obtained in plasmonic slow-light heterostructures for special cases where the group velocity of the plasmons is close to zero (1). Computations reveal that at these zero-group velocity points, full lasing operation can be reached in completely uniform (minimalistic) structures that do not require a cavity to confine light (by reflections or Bragg scattering) because successive light pulses can be stopped and strongly localized (12). Without any cavity walls restricting the lasing mode size to be above the diffraction limit, the mode can be pushed into a deep-subwavelength regime, with sizes (in 2D) of $\lambda^2/1000$ being realistically attainable. Because spontaneous emission can be efficiently channeled into the stopped-light mode, the result is low-threshold operation.

The marriage of nanoplasmonic metamaterials with quantum gain media represents an exciting frontier in nanophotonics and nanoscience, and is a precursor of active, integrated quantum nano-optics. Bringing gain in the nanoscale will open a platform for practical, loss-free nanodevices—not only electro-optic modulators and intense light sources, but also plasmonic waveguides and nanosensors exploiting intensified plasmonic hot spots for single-emitter spectroscopy or nanoscale lithography.

References and Notes

1. O. Hess *et al.*, *Nat. Mater.* **11**, 573 (2012).
2. Y.-J. Lu *et al.*, *Science* **337**, 450 (2012).
3. J. B. Khurgin, G. Sun, *Opt. Express* **20**, 15309 (2012).
4. M. A. Kats, R. Blanchard, P. Genevet, F. Capasso, *Nat. Mater.* **12**, 20 (2013).
5. S. Xiao *et al.*, *Nature* **466**, 735 (2010).
6. S. Wuestner, A. Pusch, K. L. Tsakmakidis, J. M. Hamm, O. Hess, *Phys. Rev. Lett.* **105**, 127401 (2010).
7. A. Fang, Th. Koschny, C. M. Soukoulis, *Phys. Rev. B* **82**, 121102(R) (2010).
8. J. M. Hamm *et al.*, *Phys. Rev. Lett.* **107**, 167405 (2011).
9. S. Wuestner *et al.*, *Phys. Rev. B* **85**, 201406(R) (2012).
10. A. Pusch, S. Wuestner, J. M. Hamm, K. L. Tsakmakidis, O. Hess, *ACS Nano* **6**, 2420 (2012).
11. E. K. Lau, A. Lakhani, R. S. Tucker, M. C. Wu, *Opt. Express* **17**, 7790 (2009).
12. K. L. Tsakmakidis *et al.*, <http://arxiv.org/abs/1301.5995> (2013).

Acknowledgments: Supported by the Leverhulme Trust, the Royal Academy of Engineering, and the UK Engineering and Physical Sciences Research Council.

10.1126/science.1231254

GEOCHEMISTRY

Impact and Extinction

Heiko Pälike

During the past 540 million years, five major mass extinctions have occurred on Earth. Several of them have been linked to volcanic eruptions during the formation of large flood basalts (1, 2). However, the situation is not clearcut for the most recent mass extinction at the Cretaceous-Paleogene (K-Pg) boundary (~66 million years ago), when nonavian dinosaurs became extinct. Around the time of the K-Pg boundary, a series of large eruptions formed the Deccan flood basalts. However, in 1980, Alvarez *et al.* (3) argued that the K-Pg boundary coincided with the impact of a large asteroid or comet. On page 684 of this issue, Renne *et al.* (4) provide new evidence that

the age of Chicxulub asteroid impact and the K-Pg boundary coincide precisely.

Alvarez *et al.* based their initial hypothesis on elevated concentrations of iridium and other platinum-group elements and the occurrence of shocked quartz, tektites, and tsunami-like deposits in samples roughly dated to the time of the K-Pg boundary. Tell-tale deposits of an impact by an extraterrestrial body around the time of the boundary have now been found globally. These deposits decrease in intensity and thickness away from a proposed impact site at Chicxulub in the Gulf of Mexico (5). Nevertheless, the debate about the precise sequence of events has continued. Different views persist about the relative timing of the K-Pg boundary and the impact deposits, on the one hand, and the role played by large continental flood basalts and volcanism, on the other hand.

Precise dating shows that the Chicxulub impact coincided with the mass extinction at the K-Pg boundary 66 million years ago.

For the hypothesis that the K-Pg mass extinction was caused or triggered by an impact to be true, there must be absolute correspondence between the K-Pg boundary and the impact. Detailed sedimentological analysis and stratigraphy, together with accurate geochronological dating, therefore allow the hypothesis to be tested. Renne *et al.* now apply state-of-the-art geochronological dating methods to new data collected from impact deposits and the K-Pg boundary. They resolve the existing uncertainty about the relative timing of the events.

Some of this uncertainty arose from a mismatch between the two main methods used for radioisotopic dating. One method measures the relative abundance of decay chain products of uranium/lead (U/Pb) in zircons formed in magma chambers and preserved in bentonites; the other measures potassium/

MARUM—Center for Marine Environmental Sciences, University of Bremen, Leobener Strasse, 28359 Bremen, Germany. E-mail: hpaelike@marum.de



argon isotope ratios in sanidine crystals found in volcanic ash layers. Recent studies have shown why the argon isotope method always yielded slightly younger ages than the U/Pb method (6, 7). The results from the two methods can now be compared directly to improve accuracy and confidence.

Renne *et al.* show that combining multiple U/Pb and argon isotope system measurements from several stratigraphic horizons yields ages of 66.038 ± 0.049 million years for the Chicxulub impact tektites, and 66.043 ± 0.043 million years for the K-Pg boundary itself. These ages are indistinguishable from each other with a much reduced uncertainty of 32,000 years and suggest that the Chicxulub impact event coincides with the K-Pg boundary. The results also falsify the hypothesis that the Chicxulub impact predated the K-Pg boundary by ~300,000 years (8).

Renne *et al.*'s results also have important implications for another geological dating method that relies on matching time series of climatic reconstructions to variations in Earth's orbital motion (9). The orbital motions can be computed by astronomical theory and observation (10), but the precise orbital configuration becomes uncertain in the more distant past because of the chaotic nature of the solar system. Beyond 50 million years ago, only one orbital motion—the 405,000-year orbital eccentricity cycle—can be computed with enough accuracy for a reliable astronomical calibration of the geological record (11). Previous studies agree that the K-Pg boundary is situated near a minimum of a 405,000-year eccentricity cycle but disagree on whether it is placed at ~65.28, ~65.68, or ~66.08 million years ago (7, 12–15). Renne *et al.*'s dating firmly supports the third option and could thus settle an important question about the astronomical calibration of Paleogene time.

What caused the K-Pg mass extinction? The Cretaceous-Paleogene (K-Pg) boundary section in the Bottacione gorge northeast of Gubbio, Italy. Alvarez *et al.* first described elevated iridium concentrations in the red boundary clay (3). These results formed the basis of the impact hypothesis for the K-Pg mass extinction. Renne *et al.* now show that the Chicxulub event and K-Pg boundary coincided precisely.

Dating individual points along the sequence of events around the K-Pg boundary also provides further insights into the ecological and chemical evolution around this event. The dating suggests that in Montana, the vertebrate fauna recovered much faster after the mass extinction than previously thought, perhaps within 20,000 years. Renne *et al.* suggest that the faunal recovery occurred by migration from refugia rather than by evolutionary radiation.

Does this study finally close the debate about the cause of the demise of the dinosaurs? Not quite yet. Renne *et al.* suggest that brief cold snaps in the late Cretaceous were stressful to an ecology adapted to the long-lived preceding hothouse climate, and that the Chicxulub impact delivered a final coup de grâce to ecosystems, shifting the planet permanently into a new state. The next task will be to use the improved dating methodologies to precisely date the largest individual magmatic events during Deccan flood basalt formation. These dates will help to evaluate

the role volcanism played in the initial onset of environmental and biotic change prior to the K-Pg boundary.

References

1. V. E. Courtillot, P. R. Renne, *C. R. Geosci.* **335**, 113 (2003).
2. P. B. Wignall, *Earth Sci. Rev.* **53**, 1 (2001).
3. L. W. Alvarez, W. Alvarez, F. Asaro, H. V. Michel, *Science* **208**, 1095 (1980).
4. P. R. Renne *et al.*, *Science* **339**, 684 (2013).
5. P. Schulte *et al.*, *Science* **327**, 1214 (2010).
6. P. R. Renne, G. Balco, K. R. Ludwig, R. Mundil, K. Min, *Geochim. Cosmochim. Acta* **75**, 5097 (2011).
7. K. F. Kuiper *et al.*, *Science* **320**, 500 (2008).
8. G. Keller *et al.*, *Earth Planet. Sci. Lett.* **255**, 339 (2007).
9. H. Pälike, F. J. Hilgen, *Nat. Geosci.* **1**, 282 (2008).
10. J. Laskar *et al.*, *Astron. Astrophys.* **428**, 261 (2004).
11. J. Laskar, A. Fienga, M. Gastineau, H. Manche, *Astron. Astrophys.* **532**, A89 (2011).
12. T. Westerhold *et al.*, *Palaeogeogr. Palaeoclimatol. Palaeoecol.* **257**, 377 (2008).
13. D. Huxon *et al.*, *Earth Planet. Sci. Lett.* **305**, 328 (2011).
14. T. Westerhold, U. Röhl, J. Laskar, *Geochim. Geophys. Geosyst.* **13**, Q06015 (2012).
15. F. J. Hilgen, K. F. Kuiper, L. J. Lourens, *Earth Planet. Sci. Lett.* **300**, 139 (2010).

10.1126/science.1233948

EVOLUTION

Fossils Versus Clocks

Anne D. Yoder

An extensive morphological analysis supports the conclusion that ancestors of placental mammals evolved rapidly in the Cenozoic.

It's a great story, and one that most of us learned in grade school. Dinosaurs ruled Earth for eons, shaking the ground beneath them as their colossal forms roamed the dense tropical forests of the Mesozoic. Mammals were present but were minuscule by comparison, skulking about in the undergrowth as they foraged for insects. And so it went until a massive asteroid hit Earth about 66 million years ago, causing environmental havoc, climate change, and the worldwide extinction of non-avian dinosaurs [the Cretaceous-Paleogene (K-Pg) extinction event] (1). Only then did mammals begin to flourish and diversify into the myriad forms of today. It is a compelling tale, but one where timing is everything. On page 662 of this issue,

O'Leary *et al.* (2) offer a fresh perspective on the pattern and timing of mammalian evolution drawn from a remarkable arsenal of morphological data from fossil and living mammals (see the figure).

The fossil record has always lent veracity to the classical account. Sediments from the Mesozoic (~250 million to 66 million years ago) are rich with the fossils of dinosaurs, both large and small, and less rich with mammals that were for the most part unlike those we see today (3). The record changes abruptly with the beginning of the Cenozoic (since ~66 million years ago), but it is not until about 55 million years ago that we begin to clearly see placental mammal lineages (4). Why did virtually all placental groups—such as primates, bats, ungulates, and whales—appear so abruptly in the fossil record? Where are the transitional forms that must link the dimin-

Department of Biology, Duke University, Durham, NC 27708, USA. E-mail: anne.yoder@duke.edu

tive insectivores of the Mesozoic to today's multitude of mammals?

In the 1990s, molecular phylogenetic studies yielded divergence ages far older than the fossil evidence indicated (5). In the ensuing debate among molecular phylogeneticists and paleontologists, the classical Cenozoic rapid-radiation hypothesis was renamed the explosive model. Scenarios supported by the molecular divergence dates were termed short-fuse and long-fuse models, depending

on whether they purported that extant clades began their evolutionary bursts long before (short-fuse) or just before (long-fuse) the start of the Cenozoic (6).

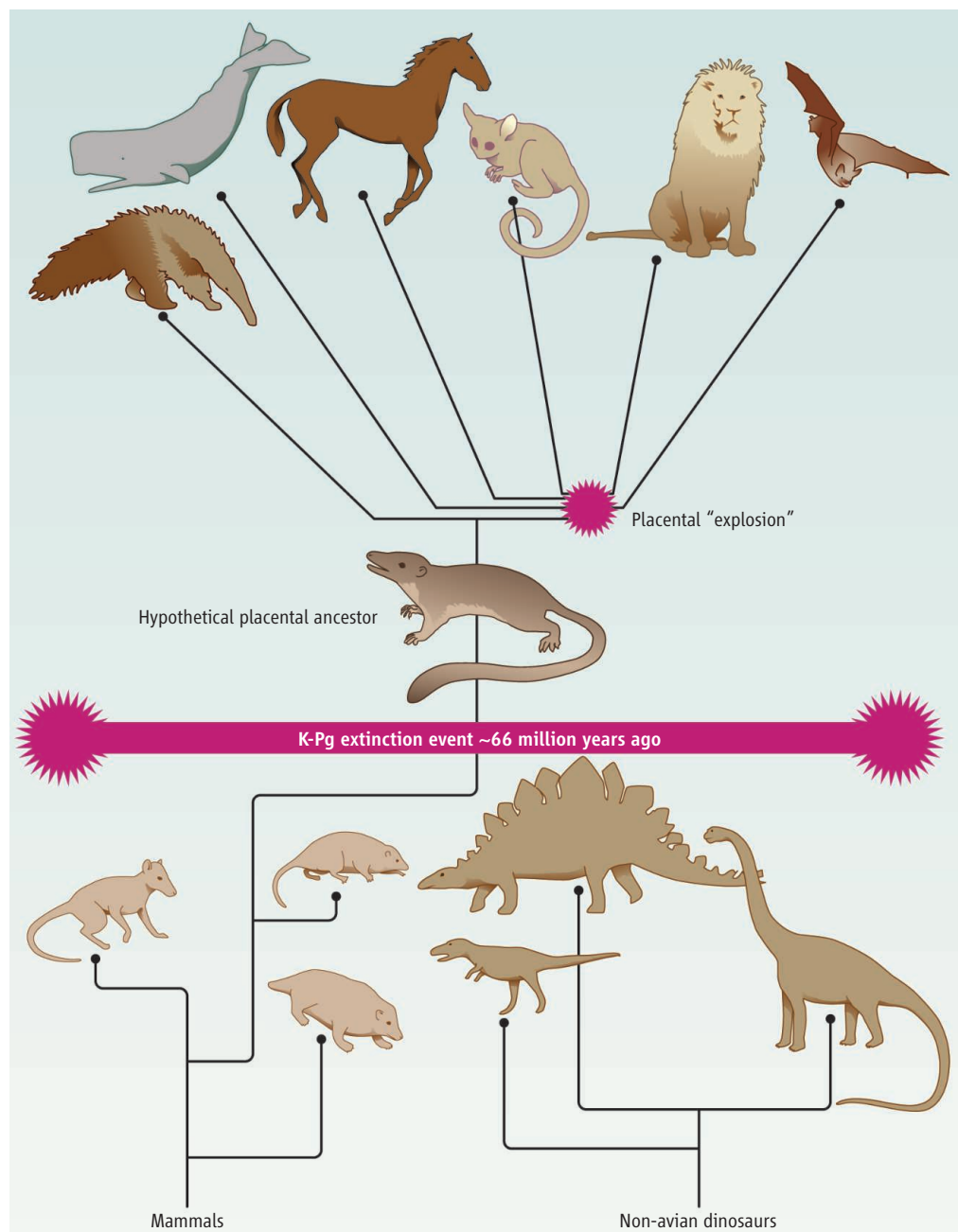
Given the notoriously incomplete nature of the fossil record, the revised and much older dates gained traction. The older dates were also attractive for their biogeographic implications. About 200 million years ago, the supercontinent Pangea began to split apart in a process that neared completion about 52 mil-

lion years ago. With dates as old as 100 million years ago, hypothesized by the molecular clock studies, the placental radiation could be explained by continental breakup (7). Taxonomy followed suit, with major clades named for the landmasses on which they were postulated to have evolved (8).

O'Leary *et al.* now shed doubt on this sequence of events. They have used cladistic methods to reconstruct the characteristics of a hypothesized placental ancestor that evolved soon after the K-Pg event and after the complete sundering of the ancient supercontinents. This ancestral mammal is inferred to be the predecessor of the explosive radiation of placental mammals at ~60 million years ago, thus requiring long-distance dispersal, perhaps over large bodies of water, to explain the present-day distribution of placental species.

Today, sophisticated theoretical and computational methods are used to estimate and calibrate molecular phylogenetic branch lengths (which represent time) (9). Together with improved methods for integrating fossil and molecular data (10), dates derived from molecular phylogenies have inched closer to those implied by the fossil record and the explosive model, though in these studies, researchers have concluded that at least some modern placental groups evolved prior to the K-Pg extinction event (11, 12). Is the approach used in the O'Leary *et al.* study directly comparable to these recent molecular phylogenetic studies? Not really, as it turns out.

Owing to the very large morphological data set evaluated by O'Leary *et al.*, the authors devoted most of their analytical energy to scoring characteristics and estimating the shape of the tree rather than the length of its branches. For age estimation, they turned to fossil calibrations and a rarely used method, ghost lineage analysis. Typical molecular phylogenetic studies use fossils as the variable for solving the molecular rate equation (13). The ghost lineage approach instead uses the defining morphological characteristics that align fossils with living clades to calibrate the phylogeny as a whole. This it does by using direct fossil evidence for the earliest appear-



Support for a classical hypothesis. The fossil record has long reinforced the hypothesis that placental mammals did not begin to evolve and diverge until after the impact of a massive asteroid ~66 million years ago. A tour-de-force morphological phylogenetic analysis by O'Leary *et al.* supports this hypothesis, positing that the ancestral placental mammal was small and insectivorous. The authors further conclude that the first split in the phylogeny was between the xenarthran clade (anteaters, sloths, and armadillos) and all other placental mammals.

ance of lineages and by inferring the presence of “ghost lineages” not documented in the fossil record but implied by sister-group relationships.

To understand the method, consider the lemurs of Madagascar. There are no known fossil lemurs, only unfossilized bones of lemurs that went extinct in the past 12,000 years. A direct reading of this record would yield the conclusion that lemurs evolved a few thousand years ago (14). However, we know that the closest relatives of lemurs are the Lorisiformes of Africa and Asia. The fossil record reveals that within the Lorisiformes, lorises and galagos diverged from each other by 39 million years ago (15), thus establishing a minimum age for lorisiforms and—because lemurs must have split off before that divergence—for lemurs. Thus, we infer that the lemurs are the product of a ghost lineage that has persisted for at least 40 million years.

O’Leary *et al.*’s study offers a level of sophistication and meticulous analysis of morphological and paleontological data that is unprecedented. By analyzing a morphological data set an order of magnitude greater than prior analyses, and integrating fossils within the phylogenetic analysis, they conclude that the origin and divergence of placental mammals must have occurred entirely after the K-Pg event. Even so, the reliance of age estimation procedures on a single phylogeny and the disregard for the consequences of branch lengths leave us wanting more. Future studies are sure to benefit from probabilistic modeling and statistical methods such as those being developed in (10). These methods bring morphological and molecular data into the same statistical analytical framework, allowing the fossils to explicitly influence the estimation of branch lengths.

References and Notes

1. L. W. Alvarez, W. Alvarez, F. Asaro, H. V. Michel, *Science* **208**, 1095 (1980).
2. M. A. O’Leary *et al.*, *Science*, **339**, 662 (2013).
3. Z.-X. Luo, *Nature* **450**, 1011 (2007).
4. G. J. Bowen *et al.*, *Science* **295**, 2062 (2002).
5. S. B. Hedges, P. H. Parker, C. G. Sibley, S. Kumar, *Nature* **381**, 226 (1996).
6. J. D. Archibald, D. H. Deutschman, *J. Mamm. Evol.* **8**, 107 (2001).
7. E. Eizirik, W. J. Murphy, S. J. O’Brien, *J. Hered.* **92**, 212 (2001).
8. W. J. Murphy *et al.*, *Nature* **409**, 614 (2001).
9. Z. Yang, B. Rannala, *Mol. Biol. Evol.* **23**, 212 (2006).
10. F. Ronquist *et al.*, *Syst. Biol.* **61**, 973 (2012).
11. R. W. Meredith *et al.*, *Science* **334**, 521 (2011).
12. M. dos Reis *et al.*, *Proc. Biol. Sci.* **279**, 3491 (2012).
13. M. Dos Reis, Z. Yang, *J. Syst. Evol.* **51**, 30 (2013).
14. R. D. Martin, *Int. J. Primatol.* **21**, 1021 (2000).
15. E. R. Seiffert, E. L. Simons, Y. Attia, *Nature* **422**, 421 (2003).

Acknowledgments: I thank J. Flynn, G. Gunnell, P. Larsen, R. Martin, J. Thorne, and Z. Yang for helpful comments.

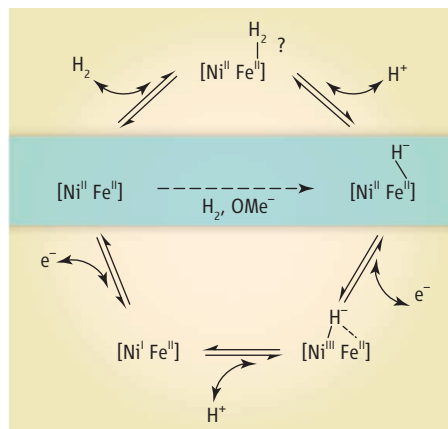
10.1126/science.1233999

CHEMISTRY

Copying Biology’s Ways with Hydrogen

Fraser A. Armstrong

Hydrogen (H_2), produced from solar energy and water, offers the ultimate solution for generation and storage of renewable energy. The challenge is to find catalysts suitable for economic large-scale production (made from earth-abundant elements) that can interconvert H_2 and water rapidly without a large excess thermodynamic cost (which would waste available energy). The most efficient catalyst for electrolysis of water is the noble metal platinum, but microbes deal very well with H_2 by exploiting iron (Fe) and nickel (Ni), dressed up with special ligands and buried inside enzymes known as hydrogenases (1). Hydrogenases are extremely efficient catalysts for producing and oxidizing H_2 at rates exceeding thousands per second near the reversible potential, and establishing their mechanism is crucial for future H_2 technology (2). On page 682 of this issue, Ogo *et al.* (3) describe a synthetic analog of the active site of [NiFe]hydrogenases that oxidizes H_2 via a hydride-containing intermediate formally equivalent to the most reduced catalytic state of the enzyme.



A minimal hydrogenase mechanism. The catalytic cycle shown for the core of [NiFe]hydrogenases is based on the constraints that only protons and electrons can enter or leave the active site, and do so singly. The reaction and species highlighted in blue is the equivalent chemical transformation reported by Ogo *et al.*; OMe[−] is the methoxide ion.

In hydrogenases, the Ni atom is coordinated by four cysteine thiolates, two of which form bridges to the Fe atom, which is further coordinated by one carbon monoxide (CO) and two cyanide ligands. Model compounds are ultimately dictated by what is synthetically feasible and stable, and in the com-

A model iron-nickel compound that mimics the core of hydrogenase enzymes provides insights into the formation of the H^- intermediate.

pounds described by Ogo *et al.*, an almost planar Ni(II) is coordinated by two N donors and two thiolate S donors—the latter bridging to an Fe(II) that is also coordinated by three triethylphosphites, which mimic the soft ligand environment of the Fe in the enzyme and provide steric stabilization.

Critics will argue that the analog lacks the outer shells of the enzyme’s active site and that the best bio-inspired catalysts have a nitrogen base fixed at close range. Nonetheless, the stepwise details of H_2 oxidation described by Ogo *et al.* reveal intrinsic aspects of the $[Ni^{II}(SR)_2Fe^{II}]$ core (where SR is a thiol group) that have otherwise been elusive. In direct studies of the enzyme mechanism, locating H atoms in intermediates is challenging, as most are highly reactive and may contribute no signal in electron paramagnetic resonance (EPR) studies.

The mechanism of [NiFe]hydrogenases outlined in the figure arises by considering the constraints governing discrete steps rather than intrinsic properties of states. Isotope exchange experiments have shown that H–H bond cleavage is heterolytic, forming a metal-bound hydride and a proton (1). Further constraints arise from the isolated nature of the active site; hydrogen can only

Department of Chemistry, Inorganic Chemistry Laboratory, University of Oxford, South Parks Road, OX1 3QR, England, UK. E-mail: fraser.armstrong@chem.ox.ac.uk

enter or leave the active site as H^+ , and electrons must do so in single, long-range transfers. For the enzyme, the five-coordinate, 16-valence-electron, low-spin Fe(II) would be the first guess for the primary target of H_2 binding, the paradigm being Kubas' compound (4), in which sideways coordination of H_2 uses the metal's d orbitals for back-bonding with the σ_u antibonding orbital. Nonetheless, the inhibitor CO binds at the Ni site of the enzyme (5), and calculations indicate that H_2 binding is equally likely at Ni or Fe (6).

There is no evidence that Fe exists in any other state than diamagnetic Fe(II) during catalysis, so how could the sixth site on the Fe remain empty, and what role does the Fe perform? In the model complex, before reaction with H_2 , the sixth site is occupied by a solvent MeCN molecule, yet the location of the H^- ligand in the product does not prove that Fe is also the site for transient binding of H_2 . No H_2 adduct of hydrogenases has ever been detected, suggesting that H–H cleavage occurs immediately upon binding; the proton transfers to a nearby base, most likely a terminal cysteine S atom.

In [FeFe]hydrogenases, a pendant (overhanging) amine lies within 3.5 Å of the Fe atom likely to bind H_2 , and the best functional analogs, which interestingly contain a single Ni atom, also depend on a pendant base (7). The NiFe analog requires a strong base,

methoxide, to abstract H^+ and form the H^- complex (highlighted in blue in the figure). The need for such a strong base reflects both the inefficient bimolecular nature of this reaction and the importance of synchronous proton transfer.

The H^- complex, structurally characterized by neutron diffraction and nuclear magnetic resonance spectroscopy, is equivalent to the enzyme state known as Ni-R, formulated as a hydrido $Ni^{II}-Fe^{II}$ species. Ogo *et al.* focus our attention on the Fe by unambiguously showing that Fe is the site of H^- binding after heterolytic cleavage and also establish its viability for the same function in the enzyme. The analogous product that formed with a similar complex, in which Fe is replaced by ruthenium (Ru), is a metal-metal bonded Ru(I)–Ni(I) species with a bridging proton located closer to the Ni (8). The $Ni(N_4S_4)$ geometry is unchanged when the Fe–H bond is formed, although the Ni–Fe distance contracts from 3.32 to 2.79 Å. The retention of ligand geometry about Ni argues against its being directly involved in the initial activation step.

In the enzyme, oxidation of Ni-R gives the intermediate Ni-C—a Ni(III) species in which H^- is coordinated to the Ni but in a bridging position with respect to Fe, as shown by EPR studies (9). If H^- formed first at Fe, one-electron oxidation might require that it relocate to the Ni, which can be formally oxi-

dized to Ni(III), unlike the Fe atom, which is difficult to oxidize above Fe(II) because it bears a CO ligand. In the next stage, the H^- is oxidized to H^+ . Departure as H^+ necessitates synchronous reduction to Ni(I) or to an intermediate with Ni(II) and Fe(I). Such a Ni(I) species has not been established as an intermediate but may be analogous to a state known as Ni-L produced upon low-temperature illumination (9). Whatever the nature of this intermediate, its one-electron oxidation completes the cycle.

Most H^- transfers in biology use NADH (dihydronicotinamide adenine dinucleotide). In contrast, transition-metal H^- ligands such as that reported by Ogo *et al.* can be generated and activated by successive electron transfers to increase hydricity for more demanding reactions. The H^- ligand adds “hidden” two-electron capacity to a d metal, and we are likely to see many more examples.

References

1. J. C. Fontecilla-Camps, A. Volbeda, C. Cavazza, Y. Nicolet, *Chem. Rev.* **107**, 4273 (2007).
2. K. A. Vincent, A. Parkin, F. A. Armstrong, *Chem. Rev.* **107**, 4366 (2007).
3. S. Ogo *et al.*, *Science* **339**, 682 (2013).
4. G. J. Kubas, *Chem. Rev.* **107**, 4152 (2007).
5. H. Ogata *et al.*, *J. Am. Chem. Soc.* **124**, 11628 (2002).
6. H. Wu, M. B. Hall, *C. R. Chim.* **11**, 790 (2008).
7. S. Raage *et al.*, *Chem. Eur. J.* **18**, 6493 (2012).
8. S. Ogo *et al.*, *Science* **316**, 585 (2007).
9. S. Foerster *et al.*, *J. Biol. Inorg. Chem.* **10**, 51 (2005).

10.1126/science.1233210

PLANT SCIENCE

Jack of All Trades, Master of Flowering

Jonas Å. H. Danielson and Wolf B. Frommer

Artists and scientists have long pondered the beauty and mystery of flowers and their origins. To Maurice Maeterlinck, the Nobel laureate in literature, the most striking feature of plants was the diversity of flowers, organs that evolved to enhance sexual reproduction (1). Charles Darwin was fascinated with the rapid expansion and dominance of flowering plants (angiosperms) in the late Cretaceous, a phenomenon he called “the abominable mystery” (2). Along with the evolution of flowers came the need for plants to trigger flowering at the right time. On page 704 of

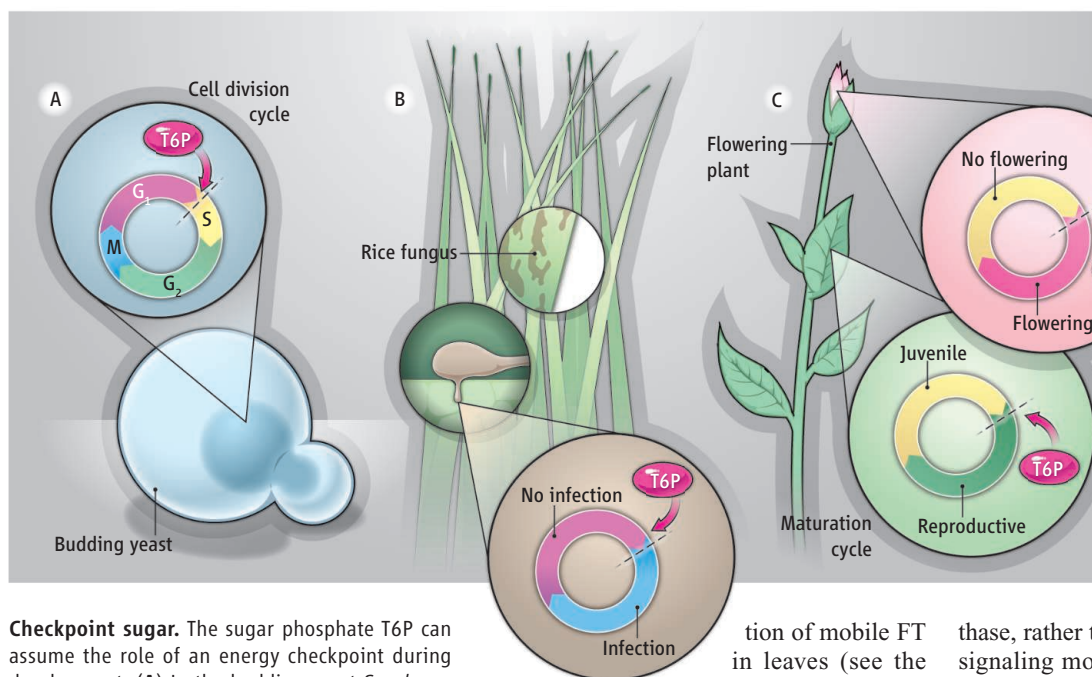
this issue, Wahl *et al.* report that an internal cue—the sugar metabolite trehalose-6-phosphate (T6P)—helps to ensure that flowering occurs at the time optimal for successful reproduction (3).

The evolution of flowering plants accelerated greatly ~100 million years ago with the development of flowers and their role in recruiting animals to help distribute pollen and seeds. The daily and seasonal timing of flowering evolved to ensure sufficient energy and nutrients to produce vigorous and healthy seeds (4, 5). In 1936, the Russian scientist Mikhail Chailakhyan proposed that a mystery substance acts as a mobile signal that underlies flowering. Analogous to a morphogen—a mobile substance that

A sugar derivative links nutrient availability in plants to the control of flowering.

helps to create asymmetry during development and patterning of organs in animals—he named this substance “florigen.” Since then, the nature of florigen remained an enigma. In the past decade, research on the model flowering plant *Arabidopsis thaliana* has led to the widely accepted hypothesis that a protein called Flowering Locus T (FT) acts as a florigen (4, 5). FT production is initiated in leaves in response to changes in the photoperiod (the relative lengths of the light and dark periods), determined by light receptors and the plant's internal circadian clock. FT then translocates, through vascular cells comprising the phloem, to the shoot apical meristem, where it triggers flowering. Although FT is the best-characterized trig-

Carnegie Institution for Science, 260 Panama Street, Stanford, CA 94305, USA. E-mail: wfrommer@stanford.edu



Checkpoint sugar. The sugar phosphate T6P can assume the role of an energy checkpoint during development. (A) In the budding yeast *Saccharomyces cerevisiae*, the decision to proceed through cell division is controlled by T6P (11). (B) The rice blast fungus *Magnaporthe oryzae* uses T6P to sense the environment and initiate infectious growth as a response to the increased sugar concentrations in the plant cell. (C) T6P regulates flowering both in the leaf and in the shoot apical meristem.

ger for flower development, day length is but one of several cues affecting flowering regulation. Other pathways, such as vernalization (prolonged cold treatment) and age, as well as substances, particularly sugars and the plant hormone gibberellin, also have been implicated in floral induction. Thus, the transition to flowering is complex and involves the convergence of multiple signals onto the flowering gene circuitry (6). In the face of this complexity—which is probably key to evolutionary bet hedging on the part of the plant (7)—we still lack an understanding of fundamental components of the process of floral regulation, specifically how the nutritional status, which is key to the production of viable seed, affects this transition.

Wahl *et al.* show how the plant's metabolic status may feed into the developmental decision to flower through the sugar phosphate T6P. Trehalose, while present at low amounts in most plants, is a jack of all trades: Insects use it as an energy source; worms and some plants use it as an osmolyte; and it protects enzymes from dehydration (trehalose stabilizes enzymes, for example, when water is scarce) (8). Wahl *et al.* reveal that T6P is sufficient to trigger flowering in *Arabidopsis* when it is produced in the shoot apical meristem and that T6P contributes to the produc-

tion of mobile FT in leaves (see the figure). The authors show that in leaves, the T6P biosynthetic pathway has a gating role for the photoperiod pathway—that is, T6P allows the plant to mature from a juvenile stage to a reproductive, flower-producing stage. Because sucrose can trigger flowering, and because T6P concentrations correlate strongly with sucrose availability (9), T6P creates a link between the carbohydrate status of the leaf and the FT-flowering pathway. This link provides a possible means to ascertain that flowering is initiated when sufficient resources are expected to be available (energy reserves and nutrients) to complete the plant's reproductive life cycle. Independent of this function, T6P also affects the transition to flowering directly at the shoot apical meristem. Wahl *et al.* observed that in the meristem, the action of T6P partially overlaps with the age-related signaling pathway that involves miR156, a microRNA that represses flowering.

The role of a unique and low-abundance sugar phosphate in decision-making in plant development is evolutionarily interesting. That T6P is a key regulator of developmental decisions in plants and fungi (10) points to the possibility of an evolutionarily conserved and ancient function in developmental transitions. Information on energy and nutritional status—whether conditions are such that enough reserves will likely be available for completion of flowering and seed production—is likely key for the decision to flower by the plant. It may be that plants use checkpoints in this process, analogous to the role of checkpoints, in the decision for cells to divide. Perhaps T6P, act-

ing as a proxy for energy status, has to increase to a concentration that meets the checkpoint requirement (11). When multiple criteria are met (plant size, energy status, and favorable conditions), florigen is produced and exported from the leaf. Although T6P may act as an allosteric effector—that is, by binding to a regulatory protein and thereby changing its activity—analysis of T6P synthesis in the rice blast fungus *Magnaporthe oryzae* indicates that the biosynthetic enzyme T6P syn-

thase, rather than its product T6P, is the key signaling molecule in fungal development (10). If so, this would be similar to the idea that hexokinase has a dual function as an enzyme and glucose sensor (12).

It remains unclear exactly how plant sucrose affects the concentration of T6P, or how T6P or T6P synthase act mechanistically as a signal. The findings of Wahl *et al.* will enable the unraveling of T6P signaling networks and further exploration of how various signals are integrated to control flowering. In many organisms, T6P serves as a stress signal in cold temperatures and during drought. It is possible that stress-induced T6P production in plants could override repressive signals and trigger premature flowering. T6P may thus not only act in gating checkpoints to optimize plant reproduction, but under less favorable conditions, it may trigger premature flowering in a last-ditch effort to produce descendants.

References

1. M. Maeterlinck, *L'Intelligence des fleurs*, E. Fasquelle, Ed. (Bibliothèque-Charpentier, Paris, 1907).
2. W. E. Friedman, *Am. J. Bot.* **96**, 5 (2009).
3. V. Wahl *et al.*, *Science* **339**, 704 (2013).
4. Y. Kobayashi, D. Weigel, *Genes Dev.* **21**, 2371 (2007).
5. R. W. King, O. M. Heide, *Funct. Plant Biol.* **36**, 1027 (2009).
6. G. Bernier, C. Périlleux, *Plant Biotechnol. J.* **3**, 3 (2005).
7. D. Z. Childs, C. J. Metcalf, M. Rees, *Proc. Biol. Sci.* **277**, 3055 (2010).
8. N. K. Jain, I. Roy, *Protein Sci.* **18**, 24 (2009).
9. M. J. Paul, L. F. Primavesi, D. Jhurreea, Y. Zhang, *Annu. Rev. Plant Biol.* **59**, 417 (2008).
10. J. Fernandez, R. A. Wilson, *Mol. Plant Microbe Interact.* **25**, 1286 (2012).
11. J. M. Thevelein, S. Hohmann, *Trends Biochem. Sci.* **20**, 3 (1995).
12. W. B. Frommer, W. X. Schulze, S. Lalonde, *Science* **300**, 261 (2003).

10.1126/science.1234601

RETROSPECTIVE

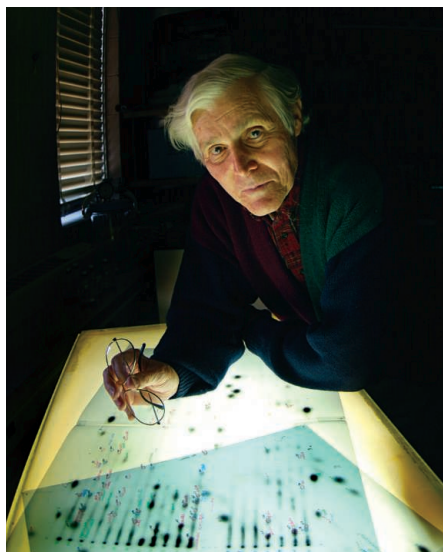
Carl R. Woese (1928–2012)

Nigel Goldenfeld¹ and Norman R. Pace²

Carl Woese was not a well-known personality outside of microbiology and evolutionary biology, but he forever changed our understanding of the biosphere and its evolution. He passed away at his home in Urbana, Illinois, on 30 December 2012. Carl Woese developed the modern gene sequence–based understanding of biological organization, showing that the evolutionary history of lineages can be tracked to a common ancestral state. In doing so, he discovered the third domain of life, which came to be known as the archaea. His story is the epitome of the outsider, a lone and dedicated visionary who overthrew a century of dogma and established thought and brought about a revolution that has touched every area of modern biology.

An unrepentant iconoclast, Woese skirted popular areas of molecular biology and chose instead to pursue evolutionary questions. He became the foremost expert on all aspects of the genetic code, which he foresaw held the key to a deep understanding of life. His 1967 book *The Genetic Code* broached the notion of a prebiotic “RNA world,” still a focus of thought on the origin of life. He made fundamental contributions to how we determine and understand large RNA structures. But Woese’s most groundbreaking achievement was his use of primitive nucleic acid sequencing technology to compare ribosomal RNA (rRNA) sequences from diverse organisms, mostly microbes, and to report in 1977, with George Fox, the first scientifically based phylogenetic tree of life—in essence a map that revealed the large-scale organization of life and the early course of evolution.

Woese’s findings and interpretations of data clashed with the prevailing scientific wisdom of the time. The model of deep evolution then—still taught in most of our textbooks today—was that all life is one of two kinds, prokaryote or eukaryote, and that prokaryotes gave rise to more modern eukaryotes. Instead, Woese’s data showed three kinds of organisms and thus, three domains: eukaryotes, the classic bacteria, and the newly discovered archaea. The concept of prokaryotes



had no phylogenetic justification; the eukaryotic nuclear lineage (in contrast to the bacterially derived mitochondria and chloroplasts) did not originate more recently than bacteria or archaea, but was primordial and a sister group to the archaea. These radical claims inflamed many evolutionists, but his three-domain classification is now widely accepted and is supported by much correlation. Woese was personally stung by the harsh criticism, but as he once exclaimed, “I point at the moon and they focus on my finger!”

One development that Woese did not anticipate was his profound impact on microbial ecology. Microbial ecosystems are the foundation of Earth’s biosphere. Yet, before Woese’s sequence-based phylogenetic framework developed, there was no meaningful way to survey the microbes that make up the natural microbial world. With Woese’s phylogenetic reference framework based on sequences, microbiologists could isolate rRNA and rRNA genes from the environment for sequence analysis, and thus identify and study environmental organisms. Microbial ecology was boosted from a moribund state to one of the most vibrant fields of biology, with important ramifications for medicine, as evidenced by the ongoing Human Microbiome Project.

Woese’s discoveries showed that all life on Earth descended from an ancestral state that existed 3.5 to 3.8 billion years ago, with the key elements of the modern cell already

A visionary microbiologist focused on evolution and discovered a third domain of life, archaea.

in place. Woese regarded the rapidity of this initial phase of life to be the most remarkable aspect of his discoveries, implying that before this time, the nature of the evolutionary process must have had a different tempo and mode from that of the present epoch.

Carl Woese was born in 1928 in Syracuse, New York. He studied mathematics and physics as an undergraduate at Amherst College in Massachusetts, and earned a Ph.D. in biophysics at Yale University in 1953. Being interested in phylogeny, he took considerable pride in his own heritage in physics. His Ph.D. mentor, the biophysicist Ernest Pollard, was a student with physics Nobel laureate James Chadwick, himself a student of the chemist, physicist, and Nobel laureate Ernest Rutherford, who was in turn a student of the physics Nobel laureate J. J. Thomson. Woese developed interests in the origin of the genetic code and ribosome while working as a biophysicist with General Electric Research Laboratory. In 1964, Sol Spiegelman invited him to join the faculty of the University of Illinois, where he remained until his death. He received much recognition over the years, including a MacArthur Fellowship; membership in the U.S. National Academy of Sciences and the Royal Society; the U.S. National Medal of Science; the Royal Netherlands Academy of Arts and Sciences Leeuwenhoek Medal, considered the highest award in microbiology; and the Royal Swedish Academy of Sciences Crafoord Prize in Biosciences, a parallel to the Nobel Prize.

Although he pursued his life’s work with a dedication, intensity, and even gravitas that has rarely been matched, Woese imbued his research with a personal sense of fun and playfulness. He was a complex man, but those with whom he was able to share his passions found him brilliant, witty, brutally honest, generous, and humble. Woese often attributed his success in biology to his training as a physicist. Once, appalled by an immodest parody of a famous quote by Newton, he quipped: “If I have seen further than others, it is because I was looking in the right direction.” Woese indeed saw miles ahead of the rest of us. His passing leaves the microbiology community feeling, as he would surely put it (and with a nod to his love of jazz), “kind of blue.”

10.1126/science.1235219

The Placental Mammal Ancestor and the Post-K-Pg Radiation of Placentals

Maureen A. O'Leary,^{1,3¶} Jonathan I. Bloch,² John J. Flynn,³ Timothy J. Gaudin,⁴ Andres Giallombardo,³ Norberto P. Giannini,^{5*} Suzann L. Goldberg,³ Brian P. Kraatz,^{3,6} Zhe-Xi Luo,^{7†} Jin Meng,³ Xijun Ni,^{3‡} Michael J. Novacek,³ Fernando A. Perini,^{3||} Zachary S. Randall,² Guillermo W. Rougier,⁸ Eric J. Sargis,⁹ Mary T. Silcox,¹⁰ Nancy B. Simmons,⁵ Michelle Spaulding,^{3,11} Paul M. Velazco,⁵ Marcelo Weksler,^{3§} John R. Wible,¹¹ Andrea L. Cirranello^{1,3}

To discover interordinal relationships of living and fossil placental mammals and the time of origin of placentals relative to the Cretaceous-Paleogene (K-Pg) boundary, we scored 4541 phenomic characters de novo for 86 fossil and living species. Combining these data with molecular sequences, we obtained a phylogenetic tree that, when calibrated with fossils, shows that crown clade Placentalia and placental orders originated after the K-Pg boundary. Many nodes discovered using molecular data are upheld, but phenomic signals overturn molecular signals to show Sundatheria (Dermoptera + Scandentia) as the sister taxon of Primates, a close link between Proboscidea (elephants) and Sirenia (sea cows), and the monophyly of echolocating Chiroptera (bats). Our tree suggests that Placentalia first split into Xenarthra and Epitheria; extinct New World species are the oldest members of Afrotheria.

It is disputed whether orders of placental mammals, the very diverse group of species that includes humans, evolved before or after the significant extinction horizon known as the Cretaceous-Paleogene (K-Pg) event 66 to 65 million years ago (Ma) (1, 2). Different models have been proposed to describe ordinal-level diversification either before (short-fuse model), near (long-fuse model), or after (explosive model) this boundary (3). The ~5100 living placental species collectively exhibit extreme size ranges (1.5-g bumblebee bat to 190,000-kg blue whale); dramatic locomotor diversity (e.g., running, flying, and swimming); and diverse degrees of encephalization (4). Moreover, extinct species in the placental fossil record are even more numerous and exhibit a broader range of adaptations (5). Given this diversity, it is of interest to determine the phenotype of the ancestral placental mammal.

The hypothesis that the oldest members of crown Placentalia [the clade of all living placental mammals (6)] were present by ~100 Ma in the Mesozoic Era has been supported by molecular clock analyses (7–9), which suggest that at least 29 mammalian lineages (7), including the stem lineages of Primates and Rodentia, appeared in Late Cretaceous ecosystems (8) and survived the massive K-Pg extinction event. However, fossil evidence has not corroborated this hypothesis, despite discovery of abundant, well-preserved, small vertebrates (10). By contrast, phenomic phylogenies incorporating fossils have placed ordinal and intraordinal specia-

tion of Placentalia after the K-Pg extinction event (11).

Determining placental origins and relationships has met with the practical challenge of codifying phenomic data on a scale comparable to that for genomic data to produce a maximally informed phylogenetic tree. We built a phenomic character matrix (4541 characters; 403 constant and 482 parsimony uninformative) using MorphoBank (12). The matrix contains newly scored characters for 86 species representing all living placental orders plus 40 fossil species, with more than 12,000 annotated images supporting the phenomic homologies. These data were examined with molecular sequences compiled from 27 nuclear genes from GenBank (table S1).

Placental orders originated after the K-Pg boundary. A single tree emerged from our combined phenomic-molecular parsimony analysis (Fig. 1; hereafter, “combined tree”); we also performed extensive sensitivity analyses using other tree-searching methods (13). We applied multiple fossil ages for the oldest members of the clades sampled and ghost lineage analysis (14) to this tree to determine minimum divergence dates using fossils alone (13). Results support the monophyly of most traditional orders originally identified on the basis of phenotypes, as well as interordinal groupings discovered using molecular sequence data (Fig. 1 and Table 1). Twenty nodes (over 40%) are congruent in partitioned molecular and phenomic analyses (fig. S2).

When time-calibrated, this tree indicates that none of the six, very complete Mesozoic fossil species (e.g., *Ukhaatherium*, *Maelestes*, and *Zalambdalestes*) sampled falls within crown clade Placentalia. Instead, these Mesozoic fossils emerge as nonplacental members of Eutheria or at lower nodes. This tree suggests that interordinal and ordinal diversification occurred within the first few hundred thousand years after the K-Pg event, and the first members of modern placental orders began appearing 2 to 3 million years (My) later during the Paleocene. All recent clock-based estimates for the ages of key clades, with few exceptions, are substantially older than indicated by the fossil record (7, 8, 15). Ghost lineage estimates are minimum divergence dates and may underestimate the timing of actual splits.

We find that only the stem lineage to Placentalia crossed the K-Pg boundary and then speciated in the early Paleocene. We estimate that the minimum age of the diversification of crown Placentalia is just younger than the K-Pg boundary, or ~36 My younger than molecular clock-based mean estimates derived from supertree (15) and supermatrix (7) analyses. We do not find support for the hypothesis that 29 to 39 (7, 15) mammalian lineages, including Afrotheria, Rodentia, Primates, Lipotyphla, Xenarthra,

¹Department of Anatomical Sciences, School of Medicine, HSC T-8 (040), Stony Brook University, Stony Brook, NY 11794–8081, USA. ²Florida Museum of Natural History, University of Florida, Gainesville, FL 32611–7800, USA. ³Division of Paleontology, American Museum of Natural History, 79th Street and Central Park West, New York, NY 10024–5192, USA. ⁴Department of Biological and Environmental Sciences, University of Tennessee at Chattanooga, 615 McCallie Avenue, Chattanooga, TN 37403–2598, USA. ⁵Department of Mammalogy, American Museum of Natural History, 79th Street and Central Park West, New York, NY 10024–5192, USA. ⁶Western University of Health Sciences, Department of Anatomy, Pomona, CA 91766–1854, USA. ⁷Section of Vertebrate Paleontology, Carnegie Museum of Natural History, 4400 Forbes Avenue, Pittsburgh, PA 15213–4080, USA. ⁸Department of Anatomical Sciences and Neurobiology, University of Louisville, Louisville, KY 40292, USA. ⁹Department of Anthropology, Yale University, Post Office Box 208277, New Haven, CT 06520–8277, USA. ¹⁰Department of Anthropology, University of Toronto Scarborough, 1265 Military Trail, Scarborough, Ontario M1C 1A4, Canada. ¹¹Section of Mammals, Carnegie Museum of Natural History, 5800 Baum Boulevard, Pittsburgh, PA 15206, USA.

*Present address: Consejo Nacional de Investigaciones Científicas y Tecnológicas, Facultad de Ciencias Naturales e Instituto Miguel Lillo, Universidad Nacional de Tucumán, Miguel Lillo 205, Código Postal 4000, Tucumán, Argentina.

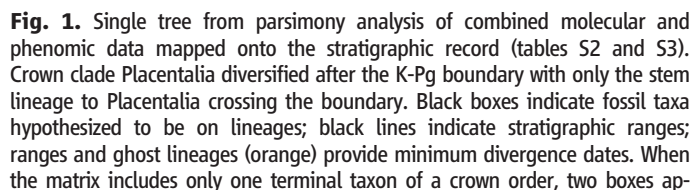
†Present address: Department of Organismal Biology and Anatomy, University of Chicago, 1027 East 57th Street, Chicago, IL 60637, USA.

‡Present address: Institute of Vertebrate Paleontology and Paleoanthropology, Chinese Academy of Sciences, 142 Xi-Zhi-Men-Wai Street, Beijing, 100044, P. R. China.

§Present address: Department of Vertebrates, Museu Nacional, Universidade Federal do Rio de Janeiro, Rio de Janeiro, RJ 20940-040, Brazil.

||Present address: Department of Zoology, Instituto de Ciências Biológicas, Universidade Federal de Minas Gerais, Avenida Antônio Carlos 6627, Belo Horizonte, Minas Gerais 31270-901, Brazil.

¶To whom correspondence should be addressed. E-mail: maureen.oleary@stonybrook.edu



pear: the oldest hypothesized member of the crown clade (the younger date) and the oldest hypothesized taxon on the stem to the crown clade (the older date). Crown clades (except Eutheria and Metatheria) are defined (table S4). Space immediately younger than 65 Ma not to scale showing early Paleocene interordinal diversification of Placentalia. Crown clades Marsupialia and Monotremata also diversified post K-Pg boundary. Bremer support (BS) (table S8) above nodes, jackknife values below nodes.

Table 1. Comparison of divergence dates for mammalian clades (tables S2 and S3) between our combined data analysis, a combined data supertree [Bininda-Emonds *et al.* (15)], and a molecules-only supermatrix [Meredith *et al.* (7)]. Ranges and ghost lineages are illus-

trated in Fig. 1; date calculations are described in (14). Names listed specify crown clades (table S4); older dates in (7, 15) are negative differences (bold). –, no data; NA, not applicable because clade not found in our study.

Taxon		Oldest crown clade member (this study)		Oldest crown clade member—Age midpoint (range) and difference from our study			
Higher clades	Orders	Taxon	Clade age (range) (Ma)	Bininda-Emonds <i>et al.</i> (Ma)	Difference	Meredith <i>et al.</i> (Ma)	Difference
Mammalia Linnaeus 1758		Dryolestida [Martin <i>et al.</i> (38)]	166.2 (167.7–164.7)	166.2*	1.5	217.8 (203.3–238.2)	–50.1
Monotremata Bonaparte 1838		<i>Obdurodon insignis</i>	20.0 (28.4–11.6)	63.6 ± 11.4	–35.2	36.7 (22.4–103.1)	–8.4
Theria Parker & Haswell 1897		<i>Sinodelphys szalayi</i>	127.5 (130.0–125.0)	–	–	190.0 (167.2–215.3)	–60.0
Marsupialia Illiger 1811		<i>Peradectes minor</i>	64.85†	82.5 ± 11.1	–17.7	81.8 (67.9–97.2)	–17.0
Placentalia Owen 1837		<i>Protungulatum donnae</i>	64.85†	101.3 ± 7.4	–36.5	101.3 (92.1–116.8)	–36.5
	Xenarthra Cope 1889	<i>Riostegotherium yanei</i>	58.3 (57.5–59.0)	72.5 ± 5.1	–13.5	65.4 (58.4–71.5)	–6.4
Epitheria McKenna (21)		<i>Protungulatum donnae</i>	64.85†	–	–	NA	–
Afrotheria Stanhope <i>et al.</i> (39)		<i>Prodiacodon crustulum</i>	64.85†	93.4 ± 3.0	–28.6	80.9 (74.4–96.5)	–16.1
Paenungulata Simpson (40)		<i>Simpsonotus praecursor</i>	61.8 (62.5–61.0)	–	–	64.3 (56.0–70.6)	–1.8
	Hyracoidea Huxley 1869	<i>Prohyrax hendeyi</i>	17.3 (23.0–11.6)	19.1 ± 0.8	–3.9	6.1 (3.9–8.3)	16.9
	Macroscelidea Butler 1956	<i>Miorhynchocyon sp.</i>	21.2 (22.4–20.0)	50.7 + 7.6	–28.3	49.1 (37.7–57.2)	–26.7
Tethytheria McKenna (21)		<i>Eritherium azzouzororum</i>	58.7	–	–	–	–
	Proboscidea Illiger 1811	<i>Primelephas gomphotheroides</i>	14.2 (23.0–5.3)	19.5 ± 12.1	–3.5	5.3 (1.8–8.0)	17.7
	Sirenia Illiger 1811	<i>Eotheroides aegyptiacum</i>	44.5 (48.6–40.4)	52.2 ± 14.4	–3.6	31.4 (25.0–34.4)	17.2
Boreoeutheria Springer & de Jong (41)		<i>Protungulatum donnae</i>	64.85†	–	–	92.0 (82.9–107.6)	–27.2
Laurasiatheria Waddell <i>et al.</i> (42)		<i>Protungulatum donnae</i>	64.85†	91.8 ± 2.6	–27.0	84.6 (78.5–93.0)	–19.8
	Lipotyphla Haeckel 1866	<i>Litolestes ignotus</i>	58.3 (58.9–57.8)	84.2 ± 2.1	–22.5	77.3 (70.7–85.8)	–15.6
	Chiroptera Blumenbach 1779	<i>Archaeonycteris praecursor</i>	55.5	74.9 ± 3.3	–19.4	66.5 (62.3–71.3)	–11.0
	Perissodactyla Owen 1848	<i>Hyracotherium angustidens</i>	52.9 (55.4–50.3)	58.2 ± 4.9	–2.8	56.8 (55.1–61.0)	–1.4
	Pholidota Weber 1904	<i>Smutsia gigantea</i>	5.0 (7.3–2.6)	19.9 ± 20.7	–12.6	25.3 (16.9–35.7)	–18.0
	Carnivora Bowditch 1821	<i>Hesperocyon gregarius</i>	43.3 (46.2–40.4)	67.1 ± 3.8	–20.9	54.7 (47.4–60.6)	–8.5
	Artiodactyla Owen 1848	<i>Cainotherium sp.</i>	44.9 (55.8–33.9)	74.1 ± 3.1	–18.3	65.4 (62.3–68.5)	–9.6
Euarchontoglires Murphy <i>et al.</i> (88)		<i>Purgatorius coracis</i>	64.85†	94.5 ± 2.0	–29.7	83.3 (74.1–97.8)	–18.5
Euarchonta Waddell <i>et al.</i> (42)		<i>Purgatorius coracis</i>	64.85†	–	–	82.0 (73.7–97.4)	–17.2
	Primates Linnaeus 1758	<i>Teilhardina brandti</i>	53.1 (55.8–50.3)	87.7 ± 2.7	–31.9	71.5 (64.3–78.4)	–15.7
	Dermoptera Illinger 1811	No crown clade fossils	No crown clade fossils	13.0 ± 5.2	–	7.4 (4.5–13.2)	–
	Scandentia Wagner 1855	<i>Eodendrogale parvum</i>	42.9 (48.6–37.2)	32.7 ± 2.6	15.9	55.9 (45.0–63.9)	–7.3

(Continued on next page)

Higher clades	Taxon	Oldest crown clade member (this study)		Oldest crown clade member—Age midpoint (range) and difference from our study			
		Taxon	Clade age (range) (Ma)	Bininda-Emonds <i>et al.</i> (Ma)	Difference	Meredith <i>et al.</i> (Ma)	Difference
Glires Linnaeus 1758		<i>Mimotona wana</i>	63.4 (65.0–61.7)	—	—	79.5 (71.5–94.1)	–14.5
	Rodentia Bowditch 1821	<i>Sciuravus</i> sp.	56.8	85.3 ± 3.0	–28.5	69.0 (64.1–74.8)	–12.2
	Lagomorpha Brandt 1885	Leporidae	53.0	66.8 ± 5.1	–13.8	50.2 (47.4–56.9)	2.8
		[Rose <i>et al.</i> (43)]					

*Fixed calibration point.

†Age between 65.0 and 64.7 Ma, in the Cenozoic portion of Chron C29r, 230 to 420 ky above the K-Pg boundary (1, 2).

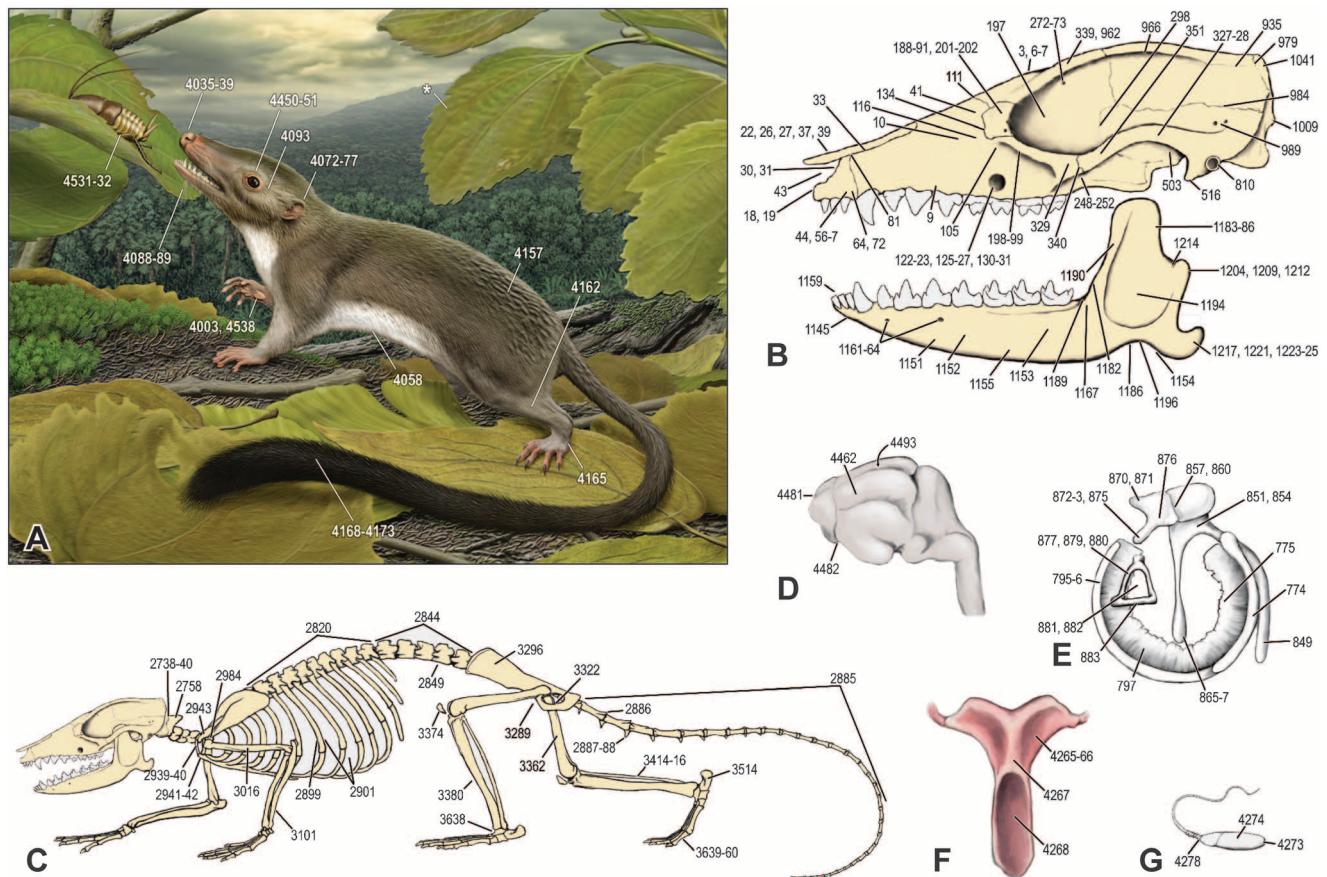


Fig. 2. Reconstructions of the phenotype of the hypothetical placental ancestor derived from the combined data matrix optimized onto the tree in Fig. 1. The mammal is shown in an early Paleocene ecosystem. (A) External body, posture, and diet of insectivory; asterisk depicts the plant *Paranymphea*

crassifolia of the early Paleocene. (B) Cranium and dentary bone, (C) skeleton, (D) brain in left lateral view, (E) ear ossicles and ectotympanic bone, (F) uterus, and (G) sperm cell. Numbers designate a subset of the numerous phenomic characters used to build these reconstructions (appendix S1).

Artiodactyla, and Chiroptera, each crossed the K-Pg boundary.

We recognize *Protungulatum donnae* as the oldest undisputed species within crown Placentalia (Fig. 1), and this species dates to the earliest Paleocene (13) within an interval extending from the K-Pg boundary to ~200,000 to ~400,000 years later (16, 17). Integration of fossils as primary data in the phylogeny indicates that ~10 interordinal speciation events might

have occurred in as little as 200,000 years. Most of the fossil species sampled across Placentalia fall either within ordinal crown clades or on the immediate stem to ordinal crown clades (exceptions are stem taxa to Glires, Tethytheria, and Euungulata).

Our results also imply that the total clade Eutheria (all species more closely related to Placentalia than to any other living species) is younger than estimated from prior studies. The

Cretaceous fossil *Eomaia scansoria* (125 Ma) has previously been called a placental (18) or eutherian (11, 18, 19); however, we find with 100% jackknife support that *Eomaia* falls outside of Eutheria as a stem taxon to Theria. The oldest age of Eutheria in our study is constrained by taxa such as *Maelestes* and is 91 Ma. The age of Theria is 127.5 Ma, a clade that some molecule-based estimates previously suggested to be 190 Ma (7).

Phenomic topologies dominate for key clades.

We resolve the basal diversification within Placentalia, a historically unstable node (20), as a split between Xenarthra and Epitheria (all other placentals; 89% jackknife and Bremer support of 14 steps). These clades were previously predicted to be monophyletic on the basis of phenomic data alone (21). The phenomic data-only tree (fig. S2A) supports the clade Sundatheria [Scandentia (treeshrews) + Dermoptera (flying lemurs)] as the sister taxon of Primates, a topology that prevails in the combined analysis, in contrast to molecules-only trees that favored Dermoptera in this role (7, 22).

The existence of two clades within bats (Chiroptera), one that echolocates (Microchiroptera) and one that does not (Megachiroptera), emerges from the phenomic-only analysis (fig. S2A), in contrast to molecule-based results (fig. S2B) (7, 23, 24). Microchiroptera in our combined data tree has low support, most likely because the molecules-only and phenomic-only trees each had 100% jackknife support for mutually incompatible hypotheses. In the combined tree, the phenomic signal is upheld relative to the molecular signal. The arrangement of two Eocene fossil bats (*Omychonycteris* + *Icaronycteris*) as a sister clade to extant Microchiroptera also differs from prior results (25). Molecules alone, here (figs. S2B and S3 to S6) and in prior studies (7), do not support Tethytheria. Phenomic data alone do support Tethytheria, and the combined data tree retains Tethytheria with relatively strong support, which corroborates previous combined data analyses (26).

Regarding extinct species, many fossil hoofed mammals are part of Laurasiatheria, and extinct relatives of Carnivora known as Creodonta lack deep linkages to African taxa (27). Endemic South American ungulates are split between Pan-Euungulata and Afrotheria (28). The fossil *Rhombomylus* has lagomorph (rabbit) affinities (29), which implies that loss of incisors occurred independently in Rodentia and Lagomorpha. Extinct Palaeonodonta (*Metacheiromys*) falls closer to Pholidota than to Xenarthra (30), and *Moeritherium* is a member of Tethytheria.

Reconstructing the placental ancestor and its dental formula. Integration of data for both fossil and living species permits reconstruction of ancestral nodes across the placental tree by using optimizations (Fig. 2 and appendix S1). We reconstructed the hypothetical placental ancestor using synapomorphic and symplesiomorphic characters. It weighed between 6 and 245 g (character 2026), was insectivorous (characters 4531 and 4532) and scansorial (character 4538), and single young were born hairless with their eyes closed (character 4290). Females had a uterus with two horns (character 4265) and a placenta with a trophoblast (character 4295), and males produced sperm with a flat head (character 4274) and had abdominal testes (characters 4228 and

4229) positioned just caudal to the kidneys. The brain was characterized by the presence of a corpus callosum (character 4493), an encephalization quotient greater than 0.25 (character 4460), facial nerve fibers that passed ventral to the trigeminal sensory column (character 4492), and a cerebral cortex that was gyrencephalic (character 4462) with distinctly separate olfactory bulbs (character 4482). A hemochorial placenta (character 4313) optimizes unambiguously to the base of Placentalia (31). The basal placental also lacked an endodermal cloaca (character 4226), having separate anal and urogenital openings.

Osteologically (Fig. 2), the placental ancestor had a triangular, perforate stapes (characters 878 and 882) and lacked epipubic bones (character 3290). Reconstructing soft tissues not preserved in fossils is best done by optimization (32) when both soft tissues and osteology have built the underlying tree. The path of the internal carotid artery sometimes leaves channels on adjacent bones and is frequently reconstructed in fossils (33). We find that this artery (scored as a soft tissue character in living species) optimizes as present in the ancestor of Placentalia; however, the three osteological correlates of the artery are each

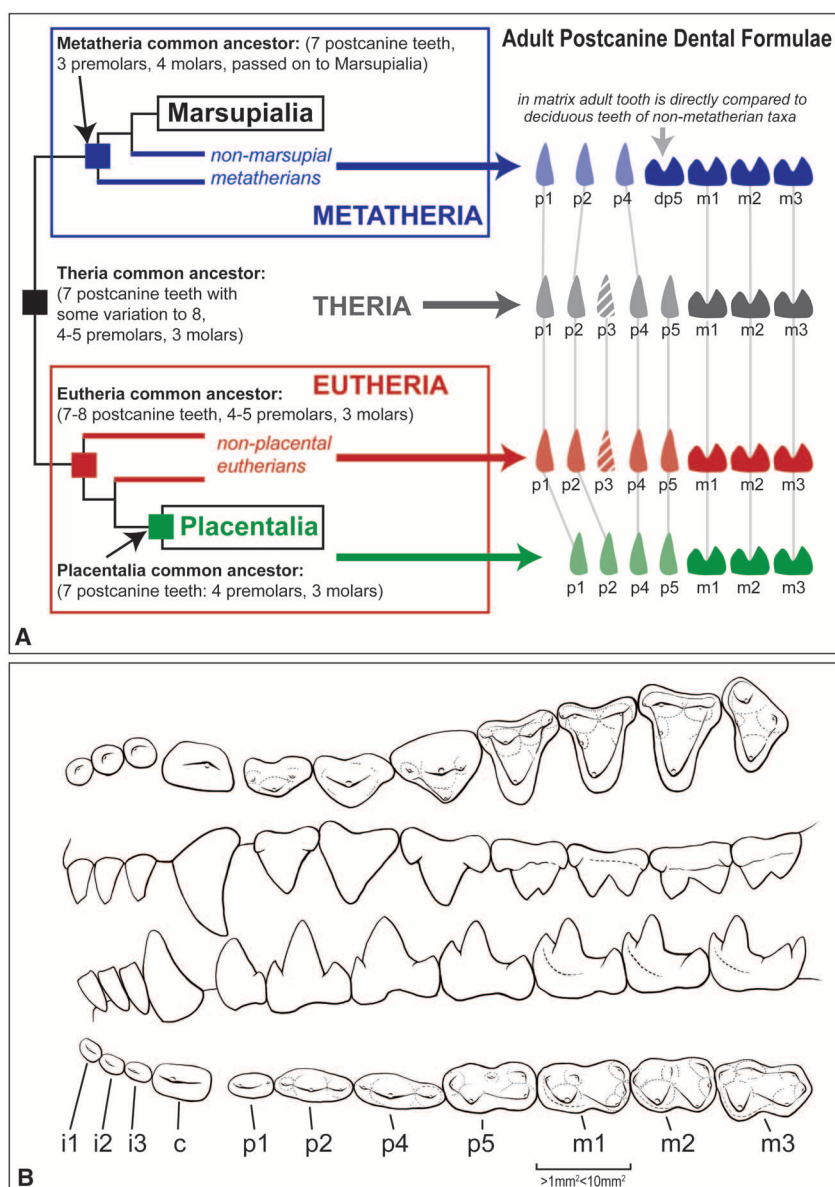


Fig. 3. (A) Split between Placentalia and Marsupialia and homologies of hypothesized adult postcanine dental formulae. Gray lines indicate adult teeth compared for cladistic scoring. **(B)** Reconstructions of the dentition of the hypothetical placental ancestor based on optimization (appendix S1, see also figs. S11 to S14). Views are left side. From top to bottom: occlusal upper teeth, labial upper teeth, labial lower teeth, and occlusal lower teeth. p, premolar; dp, deciduous premolar; m, molar.

absent (appendix S1). Thus, the conservative hypothesis is that the artery was present in the placental ancestor but did not leave an osteological correlate.

We have implemented a revised postcanine tooth formula for clades within Theria and reconstructed the dentition of the hypothetical placental ancestor (Fig. 3A). Complexities of homology arise in Theria regarding the number of premolars [any postcanine tooth with two generations (deciduous or “baby” teeth and permanent or “adult” teeth) or a postcanine tooth anterior to a tooth with two generations (34)]. Molars, by contrast, have a single generation and are posterior to teeth that are replaced. Metatheria (and Marsupialia) primitively have seven postcanine teeth, three of which are premolars. The common ancestor of Placentalia also had seven postcanine teeth, but four of these were premolars, and some nonplacental eutherians had as many as five premolars (11).

The primitive dental formula for Theria optimizes on our tree (Fig. 3) to be seven postcanine teeth: four premolars and three molars (Fig. 3A). Both Metatheria and Placentalia have each lost the third premolar (p3/P3) during evolution. We hypothesize that the first tooth in the molar series in Metatheria is homologous to the deciduous p5 (dp5) of eutherians, including placental (34, 35). What has been lost in Metatheria is the p5 locus tooth replacement. The implication for phylogenetic work is that a tooth at the fourth postcanine locus of an adult metatherian (the retained dp5) must be compared directly with a tooth in the dentition of a juvenile placental (the dp5). Accordingly, we revise the postcanine dental formula for Theria such that the primitive adult dentition for Placentalia consists of upper and lower p1, p2, p4, p5, m1, m2, and m3 [see (33)]. The reconstructed ancestral placental dentition lacks lower fourth and upper fourth and fifth incisors (characters 1327, 1388, and 1391), lacks canine dimorphism (characters 1404 and 1428), and has small styler shelves on the upper molars (characters 2330 and 2476) (Fig. 3B and appendix S1).

Biogeography and placental paleoenvironments. Our relatively younger age estimate for Placentalia means that there is no basis for linking placental interordinal diversification to the Mesozoic fragmentation of Gondwana (8). The most ancient members of Afrotheria included in our tree are extinct South American ungulates and the North American fossil *Leptictis dakotensis*, which suggests that Afrotheria did not originate in Africa. The oldest afrotherian is the North American leptictid *Prodiacodon crustulum*, whose antiquity constrains Afrotheria's minimum age and extends several afrotherian lineages into the early Paleocene (Fig. 1). Members of Afrotheria would have been present in two regions of

the New World by the early Paleocene. Given that afrotheres are not found in the Mesozoic and that South America was an island continent for most of the Late Cretaceous and Cenozoic, a vicariant explanation for this pattern is precluded. Afrotheres would have had to disperse either from North to South America, or the reverse, in the Paleocene, and then to Africa.

The early Paleocene diversification of placental occurred in a radically transformed terrestrial ecosystem lacking nonavian dinosaurs and other species terminated at the K-Pg event (10). Maximum K-Pg extinction estimates for plants are 57% of megaflores and 30% of pollen-producing plants from North American localities (36). In some areas, insects and plants were substantially affected by the K-Pg event (37), and such changes may have left available to the insectivorous placental ancestor a different diet than would have existed in the Mesozoic. This interval of dramatic environmental transformation would have bracketed several interordinal speciation events within Placentalia. The incompleteness of the fossil record will always constrain what we can infer about the past, but integration of phenomic and genomic data have here corroborated the hypothesis that ordinal and interordinal diversification of Placentalia most closely fits the explosive model (3) and that there was no Cretaceous Terrestrial Revolution (7) for Placentalia.

References and Notes

- K. F. Kuiper *et al.*, *Science* **320**, 500 (2008).
- W. A. Berggren, P. N. Pearson, *J. Foraminiferal Res.* **35**, 279 (2005).
- J. D. Archibald, D. H. Deutschman, *J. Mamm. Evol.* **8**, 107 (2001).
- R. M. Nowak, *Walker's Mammals of the World* (Johns Hopkins Univ. Press, Baltimore, MD, 1999).
- M. A. O'Leary, M. Allard, M. J. Novacek, J. Meng, J. Gatesy, in *Assembling the Tree of Life*, J. Cracraft, M. J. Donoghue, Eds. (Oxford Univ. Press, New York, 2004), pp. 490–516.
- K. de Queiroz, *Syst. Biol.* **56**, 956 (2007).
- R. W. Meredith *et al.*, *Science* **334**, 521 (2011).
- W. J. Murphy *et al.*, *Nature* **409**, 614 (2001).
- M. S. Springer, *J. Mamm. Evol.* **4**, 285 (1997).
- M. J. Novacek, *Ann. Mo. Bot. Gard.* **86**, 230 (1999).
- J. R. Wible, G. W. Rougier, M. J. Novacek, R. J. Asher, *Bull. Am. Mus. Nat. Hist.* **327**, 1 (2009).
- M. A. O'Leary, S. Kaufman, *Cladistics* **27**, 1 (2011).
- Materials and methods are available as supplementary materials on Science Online.
- M. A. Norell, in *Extinction and Phylogeny*, M. J. Novacek, Q. D. Wheeler, Eds. (Columbia Univ. Press, New York, 1992), pp. 89–118.
- O. R. P. Bininda-Emonds *et al.*, *Nature* **446**, 507 (2007).
- J. J. Eberle, *Rocky Mt. Geol.* **38**, 143 (2003).
- D. L. Lofgren, J. A. Lillegraven, W. A. Clemens, P. D. Gingerich, T. E. Williamson, in *Late Cretaceous and Cenozoic Mammals of North America*, M. O. Woodburne, Ed. (Columbia Univ. Press, New York, 2004), pp. 43–105.
- Q. Ji *et al.*, *Nature* **416**, 816 (2002).
- Z.-X. Luo, C.-X. Yuan, Q.-J. Meng, Q. Ji, *Nature* **476**, 442 (2011).
- A. B. Prasad, M. W. Allard, E. D. Green; NISC Comparative Sequencing Program, *Mol. Biol. Evol.* **25**, 1795 (2008).
- M. C. McKenna, in *Phylogeny of the Primates*, W. P. Luckett, F. S. Szalay, Eds. (Plenum, New York, 1975), pp. 21–46.
- J. E. Janecka *et al.*, *Science* **318**, 792 (2007).
- C. M. Miller-Butterworth *et al.*, *Mol. Biol. Evol.* **24**, 1553 (2007).
- E. C. Teeling *et al.*, *Science* **307**, 580 (2005).
- N. B. Simmons, K. L. Seymour, J. Habersetzer, G. F. Gunnell, *Nature* **451**, 818 (2008).
- R. J. Asher, M. J. Novacek, J. H. Geisler, *J. Mamm. Evol.* **10**, 131 (2003).
- F. Solé, E. Gheerbrant, M. Amaghazaz, B. Bouya, *Zool. J. Linn. Soc.* **156**, 827 (2009).
- F. L. Agnolín, N. R. Chimento, *Mamm. Biol.* **76**, 101 (2011).
- R. J. Asher *et al.*, *Science* **307**, 1091 (2005).
- T. J. Gaudin, R. J. Emry, J. R. Wible, *J. Mamm. Evol.* **16**, 235 (2009).
- D. E. Wildman *et al.*, *Proc. Natl. Acad. Sci. U.S.A.* **103**, 3203 (2006).
- H. N. Bryant, A. P. Russell, *Philos. Trans. R. Soc. London B Biol. Sci.* **337**, 405 (1992).
- M. J. Novacek, *Bull. Am. Mus. Nat. Hist.* **183**, 1 (1986).
- W. P. Luckett, in *Mammal Phylogeny: Mesozoic Differentiation, Multituberculates, Monotremes, Early Therians, and Marsupials*, F. S. Szalay, M. J. Novacek, M. C. McKenna, Eds. (Springer, New York, 1993), pp. 182–204.
- R. Owen, *The Anatomy of the Vertebrates*, vol. 3, *Mammals* (Longmans, Green and Co., London, 1868).
- P. Wilf, K. R. Johnson, *Paleobiology* **30**, 347 (2004).
- P. Wilf, C. C. Labandeira, K. R. Johnson, B. Ellis, *Science* **313**, 1112 (2006).
- T. Martin, A. Averianov, A. Lopatin, *J. Vert. Paleontol.* **31** (Suppl. 2), 153 (2011).
- M. J. Stanhope *et al.*, *Proc. Natl. Acad. Sci. U.S.A.* **95**, 9967 (1998).
- G. G. Simpson, *Bull. Am. Mus. Nat. Hist.* **85**, 1 (1945).
- M. S. Springer, W. W. de Jong, *Science* **291**, 1709 (2001).
- P. J. Waddell, N. Okada, M. Hasegawa, *Syst. Biol.* **48**, 1 (1999).
- K. D. Rose *et al.*, *Proc. Biol. Sci.* **275**, 1203 (2008).

Acknowledgments: We thank R. Asher, L. Jurgielewicz, M. Marotta, S. Parent, E. Seiffert, and E. Woodruff for data collection; K. Johnson for paleobotanical contributions; K. de Queiroz and A. Turner for discussion; and S. Kaufman, K. Alphonse, M. Passarotti, and D. Ferguson for software development. Artist C. Buell drew Fig. 2A and L. Betti-Nash all other figures. Research assistance came from P. Bowden, D. Malinzak, S. B. McLaren, N. Milbrodt, R. Morgan, and J. Morgan Scott. Data are archived in the supplementary materials and in Project 773 of the public repository MorphoBank.org. Supported by NSF grants 0743309 and 0827993, and by 0629959, 0629836, and 0629811 from the “Assembling the Tree of Life” program of the Divisions of Environmental Biology and Earth Sciences.

Supplementary Materials

www.sciencemag.org/cgi/content/full/339/6120/662/DC1
Materials and Methods
Supplementary Text
Figs. S1 to S15
Tables S1 to S8
References (44–323)
Appendices S1 to S4

23 August 2012; accepted 12 December 2012
10.1126/science.1229237

Gravity Field of the Moon from the Gravity Recovery and Interior Laboratory (GRAIL) Mission

Maria T. Zuber,^{1*} David E. Smith,¹ Michael M. Watkins,² Sami W. Asmar,² Alexander S. Konopliv,² Frank G. Lemoine,³ H. Jay Melosh,⁴ Gregory A. Neumann,³ Roger J. Phillips,⁵ Sean C. Solomon,^{6,7} Mark A. Wieczorek,⁸ James G. Williams,² Sander J. Goossens,⁹ Gerhard Kruizinga,² Erwan Mazarico,¹ Ryan S. Park,² Dah-Ning Yuan²

Spacecraft-to-spacecraft tracking observations from the Gravity Recovery and Interior Laboratory (GRAIL) have been used to construct a gravitational field of the Moon to spherical harmonic degree and order 420. The GRAIL field reveals features not previously resolved, including tectonic structures, volcanic landforms, basin rings, crater central peaks, and numerous simple craters. From degrees 80 through 300, over 98% of the gravitational signature is associated with topography, a result that reflects the preservation of crater relief in highly fractured crust. The remaining 2% represents fine details of subsurface structure not previously resolved. GRAIL elucidates the role of impact bombardment in homogenizing the distribution of shallow density anomalies on terrestrial planetary bodies.

The Moon is a key to deciphering the evolutionary history of the terrestrial planets because it is the most accessible planetary body that preserves a surface record spanning most of solar system history. Reconstructing the evolution of a planet requires an understanding of the structure of its interior, which contains information on bulk composition, differentiation, and the nature of heat generation and heat loss that has influenced the style, extent, and duration of volcanism and tectonics. The Gravity Recovery and Interior Laboratory (GRAIL) mission (1) was undertaken to map the lunar gravity field to address, in the context of other remote sensing and in situ observations, fundamental questions about lunar evolution.

Aside from the influence of the Moon's gravity throughout Earth history in producing oceanic tides, lunar gravity has been an observation of interest since the earliest satellites orbited the Moon and revealed the presence of mass concentrations or "mascons" associated with the large nearside impact basins (2). The Moon's synchronous rotation, which causes the same hemisphere

to always face Earth, poses a special challenge in measuring gravity. The most common method entails measuring the frequency shift of a spacecraft's radio signal directly from a tracking station on Earth, but such a measurement cannot be made on the Moon's farside. One approach to measuring farside gravity is through the use of a relay satellite, as was done by the recent Kaguya mission (3). Current spherical harmonic (4) lunar gravity models derived from tracking Lunar Prospector (LP) and earlier orbiters (5–7) and from the more recent Kaguya orbiter (3) range from degree and order 100 to 150, providing an effective block size resolution of 54 to 36 km, respectively.

GRAIL is a spacecraft-to-spacecraft tracking mission at the Moon, developed with heritage from the Gravity Recovery and Climate Experiment (GRACE) mission (8) that is currently mapping Earth's gravity field and its temporal variability. Each GRAIL spacecraft has a single science instrument, the Lunar Gravity Ranging System (LGRS), which measures the change in distance between the two co-orbiting spacecraft as they fly above the lunar surface. The spacecraft are perturbed by the gravitational attraction of topography and subsurface mass variations that can be isolated and subsequently analyzed. Doing so requires correcting for perturbations due to spacecraft maneuvers, nonconservative forces such as solar radiation pressure and spacecraft outgassing, and relativistic effects (4).

GRAIL was launched successfully from Cape Canaveral Air Force Station on 10 September 2011, aboard a Delta-II 7290H. The twin spacecraft embarked on separate low-energy trajectories to the Moon via the EL-1 Lagrange point (9) and inserted into lunar polar orbit on 31 December 2011 and 1 January 2012. After a total of 27 maneuvers (10) to lower and circularize the orbits

to ~55 km mean altitude (figs. S1 and S2) and to align the spacecraft to their ranging configuration, GRAIL executed its primary mapping mission (PM) from 1 March through 30 May 2012, transmitting to Earth 637 MB of science data corresponding to >99.99% of possible data that could be collected. During the PM, the inter-spacecraft distance varied between 82 and 218 km (fig. S3) to provide different sensitivities to the short- and longer-wavelength components of the gravity field. As exemplified in fig. S4, the root mean square (RMS) range-rate residuals from the LGRS Ka-band (32 GHz) ranging system during the PM were generally on the order of 0.02 to 0.05 $\mu\text{m s}^{-1}$, a factor of 2 to 5 better than the mission requirements.

These observations have been integrated into a spherical harmonic representation of the lunar gravitational field, which we denote model GL0420A. This model extends to degree and order 420, corresponding to a spatial block size of 13 km. Gravity field determination requires the application of numerous corrections (4), and emphasis in the production of this model has been on resolving short-wavelength structure.

The global free-air gravity field of the Moon is shown in Fig. 1A and the Bouguer gravity in Fig. 1B. The latter reveals the gravitational structure of the subsurface after subtraction of the expected contribution of surface topography from the free-air gravity. As with previous lunar gravity models, the GRAIL field shows the prominent mascons, the largest of which are associated with nearside basins, as well as the broad structure of the highlands. However, the much higher spatial resolution and greatly improved signal quality as compared with previous models combine to reveal distinctive gravitational signatures of many features not previously resolved, including impact basin rings, central peaks of complex craters, volcanic landforms, and smaller simple bowl-shaped craters.

Understanding the spectral content of the observations facilitates interpretation of the gravity maps (Fig. 2A). As with other planetary potential field representations, the RMS power of lunar gravity is greatest at low degrees (long wavelengths) and least at high degrees (short wavelengths). The empirical best-fit power law to the lunar gravity field is $2.5 \times 10^{-4} l^{-2}$, where l is the spherical harmonic degree. The degree at which the error spectrum intersects the power spectrum traditionally represents the spatial scale at which the gravitational coefficients (eqs. S1 and S2) are 100% in error. However, our best estimate of the error spectrum of model GL0420A does not intersect the model power through degree 420, which indicates that still higher-resolution fields may ultimately be derived from GRAIL's PM data set. It is notable that GL0420A fits late-stage PM data (19 to 29 May 2012) when the periapsis altitude was ~17 to 25 km, at 1 to 1.5 μm or 10 to 15 times the intrinsic quality of the Ka-band range-rate observations. The gravitational powers of the LP and Kaguya fields are comparable and

¹Department of Earth, Atmospheric and Planetary Sciences, Massachusetts Institute of Technology, Cambridge, MA 02139-4307, USA. ²Jet Propulsion Laboratory, Pasadena, CA 91109, USA. ³Solar System Exploration Division, NASA Goddard Space Flight Center, Greenbelt, MD 20771, USA. ⁴Department of Earth, Atmospheric and Planetary Sciences, Purdue University, West Lafayette, IN 47907, USA. ⁵Southwest Research Institute, Boulder, CO 80302, USA. ⁶Department of Terrestrial Magnetism, Carnegie Institution of Washington, Washington, DC 20015, USA. ⁷Lamont-Doherty Earth Observatory, Columbia University, Palisades, NY 10964, USA. ⁸Institut de Physique du Globe de Paris, Sorbonne Paris Cité, Université Paris Diderot, Case 7071, Lamarck A, 5, rue Thomas Mann, 75205 Paris Cedex 13, France. ⁹University of Maryland, Baltimore County, Baltimore, MD 21250, USA.

*To whom correspondence should be addressed. E-mail: zuber@mit.edu

approximately match that of GRAIL to about degree 100 (block size 54 km), but the GRAIL errors at spatial scales associated with large to intermediate impact basins [degrees ≤ 60 (90 km)] are three to five orders of magnitude smaller than those of the LP and Kaguya fields.

Owing to its direct sampling of farside gravity, the Kaguya field displays a higher coherence than that of LP (Fig. 2B); the Kaguya correlation peaks at approximately degree 60 and falls off rapidly with increasing degree because of an inability to sense the full gravitational power of

smaller-scale mass variations. The LP data exhibit overly low global coherence at all degrees despite the lower mapping altitude (40 to 100 km) than Kaguya (100 km), though a recent reanalysis of LP observations (11) that focused on improving resolution where direct tracking is available shows a

Fig. 1. (A) Free-air and **(B)** Bouguer gravity anomaly maps from GRAIL lunar gravity model GL0420A, to spherical harmonic degree and order 420. Maps are in Mollweide projection centered on 270°E longitude and show the nearside on the right and farside on the left. Gravity is plotted in units of milliGalileos, where 1000 mgal = 1 cm s⁻². A crustal density of 2560 kg m⁻³ was assumed in the Bouguer correction. For the Bouguer map, degrees <6 have been filtered out to highlight mid- to short-wavelength structure (4).

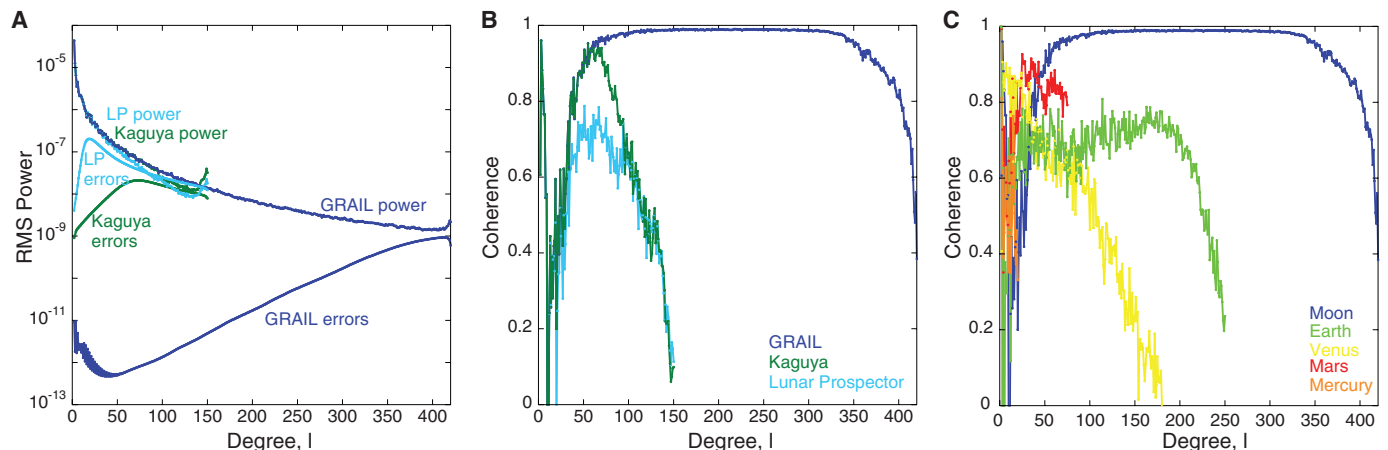
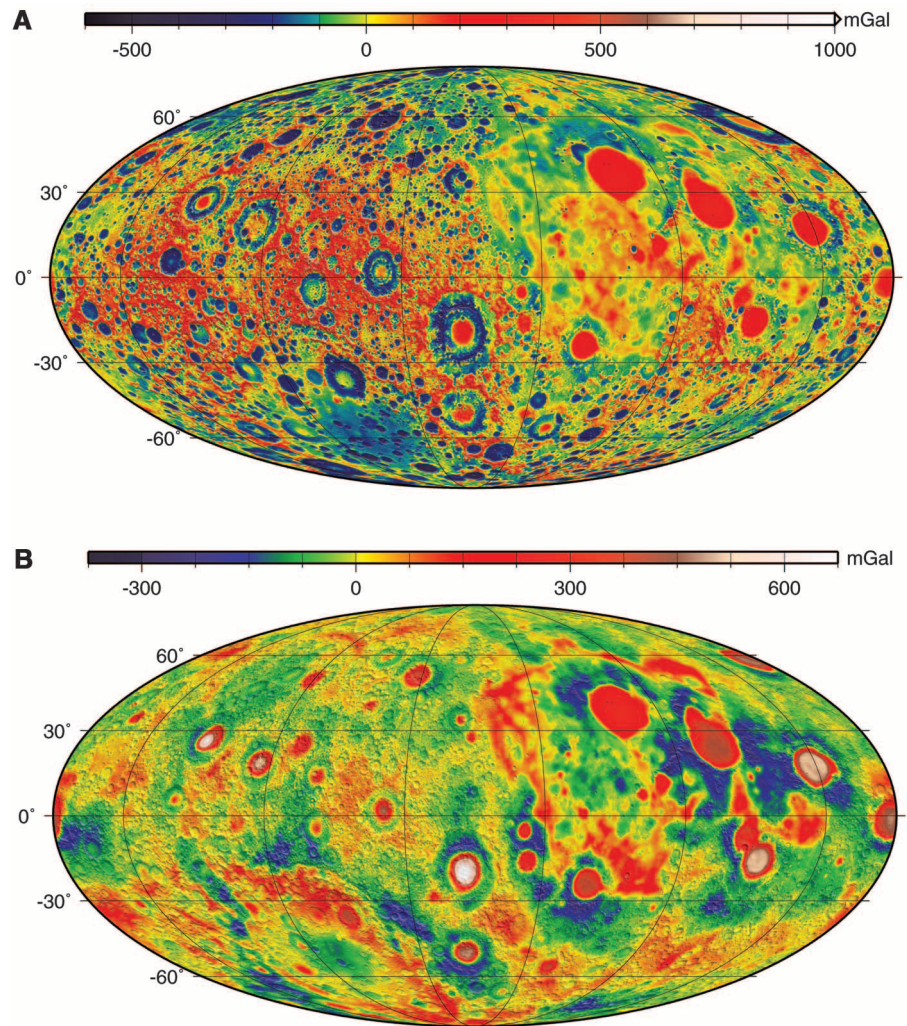


Fig. 2. (A) RMS power and **(B)** coherence versus harmonic degree for the gravity fields determined by GRAIL, Kaguya, and LP. **(C)** Comparison of coherence between gravity and topography versus degree for the Moon, with

coherence for other terrestrial planets. In **(B)**, all gravity models are compared with topography from the Lunar Orbiter Laser Altimeter (LOLA) (23). Data sets used in **(C)** are given in table S1.

higher nearside coherence. In contrast, GL0420A reveals a very high correlation with topography to high degrees. The departure of the coherence spectra of the LP and Kaguya fields from the GRAIL spectrum at degrees 30 and 60, respectively, indicates that despite approximately matching the power, these fields are significantly in error at higher degrees. Between degrees 80 (68 km) and 320 (17 km), 98.5% of the Moon's gravity signal is attributable to topography.

The magnitudes of short-wavelength Bouguer anomalies (Fig. 1B) are consistent with the high, but not perfect, coherence shown in Fig. 2B. Comparison of the maps shows that the range in Bouguer anomaly is typically up to ~10% that of the free-air gravity anomaly, which translates to a 1% ratio in terms of power. The lack of perfect correlation between gravity and topography is a result of lateral variations in subsurface density, such as those due to the presence of magmatic intrusions. Although this signal is small, the high-quality measurements ensure that it is easily resolvable (Fig. 2A) at a level that permits the investigation of processes associated with impact cratering, such as brecciation, ejecta deposition, impact melting, and magmatism.

In general, gravity and topography should become more highly correlated with increasing degree, because the strength of the lithosphere is increasingly able to support topographic loads at shorter wavelengths without compensating masses at depth, and because the signals associated with subsurface anomalies are increasingly attenuated at spacecraft altitude with increasing degree. The high coherence exhibited by the Moon (Fig. 2C) implies that the majority of the short-wavelength gravity signal is a result of surface topography, most of which is related to abundant impact craters. To retain a high coherence, the crust beneath those landforms must have been pervasively fractured and largely homogenized in density. Short-wavelength, lateral density variations due to magmatism, variable porosity, or regionally variable impact melting imparted during the early, post-accretional era of high impact flux are sparsely preserved at ~30- to 130-km scales. At harmonic degrees lower than about 60 (90 km), the coherence displays greater variability within the general pattern of a rapid decrease with decreasing degree. At these longer wavelengths, the lower coherence reflects the heterogeneity of lunar interior structure: thinning of the crust beneath impact basins, large-scale variations in crustal composition indicated by orbital remote sensing (12), and lateral variations in mantle composition and possibly temperature, such as the variations associated with the Procellarum KREEP Terrane (13, 14). At the highest degrees (>330), the coherence falls off because of longitudinal gaps in the spacecraft ground tracks. As shown in Fig. 2C, the gravity-topography coherence exhibited by the Moon is unlike that observed for any other terrestrial planet. From degrees 25 to 200, Earth's coherence is variable, with an average value of ~0.7. The coherence spectrum reflects a contribution from the continents, whose gravity-topography relation-

ships are dominated by crustal thickness variations and erosion, and include influences from compositional variability and tectonic and volcanic processes at shorter wavelengths. Earth's ocean basins also contribute to the correlation, and the interpretation of the combined contributions is complex. The coherence for Venus peaks at 0.9 at degree 3 and falls off rapidly at higher degrees. This falloff in coherence may reflect a combination of large-scale volcanic resurfacing (15) that smoothed the surface at short and intermediate length scales; the thick atmosphere, which screened small impacts; density anomalies related to mantle convection; and the orbital altitude of the Magellan spacecraft. The coherence for Mars is greatest at low degrees, at which it is governed by large-scale topography (16) such as the Tharsis province (17). Mercury's coherence does not exceed 0.6, but the spherical harmonic models of gravity

(18) and topography (19) inadequately sample the southern hemisphere of the planet because of the eccentric orbit of the MESSENGER (Mercury Surface, Space ENvironment, GEochemistry, and Ranging) spacecraft. Our expectations are that at high degrees, Mercury should display a coherence broadly similar to that of the Moon, because of its heavily cratered surface. The lithosphere of Mars is heavily cratered in the southern hemisphere, but in the northern hemisphere and on the Tharsis rise, volcanic resurfacing extended well past the period of high impact flux. The extent to which the observed coherence of Mars reflects crustal structure as opposed to the quality of the data is not clear.

The free-air and Bouguer gravity anomaly maps in Fig. 1 show the distinctive character of the lunar gravity field. The free-air map shows rich short-wavelength structure and resolves virtually all craters on the Moon greater than 30 km

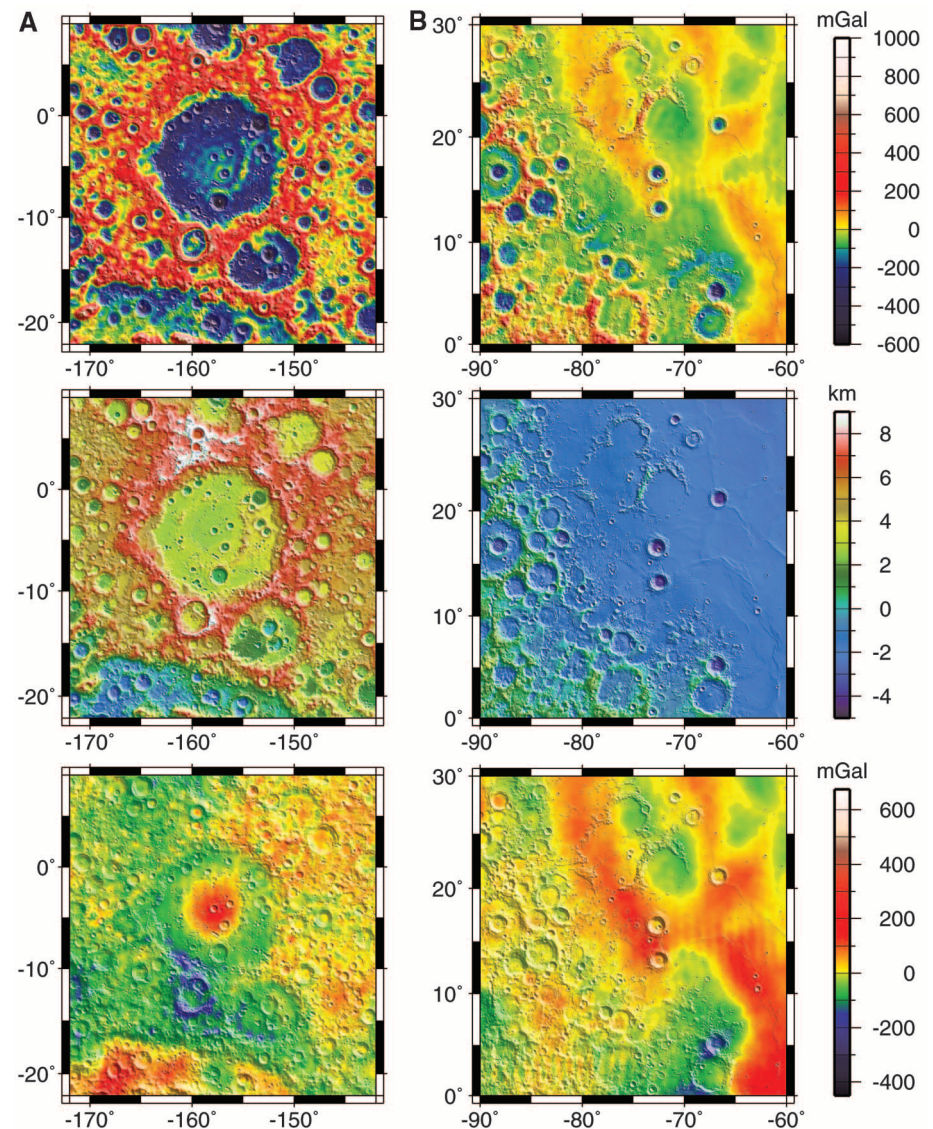


Fig. 3. (A and B) From top to bottom, Mercator projections of free-air gravity, topography, and Bouguer gravity. Frames in (A) highlight the area surrounding the Korolev impact basin, at center. Frames in (B) show the western limb of Oceanus Procellarum. Details of free-air and Bouguer gravity are the same as in Fig. 1. Topography is from a LOLA 1/64° grid.

in diameter and many less than 20 km in diameter. The highlands, because of the higher density of impact structures, show more gravitational detail at short wavelengths than the volcanic plains of the maria. In comparison with the free-air gravity, the Bouguer map is smooth at short wavelengths because the contributions to free-air gravity from impact craters derive mostly from their topography. This characteristic of lunar structure facilitates the isolation of density variations within the crust (20). As noted in previous studies (5, 21), large impact basins are accompanied by thinning of the crust beneath the basin cavity, due to excavation and rebound associated with the impact and basin formation process (22). In some cases, there is a second contribution from partial fill by mare volcanic deposits after basin formation.

Regional comparisons of the free-air gravity anomaly, topography (23), and Bouguer gravity anomaly reveal features that inform understanding of lunar structure and evolution. For instance, Fig. 3A shows an area of the farside highlands that includes the 417-km-diameter Korolev basin as well as many complex and simple craters. The maps also illustrate the ability of GRAIL to resolve Korolev's peak ring. In contrast to previous fields, GRAIL resolves Korolev's central Bouguer high to lie entirely within the central peak ring, and the annular low to reside on the crater floor and not beneath the walls. The observed gravitational structure implies that there is a density deficit under the floor due either to less dense, possibly brecciated, surface material filling the interior of Korolev but restricted to areas outside the peak ring, or to thickened crust produced by subsistostatic depression of the crust/mantle boundary.

Also evident in Fig. 3A is the spatial manifestation of the Moon's high coherence: The free-air map resembles the topography map at intermediate to short length scales. In contrast, the Bouguer map is generally smooth; removal of the gravitational attraction of topography reveals that there is much less short-wavelength structure attributable to subsurface density variations. Thinning of the crust beneath Korolev (24) represents the primary contribution to subsurface density variations in this area. The negative Bouguer signature of the rim of Doppler crater, just to the south of Korolev, may be indicative of brecciation and/or ejecta.

A region in the western part of Oceanus Procellarum (Fig. 3B) highlights the subsurface structure of maria and underlying crust in this region. Positive Bouguer gravity anomalies in the maria are part of a pattern in western and southern Oceanus Procellarum (Fig. 1B) that may indicate locally denser or thicker mare material. These Bouguer anomalies may help to define the boundary of either the Procellarum KREEP Terrane (25) or of the proposed Procellarum impact basin (26).

As exemplified by Fig. 3B, gravitational evidence for fully buried craters in the maria is not abundant. The gravitational signature of a buried crater should include two effects of opposite sign. A contribution from the subsurface, which for fresh craters tends to be fractured and brecciated

and therefore less dense than surrounding crust, should produce a negative anomaly. In contrast, because mare material is more dense than highland crust, a greater thickness over the floor of the buried crater should contribute a positive anomaly. Figure 3C shows that two partially buried craters between 20° to 30°N and -80° to -70°E display negative anomalies that suggest that for these structures, the contribution from subsurface structure dominates. Systematic study of other mare regions will provide insight into the thickness of infill and the underlying highland structure (27).

Results from GRAIL's PM provide a detailed view of the structure of the lunar crust and bring quantitative geophysical description of the internal structure of the Moon into a spatial realm commensurate with the scale of surface geological features. More broadly, the observed gravitational structure increases understanding of the role of impact bombardment on the crusts of terrestrial planetary bodies.

References and Notes

1. M. T. Zuber, D. E. Smith, D. H. Lehman, M. M. Watkins, *Int. Astronaut. Congress* **12**, B4 (2012).
2. P. M. Muller, W. L. Sjogren, *Science* **161**, 680 (1968).
3. N. Namiki *et al.*, *Science* **323**, 900 (2009).
4. Materials and methods are available as supplementary materials on Science Online.
5. A. S. Konopliv *et al.*, *Science* **281**, 1476 (1998).
6. A. S. Konopliv, S. W. Asmar, E. Carranza, W. L. Sjogren, D.-N. Yuan, *Icarus* **150**, 1 (2001).
7. E. Mazarico, F. G. Lemoine, S.-C. Han, D. E. Smith, *J. Geophys. Res.* **115**, E05001 (2010).
8. B. D. Tapley, S. Bettadpur, J. C. Ries, P. F. Thompson, M. M. Watkins, *Science* **305**, 503 (2004).
9. R. B. Roncoli, K. K. Fujii, "Mission design overview for the Gravity Recovery and Interior Laboratory (GRAIL) mission," paper presented at the AIAA Guidance, Navigation, and Control Conference, Toronto, Ontario, Canada, 2 to 5 August 2010, AIAA 2010-9393.
10. S. J. Hatch, R. B. Roncoli, T. H. Sweetser, "GRAIL trajectory design: Lunar orbit insertion through science," paper

presented at the AIAA Astrodynamics Conference, Toronto, Ontario, CA, 2 to 5 August 2010, AIAA 2010-8385.

11. S.-C. Han, E. Mazarico, D. D. Rowlands, F. G. Lemoine, S. Goossens, *Icarus* **215**, 455 (2011).
12. M. Ohtake *et al.*, *Nature* **461**, 236 (2009).
13. M. A. Wieczorek, R. J. Phillips, *J. Geophys. Res.* **105**, 20417 (2000).
14. C. K. Shearer *et al.*, *Rev. Mineral. Geochem.* **60**, 365 (2006).
15. R. J. Phillips *et al.*, *J. Geophys. Res.* **97**, 5923 (1992).
16. D. E. Smith *et al.*, *J. Geophys. Res.* **106**, 23689 (2001).
17. M. T. Zuber *et al.*, *Science* **287**, 1788 (2000).
18. D. E. Smith *et al.*, *Science* **335**, (2012).
19. M. T. Zuber *et al.*, *Science* **336**, 217 (2012).
20. J. C. Andrews-Hanna *et al.*, *Science* **339**, 675 (2013).
21. M. T. Zuber, D. E. Smith, F. G. Lemoine, G. A. Neumann, *Science* **266**, 1839 (1994).
22. H. J. Melosh, *Impact Cratering: A Geologic Process* (Oxford Univ. Press, New York, 1989).
23. D. E. Smith *et al.*, *Geophys. Res. Lett.* **37**, L18204 (2010).
24. M. A. Wieczorek *et al.*, *Science* **339**, 671 (2013).
25. B. L. Jolliffe, J. J. Gillis, L. Haskin, R. L. Korotev, M. A. Wieczorek, *J. Geophys. Res.* **105**, 4197 (2000).
26. P. H. Cadogan, *Nature* **250**, 315 (1974).
27. J. W. Head III, L. Wilson, *Geochim. Cosmochim. Acta* **56**, 2155 (1992).

Acknowledgments: The GRAIL mission is supported by NASA's Discovery Program and is performed under contract to the Massachusetts Institute of Technology and the Jet Propulsion Laboratory, California Institute of Technology. We are grateful to the GRAIL spacecraft, instrument, and operations teams for outstanding support. We thank J. Andrews-Hanna, J. Head, W. Kiefer, P. McGovern, F. Nimmo, J. Soderblom, and M. Sori for helpful comments on the manuscript. The data used in this study have been submitted to the Geosciences Node of the NASA Planetary Data System.

Supplementary Materials

www.sciencemag.org/cgi/content/full/science.1231507/DC1
Supplementary Text
Figs. S1 to S5
Table S1
References (28–43)

15 October 2012; accepted 27 November 2012
Published online 5 December 2012;
10.1126/science.1231507

The Crust of the Moon as Seen by GRAIL

Mark A. Wieczorek,^{1*} Gregory A. Neumann,² Francis Nimmo,³ Walter S. Kiefer,⁴ G. Jeffrey Taylor,⁵ H. Jay Melosh,⁶ Roger J. Phillips,⁷ Sean C. Solomon,^{8,9} Jeffrey C. Andrews-Hanna,¹⁰ Sami W. Asmar,¹¹ Alexander S. Konopliv,¹¹ Frank G. Lemoine,² David E. Smith,¹² Michael M. Watkins,¹¹ James G. Williams,¹¹ Maria T. Zuber¹²

High-resolution gravity data obtained from the dual Gravity Recovery and Interior Laboratory (GRAIL) spacecraft show that the bulk density of the Moon's highlands crust is 2550 kilograms per cubic meter, substantially lower than generally assumed. When combined with remote sensing and sample data, this density implies an average crustal porosity of 12% to depths of at least a few kilometers. Lateral variations in crustal porosity correlate with the largest impact basins, whereas lateral variations in crustal density correlate with crustal composition. The low-bulk crustal density allows construction of a global crustal thickness model that satisfies the Apollo seismic constraints, and with an average crustal thickness between 34 and 43 kilometers, the bulk refractory element composition of the Moon is not required to be enriched with respect to that of Earth.

The nature of the lunar crust provides crucial information on the Moon's origin and subsequent evolution. Because the crust is

composed largely of anorthositic materials (1), its average thickness is key to determining the bulk silicate composition of the Moon (2, 3)

and, consequently, whether the Moon was derived largely from Earth materials or from the giant impactor that is believed to have formed the Earth-Moon system (4, 5). After formation, the crust of the Moon suffered the consequences of 4.5 billion years of impact cratering. The Moon is the nearest and most accessible planetary body to study the largest of these catastrophic events, which were common during early solar system evolution (6, 7). In addition, it is an ideal laboratory for investigating the cumulative effects of the more frequent smaller impact events. Spatial variations in the Moon's gravity field are reflective of subsurface density variations, and the high-resolution measurements provided by NASA's Gravity Recovery and Interior Laboratory (GRAIL) mission (8) are particularly useful for investigating these issues.

Previous gravity investigations of the Moon have made use of data derived from radio tracking of orbiting spacecraft, but these studies were frustrated by the low and uneven spatial resolution of the available gravity models (9, 10). GRAIL consists of two co-orbiting spacecraft that are obtaining continuous high-resolution gravity measurements by intersatellite ranging over both the near- and farside hemispheres of Earth's natural satellite (8). Gravity models at the end of the primary mission resolve wavelengths as fine as 26 km, which is more than a factor of 4 times less than any previous global model. The mass anomalies associated with the Moon's surface topography are one of the most prominent signals seen by GRAIL (11), and because the measured gravity signal at short wavelengths is not affected by the compensating effects of lithospheric flexure, these data offer an opportunity to determine unambiguously the bulk density of the lunar crust. The density of the crust is a fundamental property required for geophysical studies of the Moon, and it also provides important information on crustal composition over depth scales that are

greater than those of most other remote sensing techniques.

The deflection of the crust-mantle interface in response to surface loads makes only a negligible contribution to the observed gravity field beyond spherical harmonic degree and order 150 (12). At these wavelengths, if the gravitational contribution of the surface relief were removed with the correct reduction density, the remaining signal (the Bouguer anomaly) would be zero if there were no other density anomalies present in the crust. An estimate of the crustal density can be obtained by minimizing the correlation between surface topography and Bouguer gravity. To exclude complicating flexural signals, and to interpret only that portion of the gravity field that is well resolved, we first filtered the gravity and topography to include spherical harmonic degrees between 150 and 310. Gravity and topography over the lunar maria, areas of generally low elevation resurfaced by high-density basaltic lava flows, were excluded from analysis, because their presence would bias the bulk density determination.

For our analyses, the correlation coefficient of the Bouguer gravity and surface topography was minimized using data within circles that span 12° of latitude. Analyses were excluded when more than 5% of the region was covered by mare basalt and when the minimum correlation coefficient fell outside the 95% confidence limits as estimated from Monte Carlo simulations that used the gravity coefficient

uncertainties. The average density of the highlands crust was found to be 2550 kg m^{-3} , and individual density uncertainties were on average 18 kg m^{-3} . As shown in Fig. 1, substantial lateral variations in crustal density exist with amplitudes of $\pm 250 \text{ kg m}^{-3}$. The largest positive excursions are associated with the 2000-km diameter South Pole-Aitken basin on the Moon's farside hemisphere, a region that has been shown by remote sensing data to be composed of rocks that are considerably more mafic, and thus denser, than the surrounding anorthositic highlands (13). Extensive regions with densities lower than average are found surrounding the impact basins Orientale and Moscoviense, which are the two largest young impact basins on the Moon's farside hemisphere. The bulk density determinations are robust to changes in size of the analysis region by a factor of two and are robust to changes in the spectral filter limits by more than ± 50 in harmonic degree. Nearly identical bulk densities are obtained with both a global and localized spectral admittance approach (figs. S6 and S7).

The bulk crustal densities obtained from GRAIL are considerably lower than the values of 2800 to 2900 kg m^{-3} that are typically adopted for geophysical models of anorthositic crustal materials (14). We attribute the low densities to impact-induced fractures and brecciation. From an empirical relation between the grain density of lunar rocks and their concentration of FeO and TiO_2 (15), along with surface elemental abundances derived from gamma-ray spectroscopy (16), grain densities of lunar surface materials

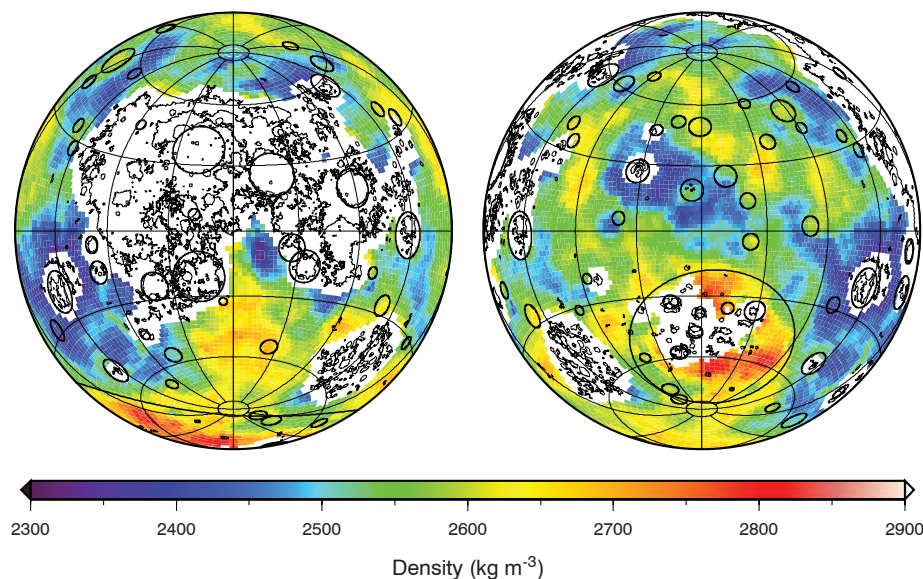


Fig. 1. Bulk density of the lunar crust from gravity and topography data. At each point on a grid of 60-km spacing, the bulk density was calculated within circles of 360-km diameter (spanning 12° of latitude). White denotes regions that were not analyzed, thin lines outline the maria, and solid circles correspond to prominent impact basins, whose diameters are taken as the region of crustal thinning in Fig. 3. The largest farside basin is the South Pole-Aitken basin. Data are presented in two Lambert azimuthal equal-area projections centered over the nearside (left) and farside (right) hemispheres, with each image covering 75% of the lunar surface, and with grid lines spaced every 30°. Prominent impact basins are annotated in Fig. 3.

¹Institut de Physique du Globe de Paris, Sorbonne Paris Cité, Université Paris Diderot, Case 7071, Lamarck A, 5, rue Thomas Mann, 75205 Paris Cedex 13, France. ²Solar System Exploration Division, NASA Goddard Space Flight Center, Greenbelt, MD 20771, USA. ³Department of Earth and Planetary Sciences, University of California, Santa Cruz, 1156 High Street, Santa Cruz, CA 95064, USA. ⁴Lunar and Planetary Institute, Houston, TX 77058, USA. ⁵Hawaii Institute of Geophysics and Planetary Science, University of Hawaii, Honolulu, HI 96822, USA. ⁶Department of Earth and Atmospheric Sciences, Purdue University, 550 Stadium Mall Drive, West Lafayette, IN 47907, USA. ⁷Planetary Science Directorate, Southwest Research Institute, Boulder, CO 80302, USA. ⁸Department of Terrestrial Magnetism, Carnegie Institution of Washington, Washington, DC 20015, USA. ⁹Lamont-Doherty Earth Observatory, Columbia University, Palisades, NY 10964, USA. ¹⁰Department of Geophysics, Colorado School of Mines, 1500 Illinois Street, Golden, CO 80401-1887, USA. ¹¹Jet Propulsion Laboratory, California Institute of Technology, Pasadena, CA 91109, USA. ¹²Department of Earth, Atmospheric, and Planetary Sciences, Massachusetts Institute of Technology, Cambridge, MA 02139-4307, USA.

*To whom correspondence should be addressed. E-mail: wieczor@ipgp.fr

may be estimated globally with a precision and spatial resolution that are comparable to those of the GRAIL bulk density measurements (fig. S3). If the surface composition of the Moon is representative of the underlying crust, the implied porosity is on average 12% and varies regionally from about 4 to 21% (Fig. 2). These values are consistent with, although somewhat larger than, estimates made from earlier longer-wavelength gravity field observations and a lithospheric flexure model (15). The crustal porosities in the interiors of many impact basins are lower than their surroundings, consistent with a reduction in pore space by high post-impact temperatures, which can exceed the solidus temperature. In contrast, the porosities immediately exterior to many basins are higher than their surroundings, a result consistent with the generation of increased porosity by the ballistic deposition of impact ejecta and the passage of impact-generated shock waves.

If the crustal density were constant at all depths greater than the lowest level of surface elevation, our bulk density estimates would represent an average over the depths sampled by the topographic relief, on average about 4 km. Because the deeper crust would not generate lateral gravity variations under such a scenario, this depth should be considered a minimum estimate for the depth scale of the GRAIL density determinations. If crustal porosity were solely a function of depth below the surface, the depth scale could be constrained using the relationship between gravity and topography in the spectral domain, because deep and short-wavelength mass anomalies are attenuated with altitude faster than shallower and longer-wavelength anomalies. We investigated two models: one in which the porosity decreases exponentially with depth below the surface, and another in which a po-

rous layer of constant thickness and constant porosity overlies a nonporous basement (12). The upper bound on both depth scales, at 1 standard deviation, is largely unconstrained, with values greater than 30 km able to fit the observations in most regions. Lower bounds at 1 standard deviation for the two depth scales were constrained to lie between about 0 and 31 km. These results imply that at least some regions of the highlands have substantial porosity extending to depths of tens of kilometers, and perhaps into the uppermost mantle.

Our density and porosity estimates are broadly consistent with laboratory measurements of lunar feldspathic meteorites and feldspathic rocks collected during the Apollo missions. The average bulk density of the most reliable of these measurements is $2580 \pm 170 \text{ kg m}^{-3}$ (12, 17), and the porosities of these samples vary from about 2 to 22% and have an average of $8.6 \pm 5.3\%$. Ordinary chondrite meteorites have a range of porosities similar to that of the lunar samples, a result of impact-induced microfractures (18). A 1.5-km drill core in the Chicxulub impact basin on Earth shows that impact deposits have porosities between 5 and 24%, whereas the basement rocks contain porosities up to 21% (19). Gravity data over the Ries, Tvären, and Granby terrestrial impact craters (with diameters of 23, 3, and 2 km, respectively) imply values of 10 to 15% excess porosity 1 km below the surface (20, 21), and for the Ries, about 7% porosity at 2 km depth. Whereas the impact-induced porosities associated with the terrestrial craters are a result of individual events, on the Moon, each region of the crust has been affected by numerous impacts.

Pore closure at depth within the Moon is likely to occur by viscous deformation at elevated temperatures; this decrease occurs over a narrow depth interval (<5 km) (fig. S12) because of the

strong temperature dependence of viscosity (22). From representative temperature gradients over 4 billion years, and taking into account the reduced thermal conductivity of porous rock, this transition depth is predicted to lie between 40 and 85 km below the surface, depending on the rheology and heat fluxes assumed. Where the crust is thinner than these values, porosity could exist in the underlying mantle. S-wave velocity profiles derived from the Apollo seismic data (23) suggest that porosity extends to depths up to 15 km below the crust-mantle interface, consistent with this interpretation.

With our constraints on crustal density and porosity, we constructed a global crustal thickness model from GRAIL gravity and Lunar Reconnaissance Orbiter (LRO) topography (24) data. Our model accounts for the gravitational signatures of the surface relief, relief along the crust-mantle interface, and the signal that arises from lateral variations in crustal grain density as predicted by remote sensing data (12). Crustal densities beneath the mare basalts were extrapolated from the surrounding highland values, and because we neglect the comparatively thin surficial layer of dense basalt (14), the total crustal thicknesses will be biased locally, but by no more than a few kilometers. As constraints to our model, we used seismically determined thicknesses of either 30 (23) or 38 (25) km near the Apollo 12 and 14 landing sites, and we assumed a minimum crustal thickness of less than 1 km because at least one of the giant impact basins should have excavated through the entire crust (14, 26). Given a porosity model of the crust, we obtained a single model that fits the observations by varying the average crustal thickness and mantle density. Because some of the short-wavelength gravity signal is the result of unmodeled crustal signals, our inversions make use of a spectral low-pass filter (27) near degree 80, yielding a spatial resolution that is 60% better than previous models (28). Remote sensing data of the central peaks of impact craters imply some subsurface compositional variability but do not require broad compositional layering (29), at least consistent with our use of a model that is uniform in composition with depth.

For a first set of models, we assumed that porosity was a function of depth below the surface. With a mantle grain density of 3360 kg m^{-3} (30), it is not possible to fit simultaneously the seismic and minimum thickness constraints as a result of the relatively small density contrast at the crust-mantle interface (12). For a second set of models, we assumed that the porosity of the entire crust was constant with depth. With 12% porosity and a 30-km crustal thickness near the Apollo 12 and 14 landing sites, a solution is found with an average crustal thickness of 34 km and a mantle density of 3220 kg m^{-3} (Fig. 3). For a 38-km crustal thickness constraint, values of 43 km and 3150 kg m^{-3} are found, respectively. By reducing the porosity to 7%, the mantle

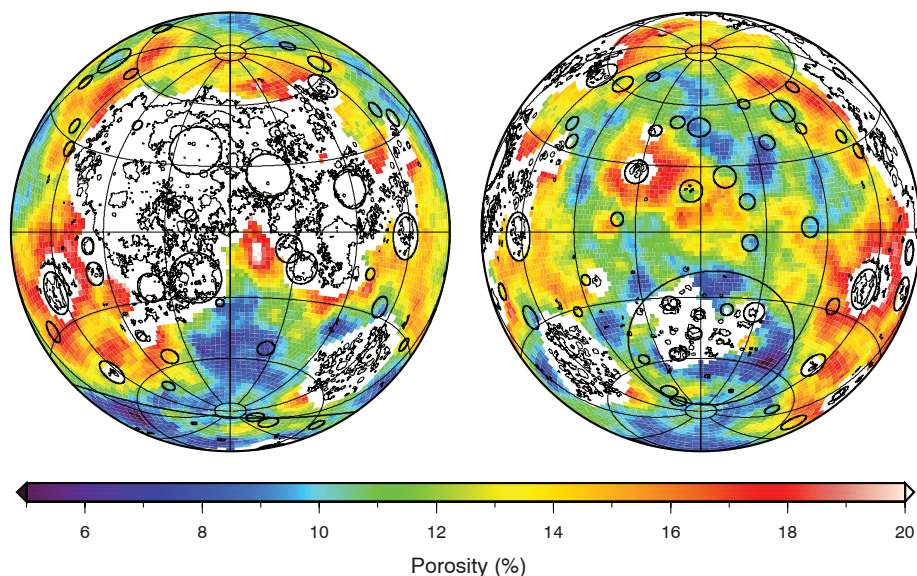


Fig. 2. Porosity of the lunar crust, using bulk density from GRAIL and grain density from sample and remote sensing analyses. Image format is the same as in Fig. 1.

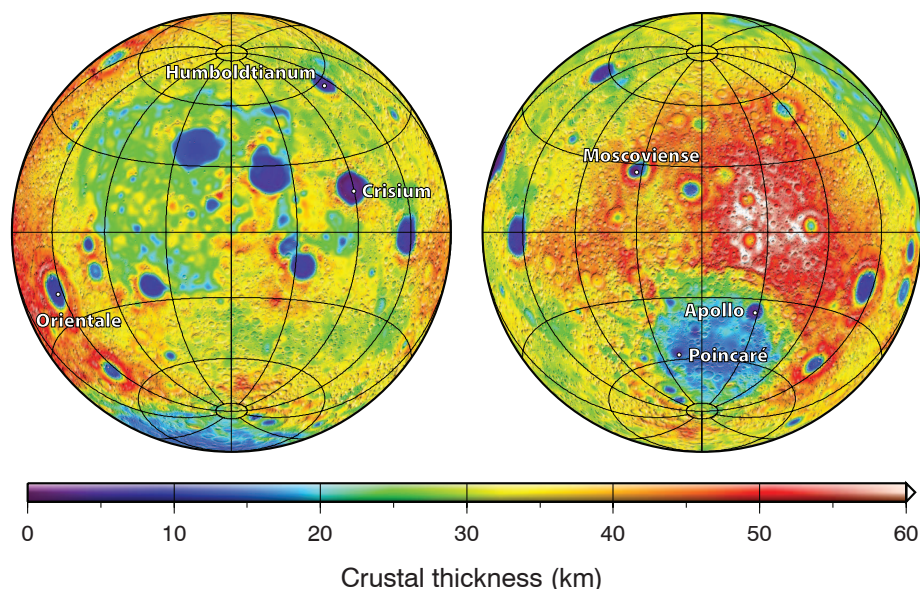


Fig. 3. Crustal thickness of the Moon from GRAIL gravity and LRO topography. With a crustal porosity of 12% and a mantle density of 3220 kg m^{-3} , the minimum crustal thickness is less than 1 km in the interior of the farside basin Moscoviense, and the thickness at the Apollo 12 and 14 landing sites is 30 km. Image format is the same as in Fig. 1, and each image is overlain by a shaded relief map derived from surface topography.

density increases by about 150 kg m^{-3} , but the average crustal thickness remains unchanged. Identical average crustal thicknesses are obtained for a crustal density map extrapolated from Fig. 1. The mantle densities should be considered representative to the greatest depths of the base of the crust ($\sim 80 \text{ km}$ below the surface), and if the grain density of mantle materials is 3360 kg m^{-3} , the uppermost mantle could have a porosity between 0 and 6%, consistent with our porosity evolution model (12).

Before GRAIL, the average thickness of the Moon's crust was thought to be close to 50 km (12, 14, 28). Published estimates for the bulk silicate abundance of the refractory element aluminum, as summarized in table 1 of Taylor *et al.* (3), fall into two categories: One group indicates that the Moon contains the same abundance as Earth, whereas the other suggests at least a 50% enrichment. We used our average crustal thickness with assumptions on crustal composition that maximize the total Al_2O_3 in the crust to test the limits of the refractory enrichment hypothesis. If the lunar crust consists of an upper megaregolith layer 5 km thick containing 28 weight percent (wt %) Al_2O_3 (3), a value based largely on lunar highland meteorite compositions, with the remainder being nearly pure anorthosite, 34 wt % Al_2O_3 (1), we calculate that a 34-km-thick crust contributes 1.7 wt % to the total bulk silicate abundance of Al_2O_3 for a crustal porosity of 7%. A 43-km-thick crust contributes 2.1 wt %. The inclusion of more mafic materials in the lower crust would act to reduce the total abundance of aluminum in the crust. For bulk lunar silicate aluminum abundances to match those for Earth (4 wt % Al_2O_3), the lunar mantle would need to

contain 1.9 to 2.4 wt % Al_2O_3 , whereas a 50% enrichment in refractory elements would require 4.1 to 4.5 wt % Al_2O_3 . Petrologic assessments indicate mantle Al_2O_3 abundances close to 1 to 2 wt % (31), supporting a lunar refractory element composition similar to that of Earth. Estimates of Al_2O_3 derived from modeling the Apollo seismic data have a broad range, from 2.3 to 3.1 wt % for the entire mantle (32), to 2.0 to 6.7 wt % for the upper and lower mantle (33), respectively. Although further constraints on the composition of the deep lunar mantle are needed, the modest contribution to the bulk lunar Al_2O_3 from the crust does not require the Moon to be enriched in refractory elements.

Crustal thickness variations on the Moon are dominated by impact basins with diameters from 200 to 2000 km. With a thinner crust, it becomes increasingly probable that several of the largest impact events excavated through the entire crustal column and into the mantle (14). Two impact basins have interior thicknesses near zero (Moscoviense and Crisium), and three others have thicknesses that are less than 5 km (Humboldtianum, Apollo, and Poincaré). Remote sensing data show atypical exposures of olivine-rich materials surrounding some lunar impact basins that could represent an admixture of crustal materials with excavated mantle materials (26), and the most prominent of these are associated with the Crisium, Moscoviense, and Humboldtianum basins. Our crustal thickness model strengthens the hypothesis that these impact events excavated into the mantle.

Because the crust of the Moon has experienced only limited volcanic modification, and in addition has not experienced aqueous or aeolian

erosion, the Moon is an ideal recorder of processes that must have affected the crusts of all terrestrial planets early in their evolution. Large impact events were common in the first billion years of solar system history, and the crusts of the terrestrial planets would have been fractured to great depths, as was the Moon. For Earth and Mars, this porosity could have hosted substantial quantities of groundwater over geologic time (34). For planets generally lacking groundwater, such as Mercury, crustal porosity may have sharply reduced the effective thermal conductivity, hindering the escape of heat to the surface and affecting the planet's thermal and magmatic evolution (35).

References and Notes

1. S. Yamamoto *et al.*, *Geophys. Res. Lett.* **39**, L13201 (2012).
2. P. H. Warren, *Meteorit. Planet. Sci.* **40**, 477 (2005).
3. S. R. Taylor, G. J. Taylor, L. A. Taylor, *Geochim. Cosmochim. Acta* **70**, 5904 (2006).
4. R. M. Canup, *Science* **338**, 1052 (2012).
5. M. Cuk, S. T. Stewart, *Science* **338**, 1047 (2012).
6. W. F. Bottke *et al.*, *Nature* **485**, 78 (2012).
7. C. I. Fassett *et al.*, *J. Geophys. Res.* **117**, E00H06 (2012).
8. M. T. Zuber *et al.*, *Space Sci. Rev.* (2013); 10.1007/s11214-012-9952-7.
9. A. S. Konopliv, S. W. Asmar, D. N. Yuan, *Icarus* **150**, 1 (2001).
10. K. Matsumoto *et al.*, *J. Geophys. Res.* **115** (E6), E06007 (2010).
11. M. T. Zuber *et al.*, *Science* **339**, 668 (2013).
12. Methods and additional materials are available as supplementary materials on Science Online.
13. P. Lucey *et al.*, *New Views of the Moon*, B. J. Jolliff, M. A. Wieczorek, C. K. Shearer, C. R. Neal, Eds., *Rev. Mineral. Geochem.* (Mineral. Soc. Am., 2006), vol. 60, pp. 83–219.
14. M. A. Wieczorek *et al.*, in *New Views of the Moon*, B. J. Jolliff, M. A. Wieczorek, C. K. Shearer, C. R. Neal, Eds., *Rev. Mineral. Geochem.* (Mineral. Soc. Am., 2006), vol. 60, pp. 221–364.
15. Q. Huang, M. A. Wieczorek, *J. Geophys. Res.* **117** (E5), E05003 (2012).
16. T. H. Prettyman *et al.*, *J. Geophys. Res.* **111** (E12), E12007 (2006).
17. W. Kiefer, R. J. Macke, D. T. Britt, A. J. Irving, G. J. Consolmagno, *Geophys. Res. Lett.* **39**, L07201 (2012).
18. G. Consolmagno, D. Britt, R. Macke, *Chemie der Erde-Geochemistry* **68**, 1 (2008).
19. T. Elbra, L. J. Pesonen, *Meteorit. Planet. Sci.* **46**, 1640 (2011).
20. J. Pohl, D. Stoeffler, H. Gall, K. Ernstson, in *Impact and Explosion Cratering: Planetary and Terrestrial Implications*, D. J. Roddy, R. O. Pepin, R. B. Merrill, Eds. (Pergamon Press, New York, 1977), pp. 343–404.
21. H. Henkel, T. C. Ekenligoda, S. Aaro, *Tectonophysics* **485**, 290 (2010).
22. F. Nimmo, R. T. Pappalardo, B. Giese, *Icarus* **166**, 21 (2003).
23. P. Lognonné, J. Gagnepain-Beyneix, H. Chenet, *Earth Planet. Sci. Lett.* **211**, 27 (2003).
24. D. E. Smith *et al.*, *Geophys. Res. Lett.* **37**, L18204 (2010).
25. A. Khan, K. Mosegaard, *J. Geophys. Res.* **107** (E6), 5036 (2002).
26. S. Yamamoto *et al.*, *Nat. Geosci.* **3**, 533 (2010).
27. M. A. Wieczorek, R. J. Phillips, *J. Geophys. Res.* **103** (E1), 1715 (1998).
28. Y. Ishihara *et al.*, *Geophys. Res. Lett.* **36**, L19202 (2009).
29. J. T. S. Cahill, P. G. Lucey, M. A. Wieczorek, *J. Geophys. Res.* **114** (E9), E09001 (2009).
30. R. Garcia, J. Gagnepain-Beyneix, S. Chevrot, P. Lognonné, *Phys. Earth Planet. Inter.* **188**, 96 (2011).

31. S. Mueller, G. J. Taylor, R. J. Phillips, *J. Geophys. Res.* **93** (B6), 6338 (1988).
32. A. Khan, J. A. D. Connolly, J. MacLennan, K. Mosegaard, *Geophys. J. Int.* **168**, 243 (2007).
33. O. L. Kuskov, V. A. Kronrod, *Phys. Earth Planet. Inter.* **107**, 285 (1998).
34. S. M. Clifford, *J. Geophys. Res.* **98** (E6), 10973 (1993).
35. S. Schumacher, D. Breuer, *J. Geophys. Res.* **111** (E2), E02006 (2006).

Acknowledgments: The GRAIL mission is supported by the Discovery Program of NASA and is performed under contract to the Massachusetts Institute of Technology and the Jet Propulsion Laboratory, California Institute of Technology. Additional support for this work was provided by the French Space Agency (CNES), the Centre National de la Recherche Scientifique, and the UnivEarthS LabEx project of Sorbonne Paris Cité. Data products will be made available from the authors upon request.

Supplementary Materials

www.sciencemag.org/cgi/content/full/science.1231530/DC1
Supplementary Text
Figs. S1 to S13
Table S1
References (36–73)

15 October 2012; accepted 27 November 2012
Published online 5 December 2012;
10.1126/science.1231530

Ancient Igneous Intrusions and Early Expansion of the Moon Revealed by GRAIL Gravity Gradiometry

Jeffrey C. Andrews-Hanna,^{1*} Sami W. Asmar,² James W. Head III,³ Walter S. Kiefer,⁴ Alexander S. Konopliv,² Frank G. Lemoine,⁵ Isamu Matsuyama,⁶ Erwan Mazarico,^{5,7} Patrick J. McGovern,⁴ H. Jay Melosh,⁸ Gregory A. Neumann,⁵ Francis Nimmo,⁹ Roger J. Phillips,¹⁰ David E. Smith,⁷ Sean C. Solomon,^{11,12} G. Jeffrey Taylor,¹³ Mark A. Wieczorek,¹⁴ James G. Williams,² Maria T. Zuber⁷

The earliest history of the Moon is poorly preserved in the surface geologic record due to the high flux of impactors, but aspects of that history may be preserved in subsurface structures. Application of gravity gradiometry to observations by the Gravity Recovery and Interior Laboratory (GRAIL) mission results in the identification of a population of linear gravity anomalies with lengths of hundreds of kilometers. Inversion of the gravity anomalies indicates elongated positive-density anomalies that are interpreted to be ancient vertical tabular intrusions or dikes formed by magmatism in combination with extension of the lithosphere. Crosscutting relationships support a pre-Nectarian to Nectarian age, preceding the end of the heavy bombardment of the Moon. The distribution, orientation, and dimensions of the intrusions indicate a globally isotropic extensional stress state arising from an increase in the Moon's radius by 0.6 to 4.9 kilometers early in lunar history, consistent with predictions of thermal models.

Planetary gravity analyses have been limited historically to large-scale features associated with high contrasts in density, due to the low resolution and low signal-to-noise ratio of the data. As a result, small-scale subsurface structures such as faults and dikes that have been inferred from their surface expressions have not been resolved in the gravity field, and structures

lacking a direct surface manifestation have been largely undocumented. This situation has posed a challenge for studies of the early evolution of the Moon, because the near saturation of the surface by impact craters has erased much of the geological record from the first ~700 million years (My) of lunar history (1), spanning the critical period of time between the solidification of the lunar magma ocean and the end of major impact basin formation ~3.8 billion years ago (Ga) (2). Data from the Gravity Recovery and Interior Laboratory (GRAIL) mission (3) now permit the expansion of the gravity field to spherical harmonic degree and order 420 (model GL0420A), corresponding to a half-wavelength resolution of ~13 km at the lunar surface (4). This resolution is sufficient to resolve short-wavelength density anomalies, such as intrusions that have a higher density than the surrounding rocks and faults that offset layers of differing density.

Here, we apply the technique of gravity gradiometry to the GRAIL gravity field, using the second spatial derivatives of the gravitational potential to highlight short-wavelength features associated with discrete structures (5). In terrestrial applications, gradients are typically measured directly by a three-axis gradiometer on an aerial or satellite-borne platform (5, 6), but in our work, we calculated the gradients from the potential

field. To emphasize subsurface structures, we used gradients of the Bouguer potential (calculated as the difference between the measured gravitational potential and the potential arising from the effects of topography) (4). We then calculated the maximum amplitude of the second horizontal derivative of the Bouguer potential at each point on the surface [Γ_{hh} , measured in Eötvös units (E), where $1E = 10^{-9} \text{ s}^{-2}$] (7). The resulting horizontal Bouguer gradient map (Fig. 1) displays a rich array of short-wavelength structures in the lunar crust.

The dominant features in the gradient map are the ring structures surrounding the large impact basins. These rings are also observed in the Bouguer gravity (Fig. 1A) (4), but they are resolved in the gradient map as discrete structures. Outside of the basins, a large number of irregular small-scale anomalies are observed with typical values of $\pm 10E$, probably arising from small-scale density anomalies in the upper crust associated with variations in composition or porosity. In addition, a number of elongated linear gravity anomalies (LGAs) characterized by negative gradients stand out clearly above the background variability. Four of the LGAs have lengths exceeding 500 km (Fig. 2). These anomalies closely follow linear paths (great circles) across the surface to within root mean square deviations of 1 to 3% of their lengths. Inspection of the most distinct LGAs yields 22 probable anomalies with a combined length of 5300 km and an additional 44 possible anomalies with a combined length of 8160 km for a total length of 13,460 km (Fig. 1C). An independent automated algorithm identified 46 anomalies with a combined length of 10,600 km (7). Such markedly linear structures in natural geologic systems are typically associated with faults or dikes. Averaged profiles of the Bouguer gravity anomaly perpendicular to the lineations show these structures to be associated with narrow positive-gravity anomalies (Fig. 3), indicating subsurface structures of increased density consistent with the interpretation that the features are mafic igneous intrusions.

We used a Monte Carlo approach to invert the average Bouguer gravity profiles across the LGAs for the physical properties of the subsurface density anomalies, treating them as tabular bodies of unknown top depth, bottom depth, width, and density contrast (7). A continuous set of solutions exists with comparable misfits to the data, as a result of the fundamental non-uniqueness of potential field data with respect

¹Department of Geophysics and Center for Space Resources, Colorado School of Mines, Golden, CO 80401, USA. ²Jet Propulsion Laboratory, Pasadena, CA 91109, USA. ³Department of Geological Sciences, Brown University, Providence, RI 02912, USA. ⁴Lunar and Planetary Institute, Houston, TX 77058, USA. ⁵Solar System Exploration Division, NASA Goddard Space Flight Center, Greenbelt, MD 20771, USA. ⁶Lunar and Planetary Laboratory, University of Arizona, Tucson, AZ 85721, USA. ⁷Department of Earth, Atmospheric and Planetary Sciences, Massachusetts Institute of Technology, Cambridge, MA 02139–4307, USA. ⁸Department of Earth and Atmospheric Sciences, Purdue University, West Lafayette, IN 47907, USA. ⁹Department of Earth and Planetary Sciences, University of California, Santa Cruz, Santa Cruz, CA 95064, USA. ¹⁰Planetary Science Directorate, Southwest Research Institute, Boulder, CO 80302, USA. ¹¹Department of Terrestrial Magnetism, Carnegie Institution of Washington, Washington, DC 20015, USA. ¹²Lamont-Doherty Earth Observatory, Columbia University, Palisades, NY 10964, USA. ¹³Hawaii Institute of Geophysics and Planetology, University of Hawaii, Honolulu, HI 96822, USA. ¹⁴Institut de Physique du Globe de Paris, Sorbonne Paris Cité, Université Paris Diderot, Case 7071, Lamarck A, 5, rue Thomas Mann, 75205 Paris Cedex 13, France.

*To whom correspondence should be addressed. E-mail: jcahanna@mines.edu

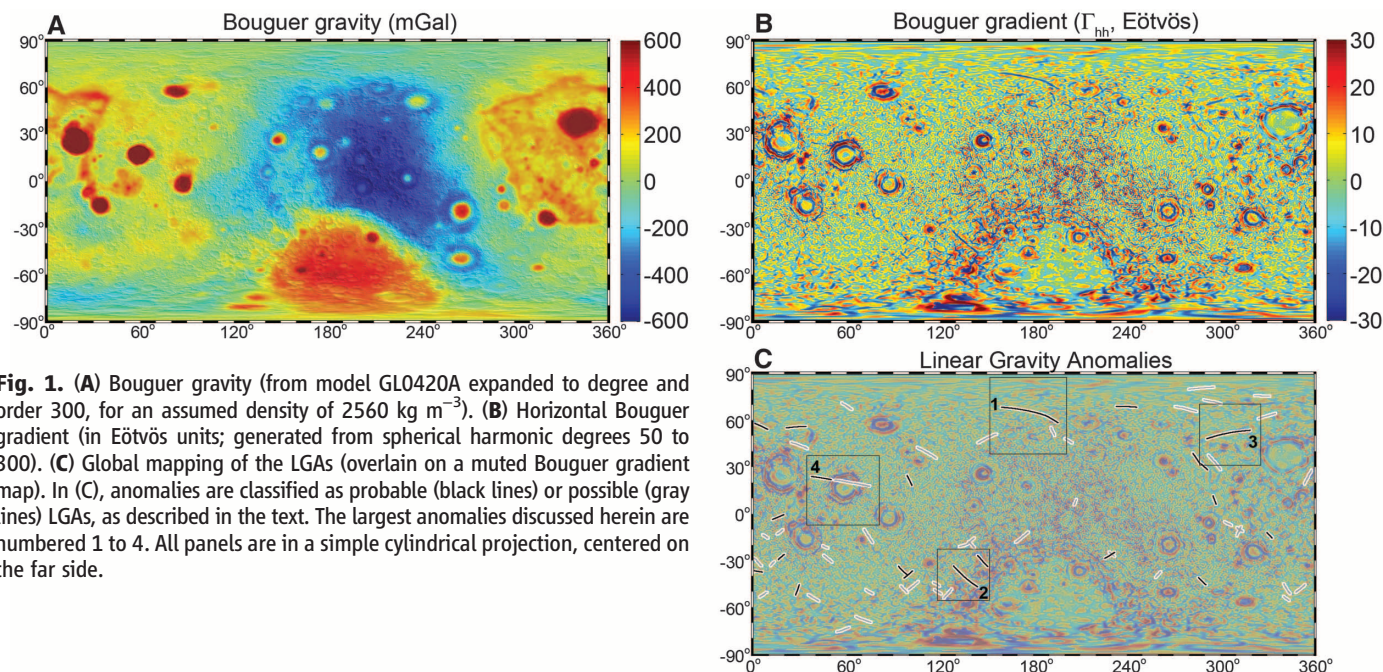


Fig. 1. (A) Bouguer gravity (from model GL0420A expanded to degree and order 300, for an assumed density of 2560 kg m^{-3}). (B) Horizontal Bouguer gradient (in Eötvös units; generated from spherical harmonic degrees 50 to 300). (C) Global mapping of the LGAs (overlain on a muted Bouguer gradient map). In (C), anomalies are classified as probable (black lines) or possible (gray lines) LGAs, as described in the text. The largest anomalies discussed herein are numbered 1 to 4. All panels are in a simple cylindrical projection, centered on the far side.

to subsurface structures. From the variability in the gravity profiles, we also determined the 95% confidence intervals of the model parameters. For one of the best-defined anomalies (LGA-1) (Fig. 2A), the best-fit solutions have density contrasts of 160 to 960 kg m^{-3} in bodies with widths of 5 to 25 km extending between a top depth of 10 to 15 km and a bottom depth of 76 to 91 km (Fig. 3 and Table 1). The top depth may correspond to either the top of the intrusion or the maximum depth of impact brecciation and gardening, above which the density contrast would become less distinct. Similarly, the bottom depth may correspond to either the base of the intrusion or the depth of the crust-mantle interface, below which the density contrast between the intrusion and the host rocks would decrease markedly. For LGA-2, a shallow top depth is suggested by the observation that the 116-km -diameter impact crater Roche, excavating the crust to a depth of $\sim 7 \text{ km}$ and brecciating it to greater depths, results in a modest reduction in the magnitude of the anomaly, whereas smaller craters have no effect (Fig. 2).

The dimensions of the anomaly sources can be further constrained with the use of independent constraints on the density contrast. The mean density of the upper crust derived from GRAIL is $2550 \pm 250 \text{ kg m}^{-3}$ (8). Although the composition of the intrusions is unknown, representative values can be taken from the measured densities of lunar igneous rocks of 3100 to 3350 kg m^{-3} (9), yielding density contrasts of 550 to 860 kg m^{-3} . For density contrasts of 550 and 800 kg m^{-3} , the best-fit solutions for LGA-1 collapse to a point in parameter space, with widths of 7.6 and 5.3 km , respectively (Table 1). However, the bottom depth (85 to 86 km) for these solutions is probably deeper than the base of the crust, below which the

reduced density contrast would contribute little to the observed gravity. If the base of the density anomaly is constrained to be 40 km , comparable to the mean crustal thickness (8), the best-fit widths for density contrasts of 550 and 800 kg m^{-3} increase to 29.1 and 23.5 km , with top depths of 24.9 and 26.9 km . A bottom depth of 60 km results in widths of 11.9 and 8.3 km and top depths of 19.0 and 19.4 km . Similar results are found from the inversions of LGAs 2 and 4, with a total range of best-fit widths of 5 to 12 km for density contrasts of 550 and 800 kg m^{-3} with the bottom depth unconstrained or 7 to 41 km for bottom depths of 40 to 60 km (7). LGA-3 requires a greater width of 13 to 18 km or 49 to 82 km with the bottom depth constrained to 40 to 60 km , in keeping with the greater width of the gravity anomaly.

Although the lengths and linearity of the density anomalies are similar to those of giant dike swarms on Earth, Mars, and Venus, their widths greatly exceed typical dike widths of tens of meters (10, 11). Vertical tabular intrusions with aspect ratios similar to those proposed here can form by diapirism when the viscosity contrast between the magma and host rock is in the range of 10^6 to 10^8 (12). For mafic intrusions, this low viscosity contrast would require either a partially crystalline intrusion or a highly ductile or partially molten host rock. The source of the gravity anomalies may be analogous to the Great Dyke of Zimbabwe, which probably formed as a result of shallow intrusive activity during ancient rifting (13). This elongated layered ultramafic intrusion measures 550 km in length, 3 to 11 km in width, and up to 12 km in vertical extent (13, 14). Intrusive bodies of similar scale have been inferred to exist beneath the Valles Marineris region of Mars on the basis of collapse features (15), formed

in response to lithospheric extension and intrusion (16). Alternatively, narrow swarms of closely spaced dikes (17) can match the gravity anomalies but would require tens to hundreds of dikes confined within zones less than $\sim 40 \text{ km}$ wide that extend over distances of hundreds of kilometers. Similar narrow dike swarms with lengths up to 100 km form above elongated axial magma chambers in rifts on Earth (18). A combination of the above processes may be responsible for the anomalies, with a single vertical tabular intrusion forming in a partially molten lower crust, sourcing a swarm of closely spaced dikes in the more brittle upper crust. The large bottom depths from the inversions permit the intrusions to extend into the mantle, as would be required if the rise of magma were governed by neutral buoyancy (19). Although the specific nature and formation mechanism of the intrusions remains uncertain, some form of intrusive activity in a horizontally extensional stress regime is indicated by all of the analogous structures.

Lunar dikes previously inferred from geological analyses (20) are not detected in the gravity data. This result is not surprising, because isolated dikes with widths of up to tens of meters would have gravity anomalies two orders of magnitude smaller than these LGAs. A linear magnetic anomaly interpreted as a dense swarm of dikes on the floor of the South Pole–Aitken basin (17) is not evident in the gravity gradients but is associated with a broad positive Bouguer gravity anomaly where it extends outside of the basin (7). This anomaly may be consistent with a dense dike swarm, with the lower-density contrast relative to the mafic crust in the floor of the basin possibly accounting for the nondetection there. Alternatively, the poor expression of the magnetic anomalies in the gravity data may

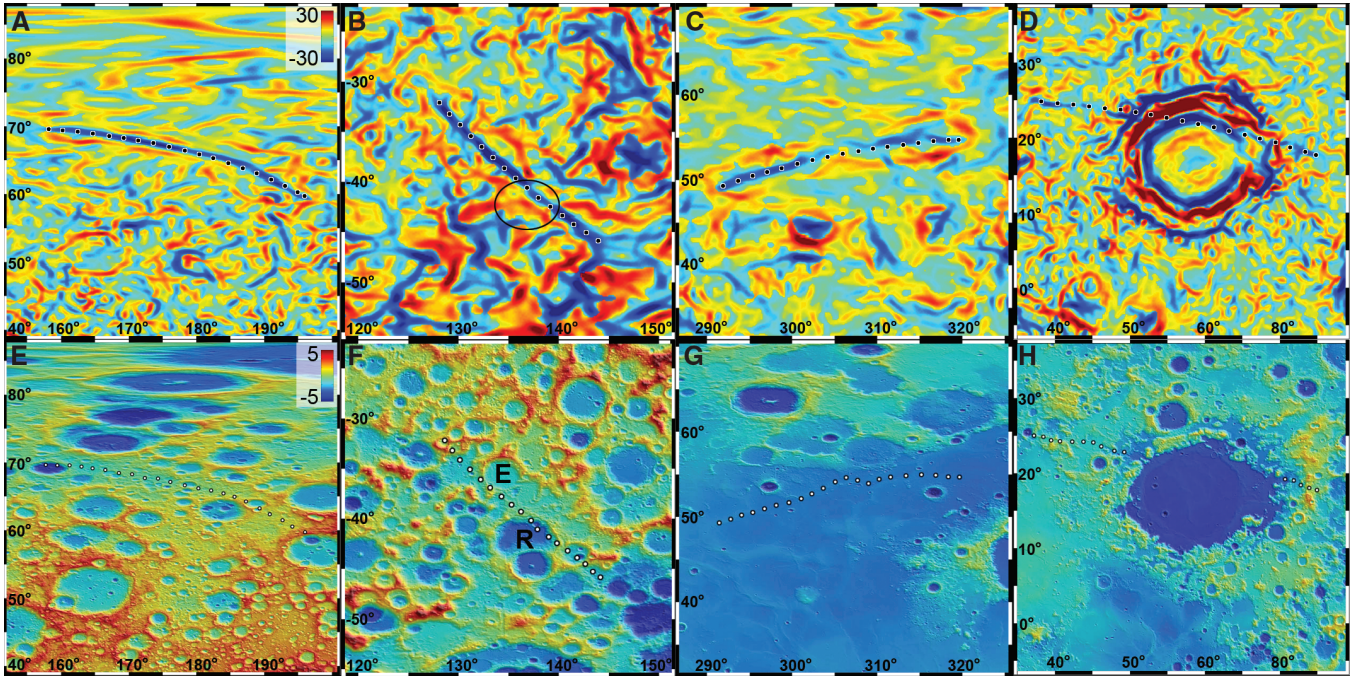


Fig. 2. (A to D) Horizontal Bouguer gradient (in Eötvös units) and (E to H) topography (in kilometers) in the vicinity of four prominent LGAs (LGAs 1 to 4 are shown in order from left to right; see Fig. 1 for context). The dots in the upper panels follow great-circle fits to the anomalies, whereas

the dots in the lower panels follow the paths of the anomalies themselves. The craters Eötvös (E) and Roche (R) are labeled in (F), and Roche is outlined in (B); the gravity gradient shows reduced amplitude within the latter crater.

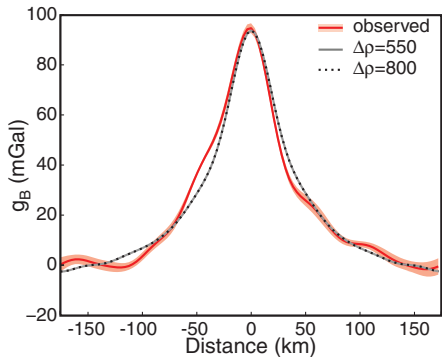


Fig. 3. Mean profile and ± 1 standard error range (in red and pink, respectively) of the Bouguer gravity anomaly (g_B) over LGA-1. The predicted gravity anomalies from the best-fit vertical tabular intrusions for density contrasts ($\Delta\rho$) of 550 and 800 kg m^{-3} are shown for comparison (overlapping gray and dashed black lines, respectively).

support Fe-rich material derived from the basin-forming projectile as the source of the magnetic anomalies (21).

Averaged magnetic (22) and topographic (23) profiles across the LGAs generally reveal no correlation of either data set with the gravity anomalies (7). Forward models of the expected magnetic anomalies require that any magnetization be substantially less than 0.1 A/m for most of the lineations, indicating that the intrusions either have very low magnetic susceptibility or cooled in the absence of an external field. A topographic signature associated with the intrusions might be

Table 1. Density contrast ($\Delta\rho$), width (w), top depth (z_{top}), and bottom depth (z_{bot}) from the inversion of LGA-1, including the best-fit range in parameters and the 95% confidence intervals (C.I.) for the full inversion (7) and the best-fit ($\pm 95\%$ C.I. range) solutions for assumed density contrasts of 550 and 800 kg m^{-3} .

	Best fit	95% C.I.	$\Delta\rho = 550$	$\Delta\rho = 800$
$\Delta\rho$ (kg m^{-3})	160–960	90–940	550	800
w (km)	4.5–24.9	5.7–46.7	$7.6^{+35.2}_{-1.4}$	$5.3^{+34.2}_{-0.9}$
z_{top} (km)	10.3–14.8	6.0–38.8	$13.0^{+28.2}_{-5.2}$	$13.3^{+30.0}_{-4.3}$
z_{bot} (km)	75.6–90.6	30–96	86^{+10}_{-55}	85^{+9}_{-56}

expected as a result of tectonic uplift, flexural subsidence, graben formation (15), yet none is observed. A number of LGAs are located in crater-saturated areas (Fig. 2) and lack any obvious surface expression in topography, image, or other remote sensing data sets. The absence of a surface expression is consistent with an age for the structures that predates the superimposed crater population and the surface geologic record.

The age of the structures can be further constrained by crosscutting relationships. Several linear anomalies are observed radial to the South Pole–Aitken impact basin, which is the oldest basin on the Moon. This radial orientation indicates that the formation of these structures was influenced by the preexisting basin. The lack of a surface signature rules out an origin as rays of dense impact ejecta (7). A 1000-km-long anomaly (LGA-4) crosses the Crisium basin at an oblique angle (Fig. 2), but no trace of the anomaly is found within the basin itself. This geometry sug-

gests that this anomaly predated Crisium and that the underlying structure was destroyed within the basin cavity by the impact. This timing is supported by the fact that the intrusion was not deflected by the strong flexural stresses associated with the pre-mare mascon (25) and later mare load within the basin. By these arguments, the South Pole–Aitken and Crisium basins place the formation of the largest intrusions within the pre-Nectarian to early Nectarian time frame, before the end of the basin-forming epoch at ~ 3.8 Ga. This age is consistent with the lunar intrusive activity between 4.2 and 4.5 Ga that was responsible for the formation of the plutonic Mg-suite rocks (26), though it is not possible to directly link these intrusions to any particular rock type with the use of gravity data alone.

Tabular igneous intrusions form perpendicular to the most extensional principal stress direction (27), leading to the formation of vertical dikes in a horizontally extensional stress field and sills in a horizontally compressional stress field.

Although local flexural stresses or structural control can alter the orientations of intrusions (7), the LGAs are distributed uniformly across the Moon and show no clear preferred orientations or association with known flexurally supported loads. This pattern indicates largely isotropic horizontal extension, as would be expected to arise from global expansion. However, the lunar lithosphere is thought to have been in a state of compression throughout most of its history as a result of interior cooling and global contraction (28). Superimposed stresses associated with the outward migration of the Moon, with or without contemporaneous true polar wander, are similarly inconsistent with the locations and orientations of the LGAs (7, 29). At the time of the intrusive activity inferred here, the lithosphere must have been in a horizontally extensional stress state to accommodate the inflation of the vertical tabular intrusions. Taking the total length of the probable intrusion population of 5300 km and the typical best-fit widths of 5 to 40 km, the resulting horizontal extensional strain of 0.035 to 0.27% equates to an increase in the lunar radius by 0.6 to 4.8 km. However, this estimate is complicated by the possibility of viscous accommodation of some of the growth of the intrusions or lithospheric extension not accompanied by intrusive activity that would go undetected by GRAIL.

Such a period of early extension was predicted by some thermal history models (28), developed to account for the absence of a global population of large thrust faults on the Moon similar to those found on Mercury. The thermal models best matched that constraint with an initial condition that included a 200- to 300-km-deep magma ocean and a cooler deep interior, leading to coupled warming of the interior and cooling of the outer shell, with net expansion in the first billion years followed by modest global contraction. Cooling and contraction of the lunar lithosphere could also have contributed to extensional strain at the depths of these intrusions within the first few tens of millions of years after lunar crustal formation. This thermal inversion may be a natural outcome of the post-accretional temperature profile of the Moon (30). Thermal history models that satisfy the constraint of <1 km decrease in radius over the past 3.8 billion years (Gy) also predict 2.7 to 3.7 km of global expansion during the first ~1 Gy, with the highest rates occurring during the first 0.5 Gy (28), consistent with our proposed period of expansion. The amount of predicted expansion is sensitive to the depth of the magma ocean and the initial temperature of the deep interior. However, no direct geological evidence for this early expansion has previously been found, as a consequence of the intense cratering of the surface at that time. This earliest epoch of lunar expansion is now revealed by GRAIL gravity data, which allows us to see through the surface geology to the hidden structures beneath. This result places a constraint on lunar evolution and raises important questions regarding the early evolution of other terrestrial

planets, because the first ~700 My of planetary evolution is poorly preserved in the geological records of all planets.

References and Notes

- W. K. Hartmann, R. W. Gaskell, *Meteoritics* **32**, 109 (1997).
- D. Stöffler, G. Ryder, *Space Sci. Rev.* **96**, 9 (2001).
- M. T. Zuber *et al.*, *Space Sci. Rev.* **10**, 1007/11214-012-9952-7 (2013).
- M. T. Zuber *et al.*, *Science* **339**, 668 (2013).
- C. Jekeli, *Surv. Geophys.* **27**, 257 (2006).
- R. Rummel, W. Yi, C. Stummer, *J. Geod.* **85**, 777 (2011).
- Materials and methods are available as supplementary materials on Science Online.
- M. A. Wieczorek *et al.*, *Science* **339**, 671 (2013).
- W. S. Kiefer, R. J. Macke, D. T. Britt, A. J. Irving, G. J. Consolmagno, *Geophys. Res. Lett.* **39**, L07201 (2012).
- R. E. Ernst, E. B. Grosfils, D. Mège, *Annu. Rev. Earth Planet. Sci.* **29**, 489 (2001).
- L. Wilson, J. W. Head III, *Lunar Planet. Sci.* **40**, abstract 1160 (2009).
- A. M. Rubin, *Earth Planet. Sci. Lett.* **119**, 641 (1993).
- A. H. Wilson, *J. Petrol.* **23**, 240 (1982).
- F. Podmore, A. H. Wilson, "A reappraisal of the structure and emplacement of the Great Dyke, Zimbabwe," *Geol. Assoc. Canada Special Paper* **33** (1985), pp. 317–330.
- D. Mège, A. C. Cook, E. Garel, Y. Lagabriele, M. Cormier, *J. Geophys. Res.* **108**, 5044 (2003).
- J. C. Andrews-Hanna, *J. Geophys. Res.* **117**, E04009 (2012).
- M. E. Purucker, J. W. Head III, L. Wilson, *J. Geophys. Res.* **117**, E05001 (2012).
- A. Gudmundsson, *J. Volcanol. Geotherm. Res.* **64**, 1 (1995).
- J. W. Head III, L. Wilson, *Geophys. Res. Lett.* **18**, 2121 (1991).
- J. W. Head III, L. Wilson, *Planet. Space Sci.* **41**, 719 (1993).
- M. A. Wieczorek, B. P. Weiss, S. T. Stewart, *Science* **335**, 1212 (2012).
- M. E. Purucker, J. B. Nicholas, *J. Geophys. Res.* **115**, E12007 (2010).
- D. E. Smith *et al.*, *Geophys. Res. Lett.* **37**, L18204 (2010).
- A. M. Rubin, *J. Geophys. Res.* **97**, 1839 (1992).
- J. C. Andrews-Hanna, *Icarus* **222**, 159 (2013).
- G. A. Snyder, C. R. Neal, L. A. Taylor, A. N. Halliday, *J. Geophys. Res.* **100**, 9365 (1995).
- E. M. Anderson, *The Dynamics of Faulting and Dyke Formation with Application to Britain* (Oliver and Boyd, London, ed. 2, 1951).
- S. C. Solomon, *Phys. Earth Planet. Inter.* **15**, 135 (1977).
- H. J. Melosh, *Icarus* **43**, 334 (1980).
- W. M. Kaula, *J. Geophys. Res.* **84**, 999 (1979).

Acknowledgments: The GRAIL mission is a component of the NASA Discovery Program and is performed under contract to the Massachusetts Institute of Technology and the Jet Propulsion Laboratory. J.C.A.-H., J.W.H., W.S.K., I.M., P.J.M., F.N., and G.J.T. were supported by grants from the NASA GRAIL Guest Scientist Program. The data used in this study will have been archived in the Geosciences Node of the NASA Planetary Data System by the time of publication.

Supplementary Materials

www.sciencemag.org/cgi/content/full/science.1231753/DC1
Materials and Methods
Supplementary Text
Figs. S1 to S13
Tables S1 to S6
References (31–47)

19 October 2012; accepted 27 November 2012
Published online 5 December 2012;
10.1126/science.1231753

Proton Donor Acidity Controls Selectivity in Nonaromatic Nitrogen Heterocycle Synthesis

Simon Duttwyler,¹ Shuming Chen,¹ Michael K. Takase,¹ Kenneth B. Wiberg,¹ Robert G. Bergman,² Jonathan A. Ellman^{1*}

Piperidines are prevalent in natural products and pharmaceutical agents and are important synthetic targets for drug discovery and development. We report on a methodology that provides highly substituted piperidine derivatives with regiochemistry selectively tunable by varying the strength of acid used in the reaction. Readily available starting materials are first converted to dihydropyridines via a cascade reaction initiated by rhodium-catalyzed carbon-hydrogen bond activation. Subsequent divergent regio- and diastereoselective protonation of the dihydropyridines under either kinetic or thermodynamic control provides two distinct iminium ion intermediates that then undergo highly diastereoselective nucleophilic additions. X-ray structural characterization of both the kinetically and thermodynamically favored iminium ions along with density functional theory calculations provide a theoretical underpinning for the high selectivities achieved for the reaction sequences.

Piperidines are saturated, nonplanar nitrogen heterocycles upon which the display of functionality has provided some of the most well-known pharmaceuticals, as exemplified by traditional drugs such as quinine, morphine (and its many synthetic analogs such as oxycodone), as well as a number of more recent blockbusters, including plavix for the treat-

ment of stroke, cialis for erectile dysfunction, and aricept for Alzheimer's treatment (Fig. 1A) (1). The physical properties and therapeutic importance of the piperidine scaffold are consistent with recent retrospective analyses of drug-discovery research suggesting that renewed emphasis should be placed on the preparation, evaluation, and development of compounds with

increased saturation and nonplanar display of functionality (2–4).

C–H bond functionalization has emerged as a powerful approach for the synthesis and modification of planar, aromatic *N*-heterocycles from cheap and readily available precursors (5–11). Recently, we reported on a cascade reaction comprising rhodium-catalyzed C–H activation of imines **1** with coupling to alkynes **2** to give azatrienes **3** followed by electrocyclization to provide densely substituted 1,2-dihydropyridines **4** (Fig. 1B) (12–15). These relatively unstable nonaromatic *N*-heterocycles can readily be aromatized to stable pyridines. Dihydropyridines **4** can also be converted to more highly saturated heterocycles (16); however, densely substituted derivatives have previously been difficult to access and pose a particular challenge in terms of regio- and stereochemical transformation. Recently, we demonstrated an in situ protonation/reduction sequence that provides tetrahydropyridines **7** with very high regio- and diastereoselectivity (17). Here, we demonstrate that tetrahydropyridines **8** with an alternative substitution pattern and stereochemical display can be accessed by tuning the strength of the acid used. In addition to

hydride, a range of carbon nucleophiles have also been added to both iminium intermediates **5** and **6** to provide even more densely substituted derivatives of **7** and **8**.

Consider the addition of a proton, the simplest of all electrophiles, to highly substituted 1,2-dihydropyridine **4a** (Fig. 2). The four most likely products are *cis* and *trans* stereoisomers of reactive iminium ions **5a** and **6a**, obtained by protonation at the α and γ positions, respectively. Each of these reactive intermediates might also be expected to undergo additional transformations to give undesired by-products such as enamine tautomers or dimers and higher-order oligomers.

Despite the large potential number of products, we directed our efforts at the selective formation of single iminium isomers (18, 19). When a strong acid with a pK_a (where K_a is the acid dissociation constant) several units below that of **4a** is used, α protonation occurs under kinetic control to give **5a** as the major product (Fig. 2). Preferred kinetic protonation at the α position is consistent with electrophilic attack reported for conjugated dienolates (20). A screening of acids and solvents showed that arylsulfonic acids in dichloromethane afford α -protonated *cis*-**5a** as a single diastereomer with >95% selectivity. Thus, treatment of **4a** with 1.1 equivalents of PhSO_3H in dichloromethane at room temperature resulted in complete protonation within 15 min as evidenced by ^1H nuclear magnetic resonance (NMR) spectroscopy. Isomerization to other species, eventually *trans*-**6a**, took place with a half life of 38 hours.

Protonation of **4a** under thermodynamic control was achieved using two equivalents of a weaker acid and equilibration over 12 to 16 hours at room temperature. Treatment with $(\text{PhO})_2\text{PO}_2\text{H}$ in tetrahydrofuran (THF) at room temperature gave γ -protonated *trans*-**6a** with >95% regio- and diastereoselectivity. Solutions of *trans*-**6a** remained unchanged at room temperature over weeks and upon heating to 80°C for 1 day, indicating that the thermodynamically most stable ion had formed. From a practical point of view, benzenesulfonic acid and diphenyl phosphoric acid not only permit the directed formation of **5a** and **6a** but also have the advantage of being easily weighable solids that provide iminium salts that are soluble in organic solvents.

To rigorously define the relative stereochemistry and obtain a better understanding of the conformations of the products of protonation, x-ray structures were obtained for kinetically favored iminium ion *cis*-**5a** and thermodynamically favored iminium ion *trans*-**6a**. Moreover, for kinetic iminium ion *cis*-**5a**, a fast crystallization process (2 hours), rather than the typically preferred slow crystal formation, was necessary to prevent iminium equilibration. The ring in kinetic ion *cis*-**5a** adopts a boatlike conformation with the C3-Me and C6-Et substituents in pseudoaxial positions (Fig. 3A1). The piperidine ring in the thermodynamic ion *trans*-**6a** exhibits a more planar geometry of the N–C1–C2–C3 moiety with the C5-Et and C6-Et substituents now disposed in pseudoaxial positions (Fig. 3A2). Presumably, the pseudoaxial

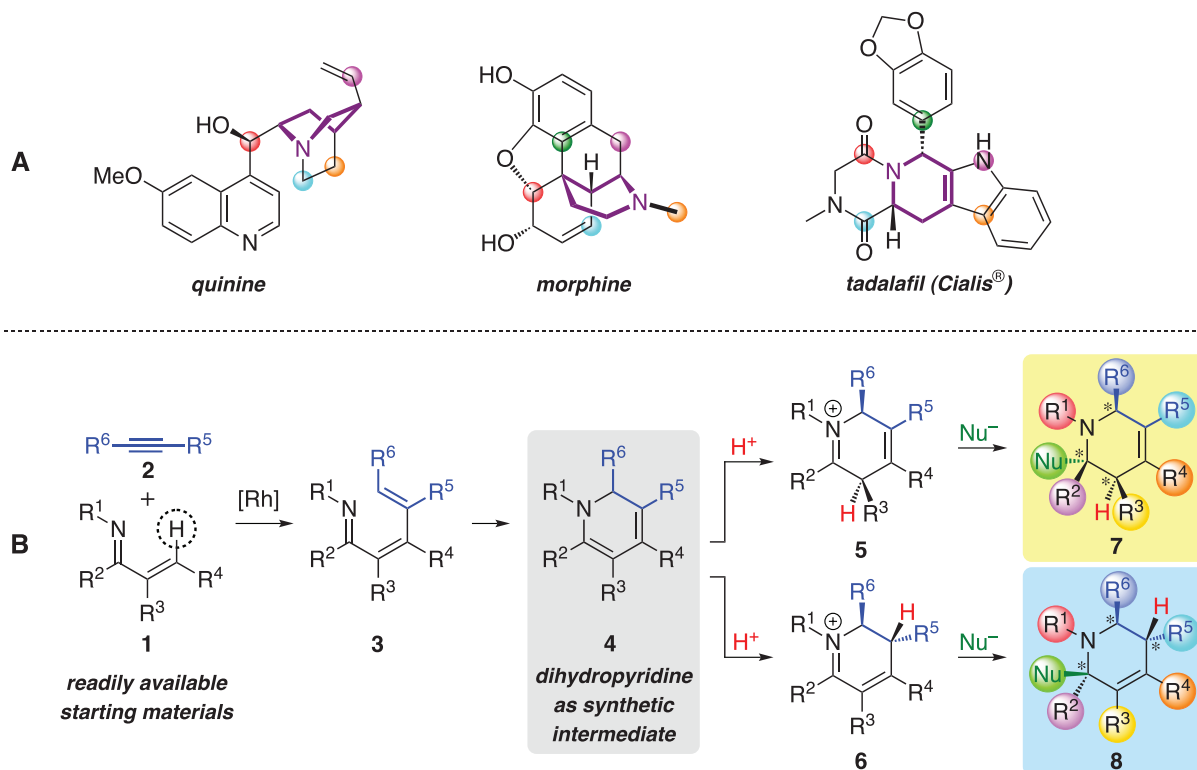


Fig. 1. (A) Drugs containing a multiply substituted piperidine core. **(B)** Rhodium-catalyzed synthesis of dihydropyridine intermediates leading to piperidine derivatives.

orientation of the substituents on the saturated carbons for both the kinetic and thermodynamic iminium ions avoids unfavorable A-1,2-interactions.

Density functional theory (DFT) calculations were carried out at the B3LYP/6-311G+(d,p) level of theory to further characterize the energies and conformations for the four possible protonation products (21). The kinetic iminium ion *cis*-**5a** was calculated to adopt a boatlike conformation with the C3-Me and C6-Et groups in pseudoaxial positions, consistent with the x-ray structure (Fig. 3B1). The alternative boatlike conformation with the C3-Me and C6-Et groups in pseudoequatorial positions was calculated to be higher in energy by 8.3 kcal/mol, consistent with the unfavorable A-1,2-interactions imparted by adjacent alkenyl methyl groups (22). The thermodynamic protonation product *trans*-**6a** was calculated to be the most stable of the four possible iminium ions by >3 kcal/mol, consistent with its being the only observable isomer under thermodynamic control (Fig. 3B2). The overall geometry, bond distances, and angles obtained with the DFT calculations are in very good agreement with the structures obtained for both *cis*-**5a** and *trans*-**6a**.

The conditions developed for kinetic and thermodynamic protonation to provide single diastereomers of reactive iminium ions set the stage for an extremely efficient protocol to prepare distinct regio- and diastereomeric tetrahydropyridines **7** and **8** with multiple stereogenic centers. Dihydropyridines **4** are first prepared by the aforementioned Rh-catalyzed cascade process from commercially available alkynes **2** and imines **1**, which are in turn readily prepared from common enones and primary amines. Kinetic protonation of **4** at the α position provides iminium ions **5**, which upon nucleophilic addition should provide tetrahydropyridines **7**. Alternatively, thermodynamic protonation at the γ position provides ions **6**, to which nucleophilic addition should provide tetrahydropyridines **8**, respectively. Variation of the substitution pattern in each starting component should result in a vast number of potential permutations for the differential display of functionality in the stable piperidine derivatives **7** and **8**.

We first sought to explore reductions to provide hydride addition products **7** and **8** obtained from kinetic and thermodynamic protonation, respectively (Fig. 4). We recently reported that upon formation of dihydropyridine **4** treatment with Na[(AcO)₃BH] in the presence of acetic acid provides **7** (Nu = H) in good overall yields based upon starting imine **2** with uniformly very high stereoselectivity (17). This reaction presumably proceeded by in situ formation and then reduction of kinetic iminium **5**.

To explore reduction of the thermodynamically favored iminiums **6**, formation of **6a** under thermodynamic control was followed by reduction with the mild hydride donor [(AcO)₃BH][−] in THF to afford tetrahydropyridine **8a** in an 80% overall yield with respect to imine **1a** (Fig. 4, conditions B and C). Compound **8a** was formed as a single diastereomer as evidenced by NMR

spectra of the crude product mixture; its relative configuration of the saturated ring carbon atoms was established unambiguously by x-ray crystallography (fig. S4). Starting from differently substituted imine and alkyne precursors, products **8b–i** were obtained in high overall yields of 61 to 87% (Fig. 4). More importantly, very high diastereoselectivities were observed uniformly except for **8b** and **8g**, which were obtained as a 10:1 and 8.5:1 mixture of two diastereomers, respectively. In the case of **8g**, reduction using Li[*i*-Bu₃BH] increased the diastereoselectivity to >95% and showed that

improvement of diastereomeric ratio was possible using a sterically more demanding reducing agent. Tolerance of different *N*-substituents (**8a–c**), unsymmetrical and functionalized alkynes (**8d–f**), as well as (hetero-)aryl substituents (**8g–i**) underscored the generality of the methodology.

Through this sequence, the piperidine products **8** were obtained via the direct generation of iminium ions **6** from imine and alkyne inputs. Isolation of the dihydropyridine intermediate **4** before protonation and reduction was only necessary for the preparation of products **8e** and **8f**. All other highly

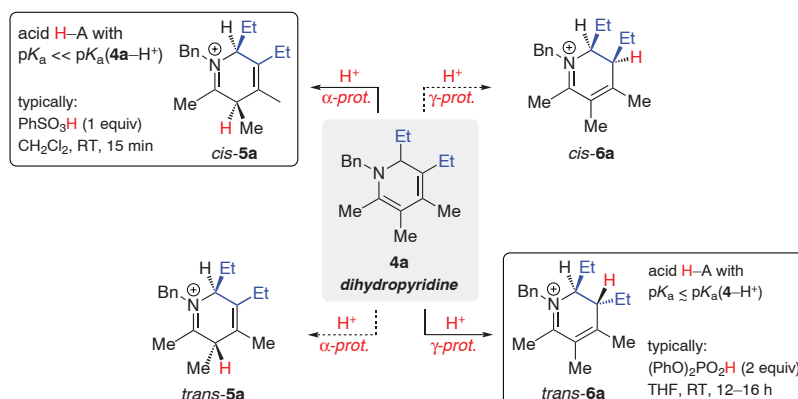


Fig. 2. Four possible iminium ions resulting from protonation of dihydropyridine **4a**. RT, room temperature.

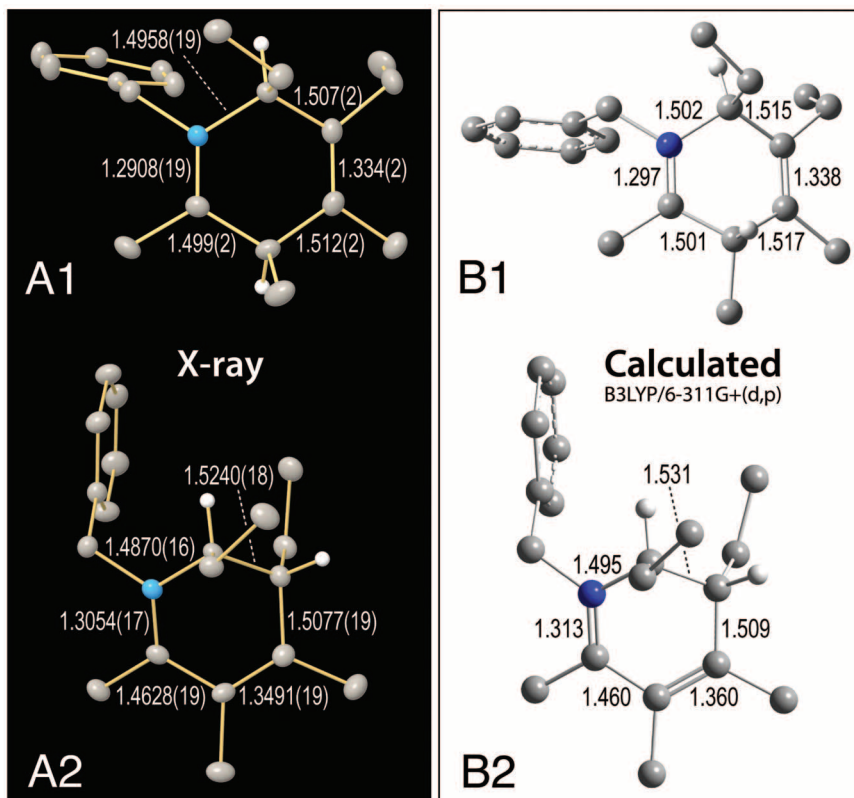


Fig. 3. X-ray crystal structures (displayed with 50% displacement ellipsoids) of iminium ions (**A1**) *cis*-**5a** and (**A2**) *trans*-**6a**; calculated structures of (**B1**) *cis*-**5a** and (**B2**) *trans*-**6a**. Numbers are bond lengths in Å; H atoms have been omitted except when attached to saturated ring atoms.

substituted piperidine derivatives required only a single workup and purification at the end of the sequence.

Successful hydride reduction of the iminium ions suggested the feasibility of diastereoselective addition of carbon nucleophiles, although competitive deprotonation pathways posed a challenge. Iminium ions **5** and **6** both exhibited *C*-electrophilic C2 positions but also Brønsted-acidic α and γ sites where protonation of the π system of **4** had oc-

curred. Organometallic reagents $R-[M]$ of high Brønsted basicity, such as alkylolithiums and alkyl Grignard reagents, led to mixtures of C2-addition products **7** or **8** and dihydropyridines **4** resulting from deprotonation. We identified several nucleophiles that underwent clean 1,2-addition and afforded only minor amounts of undesired elimination products. Allyl, benzyl, alkynyl, and ester groups could be introduced using allyl- $[CeCl_2]$, $ArCH_2-[CeCl_2]$, $RC\equiv C-[MgCl]$, and $ROC(O)CH_2-[ZnBr]$

reagents, respectively. Organometallic reagents were selected that favor electrophilic addition over competitive deprotonation pathways (23).

Addition reactions to both *cis*-**5** and *trans*-**6** proceeded in high yields and excellent diastereoselectivities (Fig. 4). For these transformations, the dihydropyridine intermediates **4** were separated from the rhodium catalyst by filtration through alumina, converted to the iminium ions with $PhSO_3H$ or $(PhO)_2PO_2H$, and added to an excess of the carbon nucleophile in THF or diethyl ether. Tetrahydropyridines **7a–g** and **8j–q** were obtained in yields of 66 to 94% and with diastereoselectivities of 94:6 or higher. NMR spectra of the crude products confirmed that the diastereoselectivities were not a result of selective isolation of one particular stereoisomer. In analogy to the hydride reductions of **6**, exclusive 1,2-addition (no 1,4-derivatization) was observed. Relative configurations were inferred on the basis of crystal structures of **7a** (17), **7e**, and **8m** (figs. S3 and S5) and the similarities of the NMR spectra of the two sets of products. Compounds **7** exhibited all-*cis* stereochemistry of the substituents R^2 , R^3 , and R^6 , whereas for **8** *trans*- R^5/R^6 and *trans*- R^6/R^2 stereochemistry was observed. Thus, the facial selectivity for the addition step was the same for $[(AcO)_3BH]^+$ and the organometallic reagents, suggesting that the preferred trajectory was mainly determined by the geometry of the iminium ions **5** and **6** and to a lesser extent by the nature of the nucleophile. Tetrahydropyridine **8q** features seven different substituents as a result of coupling of a differentially substituted imine with an unsymmetrical alkyne and addition of an alkynyl nucleophile. Such a level of directed placement of substituents around a piperidine ring has not been reported to the best of our knowledge (21, 22).

The x-ray structures of the reactive iminium ions *cis*-**5a** and *trans*-**6a** offer prospective insight into the high diastereoselectivities that were consistently observed in the nucleophilic addition steps. Nucleophilic addition to ion *cis*-**5a** is most likely directed by the pseudoaxial C3 substituent, which exerts the strongest steric hindrance to nucleophiles approaching the C2 electrophilic center. The relatively planar C2–C3–C4 moiety of *trans*-**6a** provides little facial steric bias for the incoming nucleophile. We therefore hypothesize that the conformation of the benzyl group might govern diastereoselectivity in the addition step.

Although pharmaceutical researchers now routinely and reliably separate enantiomers by preparative chiral high-performance liquid chromatography (24, 25), an asymmetric variant of the present reaction sequence could be contemplated through the use of chiral directing groups or asymmetric electrocyclic catalysts (26, 27). Moreover, the addition of many other types of nucleophiles should be possible, and the 1,2-dihydropyridine intermediates **4** could conceivably react with electrophiles other than protons to enable the regio- and stereoselective synthesis of even more densely substituted products.

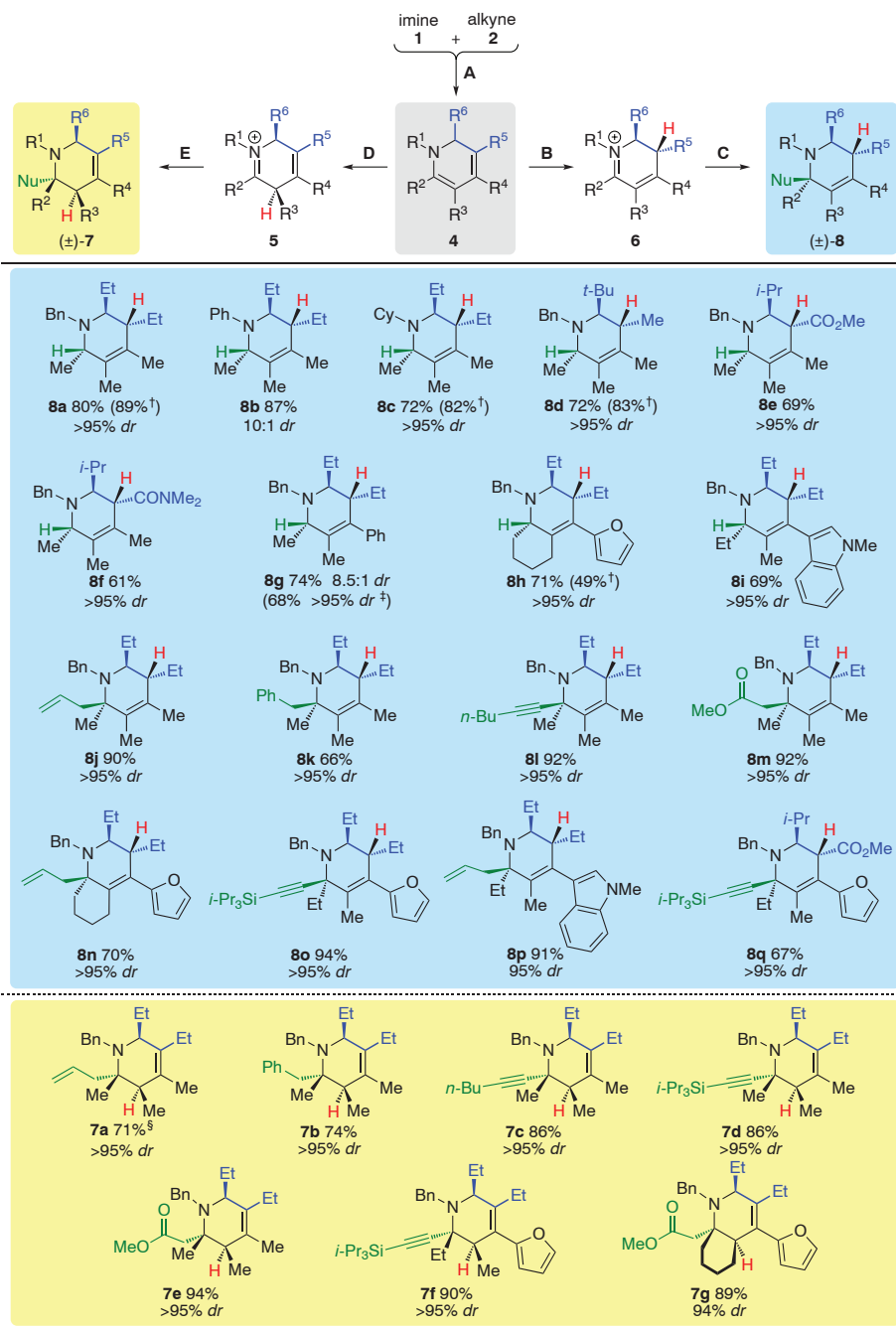


Fig. 4. Substrate scope for the synthesis of products **7** and **8**. Conditions: (A) 1:2 $[RhCl(cyclooctene)]_2/4-Me_2NC_6H_4-PtEt_2$ (1 to 2.5 mol %), $PhMe$. (B) $(PhO)_2PO_2H$, THF. (C) $Na[(AcO)_3BH]$, THF or $R-[M]$, THF or Et_2O . (D) $PhSO_3H$, CH_2Cl_2 . (E) $R-[M]$, THF or Et_2O ; for experimental details, see the supplementary Materials. †[Rh] step run in THF, and reaction carried out as a one-pot procedure; ‡[Rh] step run in THF, and reduction conducted using $Li[i-Bu_3BH]$; §(17).

References and Notes

- Typing the name of these drug and drug candidates into PubChem (<http://pubchem.ncbi.nlm.nih.gov/>) provides the compound structure, bioactivity, full list of published studies, and information regarding ongoing clinical trials, applications, and usage: plavix (CID 60606), cialis (110635), and aricept (CID 5741).
- F. Lovering, J. Bikker, C. Humblet, *J. Med. Chem.* **52**, 6752 (2009).
- W. P. Walters, J. Green, J. R. Weiss, M. A. Murcko, *J. Med. Chem.* **54**, 6405 (2011).
- T. J. Ritchie, S. J. F. Macdonald, *Drug Discov. Today* **14**, 1011 (2009).
- M. P. Doyle, K. I. Goldberg, *Acc. Chem. Res.* **45**, 777 (2012).
- H. M. L. Davies, J. Du Bois, J.-Q. Yu, *Chem. Soc. Rev.* **40**, 1855 (2011).
- R. H. Crabtree, *Chem. Rev.* **110**, 575 (2010).
- J. Yamaguchi, A. D. Yamaguchi, K. Itami, *Angew. Chem. Int. Ed.* **51**, 8690 (2012).
- H. M. L. Davies, J. R. Manning, *Nature* **451**, 417 (2008).
- M. Wasa, K. M. Engle, J.-Q. Yu, *J. Am. Chem. Soc.* **132**, 3680 (2010).
- N. Guimond, S. I. Gorelsky, K. Fagnou, *J. Am. Chem. Soc.* **133**, 6449 (2011).
- D. A. Colby, R. G. Bergman, J. A. Ellman, *J. Am. Chem. Soc.* **130**, 3645 (2008).
- L. F. Tietze, G. Brasche, K. Gericke, *Domino Reactions in Organic Synthesis* (Wiley, Weinheim, Germany, 2006).
- H. M. Davies, E. M. Sorensen, *Chem. Soc. Rev.* **38**, 2981 (2009).
- C. Grondal, M. Jeanty, D. Enders, *Nat. Chem.* **2**, 167 (2010).
- J. A. Bull, J. J. Mousseau, G. Pelletier, A. B. Charette, *Chem. Rev.* **112**, 2642 (2012).
- S. Duttwyler, C. Lu, A. L. Rheingold, R. G. Bergman, J. A. Ellman, *J. Am. Chem. Soc.* **134**, 4064 (2012).
- R. E. Lyle, D. A. Nelson, P. S. Anderson, *Tetrahedron Lett.* **3**, 553 (1962).
- P. S. Anderson, R. E. Lyle, *Tetrahedron Lett.* **5**, 153 (1964).
- D. A. Evans, in *Asymmetric Synthesis*, Vol. 3 (Academic Press, New York, 1984), pp. 20–21 and 65–68.
- M. J. Frisch *et al.*, Gaussian 09, Revision A.1 (Gaussian, Inc., Wallingford, CT, 2009).
- R. W. Hoffmann, *Chem. Rev.* **89**, 1841 (1989).
- H.-J. Liu, K.-S. Shia, X. Shang, B.-Y. Zhu, *Tetrahedron* **55**, 3803 (1999).
- T. J. Ward, K. D. Ward, *Anal. Chem.* **82**, 4712 (2010).
- Y. Okamoto, T. Ikai, *Chem. Soc. Rev.* **37**, 2593 (2008).
- S. Thompson, A. G. Coyne, P. C. Knipe, M. D. Smith, *Chem. Soc. Rev.* **40**, 4217 (2011).
- S. Müller, B. List, *Angew. Chem. Int. Ed.* **48**, 9975 (2009).

Acknowledgments: This work was supported by NIH grant GM069559 (to J.A.E.). R.G.B. acknowledges funding from the Director, Office of Energy Research, Office of Basic Energy Sciences, Chemical Sciences Division, U.S. Department of Energy, under contract DE-AC02-05CH11231. S.D. is grateful to the Swiss National Science Foundation for a postdoctoral fellowship (PBZHP2-130-966). Metrical parameters for the structures of compounds 5a, 6a, 7e, 8a, and 8m are available free of charge from the Cambridge Crystallographic Data Centre under reference nos. CCDC 911314–911318.

Supplementary Materials

www.sciencemag.org/cgi/content/full/339/6120/678/DC1
Materials and Methods
Figs. S1 to S5
Tables S1 to S7
References (28–35)

25 September 2012; accepted 3 December 2012
10.1126/science.1230704

A Functional [NiFe]Hydrogenase Mimic That Catalyzes Electron and Hydride Transfer from H₂

Seiji Ogo,^{1,2,3*} Koji Ichikawa,² Takahiro Kishima,² Takahiro Matsumoto,^{1,2} Hidetaka Nakai,^{1,2} Katsuhiko Kusaka,⁴ Takashi Ohhara⁵

Chemists have long sought to mimic enzymatic hydrogen activation with structurally simpler compounds. Here, we report a functional [NiFe]-based model of [NiFe]hydrogenase enzymes. This complex heterolytically activates hydrogen to form a hydride complex that is capable of reducing substrates by either hydride ion or electron transfer. Structural investigations were performed by a range of techniques, including x-ray diffraction and neutron scattering, resulting in crystal structures and the finding that the hydrido ligand is predominantly associated with the Fe center. The ligand's hydridic character is manifested in its reactivity with strong acid to liberate H₂.

Nickel-iron hydrogenase enzymes ([NiFe]H₂ases) catalyze the transfer of electrons from hydrogen gas (H₂) to a redox partner (1–5). This activation of H₂ for the release of electrons and/or hydride ions has tremendous potential applications from energy generation to industrial synthesis, and so H₂ases

are currently the focus of much research across many disciplines.

We have previously reported a [NiRu]model complex ([Ni^{II}(X)(H₂O)(μ-H)Ru^{II}(C₆Me₆)(NO₃)₃]{[3](NO₃), where X = *N,N'*-dimethyl-3,7-diazanonane-1,9-dithiolato and Me indicates a methyl group}) that can mimic the chemical functions of [NiFe]H₂ases (6, 7). Based on the [NiRu] core, this complex could activate H₂ in water, at room temperature, and use the extracted electrons to reduce substrates as part of a catalytic cycle. A central finding of this study was that the so-called hydride complex actually took the form of a three-center Ni–H–Ru bond—in other words, the electrons from the hydride were used to form a Ni^I–Ru^I bond with the proton. Because no functional hydride-type model had been reported, we were confident that the protic form was the best descriptor of the active state of [NiFe]H₂ases.

As a result of our efforts to improve this original model, we can now report a functional model complex based on a [NiFe] core. Furthermore, this complex bears a true hydride ion in the reactive form. Not only is this catalyst far

cheaper than our previous complex, it constitutes a major step forward in the understanding of [NiFe]H₂ases. Here, we describe the synthesis of this model and report its chemical and structural features.

Model complex ([Ni^{II}(X')Fe^{II}(MeCN){P(OEt)₃}]₃(BPh₄)₂ {[1](BPh₄)₂, where X' = *N,N'*-diethyl-3,7-diazanonane-1,9-dithiolato, Et indicates an ethyl group, and Ph a phenyl group}) bears the characteristics that we have previously described as necessary for a [NiFe]H₂ase model complex: a bimetallic core, a μ-S bridge between the metal centers to allow close approach, and ligands capable of accepting π-back donation from the Fe (or Ru) center. The three most important developments in this complex are the replacement of Ru with Fe, the replacement of an aryl ligand with three triethylphosphite {P(OEt)₃} ligands, and, crucially, the use of sodium methoxide (MeONa) as a base instead of water.

The structure of **1**, bearing a MeCN ligand at the vacant site, was determined by x-ray diffraction (fig. S1), proton nuclear magnetic resonance (¹H NMR) spectroscopy (fig. S2), and mass spectrometry (fig. S3) (8). The Ni···Fe distance is 3.3189(6) Å. The Ni–S–Fe angles are 94.93(4) and 94.79(4)°.

Complex **1** heterolytically activated H₂ in MeCN/MeOH at room temperature and atmospheric pressure. Abstraction of a proton from bound H₂ by a strong base (MeONa) resulted in formation of hydride-bearing complex ([Ni^{II}(X')(μ-H)Fe^{II}{P(OEt)₃}]₃(BPh₄)₂ {[2](BPh₄)₂}) (8).

The structure of the hydride-bearing complex **2** was determined by x-ray diffraction (Fig. 1), neutron scattering (fig. S4), ¹H NMR (fig. S5) and infrared (IR) spectroscopy (fig. S6), and mass spectrometry (fig. S7). The Ni atom adopts the same planar structure as in **1**, and the Ni···Fe distance is 2.7930(6) Å, which is also comparable to the Ni···Ru distance in **3**. These distances are, however, longer than the Ni···Fe separation in

¹World Premier International Research Center Initiative—International Institute for Carbon-Neutral Energy Research (WPI-I2CNER), Kyushu University, 744 Moto-oka, Nishi-ku, Fukuoka 819-0395, Japan. ²Department of Chemistry and Biochemistry, Graduate School of Engineering, Kyushu University, 744 Moto-oka, Nishi-ku, Fukuoka 819-0395, Japan. ³Core Research for Evolutional Science and Technology (CREST), Japan Science and Technology Agency (JST), Kawaguchi Center Building, 4-1-8 Honcho, Kawaguchi, Saitama 332-0012, Japan.

⁴Frontier Research Center for Applied Atomic Sciences, Ibaraki University, IBARAKI Quantum Beam Research Center (IQBRC) Building, 162-1 Shirakata, Tokai, Ibaraki 319-1106, Japan. ⁵Research Center for Neutron Science and Technology, Comprehensive Research Organization for Science and Society, IQBRC Building, 162-1 Shirakata, Tokai, Ibaraki 319-1106, Japan.

*To whom correspondence should be addressed. E-mail: ogotcm@mail.cstm.kyushu-u.ac.jp

the reduced state of [NiFe]H₂ase (9) and that in a nonfunctional [NiFe]complex ([Ni^{II}(dppe)(μ-H)Fe^{II}(pdt)(CO)₃](BF₄) {4}(BF₄), where dppe = 1,2-bis(diphenylphosphino)ethane and pdt = 1,3-propanedithiolate}) reported by Rauchfuss and co-workers (10). Neutron-scattering analysis allowed us to confirm the position of the hydride ion in **2** (strictly speaking, the deuterido ligand). For this analysis, we synthesized D-labeled **2** by using D₂ in place of H₂ ([Ni^{II}(X')(μ-D)Fe^{II}{P(OEt)₃}₃](BPh₄) {D-labeled **2**}(BPh₄)). The results show that the Fe–D bond distance [1.577(17) Å] is much shorter than the Ni–D bond length [2.18(4) Å], suggesting that the hydride ion is located on the Fe center. This

is a marked difference from the metrics for **3** and **4**, which both have similar values for the Ni–H and Ru–H/Fe–H distances, suggesting three-center bonds for these complexes [for **3**, Ni–H = 1.859(7) Å and Ru–H = 1.676(8) Å; for **4**, Ni–H = 1.64(6) Å and Fe–H = 1.46(6) Å].

The ¹H NMR spectrum of **2** exhibits a double triplet resonance at –3.57 parts per million that is derived from the hydrido ligand coupling with the nuclear spin of three P atoms (fig. S5). In the case of D-labeled **2** (discussed further below), no hydride-derived signal was observed in the ¹H NMR spectrum. Complex **2** is diamagnetic, as evidenced by the appearance of its ¹H NMR

spectrum and the electron spin resonance silence at 128 K. The IR spectrum of **2** shows an isotope-sensitive band at 1687 cm^{–1}, which is assigned as ν(Ni–H–Fe) (fig. S6). The band shifted to 1218 cm^{–1} by using D-labeled **2**. The positive-ion electrospray ionization (ESI) mass spectrum of **2** in MeOH shows a prominent signal at mass-to-charge ratio (*m/z*) = 861.2 that corresponds to [2]⁺ and a characteristic isotopic distribution that matches well with the calculated isotopic distribution (fig. S7). To establish the origin of the hydrido ligand of **2**, D-labeled **2** was used. The mass spectrum shows the signal at *m/z* = 862.2, thus demonstrating that the hydrido ligand is derived from D₂. The redox property of **2** was analyzed by cyclic voltammetry (fig. S8).

In common with [NiFe]H₂ases, complex **2** can perform both hydride and electron transfers (Fig. 2). 10-Methylacridinium ion (AcrH⁺) and methylene blue (MB⁺) as a nicotinamide adenine dinucleotide (NAD⁺) model were reduced to 10-methyl-9,10-dihydroacridine (AcrH₂) and MBH, respectively (8). When using D-labeled **2**, deuterium was incorporated into the substrate (AcrHD). When **2** reacted with HBF₄ in MeCN, gas chromatography detected evolved H₂ gas, and HD gas was evolved when using D-labeled **2** instead of **2**. The reaction of **2** with an excess amount of HBF₄ obeyed pseudo-first-order kinetics with respect to **2**, in which the rate constant was determined as 6.5 × 10^{–2} s^{–1} (fig. S9). As an electron donor, **2** was able to reduce methyl viologen (MV²⁺) and ferrocenium ion {[Fe^{III}(C₅H₅)₂]⁺} to their one-electron reduced forms, as evidenced by the relevant changes in the ¹H NMR and ultraviolet/visible spectra of the solutions (8). After these reductions, **2** returned to its oxidized form, **1**, which activated H₂ with MeONa to re-form **2** (single turnover).

It is worth comparing the chemical and structural characteristics of **2** with previous model compounds. Complex **2** can perform both hydride and electron transfers, whereas **3** can only perform the electron transfer and **4** is nonfunctional. Complexes **3** and **4** both exchange bound H⁺ for solution-phase D⁺, indicating that their hydride ligands have a strong protic character, whereas H[–] and D[–]-bound **2** react with an acid to produce H₂ and HD, indicating a hydridic character. These differences in chemical behavior are nicely reflected in the structural differences, notably the equidistant positioning of the bound proton in **4** versus the Fe-bound hydride in **2**.

The reactivity of **2** may also shed important light on the reactive species in natural H₂ases. Whether the hydride ion was predominantly bound to the Ni or Fe center has never been conclusively proved, although some opinion has tended toward a Ni-bound hydride (1). This study indicates that a Fe-bound hydride might be a better picture.

References and Notes

1. R. Cammack, M. Frey, R. Robson, *Hydrogen as a Fuel: Learning from Nature* (Taylor and Francis, London, 2001).
2. C. Tard, C. J. Pickett, *Chem. Rev.* **109**, 2245 (2009).
3. F. Gloaguen, T. B. Rauchfuss, *Chem. Soc. Rev.* **38**, 100 (2009).

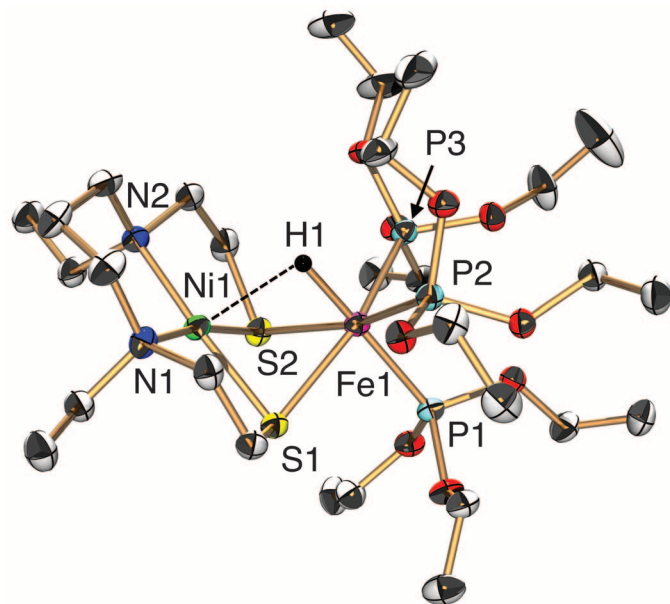


Fig. 1. An Oak Ridge thermal ellipsoid plot drawing of the solid-state structure of [2](BPh₄) with ellipsoids at the 50% probability level. The counteranion (BPh₄) and hydrogen atoms of *N,N'*-diethyl-3,7-diazanonane-1,9-dithiolato (X') and P(OEt)₃ are omitted for clarity. Selected interatomic distances and angles are as follows: Ni1–H1, 2.16(4) Å; Fe1–H1, 1.57(5) Å; Ni1...Fe1, 2.7930(6) Å; Ni1–S1–Fe1, 75.76(3)°; Ni1–S2–Fe1, 75.82(3)°.

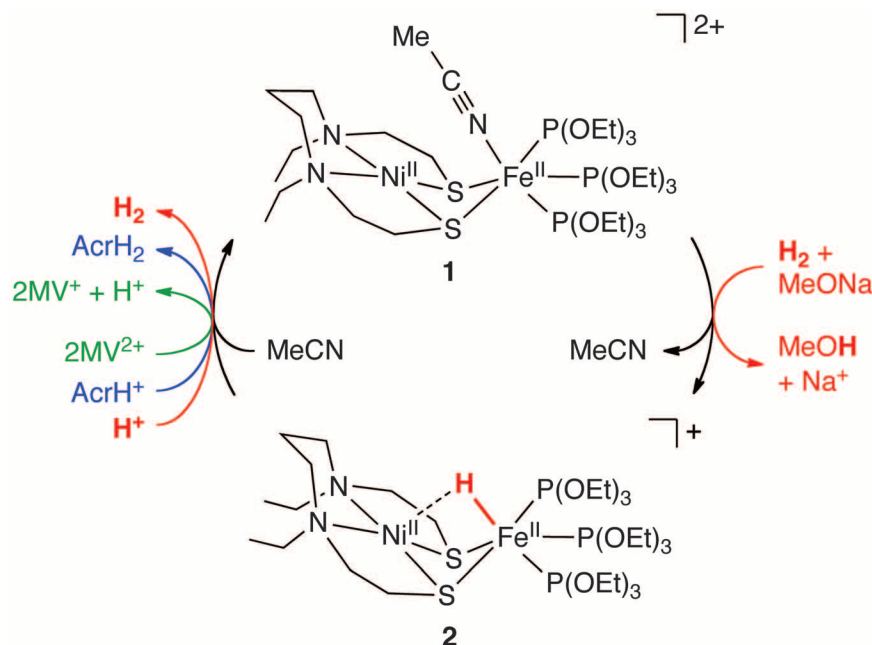


Fig. 2. Heterolytic activation of H₂ (0.1 MPa) by [NiFe]complex **1** in MeCN/MeOH containing MeONa to form [NiFe]hydride complex **2** and transfer of hydride or electrons from **2** to H⁺, AcrH⁺, or MV²⁺, respectively, resulting in their reduction.

4. G. J. Kubas, *Chem. Rev.* **107**, 4152 (2007).
5. J. W. Tye, M. B. Hall, M. Y. Darenbourg, *Proc. Natl. Acad. Sci. U.S.A.* **102**, 16911 (2005).
6. S. Ogo *et al.*, *Science* **316**, 585 (2007).
7. S. Ogo, *Chem. Commun.* **2009**, 3317 (2009).
8. Materials and methods and spectroscopic and mass spectrometric data are available on *Science Online*.
9. Y. Higuchi, H. Ogata, K. Miki, N. Yasuoka, T. Yagi, *Structure* **7**, 549 (1999).
10. B. E. Barton, C. M. Whaley, T. B. Rauchfuss, D. L. Gray, *J. Am. Chem. Soc.* **131**, 6942 (2009).

Acknowledgments: This work was supported by the WPI; grants-in-aid 23655053, 24750058, and 24109016 (Scientific Research on Innovative Areas “Stimuli-responsive Chemical Species”) from the Ministry of Education, Culture, Sports, Science and Technology (MEXT), Japan; and the Basic Research Programs CREST Type, “Development of the Foundation for Nano-Interface Technology” from JST, Japan. Crystallographic data for [1](BPh₄)₂, [2](BPh₄)₂, and [Ni^{II}(X⁻)Fe^{II}(Br)₂] have been deposited with the Cambridge Crystallographic Data Center under reference numbers CCDC-904876 (x-ray diffraction, 1), 904877 (x-ray diffraction,

2), 904874 (neutron scattering, 2), and 904875 {x-ray diffraction, [Ni^{II}(X⁻)Fe^{II}(Br)₂]}, respectively.

Supplementary Materials

www.sciencemag.org/cgi/content/full/339/6120/682/DC1
Materials and Methods
Figs. S1 to S12
References (11–21)

10 October 2012; accepted 27 November 2012
10.1126/science.1231345

Time Scales of Critical Events Around the Cretaceous-Paleogene Boundary

Paul R. Renne,^{1,2*} Alan L. Deino,^{1†} Frederik J. Hilgen,^{3†} Klaudia F. Kuiper,^{4†} Darren F. Mark,^{5†} William S. Mitchell III,^{2,6†} Leah E. Morgan,^{5†} Roland Mundil,^{1†} Jan Smit^{4†}

Mass extinctions manifest in Earth’s geologic record were turning points in biotic evolution. We present ⁴⁰Ar/³⁹Ar data that establish synchrony between the Cretaceous-Paleogene boundary and associated mass extinctions with the Chicxulub bolide impact to within 32,000 years. Perturbation of the atmospheric carbon cycle at the boundary likely lasted less than 5000 years, exhibiting a recovery time scale two to three orders of magnitude shorter than that of the major ocean basins. Low-diversity mammalian fauna in the western Williston Basin persisted for as little as 20,000 years after the impact. The Chicxulub impact likely triggered a state shift of ecosystems already under near-critical stress.

The mass extinction at the boundary (KPB) between the Cretaceous and Paleogene periods, ~66 million years ago (Ma), likely involved the catastrophic effects of a bolide impact (1), although other factors may have played an important role (2–5). To a large extent, ambiguity between the possible causes stems from inadequate age resolution of relevant events near KPB time. Existing geochronologic data surrounding the linkage between the KPB and the Chicxulub structure in the northern Yucatán Peninsula of Mexico actually exclude synchrony, indicating that the Chicxulub impact and co-genetic impact melt droplets, termed “tektites” (6–8), postdated the KPB by 183 ± 65 (9) thousand years (ky) and 181 ± 71 ky, respectively (see supplementary materials). In contrast, some data suggest that the Chicxulub impact predated the KPB by several hundred thousand years, and that discrete tektite-bearing horizons in the Gulf of Mexico region were derived from multiple impact events (10).

We acquired high-precision ⁴⁰Ar/³⁹Ar data to clarify these temporal relationships and thereby

facilitate a clearer sequencing of events associated with the KPB extinctions and subsequent ecosystem recovery. We analyzed multiple samples of the tektites to refine the age of the Chicxulub impact, and of bentonites (altered volcanic ashes; Fig. 1) clearly associated with the KPB to test for synchrony of the boundary with the impact. ⁴⁰Ar/³⁹Ar ages (Figs. 2 and 3) were determined (see supplementary materials) by incremental heating of 14 tektites from Beloc, Haiti, giving a weighted mean age of 66.032 ± 0.058/0.072 Ma (11) that is indistinguishable from that determined by previous studies (12, 13) when normalized to the same calibration. Combining all data yields an age of 66.038 ± 0.025/0.049 Ma for the tektites.

We also performed ⁴⁰Ar/³⁹Ar dating on sandine separated from four bentonites in three distinct coal beds within two widely separated stratigraphic sections in the Hell Creek region of northeastern Montana. Extensive studies in this region have documented faunal, floral, and chemostratigraphic aspects of latest Cretaceous through early Paleogene terrestrial strata. Both sections contain well-documented Ir anomalies coincident with the biostratigraphically defined KPB (Fig. 1). In the Hauso Flats section, we analyzed samples from two localities ~200 m apart of a bentonite from the IrZ coal, located stratigraphically only a few centimeters above the horizon yielding the largest iridium anomaly [up to 11.7 parts per billion (ppb) at the nearby Herpikunk locality; (14)] reported from this area and 5 cm above the highest occurrence of Cretaceous pollen in the section (15). All of our data combined yield a weighted mean age of 66.043 ± 0.011/0.043 Ma.

A bentonite from the Hauso Flats Z (HFZ) coal, 18 m stratigraphically above the IrZ coal, yielded an age of 65.990 ± 0.032/0.053 Ma. Isotope dilution–thermal ionization mass spectrometry (ID-TIMS) U-Pb analyses of 15 chemically abraded zircons from the same HFZ coal bentonite yielded a weighted mean age of 65.988 ± 0.074 Ma, in agreement with the ⁴⁰Ar/³⁹Ar results. In the Hell Creek Marina road section, we analyzed two bentonites within the Z coal, which lies 50 to 60 cm above a 0.57-ppb Ir anomaly (16). The two bentonites are separated stratigraphically by ~30 cm and yield results for the lower (Z₂) and upper (Z₁) bentonites of 66.019 ± 0.021/0.046 Ma and 66.003 ± 0.033/0.053 Ma, respectively.

The IrZ coal bentonite is much closer stratigraphically to both impact signals and the biostratigraphically defined KPB than the Z coal bentonites; thus, it should be regarded as the closest stratigraphic proxy for the KPB. Accordingly, a comparison with the pooled age for the Beloc tektites indicates a statistically insignificant age difference of 5 ± 27 ky between the two events. Thus, the hypothesis that the Chicxulub impact predated the KPB by ~300 ky (10) is unsupported by our data. Our preferred absolute age for the KPB, including propagated systematic uncertainties, is 66.043 ± 0.043 Ma. This age, which is intrinsically calibrated by both ⁴⁰K and ²³⁸U decay constants (17), is sufficiently precise to discriminate between 100-ky orbital eccentricity cycles at 66 Ma, in principle allowing comparison with astronomical tuning approaches to dating the KPB. However, the uncertainty in the astronomical solution (~40,000 years ago) at 66 Ma (18) effectively limits this discrimination because the 100-ky cycle is not reliable in the solution due to chaotic behavior of the solar system. Our age for the KPB, if based on the Kuiper *et al.* (19) calibration, would be 65.836 ± 0.061 Ma, which would be sufficiently precise to discriminate between 405-ky but not 100-ky orbital cycles. Because circum-KPB marine records generally lack appropriate materials for high-resolution radioisotopic dating, astronomical tuning potentially represents the best means of temporally calibrating marine records and enabling their comparison with terrestrial records in this time interval. A fully calibrated astronomical solution can potentially enable deconvolution of orbital forcing from other causes of climate change.

The KPB age as determined by our data for the IrZ coal bentonite agrees with the astronomical age (66 ± 0.07 Ma; option 2) derived

¹Berkeley Geochronology Center (BGC), 2455 Ridge Road, Berkeley, CA 94709, USA. ²Department of Earth and Planetary Science, University of California, Berkeley, CA, 94720, USA. ³Faculty of Geosciences, Department of Earth Sciences, Utrecht University, Budapestlaan 4, 3584 CD Utrecht, Netherlands. ⁴Faculty of Earth and Life Sciences, Institute of Earth Sciences, Vrije Universiteit Amsterdam, De Boelelaan 1085, 1081 HV Amsterdam, Netherlands. ⁵Scottish Universities Environmental Research Centre, Rankine Avenue, East Kilbride, G75 0QF, UK. ⁶Department of Chemistry, University of California, Berkeley, CA, 94720, USA.

*To whom correspondence should be addressed. E-mail: prene@bgc.org

†These authors contributed equally to this work.

from deep-sea cores (20) and the preferred astronomical age (65.957 ± 0.040 Ma) inferred by Kuiper *et al.* (19) from the Zumaia section of Spain, but not with that (65.25 ± 0.06 Ma) of Westerhold *et al.* (21) (fig. S6). We conclude that the younger age inferred by Westerhold *et al.* (21) is a consequence of miscalibration by two 405-ky eccentricity cycles (see supplementary materials) and that the terrestrial and marine Ir anomalies are synchronous. This conclusion is strengthened by our concordant U-Pb and $^{40}\text{Ar}/^{39}\text{Ar}$ dates for the HFZ coal, which indicate that the KPB is older than 65.988 ± 0.074 Ma and 65.990 ± 0.053 Ma, respectively.

Our data indicate that the stratigraphic interval of ~18 m between the IrZ and HFZ coals in the Hauso Flats section corresponds to a duration of 53 ± 34 ky, whereas the previous $^{40}\text{Ar}/^{39}\text{Ar}$ data from the same section (15) suggested a duration of 390 ± 70 ky. This interval spans most of the Pu1 basal Puercan (North American Land Mammal Age) mammalian fauna known from northeastern Montana and adjacent areas in Canada, containing only 15 recognized species compared with 27 in the preceding (pre-KPB) Lancian stage (22). The brevity of the IrZ-HFZ interval of the basal Tullock Formation implied by our new data indicates that the depauperate Pu1

fauna persisted as briefly as 20 ky and supports the hypothesis (22) that much of the post-KPB vertebrate faunal recovery in the Hell Creek area occurred by immigration rather than evolutionary radiation, given that the duration of speciation events for mammals (at least, late Cenozoic ones) typically exceeds hundreds of thousands of years (23).

Our dating of the IrZ and HFZ bentonites constrains the terrestrial, hence atmospheric, -1.5 per mil (‰) $\delta^{13}\text{C}$ isotope anomaly in the Hauso Flats section (24) to have occurred early within the first 53 ± 34 ky of the Paleogene. Scaling the sediment accumulation rate by linear interpolation between the two dated horizons and allowing the maximum possible stratigraphic extent of the anomaly (considering sample interval) yield a maximum duration of 5 ± 3 ky for the anomaly. Similarly, applying our date for the IrZ bentonite to the iridium anomaly and scaling to the Z_2 bentonite in the Hell Creek Marina road section (24) yields a maximum duration of 13 ± 13 ky for the -2.0 ‰ $\delta^{13}\text{C}$ anomaly there.

The terrestrial $\delta^{13}\text{C}$ anomaly is markedly consistent in magnitude, timing, and rapidity of onset with marine records, although the latter commonly show much longer recovery time scales. Some marine records [e.g., (1)] show an

initial decrease of 1 to 2‰ followed by a rapid increase of ~1‰ on the time scale of several thousand years, succeeded by a much more gradual increase over several million years to pre-KPB values. Other cases show more rapid recovery of marine $\delta^{13}\text{C}$ to pre-KPB values, as in the Agost section of southern Spain, where the duration of the anomaly and partial recovery are estimated to have occurred over 3 to 5 ky, and full recovery to have occurred over <100 ky (25). Differences between $\delta^{13}\text{C}$ values in planktic versus benthic foraminifera from Atlantic and Pacific cores also show precipitous drops at the KPB, interpreted to reflect a major disruption in mixing between surface- and deep-water masses (26). Restoration of pre-KPB values of the differential, hence of normal ocean circulation, experienced a protracted recovery spanning several millions of years and was likely the rate-limiting determinant in recovery of general marine productivity (26).

Our results strengthen conclusions that the Chicxulub impact played an important role in the mass extinctions. However, global climate instability preceded the KPB (and thus, in view of our data, the Chicxulub impact) by ~1 million years (My) (27–29). During this interval, six abrupt shifts of $>2^\circ\text{C}$ in continental mean annual temperatures have been inferred from paleoflora in North Dakota (29). The most dramatic of these temperature oscillations, a drop of 6° to 8°C , occurred <100 ky before the KPB (29) and was closely synchronous with notable mammalian turnover in the Hell Creek area (30). Several cycles of latest Cretaceous sea-level oscillations are recorded in the Williston basin with an overall regression peaking just before the KPB (31), possibly a glacio-eustatic response to climatic cooling. Cooling at this time is consistent with a global sea-level drop of ~40 m beginning in geomagnetic polarity chron 30n and ending in chron 28r (32), clearly spanning the KPB. This event followed closely on a sharp sea-level drop and subsequent rise of ~30 m, coincident with the highest $\delta^{18}\text{O}$ values recorded for the 30 My before or afterward, which occurred in the middle of chron 30n (32), ~1 My before the KPB. Recognition of these and other relatively brief events led Miller *et al.* (32) to infer the existence of multiple ephemeral Antarctic ice sheets between 100 and 33 Ma.

We suggest that the brief cold snaps in the latest Cretaceous, though not necessarily of extraordinary magnitude, were particularly stressful to a global ecosystem that was well adapted to the long-lived preceding Cretaceous hothouse climate. The Chicxulub impact then provided a decisive blow to ecosystems thus already under critical stress, and in essence pushed the global ecosystem across a threshold that triggered a planetary state shift (33, 34). Although the atmospheric carbon cycle was disrupted only briefly, and initial mammalian faunal changes after the KPB may have been dominated by migration, some changes such as the disappearance

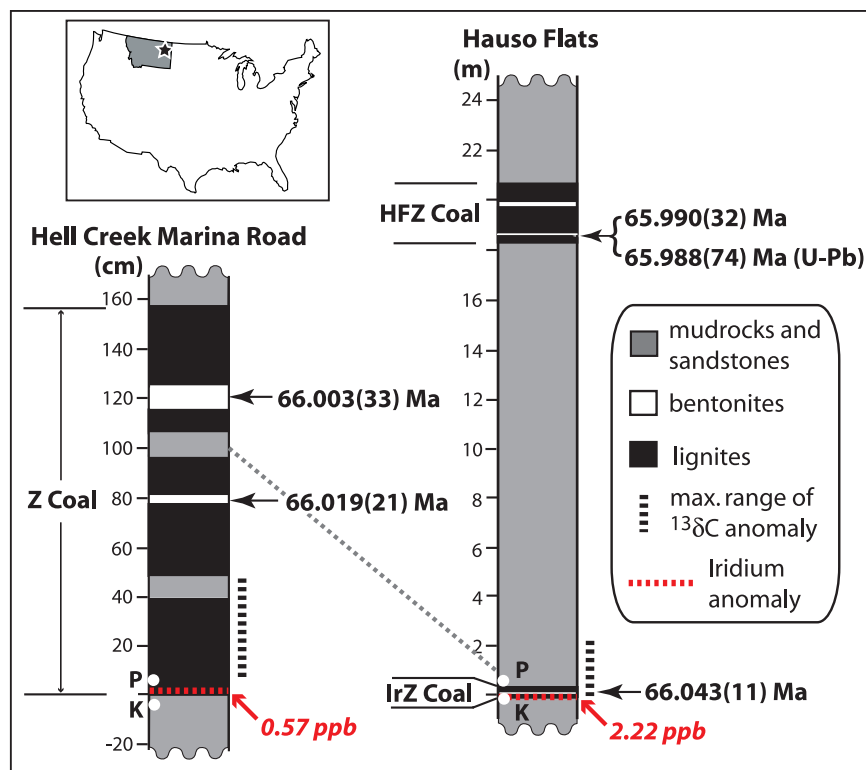


Fig. 1. Stratigraphic sections in the Hell Creek area of northeastern Montana (inset) showing positions of dated bentonites in relation to Ir anomalies (16, 41) and carbon isotope records (24) from the same sections. The two sections have different vertical scales; thin dotted line connects horizons at 1 m above the Ir anomaly in the two sections. Ages shown are from $^{40}\text{Ar}/^{39}\text{Ar}$ analysis of sanidine except one (U/Pb) from U-Pb analysis of zircon. Age uncertainties (in parentheses) refer to last significant figures shown and include analytical sources only. White dots labeled P and K on both sections show the lowest occurrence of Paleocene pollen and the highest occurrence of Cretaceous pollen, respectively (15).

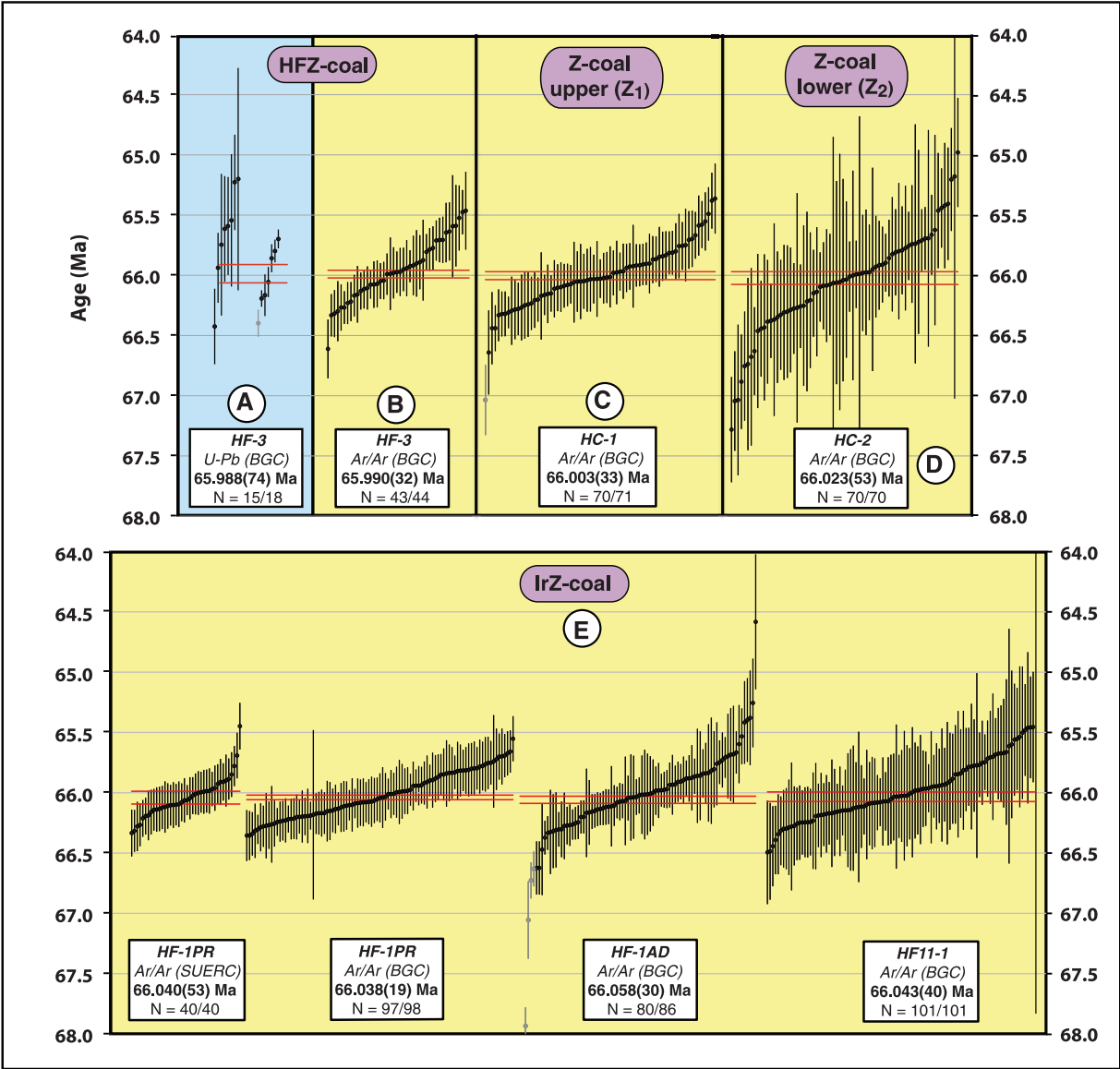
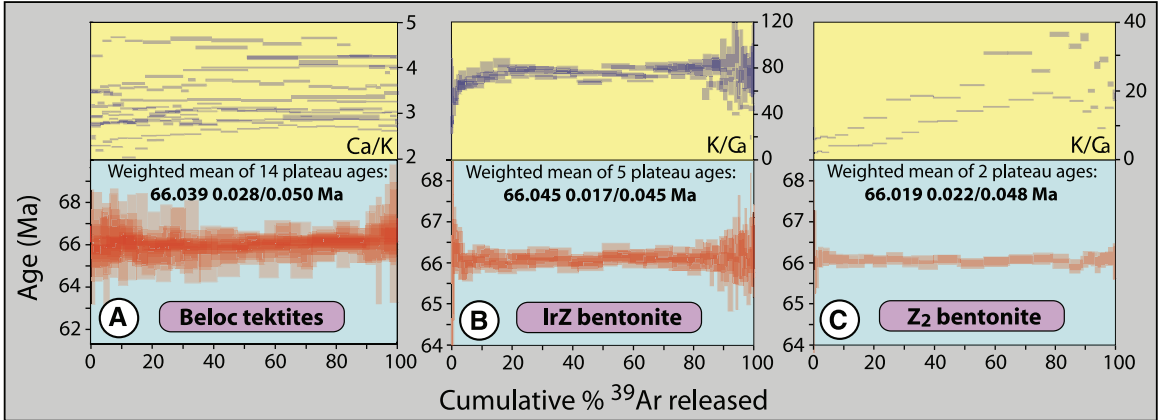


Fig. 2. Summary of single-crystal geochronology results for volcanic ashes whose stratigraphic relations are shown in Fig. 1. Individual ages are shown in ranked order with 1σ analytical uncertainty limits. Samples interpreted as xenocrysts are shown in gray and are excluded from age calculations. Uncertainty limits for the weighted mean age for each sample are shown by red lines. U-Pb results for zircon crystals (A) and $^{40}\text{Ar}/^{39}\text{Ar}$ results for sanidine

(B) from an ash in the Hauso Flats Z (HFZ) coal, 18 m above the KPB, yield indistinguishable results. Two ashes in the Z-coal in the Hell Creek marina road section (C and D) yield ages consistent with stratigraphic order although they are mutually indistinguishable at 68% confidence. Four independent data sets, from three irradiations and two labs, for the IrZ coal bentonite (E) yield consistent results.

Fig. 3. Summary of incremental heating $^{40}\text{Ar}/^{39}\text{Ar}$ age (lower panels) and Ca-K composition data (upper panels) for (A) fourteen tektites from Beloc, Haiti, and multigrained feldspar samples from the IrZ (B) and Z₂ (C) bentonites shown in Fig. 1.



of nonavian dinosaurs were permanent. Thus, whereas some paleoenvironments may have been restored relatively rapidly, terrestrial and marine ecosystems changed forever.

The cause of the precursory climate perturbations that pushed some ecosystems to the tipping point is unclear, but a leading candidate is volcanogenic volatile emissions (35) from early pulses of the episodically erupted Deccan Traps (36, 37). The magmatic event producing the Deccan Traps was clearly initiated prior to the KPB (38), and the most voluminous middle pulse of volcanism may be linked to either (i) the inception of a two-staged decline in marine $^{187}\text{Os}/^{188}\text{Os}$ beginning about 300 ky before the KPB (39) or (ii) the KPB itself (36, 37, 40). Existing geochronological data are insufficiently precise to constrain these relationships with age resolution comparable to that presented here for the KPB and the Chicxulub impact. Refining the timing and tempo of Deccan volcanism remains a considerable challenge whose resolution is key to evaluating the role of this event in the causes of biotic and environmental change at the KPB.

References and Notes

- P. Schulte *et al.*, *Science* **327**, 1214 (2010).
- J. D. Archibald *et al.*, *Science* **328**, 973, author reply 975 (2010).
- V. Courtillot, F. Fluteau, *Science* **328**, 973, author reply 975 (2010).
- G. Keller *et al.*, *Science* **328**, 974, author reply 975 (2010).
- N. C. Arens, I. D. West, *Paleobiology* **34**, 456 (2008).
- H. Sigurdsson *et al.*, *Nature* **353**, 839 (1991).
- F. J. Maurrasse, G. Sen, *Science* **252**, 1690 (1991).
- A. R. Hildebrand *et al.*, *Geology* **19**, 867 (1991).
- Uncertainties here and throughout are stated at the 68% confidence level.
- G. Keller *et al.*, *Earth Planet. Sci. Lett.* **255**, 339 (2007).
- Uncertainties given as $\pm XY$ refer to values excluding (X) and including (Y) systematic sources as defined in the supplementary materials.
- C. C. Swisher III *et al.*, *Science* **257**, 954 (1992).
- G. B. Dalrymple, G. A. Izett, L. W. Snee, J. D. Obradovich, *U.S. Geol. Surv. Bull.* **2065**, 1 (1993).
- J. Smit, S. van der Kaars, *Science* **223**, 1177 (1984).
- C. C. Swisher III, L. Dingus, R. F. Butler, *Can. J. Earth Sci.* **30**, 1981 (1993).
- H. Baadsgaard, J. F. Lerbekmo, I. McDougall, *Can. J. Earth Sci.* **25**, 1088 (1988).
- P. R. Renne, G. Balco, K. R. Ludwig, R. Mundil, K. Min, *Geochim. Cosmochim. Acta* **75**, 5097 (2011).
- J. Laskar *et al.*, *Astron. Astrophys.* **428**, 261 (2004).
- K. F. Kuiper *et al.*, *Science* **320**, 500 (2008).
- D. Husson *et al.*, *Earth Planet. Sci. Lett.* **305**, 328 (2011).
- T. Westerhold, U. Rohl, J. Laskar, *Geochim. Geophys. Geosyst.* **13**, Q06015 (2012).
- W. A. Clemens, in *The Hell Creek Formation and the Cretaceous-Tertiary Boundary in the Northern Great Plains: An Integrated Continental Record of the End of the Cretaceous*, J. H. Hartman, K. R. Johnson, D. J. Nichols, Eds. (Geological Society of America, Boulder, CO, 2002), vol. 361, pp. 217–245.
- J. C. Avise, D. Walker, G. C. Johns, *Proc. R. Soc. Lond. B Biol. Sci.* **265**, 1707 (1998).
- N. C. Arens, A. H. Jahren, *Palaio* **15**, 314 (2000).
- J. Smit, *Geol. Mijnb.* **69**, 187 (1990).
- S. D'Hondt, *Annu. Rev. Ecol. Evol. Syst.* **36**, 295 (2005).
- L. Q. Li, G. Keller, *Mar. Micropaleontol.* **33**, 55 (1998).
- E. Barrera, S. M. Savin, in *Evolution of the Cretaceous Ocean-Climate System*, E. Barrera, C. C. Johnson, Eds. (Geological Society of America, Boulder, CO, 1999), vol. 332, pp. 245–282.
- P. Wilf, K. R. Johnson, B. T. Huber, *Proc. Natl. Acad. Sci. U.S.A.* **100**, 599 (2003).
- G. P. Wilson, *J. Mamm. Evol.* **12**, 53 (2005).
- E. C. Murphy, J. W. Hoganson, K. R. Johnson, in *The Hell Creek Formation and the Cretaceous-Tertiary Boundary*

in the Northern Great Plains: An Integrated Continental Record of the End of the Cretaceous, J. H. Hartman, K. R. Johnson, D. J. Nichols, Eds. (Geological Society of America, Boulder, CO, 2002), pp. 9–34.

- K. G. Miller *et al.*, *Science* **310**, 1293 (2005).
- A. D. Barnosky *et al.*, *Nature* **486**, 52 (2012).
- M. Scheffer *et al.*, *Nature* **461**, 53 (2009).
- S. Self, *Philos. Trans. R. Soc. Lond. A* **364**, 2073 (2006).
- A. L. Chenet *et al.*, *J. Geophys. Res. Solid Earth* **114**, B06103 (2009).
- G. Keller, *Cretac. Res.* **29**, 754 (2008).
- V. E. Courtillot, P. R. Renne, *C. R. Geosci.* **335**, 113 (2003).
- N. Robinson, G. Ravizza, R. Coccioni, B. Peucker-Ehrenbrink, R. Norris, *Earth Planet. Sci. Lett.* **281**, 159 (2009).
- T. S. Tobin *et al.*, *Palaeogeogr. Palaeoclimatol. Palaeoecol.* **350–352**, 180 (2012).
- L. W. Alvarez, *Proc. Natl. Acad. Sci. U.S.A.* **80**, 627 (1983).

Acknowledgments: We thank the Ann and Gordon Getty Foundation, U.C. Berkeley's Esper S. Larsen Jr. Fund, and NSF (grants EAR 0844098 and EAR 0451802) for support of B.G.C.'s work; the Natural Environment Research Council for continued funding of the Argon Isotope Facility at the Scottish Universities Environmental Research Centre; the GTSNext project of the Marie Curie Foundation; the Marie Curie Fellowship program for support of L.E.M.; the Netherlands Organisation for Scientific Research (grant 863.07.009) for support of K.F.K.; F. Maurrasse for providing the tektites; W. Alvarez, A. Barnosky, W. Clemens, T. White, and G. Wilson for discussion and comments on the manuscript; and three anonymous reviewers for helpful suggestions. Data are available in the supplementary materials.

Supplementary Materials

www.sciencemag.org/cgi/content/full/339/6120/684/DC1
Materials and Methods
Supplementary Text
Figs. S1 to S7
Tables S1 to S4
References (42–66)

20 September 2012; accepted 14 December 2012
10.1126/science.1230492

Stress State in the Largest Displacement Area of the 2011 Tohoku-Oki Earthquake

Weiren Lin,^{1,2,3*} Marianne Conin,^{4†} J. Casey Moore,⁵ Frederick M. Chester,⁶ Yasuyuki Nakamura,⁷ James J. Mori,⁸ Louise Anderson,⁹ Emily E. Brodsky,⁵ Nobuhisa Eguchi,¹⁰ Expedition 343 Scientists‡

The 2011 moment magnitude 9.0 Tohoku-Oki earthquake produced a maximum coseismic slip of more than 50 meters near the Japan trench, which could result in a completely reduced stress state in the region. We tested this hypothesis by determining the in situ stress state of the frontal prism from boreholes drilled by the Integrated Ocean Drilling Program approximately 1 year after the earthquake and by inferring the pre-earthquake stress state. On the basis of the horizontal stress orientations and magnitudes estimated from borehole breakouts and the increase in coseismic displacement during propagation of the rupture to the trench axis, in situ horizontal stress decreased during the earthquake. The stress change suggests an active slip of the frontal plate interface, which is consistent with coseismic fault weakening and a nearly total stress drop.

The huge tsunami associated with the 2011 Tohoku-Oki earthquake [moment magnitude (M_w) 9.0] was caused by the very large coseismic fault displacement of the shallow portion of the subduction zone near the Japan

trench (1–5). Besides the unprecedented large coseismic slip of >50 m, the other surprising feature of the earthquake is that the large slip on the frontal plate interface reached the sea floor at the trench axis (6). The state of stress and fric-

tional behavior of the frontal plate interface is important for controlling coseismic displacement. Indirect analyses on stress state change and/or stress drop associated with the 2011 Tohoku-Oki earthquake have been carried out from remotely sensed observations (7–12).

To investigate the stress change associated with the 2011 Tohoku-Oki earthquake, we analyzed geophysical logs collected by the Integrated

¹Kochi Institute for Core Sample Research, Japan Agency for Marine-Earth Science and Technology (JAMSTEC), Nankoku, Japan. ²Geology Course, Graduate School of Arts and Sciences, Kochi University, Kochi, Japan. ³Key Laboratory of Tectonics and Petroleum Resources of Ministry of Education, China University of Geosciences, Wuhan, China. ⁴Centre Européen de Recherche et d'Enseignement des Géosciences de l'Environnement (CEREGE), Europôle Méditerranéen de l'Arbois, Aix en Provence, France. ⁵Earth and Planetary Sciences Department, University of California, Santa Cruz, CA, USA. ⁶Center for Tectonophysics, Department of Geology and Geophysics, Texas A&M University, College Station, TX, USA. ⁷Institute for Research on Earth Evolution, JAMSTEC, Yokohama, Japan. ⁸Disaster Prevention Research Institute, Kyoto University, Uji, Japan. ⁹Department of Geology, University of Leicester, Leicester, UK. ¹⁰Center for Deep Earth Exploration, JAMSTEC, Yokohama, Japan.

*To whom correspondence should be addressed. E-mail: lin@jamstec.go.jp

†Present address: EA4098 LaRGE, Université des Antilles et de la Guyane, Pointe-à-Pitre, France.

‡All authors with their affiliations appear at the end of this paper.

Ocean Drilling Program (IODP) Expedition 343 (13, 14), Japan Trench Fast Drilling Project (JFAST), at site C0019 (Fig. 1, A and B), located ~93 km seaward from the epicenter of the mainshock and ~6 km landward of the trench axis. At this location, three boreholes successfully penetrated the interface between the subducting Pacific Plate and the overriding North American Plate. The boreholes enabled geophysical logging, core sampling, and long-term temperature monitoring (15).

The JFAST borehole C0019B reached ~850 m below sea floor (mbsf) in a water depth of 6890 m and was used mainly to collect geophysical logging data. From borehole wall resistivity images, we observed clear borehole breakouts (16) in the depth range of ~44 to 813 mbsf (Fig. 2C). These drilling-induced compressive failures are reliable indicators of the orientations of current maximum and minimum horizontal stresses (S_{Hmax} and S_{Hmin} , respectively) and can be used to constrain stress magnitudes (17). C0019B penetrated through the plate-interface fault around 820 mbsf, the probable principal slip zone of the 2011 earthquake;

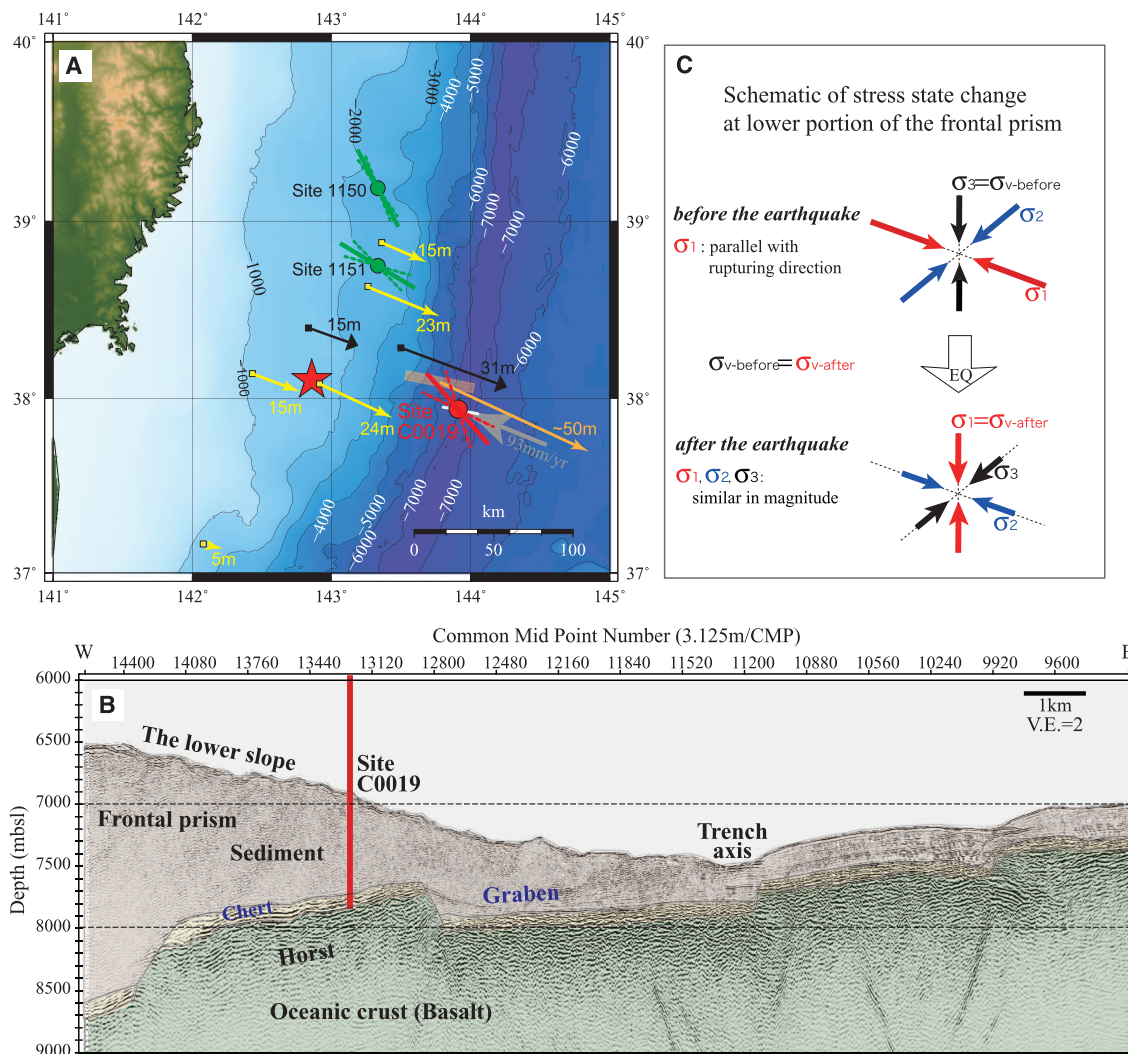
no breakouts are observed below the fault (15). Above the plate interface, a Pleistocene accretionary prism consists of hemipelagic deposits lacking resolvable structural features on seismic reflection data (Fig. 1B) (18–20). The frontal plate interface, beneath the accretionary prism, marks the transition to dominantly pelagic deposits.

The S_{Hmax} azimuth and its variability differ markedly in the shallow and deep parts of the borehole (Fig. 2C). At shallow depths of ~44 to 197 mbsf within slope facies [unit I, derived mean porosity from logging-while-drilling resistivity and its standard deviation (SD) of $\sim 62 \pm 6\%$ (15)], the S_{Hmax} varies from approximately parallel to the convergence direction to perpendicular (~100 mbsf) and back toward parallel again (~140 mbsf) (Fig. 2C). This suggests the presence of a discontinuity such as a fault, which is supported by changes in bedding dips and conductive peaks in the resistivity log (Fig. 2B). In the upper half of the wedge sediments from 197 to 537 mbsf [unit IIa, porosity of $\sim 51 \pm 3\%$ (15)], the S_{Hmax} azimuth is highly variable. Such diverse

breakout orientations have not previously been recognized at subduction and thrust-fault zones such as the Nankai Trough (21–24), the Japan Trench margin before the 2011 earthquake (25), Costa Rica (26), and the Taiwan Chelungpu Fault (27, 28). Our observations suggest that S_{Hmax} and S_{Hmin} are close in magnitude, so that localized stress perturbations such as faults or topographic effects can be responsible for the scattered distribution. Correlation of the depth intervals, defined on the basis of S_{Hmax} azimuth distributions, and of the logging units, primarily defined by natural gamma-ray intensity, suggests some possible lithological influence on S_{Hmax} distributions (Fig. 2).

At the greater depths of ~537 to 813 mbsf [unit IIb, porosity of $\sim 45 \pm 3\%$ (15)] within the accretionary prism and above the plate boundary, the S_{Hmax} azimuth has a clear preferred orientation in a northwest-to-southeast direction ($319 \pm 23^\circ$) (Fig. 2C). This stress orientation is consistent with the plate convergence direction of 292° (29) and also roughly consistent with stress orientations determined at sites 1150 and 1151 (drilled

Fig. 1. (A) Location of JFAST site C0019 and S_{Hmax} orientation in the deep part of the borehole. Red solid and dashed lines show the mean S_{Hmax} orientation and 1 SD, respectively. Green circles and lines show Ocean Drilling Program sites drilled in 1999 and their S_{Hmax} orientations before the 2011 earthquake (25). The red star denotes the epicenter of the 2011 earthquake mainshock. Yellow (31), black (32), and orange arrows (1) indicate coseismic horizontal displacements of sea floor, and the orange rectangle denotes the bathymetric survey area. The gray arrow shows relative plate motion (29). The white line around site C0019 shows the location of (B). **(B)** Interpreted seismic line crossing site C0019. The red vertical line shows the location and approximate drilled depth range. The subducting Pacific plate dips gently $\sim 5^\circ$; the landward lower trench slope dips $\sim 7^\circ$. CMP, common midpoint; mbsf, meters below sea level; V.E., vertical exaggeration. **(C)** Schematic of inferred coseismic three-dimensional stress state change in the lower portion of the frontal prism. σ_1 , σ_2 , σ_3 , and σ_v are the maximum, intermediate, minimum, and vertical stresses, respectively.



in 1999 before the 2011 earthquake) (Fig. 1A) (25). In a similar study of the Chelungpu fault that ruptured during the 1999 Chichi, Taiwan earthquake (M_w 7.6, thrust focal mechanism), two boreholes that penetrated the fault were drilled about 5 years after the earthquake. Observations of borehole breakouts after this incident indicate that the S_{Hmax} azimuth orientation changed by 90° in the vicinity of the fault (27, 28). Although a similar change in stress directions was not observed across the plate interface at ~ 820 mbsf in the JFAST hole, the analysis described below shows a large change in the stress state before and after the earthquake. The absence of breakouts below ~ 820 mbsf may be indicative of a change in stress state across the plate interface (Fig. 2).

The magnitudes of S_{Hmax} and S_{Hmin} are constrained from observed widths of breakouts (WOBs) and measured unconfined compressive strengths (UCSs) for two depth intervals around 720 and 812 mbsf, where both the WOBs and UCSs could be measured (16). We assume Andersonian stress states and a vertical stress S_V calculated from a sediment density profile derived from the logging data (15): The values of S_V , S_{Hmax} , and S_{Hmin} at 720 mbsf are approximately the maximum, intermediate, and minimum principal stresses (σ_1 , σ_2 , and σ_3), respectively. At 812 mbsf, however, there is some uncertainty if S_{Hmax} is necessarily less than S_V ; the constrained stress state is

close to the boundary of the normal faulting and strike-slip faulting regimes. Overall, these results indicate that the postearthquake stress states in the frontal prism are either in or close to the normal faulting stress regime (Fig. 2E).

Assuming that S_V , S_{Hmax} , and S_{Hmin} are the three principal stresses, the current shear stress on a plane at 812 mbsf parallel with the plate interface at ~ 820 mbsf (for thrust motion in the convergence direction) can be calculated from S_V , S_{Hmax} , and the dip of the interface ($\sim 5^\circ$). Using the greatest estimated value of S_{Hmax} (87 MPa), the shear stress on the plane at 812 mbsf after the earthquake is very small, less than ~ 0.3 MPa; the shear stress on the nearby plate interface can be inferred to be similar. In addition, we infer that decreases of S_{Hmax} , S_{Hmin} , and the mean stress of three principal stresses above the ~ 820 -mbsf plate interface are around 2, 1, and 1 MPa, respectively, on the basis of Andersonian stress states before and after the earthquake, coseismic slip distribution near the trench, and elastic elongation of the frontal prism during the earthquake (16).

Unconfined compressive strengths of rocks in the range of ~ 800 to 820 mbsf (the bottom of unit IIb) are higher than those in the 821- to 836-mbsf range (unit III, sheared brown claystone) (16). Thus, the presence of breakouts in the stronger interval above the interface (and not in the weaker interval below the interface) is noteworthy. In

general, for horizontal stresses of similar magnitude, breakouts occur more easily or are wider in weaker rock. Therefore, we believe that the horizontal stress (especially S_{Hmax}) just below the interface (unit III) is lower than that above the interface (the bottom of unit IIb). Namely, the magnitude of horizontal stress appears to abruptly change across the 820-mbsf fault.

The frontal portion of the accretionary wedge is considered to have been under trench-normal compression before the earthquake, on the basis of the orientations of minor faults and bedding observed in the logging data and in core samples. The faults and bedding are variable in dip magnitude, but faults at depths greater than ~ 690 mbsf display predominantly reverse shear sense. Bedding at all depths in the prism shows a preferred northeast strike direction reflecting horizontal contraction and local extension at shallower depths, approximately parallel to the plate convergence direction (15). These observations show that the overall structure in the hanging wall of the frontal interface is characterized as folding and thrusting. Also, a comparison of seismic reflection data before and after the Tohoku-Oki earthquake, from just 15 km north of the JFAST drill site (the orange rectangle in Fig. 1A), reveals that deformation at the trench axis formed as a result of compression during coseismic slip on the shallow plate interface (6). Therefore, we conclude that the stress state in the frontal prism has changed from a thrust faulting regime before the earthquake to the present normal faulting, or near-normal faulting regime. The present S_{Hmax} is approximately parallel to the plate convergence direction and is inferred to have changed from the maximum to intermediate principal stress (Fig. 1C) due to the nearly complete shear-stress drop. Most earthquakes are thought to have partial stress drops, but the results of this study and other indirect measurements or modeling (2, 7, 8, 30) suggest that the change in the stress state associated with the very large slip in this region is an indication of coseismic fault weakening and a nearly total stress drop for the Tohoku-Oki earthquake. This finding is consistent with increased coseismic displacement of the sea floor toward the trench axis, as observed in changes of bathymetric data and rupture models obtained from the inversion of seismic, geodetic, and tsunami data (Fig. 1A) (1, 3, 5, 31–33).

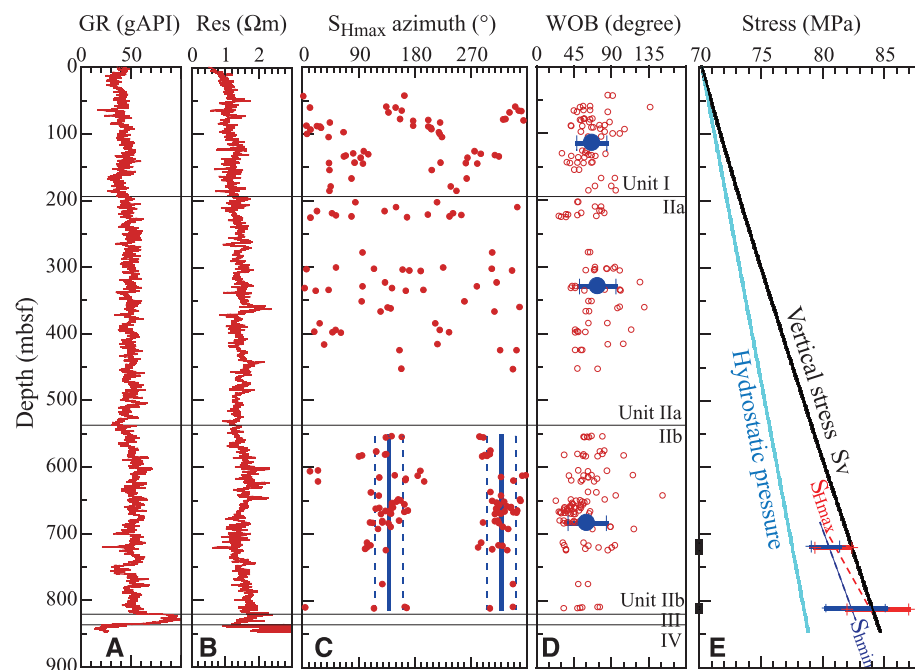


Fig. 2. (A) Natural gamma-ray (GR) intensity (gAPI, a standard gamma-ray unit calibrated at the American Petroleum Institute) and (B) resistivity (Res). (C) S_{Hmax} azimuth determined from breakouts (red dots). Blue solid and dashed lines show the mean and SD, respectively, of S_{Hmax} azimuth in the deep part of the borehole (mean \pm SD: $139 \pm 23^\circ$ or $319 \pm 23^\circ$). (D) Widths of breakouts (WOB) (red circles) and their mean and SD in various units (blue solid circles and bars). Horizontal lines through (A) to (D) show the boundaries of the lithological units primarily defined by natural gamma-ray intensity (15). (E) Hydrostatic pressure and stress magnitudes [S_V (black) was calculated from density; S_{Hmax} (red) and S_{Hmin} (blue) were constrained from breakout widths and rock strengths]. Thick black bars on the y axis show the depth range from where breakout data and UCSs constrained stress magnitude.

References and Notes

1. T. Fujiwara *et al.*, *Science* **334**, 1240 (2011).
2. S. Ide, A. Baltay, G. C. Beroza, *Science* **332**, 1426 (2011).
3. Y. Fujii, K. Satake, S. Sakai, M. Shinohara, T. Kanazawa, *Earth Planets Space* **63**, 815 (2011).
4. Y. Ito *et al.*, *Geophys. Res. Lett.* **38**, L00G05 (2011).
5. T. Lay, C. J. Ammon, H. Kanamori, L. Xue, M. J. Kim, *Earth Planets Space* **63**, 687 (2011).
6. S. Kodaira *et al.*, *Nat. Geosci.* **5**, 646 (2012).
7. A. Hasegawa, K. Yoshida, T. Okada, *Earth Planets Space* **63**, 703 (2011).
8. A. Hasegawa *et al.*, *Earth Planet. Sci. Lett.* **355–356**, 231 (2012).
9. A. Kato, S. Sakai, K. Obara, *Earth Planets Space* **63**, 745 (2011).
10. K. Imanishi, R. Ando, Y. Kuwahara, *Geophys. Res. Lett.* **39**, L09306 (2012).

11. K. Yoshida *et al.*, *Geophys. Res. Lett.* **39**, L03302 (2012).
12. K. Obana *et al.*, *Geophys. Res. Lett.* **39**, L00G24 (2012).
13. N. Jones, *Nature* **479**, 16 (2011).
14. J. J. Mori, F. M. Chester, N. Eguchi, S. Toczko, Japan Trench Fast Earthquake Drilling Project (JFAST). *IODP Sci. Prosp.* **343** (2012); 10.2204/iodp.sp.343.2012
15. F. M. Chester, J. J. Mori, S. Toczko, N. Eguchi, the Expedition 343/343T Scientists, Japan Trench Fast Drilling Project (JFAST). *IODP Prel. Rept.* **343/343T** (2012); 10.2204/iodp.pr.343343T.2012
16. Material and methods are available as supplementary materials on Science Online.
17. M. D. Zoback, *Reservoir Geomechanics* (Cambridge Univ. Press, New York, 2007).
18. R. von Huene, D. Klaeschen, B. Cropp, J. Miller, *J. Geophys. Res.* **99**, 22349 (1994).
19. G. Kimura *et al.*, *Earth Planet. Sci. Lett.* **339–340**, 32 (2012).
20. T. Tsuru *et al.*, *J. Geophys. Res.* **107**, 2357 (2002).
21. L. C. McNeill *et al.*, *Geophys. Res. Lett.* **31**, L02602 (2004).
22. M. Ienaga *et al.*, *Tectonophysics* **426**, 207 (2006).
23. C. Chang *et al.*, *Geochem. Geophys. Geosyst.* **11**, Q0AD04 (2010).
24. W. Lin *et al.*, *Geophys. Res. Lett.* **37**, L13303 (2010).
25. W. Lin *et al.*, *Geophys. Res. Lett.* **38**, L00G10 (2011).
26. P. Vannucchi, K. Ujiie, N. Stronck, A. Malinverso, the Expedition 334 Scientists, *Proceedings of the Integrated Ocean Drilling Program* (IODP, Tokyo, 2012), vol. 334; 10.2204/iodp.proc.334.103.2012
27. H.-Y. Wu *et al.*, *Geophys. Res. Lett.* **34**, L01303 (2007).
28. W. Lin *et al.*, *Geophys. Res. Lett.* **34**, L16307 (2007).
29. D. F. Argus, R. G. Gordon, C. DeMets, *Geochem. Geophys. Geosyst.* **12**, Q11001 (2011).
30. M. Conin, P. Henry, V. Godard, S. Bourlange, *Earth Planet. Sci. Lett.* **341–344**, 170 (2012).
31. M. Sato *et al.*, *Science* **332**, 1395 (2011).
32. M. Kido, Y. Osada, H. Fujimoto, R. Hino, Y. Ito, *Geophys. Res. Lett.* **38**, L24303 (2011).
33. K. Koketsu *et al.*, *Earth Planet. Sci. Lett.* **310**, 480 (2011).

Acknowledgments: For our research, we used data provided by IODP. The data will be distributed by IODP (www.iodp.org/access-data-and-samples). We thank all drilling and logging operation staff on board the D/V *Chikyu* during expedition 343. We gratefully acknowledge two anonymous reviewers for their constructive comments, which helped us to greatly improve this manuscript. Part of this work was supported by grant KAKENHI 22403008 (Japan Society for the Promotion of Science), grant 21107006 (Ministry of Education, Culture, Sports, Science and Technology of Japan), and the U.S. Science Support Program of IODP.

Expedition 343 Scientists

Becky Cook,¹ Tamara Jeppson,² Monica Wolfson-Schwehr,³ Yoshinori Sanada,⁴ Saneatsu Saito,⁴ Yukari Kido,⁴ Takehiro Hirose,⁴ Jan H. Behrmann,⁵ Matt Ikari,⁶ Kohtaro Ujiie,⁷ Christie Rowe,⁸ James Kirkpatrick,^{9a} Santanu Bose,¹⁰ Christine Regalla,¹¹ Francesca Remitti,¹² Virginia Toy,¹³ Patrick Fulton,¹⁴ Toshiaki Mishima,¹⁵ Tao Yang,¹⁶ Tianhaoze Sun,¹⁷ Tsuyoshi Ishikawa,⁴ James Sample,¹⁸ Ken Takai,⁴ Jun Kameda,¹⁹ Sean Toczko,⁴ Lena Maeda,⁴ Shuichi Kodaira,⁴ Ryota Hino,²⁰ Demian Saffer¹¹

¹University of Southampton, Southampton, UK. ²University of Wisconsin-Madison, Madison, WI, USA. ³University of New Hampshire, Durham, NH, USA. ⁴JAMSTEC, Yokosuka, Japan. ⁵GEOMAR, Kiel, Germany. ⁶University of Bremen, Bremen, Germany. ⁷University of Tsukuba, Tsukuba, Japan. ⁸McGill University, Montreal, Quebec, Canada. ⁹University of California, Santa Cruz, CA, USA. ¹⁰University of Calcutta, Calcutta, India. ¹¹The Pennsylvania State University, University Park, PA, USA. ¹²Università di Modena e Reggio Emilia, Modena, Italy. ¹³University of Otago, Dunedin, New Zealand. ¹⁴University of Texas, Austin, TX, USA. ¹⁵Osaka City University, Osaka, Japan. ¹⁶Institute of Geophysics, China Earthquake Administration, Beijing, China. ¹⁷University of Victoria, Victoria, British Columbia, Canada. ¹⁸Northern Arizona University, Flagstaff, AZ, USA. ¹⁹University of Tokyo, Tokyo, Japan. ²⁰Tohoku University, Sendai, Japan.

*Present address: Colorado State University, Fort Collins, CO, USA.

†Present address: University of California, Santa Cruz, CA, USA.

Supplementary Materials

www.sciencemag.org/cgi/content/full/339/6120/687/DC1

Materials and Methods

Supplementary Text

Figs. S1 to S5

Table S1

Reference (34)

27 August 2012; accepted 30 November 2012

10.1126/science.1229379

Paramyxovirus V Proteins Disrupt the Fold of the RNA Sensor MDA5 to Inhibit Antiviral Signaling

Carina Motz,¹ Kerstin Monika Schuhmann,² Axel Kirchhofer,^{1*} Manuela Moldt,¹ Gregor Witte,¹ Karl-Klaus Conzelmann,² Karl-Peter Hopfner^{1,3,†}

The retinoic acid–inducible gene I (RIG-I)–like receptor (RLR) melanoma differentiation–associated protein 5 (MDA5) senses cytoplasmic viral RNA and activates antiviral innate immunity. To reveal how paramyxoviruses counteract this response, we determined the crystal structure of the MDA5 adenosine 5′-triphosphate (ATP)–hydrolysis domain in complex with the viral inhibitor V protein. The V protein unfolded the ATP–hydrolysis domain of MDA5 via a β -hairpin motif and recognized a structural motif of MDA5 that is normally buried in the conserved helicase fold. This leads to disruption of the MDA5 ATP–hydrolysis site and prevention of RNA-bound MDA5 filament formation. The structure explains why V proteins inactivate MDA5, but not RIG-I, and mutating only two amino acids in RIG-I induces robust V protein binding. Our results suggest an inhibition mechanism of RLR signalosome formation by unfolding of receptor and inhibitor.

RIG-I–like receptors (RLRs) play a central role in the recognition of viral nucleic acids by the innate immune system (1–3). RLRs comprise the three family members retinoic acid–inducible gene I (RIG-I), melanoma differentiation–associated protein 5 (MDA5), and

laboratory of genetics and physiology 2 (LGP2). RIG-I and MDA5 differentially sense a broad range of viruses (4), and their domain structure consists of N-terminal tandem caspase activation and recruitment domains (CARDs), a superfamily 2 (SF2) adenosine triphosphatase (ATPase), and a C-terminal RNA binding domain (RD). LGP2 lacks CARDs, and its functions remain unclear (5, 6). RIG-I is activated by pathogen-associated nucleic acid patterns such as 5′-triphosphate-containing and double-stranded RNA, whereas MDA5 responds to longer or more complex double-stranded RNA (dsRNA) networks (7–12). RNA sensing unmasks the CARDs in RIG-I (2, 13–15), leading to downstream signaling in a process that involves K63 ubiquitin

chains and polymerization of the mitochondrial antiviral-signaling protein MAVS (16–18).

Viruses have evolved diverse means to evade innate immune signaling and the antiviral interferon response (19). Paramyxoviruses (e.g., measles, parainfluenza, Sendai and Nipah viruses) synthesize V proteins, which enhance pathogenicity and limit interferon production by targeting MDA5 and LGP2, but not RIG-I (20–22). V proteins share the N-terminal domain (NTD) with viral P proteins but contain a distinct, highly conserved C-terminal domain (CTD). The CTD binds the SF2 domain of MDA5 and is necessary and sufficient for inhibiting ATPase activity and cellular aggregation of MDA5 (20–23).

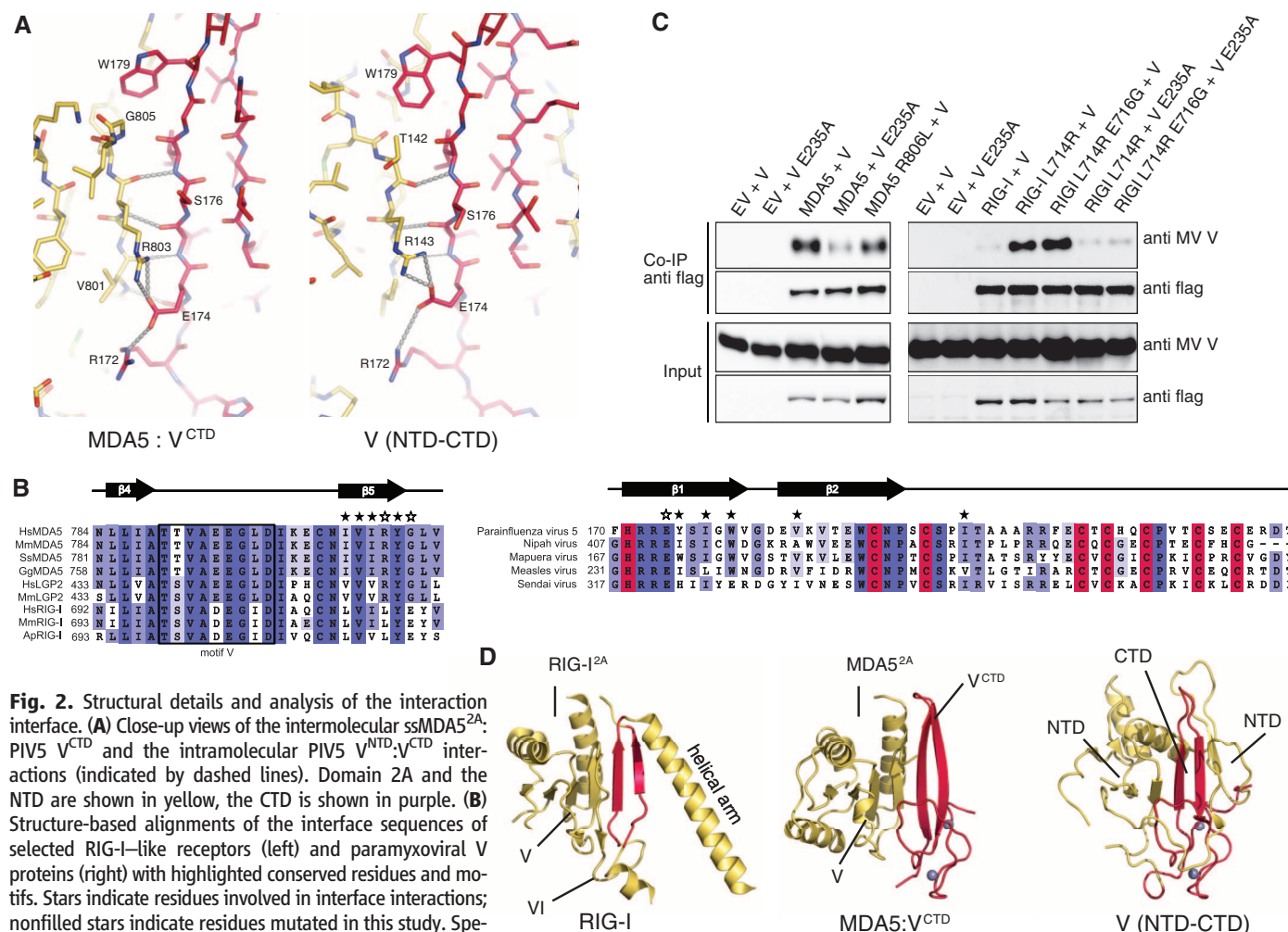
To understand a structural mechanism by which a viral inhibitor targets an RLR signaling component, we crystallized and determined the 2.3 Å resolution crystal structure of a complex between parainfluenza virus 5 (PIV5) V protein and the SF2 domain of porcine MDA5 (*Sus scrofa* ssMDA5) (Fig. 1, fig. S1, and table S1). We obtained crystals of a copurified complex of ssMDA5 SF2 (residues 546 to 808) and PIV5 V protein (residues 168 to 219) only after adding trace amounts of trypsin. This treatment cleaved away several flexible parts due to partial unfolding (see below) that had hampered crystallization despite extensive trials with different V proteins and MDA5 species and constructs.

Our structure represents the evolutionarily conserved, necessary, and sufficient core of the MDA5:V protein complex (21–24). It comprises domains 2A and 2B of the MDA5 SF2 domain and the PIV5 CTD in a 1:1 complex (Fig. 1 and fig. S1). Of particular importance is domain 2A, which together with 1A (not present in our structure) forms the ATP binding site and together

¹Department of Biochemistry and Gene Center, Ludwig-Maximilians-University, Munich, Germany. ²Max von Pettenkofer-Institute and Gene Center, Ludwig-Maximilians-University, Munich, Germany. ³Center for Integrated Protein Sciences, Munich, Germany.

*Present address: Business Consulting, Bayer Business Services GmbH, Leverkusen, Germany.

†To whom correspondence should be addressed at Gene Center, Feodor-Lynen-Strasse 25, 81377 Munich, Germany. E-mail: hopfner@genzentrum.lmu.de



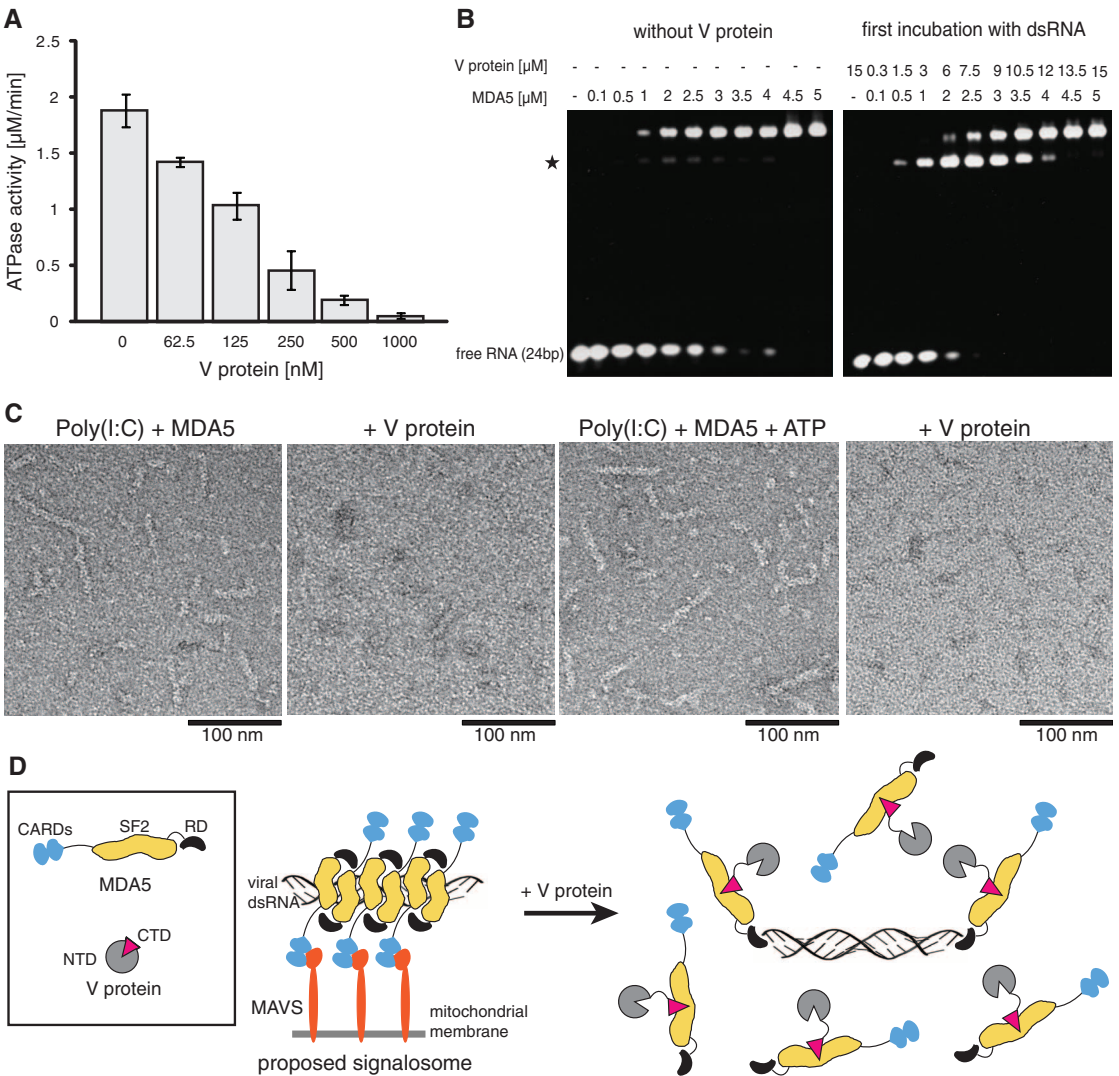
hsMDA5 or hsRIG-I and MV V protein ($n = 3$). EV, empty vector. Left: Mutations affecting the salt-bridge formation between the conserved glutamate of V protein and arginine of MDA5. Right: Mutation of RIG-I to mimic the critical MDA5 arginine. **(D)** Comparison of RIG-I^{2A} (PDB code: 3TBK), MDA5^{2A}:PIV5^{V^{CTD}}, and full-length PIV5 V (PDB code: 2HYE).

with 1A and 2B forms the RNA binding site of RLRs (13–15, 25). MDA5 domain 2A had the “RecA-like fold” typical of ATPases, which harbored a central β sheet with parallel strands in the order $\beta 3$ - $\beta 4$ - $\beta 2$ - $\beta 5$ - $\beta 1$ - $\beta 6$. To our surprise, although strands $\beta 3$ - $\beta 4$ - $\beta 2$ - $\beta 5$ formed the expected sheet, $\beta 1$, $\beta 6$, and the ATPase motif VI between $\beta 5$ and $\beta 6$ were missing, despite being highly conserved in MDA5. Instead, we found the CTD at the expected position of $\beta 1$ and $\beta 6$ (Fig. 1 and fig. S1C). The CTD contained a small core with two zinc ions that stabilize a large protruding β hairpin as well as a flanking, protruding loop. The β hairpin of the CTD formed a continuous β sheet with domain 2A in the order $\beta 3^{\text{MDA5}}$ - $\beta 4^{\text{MDA5}}$ - $\beta 2^{\text{MDA5}}$ - $\beta 5^{\text{MDA5}}$ - $\beta 1^{\text{CTD}}$ - $\beta 2^{\text{CTD}}$, while the loop occupied the usual position of motif VI in SF2 domain-containing enzymes. Thus, our data imply that V protein unfolds the core β sheet of MDA5 and disrupts its ATPase domain by displacing motif VI. We found three particularly noteworthy contacts between the V protein CTD and the SF2

domain of ssMDA5 (Fig. 2A). First, the β sheet formed between $\beta 5^{\text{MDA5}}$ and $\beta 1^{\text{CTD}}$ mediated the central part of the interaction and extended over four residues from MDA5 and four residues from CTD. Second, two contacts at the base and tip of the hairpin provided sequence-specific interactions with MDA5. E174^{PIV5} formed hydrogen bonds and ion-pair interactions with R803^{ssMDA5}, whereas W179^{PIV5} at the tip of the β hairpin inserted like a hook into a cavity between domains 2A and B of MDA5 and stacked to G805^{ssMDA5} at the tip of $\beta 5$. Additional interactions were formed between the loop of V protein and MDA5 and altogether, the CTD bound to domain 2A via a 1154 Å² large and highly complementary interface. Notably, R803^{ssMDA5}, G805^{ssMDA5}, W179^{PIV5}, and E174^{PIV5} were highly conserved among MDA5 and V proteins, respectively (Fig. 2B). Furthermore, LGP2 proteins had arginine and glycine at positions of R803^{ssMDA5} and G805^{ssMDA5}, whereas RIG-I proteins had leucine instead of arginine and glutamate instead of glycine. Hence, RIG-I proteins cannot form the conserved salt bridge to

E174^{PIV5} and sterically hinder W179^{PIV5}. Thus, our structural results explained why V proteins can bind to MDA5 and LGP2 but not to RIG-I (21, 22, 26). To test the importance of the observed interactions and validate the structure, we mutated MDA5 and V protein and tested complex formation by coimmunoprecipitations (co-IPs) of human MDA5 (*Homo sapiens* hMDA5) and measles virus (MV) V protein coexpressed in human embryonic kidney–293T (HEK-293T) cells (Fig. 2C) and by gel filtration of purified murine MDA5 (*Mus musculus* mmMDA5) and PIV5 V protein in vitro (fig. S2A). Mutating R806^{mmMDA5} (equivalent to R803^{ssMDA5}) to leucine (as seen in RIG-I) abolished PIV5 V protein binding in gel filtration and reduced the interaction between hMDA5 and MV V protein in co-IPs. Likewise, mutating E235^{MV} (equivalent to E174^{PIV5}) to alanine strongly reduced binding to hMDA5 in co-IPs. A similar substitution with alanine in E174^{PIV5} also reduced the interaction with mmMDA5 in vitro. These data demonstrated the importance of

Fig. 3. Impact of V protein on the ATPase- and the RNA-binding activity of MDA5. (A) The ATPase activity of hs Δ CARD-MDA5 (100 nM final) in response to MV V protein. Data represent the mean ATPase activity (\pm SEM) determined by analyzing the initial linear slopes of the ATPase reactions ($n = 3$). (B) RNA-binding affinities analyzed by electrophoretic mobility-shift assays of mmMDA5 in the presence and absence of PIV5 V protein ($n = 3$). The accumulation of a faster-migrating species is marked by a star. (C) mmMDA5 filament formation on poly(I:C), visualized by negative-stain EM in the presence and absence of ATP and PIV5 V protein. (D) Proposed model for inhibition of MDA5 signaling assemblies by paramyxoviral V proteins (29, 30). dsRNA-bound MDA5 filaments might interact with MAVS and induce the formation of MAVS fibrils postulated to be active signal entities (17). V proteins disrupt the MDA5-SF2 architecture by a β -strand-replacement mechanism accompanied by double-unfolding of both V protein and MDA5, resulting in disruption of MDA5:dsRNA filaments and hence of signal transmission of the antiviral response. The structure and interactions of the NTD in the MDA5 complex are only illustrated here and need to be addressed in future studies.



both sides of the salt bridge and validated the interaction with proteins of four different species. Previous mutational analysis conducted on the basis of sequence conservation is also fully compatible with the crystal structure and highlighted the importance of residues in $\beta 1^{CTD}$ in inactivating MDA5 in living cells (24, 27). Finally, mutating the conserved salt bridge in the MDA5:V protein interface reduced the ability of MV V protein to inhibit activation of the interferon- β promoter via hsMDA5 signaling in living cells (fig. S3).

The sequence and structural similarity to RIG-I (Fig. 2B and fig. S1C) suggested that R803, $\beta 1$, and $\beta 6$ of MDA5 domain 2A were mostly buried between motif VI and the helical arm that connects domains 2A and 1A in RIG-I (Fig. 2D). To further validate the importance of R803, we mutated the equivalent residue L714^{hsRIG-I} (or the equivalent L715^{mmRIG-I}) to arginine and analyzed the interaction of the mutated RIG-I with MV or PIV5 V protein (Fig. 2C and fig. S2B). We also analyzed the double mutants L714R,E716G^{hsRIG-I} (or L715R,E717G^{mmRIG-I}) to account for the likely clash between W179^{PIV5} and the glutamate that RIG-I has instead of the glycine found in MDA5. A single L714^{hsRIG-I}→R mutation induced binding of V protein to hsRIG-I in co-IPs (Fig. 2C). Introduction of a second mutation in mmRIG-I (L715R,E717G^{mmRIG-I}) led to interaction with PIV5 V protein that was stable in gel filtration (fig. S2B), and L714R,E716G^{hsRIG-I} was as efficiently coimmunoprecipitated with MV V protein as MDA5 (Fig. 2C). Thus, we conclude that our model describes the recognition of MDA5 by V proteins sufficiently well that we can engineer robust binding by V proteins into RIG-I by exchanging only two amino acids.

Some V proteins also target host signal transducer and activator of transcription (STAT) proteins to the DDB1-Cul4A ubiquitin ligase complex for proteasomal degradation to disrupt interferon signaling (28). PIV5 V protein bound to DDB1 [Protein Data Bank (PDB) code: 2HYE] is a globular protein with a central β sheet (29) (Fig. 2D). The β hairpin of the CTD in this complex was surrounded by the NTD and did not participate in DDB1 binding (Fig. 2D). Thus, not only was the interaction of V protein with MDA5 fundamentally different from its interaction with DDB1, but V protein also must undergo a large structural change to expose the β hairpin for binding to MDA5 (Fig. 2A). The NTD contains an arginine (R143^{PIV5}) that binds to E174^{PIV5} and structurally “mimics” R803^{ssMDA5} (Fig. 2A). We used R143^{PIV5} to further validate our structural results. If the NTD is only a cocoon before β -hairpin liberation, mutating R143^{PIV5} should not affect complex formation of V protein with MDA5. Consistently, we found that R143A^{PIV5} formed a highly stable complex with mmMDA5 (fig. S2A). These data support a “spring blade” model for V protein. In the absence of MDA5, the β hairpin is bound by the NTD. In the pres-

ence of MDA5, the β hairpin unfolds and disrupts the ATPase domain of MDA5, whereas the NTD might adopt the unfolded conformation seen in P protein (30). In agreement with this, we also observed an increase in the maximum particle size (D_{max}) and intramolecular distances of MDA5 in the presence of the PIV5 V protein in small-angle x-ray scattering experiments. This increase is in good agreement with the structural data, because V protein wedged between domains 1 and 2 of MDA5 and likely increased flexibility between domains 1 and 2 and expanded the MDA5 fold (figs. S4 and S5). Taken together, inhibition of MDA5 by V proteins involves unfolding of both the receptor and the inhibitor.

Consistent with the unfolding mechanism, MDA5 and LGP2 bound by coexpressed V proteins lacked or had reduced ATPase activity (21), and titrating purified MV V protein into a solution containing purified hs Δ CARD-MDA5, poly(I:C), and ATP progressively inactivated MDA5's ATPase activity (Fig. 3A). In addition, we noticed substantial changes in the way MDA5 bound RNA in the presence of PIV5 V protein (Fig. 3B and fig. S6A). In the absence of V protein, mmMDA5 shifted 24-base pair (bp) RNA predominantly to a single species, with a slight amount of a faster-migrating species at low MDA5 concentrations. V protein strongly increased the amount of faster-migrating species at low MDA5 concentrations. A plausible explanation is that V protein prevents cooperative binding of MDA5 to dsRNA (31, 32) by disrupting the SF2 domain architecture, but still allows noncooperative binding of MDA5 via RD (fig. S6B). Consistently, it has been observed that V protein reduces the size of MDA5-containing oligomers in cells (23).

To directly determine whether binding of V protein prevents the cooperative assembly of MDA5 on dsRNA into filaments that are postulated as signaling entities (31, 32), we visualized mmMDA5 and mmMDA5:PIV5 V protein complexes in the presence of poly(I:C) (a synthetic analog of dsRNA) with or without ATP by negative-stain electron microscopy (EM) (Fig. 3C and fig. S7). In the absence of V protein, mmMDA5 robustly formed filaments on poly(I:C), as observed previously (31, 32). Addition of V protein drastically reduced the number of filaments both in the presence and absence of ATP. These data suggest that unfolding of MDA5 by V protein also prevents formation of RNA-bound signaling oligomers (Fig. 3D)—for instance, by disrupting SF2-SF2 or SF2-RD contacts between filament protomers (33).

References and Notes

1. Y. M. Loo, M. Gale Jr., *Immunity* **34**, 680 (2011).
2. M. Yoneyama et al., *Nat. Immunol.* **5**, 730 (2004).
3. H. Kato, K. Takahashi, T. Fujita, *Immunol. Rev.* **243**, 91 (2011).
4. H. Kato et al., *Nature* **441**, 101 (2006).
5. S. Rothenfusser et al., *J. Immunol.* **175**, 5260 (2005).
6. T. Satoh et al., *Proc. Natl. Acad. Sci. U.S.A.* **107**, 1512 (2010).

7. V. Hornung et al., *Science* **314**, 994 (2006).
8. A. Pichlmair et al., *Science* **314**, 997 (2006).
9. A. Pichlmair et al., *J. Virol.* **83**, 10761 (2009).
10. K. Malathi, B. Dong, M. Gale Jr., R. H. Silverman, *Nature* **448**, 816 (2007).
11. C. Lu et al., *Structure* **18**, 1032 (2010).
12. Y. Wang et al., *Nat. Struct. Mol. Biol.* **17**, 781 (2010).
13. E. Kowalinski et al., *Cell* **147**, 423 (2011).
14. D. Luo et al., *Cell* **147**, 409 (2011).
15. F. Jiang et al., *Nature* **479**, 423 (2011).
16. M. U. Gack et al., *Nature* **446**, 916 (2007).
17. F. Hou et al., *Cell* **146**, 448 (2011).
18. X. Jiang et al., *Immunity* **36**, 959 (2012).
19. A. G. Bowie, L. Unterholzner, *Nat. Rev. Immunol.* **8**, 911 (2008).
20. J. Andrejeva et al., *Proc. Natl. Acad. Sci. U.S.A.* **101**, 17264 (2004).
21. J. P. Parisien et al., *J. Virol.* **83**, 7252 (2009).
22. K. Childs et al., *Virology* **359**, 190 (2007).
23. K. S. Childs, J. Andrejeva, R. E. Randall, S. Goodbourn, *J. Virol.* **83**, 1465 (2009).
24. A. Ramachandran, C. M. Horvath, *J. Virol.* **84**, 11152 (2010).
25. F. Civril et al., *EMBO Rep.* **12**, 1127 (2011).
26. K. Childs, R. Randall, S. Goodbourn, *J. Virol.* **86**, 3411 (2012).
27. A. Schaap-Nutt et al., *J. Virol.* **85**, 4007 (2011).
28. J. Andrejeva, E. Poole, D. F. Young, S. Goodbourn, R. E. Randall, *J. Virol.* **76**, 11379 (2002).
29. T. Li, X. Chen, K. C. Garbutt, P. Zhou, N. Zheng, *Cell* **124**, 105 (2006).
30. D. Karlin, S. Longhi, V. Receveur, B. Canard, *Virology* **296**, 251 (2002).
31. A. Peisley et al., *Proc. Natl. Acad. Sci. U.S.A.* **108**, 21010 (2011).
32. I. C. Berke, Y. Modis, *EMBO J.* **31**, 1714 (2012).
33. I. C. Berke, X. Yu, Y. Modis, E. H. Egelman, *Proc. Natl. Acad. Sci. U.S.A.* **109**, 18437 (2012).

Acknowledgments: We thank S. Cui and F. Civril for help in the initial stages of the project and K. Lammens, M. Bennett, and N. Fenn for technical advice. We thank O. Berninghausen, C. Ungewickell, and G. Pfeifer for help with EM. We thank the Max Planck Crystallization Facility (Max Planck Institute Martinsried) for screening of crystallization conditions. We thank T. Fröhlich for mass spectrometry analysis, I. Mathes for N-terminal sequencing data, and C. Basquin for support in static light-scattering analysis. We thank the Swiss Light Source (Villingen, Switzerland), the European Synchrotron Radiation Facility (Grenoble, France), and the European Molecular Biology Laboratory (DESY, Hamburg, Germany) for beamtime and on-site support. The data reported in this paper are tabulated in the main paper and in the supplementary materials. Atomic coordinates and structure factors of the reported crystal structure have been deposited in the Protein Data Bank under accession code 4115. Details and supplementary materials are available on Science Online. The authors declare no conflict of interest. Correspondence and requests for materials should be addressed to K.-P.H. (hopfner@genzentrum.lmu.de). This work is funded by grants from the German Research Council [Deutsche Forschungsgemeinschaft (DFG) GRK1721] to K.-P.H. and G.W., NIH (U19AI083025), the Bavarian government (BioSysNet), and the Excellence Initiative of the German Ministry of Education and Science (Center for Integrated Proteins Science) to K.-P.H. A.K. and K.M.S. were funded by DFG GRK1202.

Supplementary Materials

www.sciencemag.org/cgi/content/full/science.1230949/DC1
Materials and Methods

Figs. S1 to S7

Table S1

References (34–50)

1 October 2012; accepted 18 December 2012

Published online 17 January 2013;

10.1126/science.1230949

Structural Basis for Hijacking of Cellular LxxLL Motifs by Papillomavirus E6 Oncoproteins

Katia Zanier,^{1*} Sebastian Charbonnier,^{1*} Abdellahi Ould M'hamed Ould Sidi,¹ Alastair G. McEwen,² Maria Giovanna Ferrario,² Pierre Poussin-Courmontagne,² Vincent Cura,² Nicole Brimer,³ Khaled Ould Babah,¹ Tina Ansari,³ Isabelle Muller,¹ Roland H. Stote,² Jean Cavarelli,^{2†} Scott Vande Pol,^{3†} Gilles Trave^{1†}

E6 viral oncoproteins are key players in epithelial tumors induced by papillomaviruses in vertebrates, including cervical cancer in humans. E6 proteins target many host proteins by specifically interacting with acidic LxxLL motifs. We solved the crystal structures of bovine (BPV1) and human (HPV16) papillomavirus E6 proteins bound to LxxLL peptides from the focal adhesion protein paxillin and the ubiquitin ligase E6AP, respectively. In both E6 proteins, two zinc domains and a linker helix form a basic-hydrophobic pocket, which captures helical LxxLL motifs in a way compatible with other interaction modes. Mutational inactivation of the LxxLL binding pocket disrupts the oncogenic activities of both E6 proteins. This work reveals the structural basis of both the multifunctionality and the oncogenicity of E6 proteins.

Papillomaviruses (PV) infect the epithelia of vertebrates. More than 200 PV types have been identified (1), among which a subset

is tumorigenic. Cervical cancers are caused by “high-risk” mucosal human PVs (hrm-HPVs), of which HPV16 is the most prevalent and best

studied type (2), whereas some skin cancers have been associated with “high-risk” cutaneous HPVs (3). Bovine papillomavirus 1 (BPV1) also induces tumors in its natural host (cattle) and in horses (4).

PV carcinogenesis is primarily linked to two PV oncoproteins, E6 and E7. Hrm-HPV E6 recruits the ubiquitin ligase E6AP (5) and tumor suppressor p53, leading to ubiquitin-mediated degradation of p53 (6). E6 also interacts with many other cellular proteins related to cancer pathways (7, 8). Mucosal and cutaneous HPV E6 oncoproteins recognize some of their target proteins, including E6AP, interferon regulatory factor-3 (IRF-3) (9), and the notch co-activator MAML1 (8, 10, 11) through

¹Biotechnologie et Signalisation Cellulaire UMR 7242, Ecole Supérieure de Biotechnologie de Strasbourg, Boulevard Sébastien Brant, BP 10413, F-67412 Illkirch, France. ²Institut de Génétique et de Biologie Moléculaire et Cellulaire (IGBMC)/INSERM U964/CNRS UMR 7104/Université de Strasbourg, 1 rue Laurent Fries, BP 10142, F-67404 Illkirch, France. ³Department of Pathology, University of Virginia, Post Office Box 800904, Charlottesville, VA 22908-0904, USA.

*These authors contributed equally to this work.
†To whom correspondence should be addressed. E-mail: gilles.trave@unistra.fr (G.T.); vandepol@virginia.edu (S.V.P.); cava@igbmc.fr (J.C.)

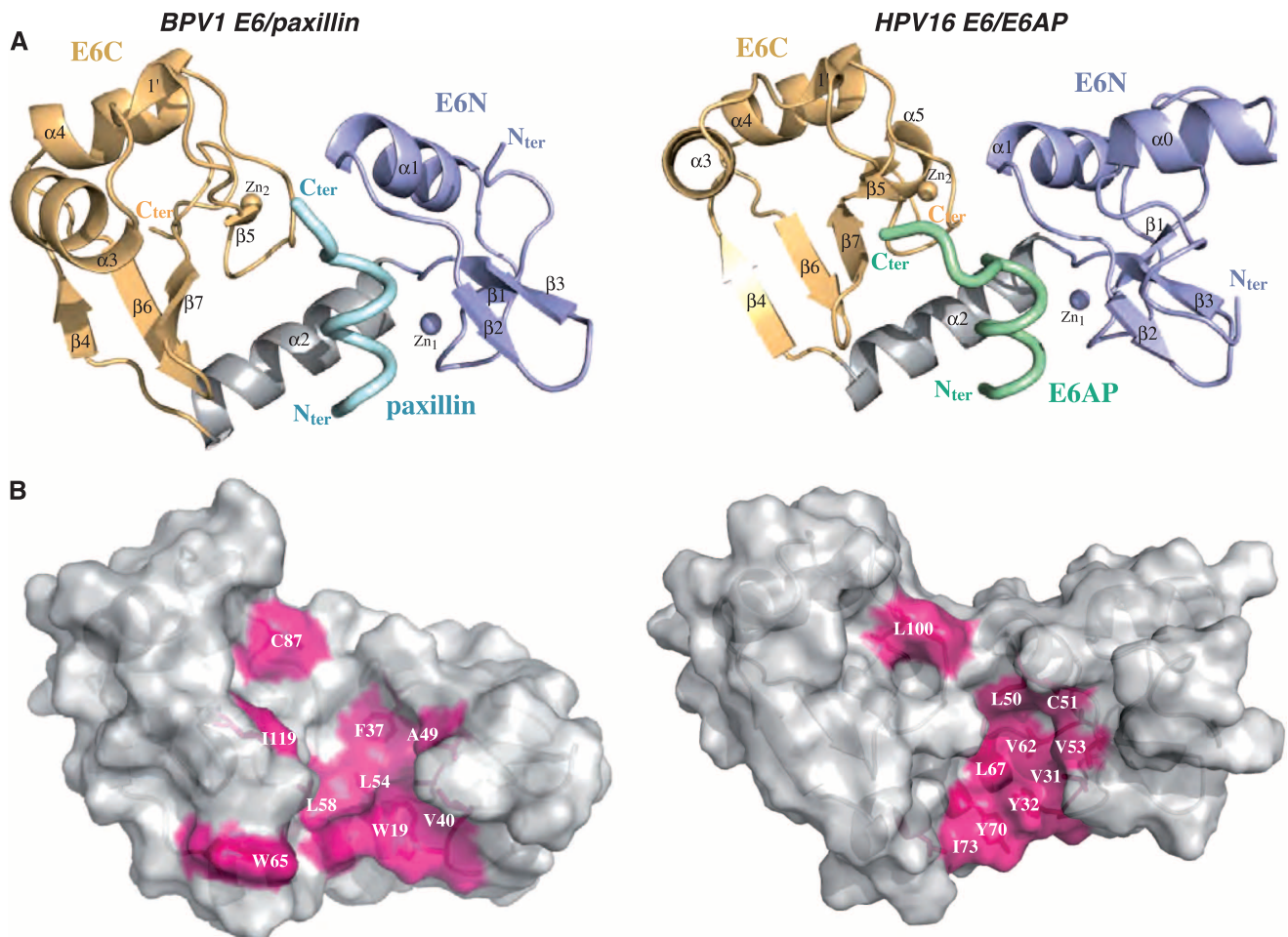


Fig. 1. X-ray structures of E6/LxxLL complexes. **(A)** The structure of BPV1 E6 bound to residues 1 to 10 of paxillin (left) and that of HPV16 E6 bound to residues 403 to 414 of E6AP (right). Blue indicates E6N; gray, linker helix; gold, E6C; and cyan or green, LxxLL peptides. **(B)** The hydrophobic pocket (pink)

responsible for LxxLL motif recognition in BPV1 E6 (left) and HPV16 E6 (right). These structures show helical LxxLL peptides inserted in a deep pocket formed by the two domains, unlike other cellular domains (FAT, CH, and LBD) interacting through shallow surfaces with the cognate LxxLL peptides (fig. S5B).

acidic leucine (L)-rich motifs containing the LxxLL consensus sequence (where x indicates any amino acid) (12, 13). BPV1 E6 recognizes a particular subclass of acidic LxxLL sequences termed LD motifs, which mediate protein-protein interactions regulating cell motility, cell adhesion, and gene expression (14). BPV1 E6 recognizes several LD motifs of the focal adhesion protein paxillin, and this interaction is required for cellular transformation (15–17). Despite their small size (about 150 residues), E6 proteins combine multiple interaction sites. For instance, hrm-HPV E6 interacts not only with LxxLL motifs but also with PDZ domains involved in cell polarity and adhesion (18) and possesses a self-association interface required for the p53 degradation activity (19).

Mammalian PV E6 proteins are cysteine-rich proteins consisting of two zinc-binding domains

named E6N and E6C. Whereas structures of isolated E6N and E6C domains have been determined (19, 20), full-length E6 proteins undergo self-oligomerization (21), which has precluded structural analysis.

To circumvent this problem, we applied two solubilizing strategies to the BPV1 and the HPV16 E6 proteins (22). For BPV1 E6, we fused a crystallization-prone mutant of the bacterial maltose binding protein (MBP) to an E6-binding LxxLL sequence present in the paxillin LD1 motif that is known to solubilize E6 (23) and then to the BPV1 E6 protein (fig. S1A). The resulting MBP-LxxLL-E6 triple fusion protein was purified as a soluble monomer and yielded crystals that diffracted at a resolution better than 2.3 Å (table S1). For HPV16 E6, we purified the monomeric E6 F47R 4C/4S (24) mutant that combines

the F⁴⁷→R⁴⁷ (F47R) mutation disrupting E6N dimerization and four mutations at nonconserved cysteines preventing disulfide-mediated aggregation (19). Purified E6 F47R 4C/4S was mixed with equimolar amounts of an MBP-LxxLL fusion containing the E6-binding LxxLL sequence of E6AP (fig. S1B). The complex yielded crystals that diffracted at a resolution better than 2.6 Å (table S1). Both structures were solved by molecular replacement using the known structure of MBP as a template (Fig. 1 and fig. S2).

The overall structures of the two E6/LxxLL complexes are very similar (fig. S3A) despite low sequence identity (30%), suggesting that crystallization-promoting strategies did not introduce artifacts. Indeed, MBP is differently positioned relative to E6 in the two crystals (fig. S2), and the five solubilizing mutations of E6

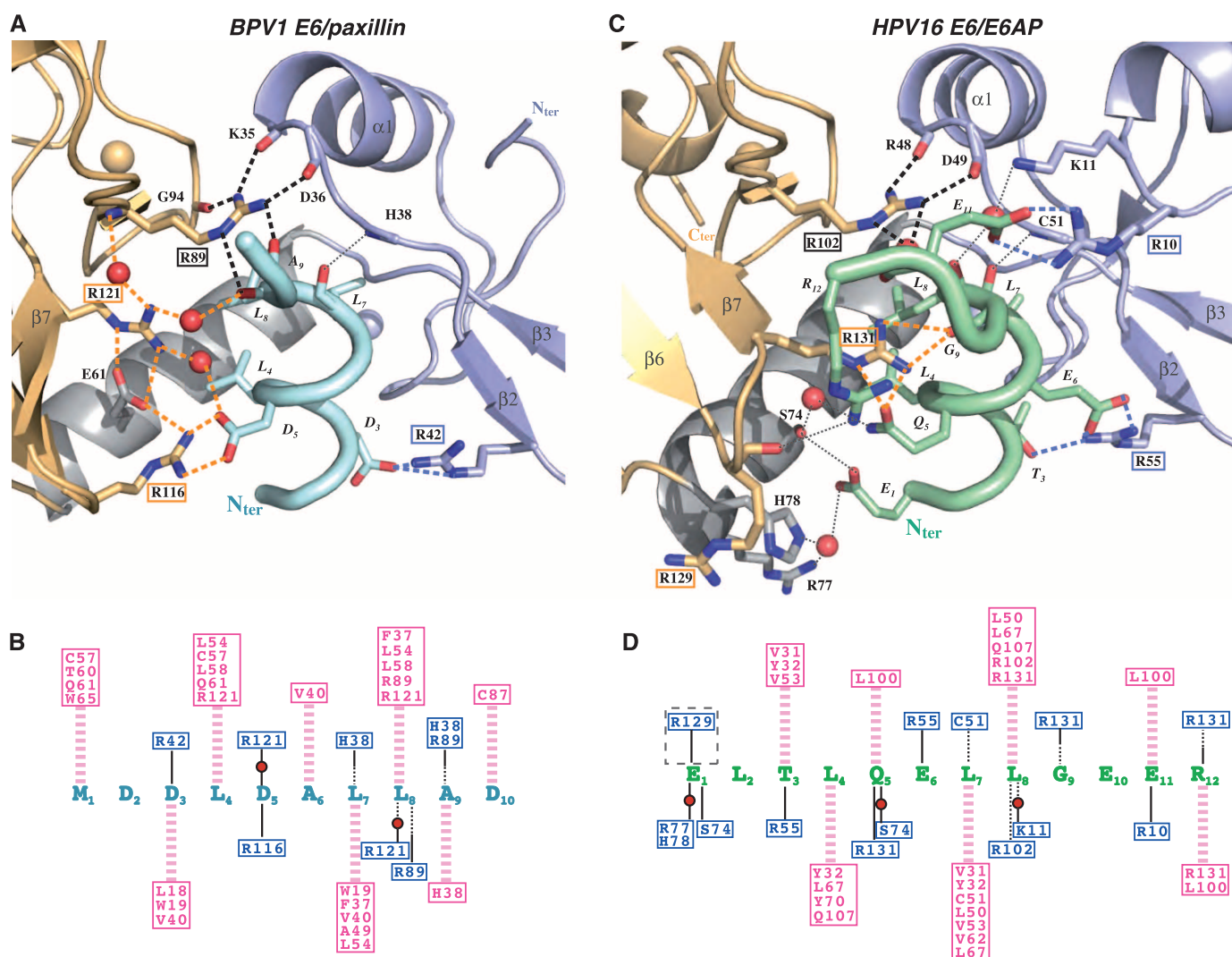


Fig. 2. Networks of E6/LxxLL peptide interactions. (A) Polar interactions between BPV1 E6 and paxillin. Red spheres, water molecules; black dashed lines, interactions mediated by keystone R⁸⁹; blue or orange dashed lines, intermolecular interactions mediated by E6N or E6C arginines, respectively; and dotted lines, other polar interactions. (B) All contacts between BPV1 E6 and paxillin. Pink dashed lines, hydrophobic contacts; black lines, polar contacts mediated by side chain (continuous lines) or main chain (dotted

lines); and pink or blue boxed residues, E6 hydrophobic or polar contributors, respectively. E6 polar residues displaying favorable van der Waals terms (energy change < −1 kcal/mol, fig. S6A) are included as hydrophobic contributors. (C) Polar interactions between HPV16 E6 and E6AP. (D) All contacts between HPV16 E6 and E6AP. R¹²⁹-E¹ (dashed gray line) is revealed by MD simulations (fig. S7). Note that the polar contacts of E6AP E1 are substituted by hydrophobic contacts for paxillin M1 (fig. S7C).

F47R 4C/4S are distal from the E6-peptide interface (fig. S3C). In both LxxLL-bound E6 proteins, the two zinc-binding domains are joined by a linker helix (Fig. 1 and fig. S4). Although the BPV1 and HPV16 E6C domains have a similar fold, the two E6N domains have structurally resolved regions that are essentially superposable but differ in their N-terminal regions (fig. S3B and S4). E6 sequence alignments (fig. S9) show that BPV E6N lacks an N-terminal extension found in HPV E6N. In addition, the first 10 residues of BPV1 E6N are not visible in the electron density map. The E6-bound LxxLL motifs of both paxillin (M¹D²D³L⁴D⁵A⁶L⁷L⁸A⁹D¹⁰) and E6AP (E¹L²T³L⁴Q⁵E⁶L⁷L⁸G⁹E¹⁰E¹¹R¹²) (24) adopt a α -helical conformation from residues one to eight (Figs. 1 and 2). Both motifs are inserted within a deep pocket formed by the two zinc-binding domains and the linker helix of E6 (Fig. 1, A and B). By contrast, previously solved complexes of cellular FAT, CH, and LBD domains bound to LxxLL motifs (25–27) all showed the helical motif interacting with a shallow surface of the domain (fig. S5A).

The three leucine residues (L⁴, L⁷, and L⁸) of the motif are accommodated within a hydrophobic cavity mostly contributed by the E6N domain and linker helix (Figs. 1B and 2, B and D, and fig. S9). Point mutations altering hydrophobic residues of the cavity (i.e., F37S and L58S in BPV1 E6, and L50E in HPV16 E6) decrease both LxxLL peptide binding and E6 transformation (BPV1 E6/paxillin) or p53 degradation (HPV16 E6/E6AP) activities (Fig. 3 and fig. S8A). Surrounding the hydrophobic cavity, a positively charged surface (fig. S5B), favorable to the acidic moieties of the peptide, includes a number of arginine residues that play specific roles in the architecture of the complex. The side chain of a strictly conserved arginine (R⁸⁹ in BPV1 and R¹⁰² in HPV16) holds together, like a keystone, the E6C domain, the E6N domain and the peptide by interacting with L⁸ of the peptide and with main chain atoms at the C termini of both E6N α 1 helix and the peptide's helix (Fig. 2). Adjacent to R⁸⁹ and R¹⁰², BPV1 R¹²¹ and HPV16 R¹³¹ provide structurally equivalent contacts to backbone and side-chain moieties

of the peptide (Fig. 2). Free-energy decomposition analysis (28) coupled to prior molecular dynamics (MD) simulations of the complexes revealed favorable van der Waals terms for BPV1 E6 R⁸⁹ and R¹²¹ and for HPV16 E6 R¹⁰² and R¹³¹ (fig. S6) that are consistent with their multiple interactions at the complex interface. Mutagenesis of all these arginine residues markedly decreased peptide binding and biological activities of the two E6 proteins (Fig. 3 and fig. S8). A number of peripheral E6 arginine side chains selectively clamp acidic and/or polar side chains of the LxxLL peptide (Fig. 2). In BPV1 E6, R⁴² and R¹¹⁶ interact with D³ and D⁵, respectively (Fig. 2A). In HPV16 E6, R⁵⁵ (equivalent to BPV1 R⁴²) interacts with T³ and E⁶. R¹²⁹ (equivalent to BPV1 R¹¹⁶) displays conformational disorder in the crystal (fig. S6A), where it is oriented away from the peptide toward MBP (Fig. 2C and fig. S7A). However, upon MD simulation of the E6/E6AP complex devoid of MBP, the side chain of R¹²⁹ readily reorients to form a direct interaction with residue E₁ of the E6AP peptide (fig. S7, B and C). In HPV16 E6, R¹⁰ at

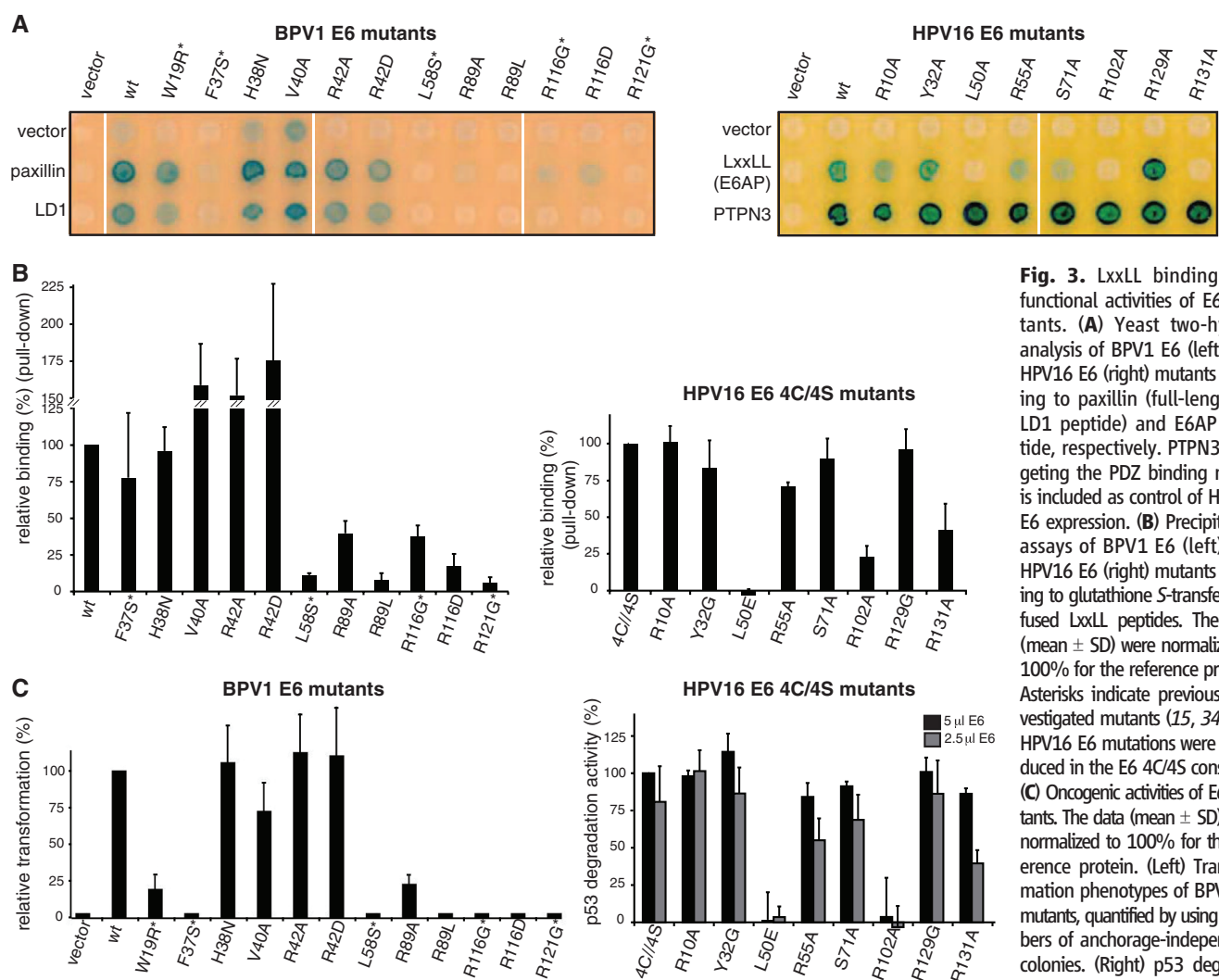


Fig. 3. LxxLL binding and functional activities of E6 mutants. (A) Yeast two-hybrid analysis of BPV1 E6 (left) and HPV16 E6 (right) mutants binding to paxillin (full-length or LD1 peptide) and E6AP peptide, respectively. PTPN3 (targeting the PDZ binding motif) is included as control of HPV16 E6 expression. (B) Precipitation assays of BPV1 E6 (left) and HPV16 E6 (right) mutants binding to glutathione S-transferase-fused LxxLL peptides. The data (mean \pm SD) were normalized to 100% for the reference protein. Asterisks indicate previously investigated mutants (15, 34, 35). HPV16 E6 mutations were introduced in the E6 4C/4S construct. (C) Oncogenic activities of E6 mutants. The data (mean \pm SD) were normalized to 100% for the reference protein. (Left) Transformation phenotypes of BPV1 E6 mutants, quantified by using numbers of anchorage-independent colonies. (Right) p53 degradation activities of HPV16 E6 mutants. See also fig. S8.

the N terminus of E6N forms an additional ion bridge with E¹¹ of the C terminus of the target peptide (Fig. 2, C and D). Alanine mutagenesis of these peripheral arginine residues had little or no influence on peptide binding or the tested biological activities, with the exception of BPV1 R¹¹⁶, whose mutation markedly decreased paxillin binding and cellular transformation (Fig. 3 and fig. S8). Indeed, the side chain of R¹¹⁶ is involved in a network of direct or water-mediated polar interactions at the E6C-peptide interface and in cation- π stacking with the aromatic side chain of W⁶⁵ (Fig. 2A and fig. S7C). This environment appears to strongly stabilize the R¹¹⁶-D⁵ salt bridge, as confirmed by the high electrostatic free-energy term displayed by both R¹¹⁶ and D⁵ (fig. S6A).

A salient difference between the two structures concerns the mode of recognition of the N terminus of the bound peptide, which is exclusively hydrophobic for paxillin and purely electrostatic for E6AP (fig. S6). Indeed, in the BPV1 E6/paxillin complex, M¹ of paxillin interacts with a hydrophobic patch at the C terminus of the linker helix constituted by W⁶⁵ and L⁶⁴ (fig. S7C). In HPV16 E6, E6 residues L⁶⁴ and W⁶⁵ are substituted by basic residues R⁷⁷ and H⁷⁸, which together with R¹²⁹ form a favorable electrostatic environment for the interaction with E¹ of the E6AP peptide (Fig. 2C and fig. S7C).

Many cellular functions are mediated by short linear interaction motifs (SLIMs), whose simple and redundant sequences constitute an Achilles's heel for viral attack (29). Whereas viral

proteins very often contain mimics of cellular SLIMs (29), E6 has an original fold that captures cellular acidic LxxLL motifs. In contrast to cellular proteins, which recruit LxxLL motifs on shallow surfaces of globular helical domains (fig. S5), E6 captures these motifs within a binding pocket composed of three structural modules (Fig. 1). LxxLL-contacting residues are located at equivalent positions in BPV1 and HPV16 E6 sequences, and these positions are generally conserved (fig. S9), suggesting that all mammalian PV E6 proteins contain a LxxLL-binding pocket. Furthermore, BPV1 and HPV16 E6 mutants disrupted for LxxLL-motif binding systematically lost transformation and degradation activities (Fig. 3), indicating that the conserved LxxLL-binding pocket is essential for the tumorigenic phenotype of E6 proteins. This pocket thus represents a promising target for therapeutic drugs.

E6 peptide-contacting residues play distinct roles. Hydrophobic pocket residues, as well as the “keystone” arginines R⁸⁹ and R¹⁰², only establish contacts with the invariable leucine side chains of the motif and/or sequence-independent contacts with the peptide backbone. Other E6 residues function as “readers,” which discriminate variations of the LxxLL motif through sequence-dependent contacts to variable side chains of the peptide. In particular, the nature of residues located at the C terminus of the E6 linker helix or at the N terminus of E6N domain may influence the selection of residues at the N or C terminus of the peptide, respectively. Conversely,

some reader residues may tolerate variations in the position of key acidic residues in the LxxLL motif sequence, because equivalent arginine residues in BPV1 E6 and HPV16 E6 can interact with acidic side chains belonging to different turns of the peptide helix (Fig. 2). Such combinations of discriminative and tolerant reading mechanisms should allow different E6 proteins to capture different panels of host proteins bearing variations of the LxxLL motif.

In the absence of target peptide, E6 is likely to adopt a different overall structure, because the few interactions connecting the E6N, linker helix, and E6C modules (fig. S10) are likely to be insufficient to maintain the E6 architecture observed in the complex structures. The propensity for self-association (21) and the strong affinity for target motifs (23, 30, 31) suggest that most E6 molecules preferentially exist as target-bound complexes in infected cells.

The data suggest that different modes of interaction can coexist in one single molecule of E6. The LxxLL binding region, the PDZ domain-binding motif at the extreme C terminus of E6 (32, 33), and the E6N self-association interface required for p53 degradation (19) do not overlap when they are mapped onto the structure of HPV16 E6 (Fig. 4). Solvent-accessible surfaces not involved in these three interactions represent candidate E6 regions for p53 binding. Structural studies of E6 in complex with multiple partners are now required to decipher the mechanisms of E6 oncogenic activities such as the degradation of host target proteins.

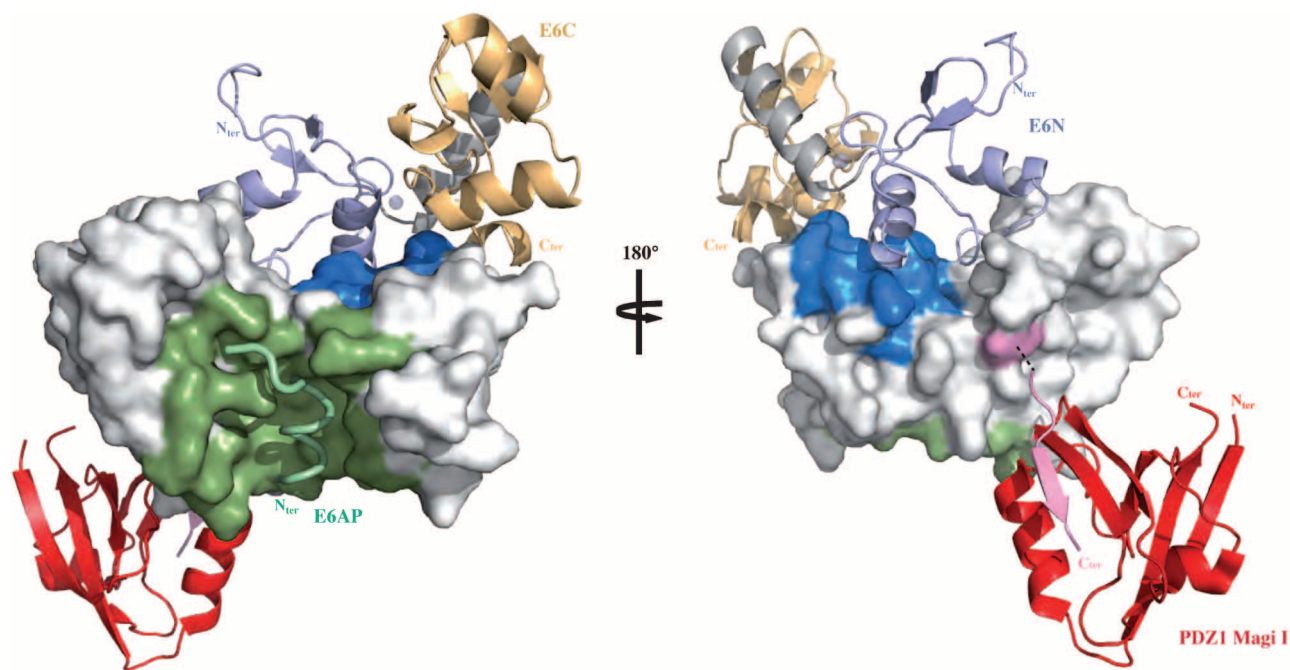


Fig. 4. Mapping HPV16 E6 functional regions. The different binding sites of HPV16 E6 map to distinct regions of the protein's solvent-accessible surface. LxxLL binding and E6 self-association residues are colored green and blue, respectively. The position of the second E6 molecule shown in the ribbon representation was modeled on the basis of the geometry of the E6N homodimer

interface (2LJY.pdb). The C-terminal PDZ binding motif (pink) is disordered in the nuclear magnetic resonance structure of the isolated HPV16 E6C domain and adopts a β -strand conformation upon binding to the PDZ1 of Magi 1 (red) (2KPL.pdb). The relative orientation of E6 and the PDZ domain shown is arbitrary. Surfaces colored white are potentially available for binding to p53. See also fig. S9.

References and Notes

1. H. U. Bernard *et al.*, *Virology* **401**, 70 (2010).
2. H. zur Hausen, *Semin. Cancer Biol.* **9**, 405 (1999).
3. H. Pfister *et al.*, *Arch. Dermatol. Res.* **295**, 273 (2003).
4. L. Nasir, M. S. Campo, *Vet. Dermatol.* **19**, 243 (2008).
5. J. M. Huibregtse, M. Scheffner, P. M. Howley, *EMBO J.* **10**, 4129 (1991).
6. M. Scheffner, B. A. Werness, J. M. Huibregtse, A. J. Levine, P. M. Howley, *Cell* **63**, 1129 (1990).
7. S. S. Tungteakkhun, P. J. Duerksen-Hughes, *Arch. Virol.* **153**, 397 (2008).
8. O. Rozenblatt-Rosen *et al.*, *Nature* **487**, 491 (2012).
9. L. V. Ronco, A. Y. Karpova, M. Vidal, P. M. Howley, *Genes Dev.* **12**, 2061 (1998).
10. N. Brimer, C. Lyons, A. E. Wallberg, S. B. Vande Pol, *Oncogene* **31**, 4639 (2012).
11. M. J. Tan *et al.*, *Proc. Natl. Acad. Sci. U.S.A.* **109**, E1473 (2012).
12. J. M. Huibregtse, M. Scheffner, P. M. Howley, *Mol. Cell Biol.* **13**, 4918 (1993).
13. J. J. Chen, Y. Hong, E. Rustamzadeh, J. D. Baleja, E. J. Androphy, *J. Biol. Chem.* **273**, 13537 (1998).
14. D. A. Tumbarello, M. C. Brown, C. E. Turner, *FEBS Lett.* **513**, 114 (2002).
15. S. B. Vande Pol, M. C. Brown, C. E. Turner, *Oncogene* **16**, 43 (1998).
16. X. Tong, P. M. Howley, *Proc. Natl. Acad. Sci. U.S.A.* **94**, 4412 (1997).
17. R. Wade, N. Brimer, S. Vande Pol, *J. Virol.* **82**, 5962 (2008).
18. M. Thomas *et al.*, *Oncogene* **27**, 7018 (2008).
19. K. Zanier *et al.*, *Structure* **20**, 604 (2012).
20. Y. Nominé *et al.*, *Mol. Cell* **21**, 665 (2006).
21. K. Zanier *et al.*, *J. Mol. Biol.* **396**, 90 (2010).
22. Materials and methods are available as supplementary materials on Science Online.
23. A. O. Sidi *et al.*, *Protein Expr. Purif.* **80**, 8 (2011).
24. Single-letter abbreviations for the amino acid residues are as follows: A, Ala; C, Cys; D, Asp; E, Glu; F, Phe; G, Gly; H, His; I, Ile; K, Lys; L, Leu; M, Met; N, Asn; P, Pro; Q, Gln; R, Arg; S, Ser; T, Thr; V, Val; W, Trp; and Y, Tyr.
25. M. K. Hoellerer *et al.*, *Structure* **11**, 1207 (2003).
26. S. Lorenz *et al.*, *Structure* **16**, 1521 (2008).
27. A. K. Shiao *et al.*, *Cell* **95**, 927 (1998).
28. V. Lafont, M. Schaefer, R. H. Stote, D. Altschuh, A. Dejaegere, *Proteins* **67**, 418 (2007).
29. N. E. Davey, G. Travé, T. J. Gibson, *Trends Biochem. Sci.* **36**, 159 (2011).
30. K. Zanier *et al.*, *J. Mol. Biol.* **349**, 401 (2005).
31. P. Sekaric, J. J. Cherry, E. J. Androphy, *J. Virol.* **82**, 71 (2008).
32. S. Charbonnier *et al.*, *J. Mol. Biol.* **406**, 745 (2011).
33. Y. Zhang *et al.*, *J. Virol.* **81**, 3618 (2007).
34. K. Das, J. Bohl, S. B. Vande Pol, *J. Virol.* **74**, 812 (2000).
35. R. Ned, S. Allen, S. Vande Pol, *J. Virol.* **71**, 4866 (1997).

Acknowledgments: This work was supported by institutional support from CNRS, Université de Strasbourg, INSERM, the European Commission SPINE2-Complexes project (contract no. LSHG-CT-2006-031220) and grants from Association pour la Recherche contre le Cancer (ARC) (no. 3171), Agence Nationale de la Recherche (ANR-MIME-2007 EPI-HPV-3D), and

NIH (grant R01CA134737). S.C. was supported by ANR, A.o.M.o.S. by ARC, and K.o.B. by College Doctoral Européen. S.V.P., N.B., and T.A. were supported by NIH grants (CA120352, CA134737 and CA08093) to S.V.P. and institutional support from the University of Virginia. S.C., K.o.B., and M.G.F. were supported by NIH grant CA134737. MD calculations were performed at the Meso-Centre of the University of Strasbourg. The authors thank members of the European Synchrotron Radiation Facility–European Molecular Biology Laboratory joint Structural Biology groups for the use of beamline facilities and for help during data collection; members of the IGBMC common services for assistance; and B. Kieffer, A. Dejaegere, and all members of the Oncoproteins team for helpful discussions and advice. Coordinates and structure factors have been deposited at the Protein Data Bank with accession codes 3PV7 and 4GIZ. K.Z., S.C., N.B., A.o.M.o.S., T.A., K.o.B., I.M., A.G.McE., P.P.-C., V.C., and S.V.P. performed experiments; M.G.F. and R.H.S. performed computational analysis; and J.C. and A.G.McE. performed structure determination. S.C., K.Z., J.C., S.V.P., and G.T. analyzed the data. G.T., K.Z., S.C., S.V.P., J.C., and R.S. prepared the manuscript. G.T., S.V.P., J.C., and R.S. supervised the work.

Supplementary Materials

www.sciencemag.org/cgi/content/full/339/6120/694/DC1
Materials and Methods
Figs. S1 to S10
Table S1
References (36–57)

10 September 2012; accepted 11 December 2012
10.1126/science.1229934

A Histone Mutant Reproduces the Phenotype Caused by Loss of Histone-Modifying Factor Polycomb

Ana Raquel Pengelly,^{1*} Ömer Copur,^{1*} Herbert Jäckle,² Alf Herzig,^{2†} Jürg Müller^{1†}

Although many metazoan enzymes that add or remove specific modifications on histone proteins are essential transcriptional regulators, the functional significance of posttranslational modifications on histone proteins is not well understood. Here, we show in *Drosophila* that a point mutation in lysine 27 of histone H3 (H3-K27) fails to repress transcription of genes that are normally repressed by Polycomb repressive complex 2 (PRC2), the methyltransferase that modifies H3-K27. Moreover, differentiated H3-K27 mutant cells show homeotic transformations like those seen in PRC2 mutant cells. Taken together, these analyses demonstrate that H3-K27 is the crucial physiological substrate that PRC2 modifies for Polycomb repression.

Posttranslational modifications on histone proteins are thought to be important for regulating gene transcription in eukaryotes (1). In metazoans, this view is mainly based on the fact that many transcriptional regulators that modify histones are essential for organism viability. However, in animals and plants, it is not known whether mutation of a modified histone residue reproduces the phenotype caused by mutation of the modifying enzyme. Moreover, many

of these enzymes modify not only histones but also other proteins, which raises the possibility that some of these may be the physiologically relevant substrates (2). A key transcriptional regulator in animals and plants is Polycomb repressive complex 2 (PRC2), a histone methyltransferase that specifically methylates H3 at lysine 27 (H3-K27) (3–6). PRC2 represses transcription of specific target genes and trimethylates H3-K27 (H3-K27me3) in their chromatin (3–6). To investigate the physiological role of H3-K27 modification, we examined the phenotype of developing *Drosophila* larvae in which wild-type nucleosomes were replaced by H3^{K27R} mutant nucleosomes.

In *Drosophila*, the canonical histone genes are located in a single cluster (*HisC*) that comprises 23 repeats of the histone gene unit (*His-GU*) containing the four canonical core histones and linker histone H1. Animals that are homozygous for

a chromosomal deletion that removes the histone gene cluster ($\Delta HisC$) die at the blastoderm stage, after exhaustion of the supply of maternally deposited histones (7). A transgene cassette providing a total of 12 copies of the wild-type *His-GU* (12 $\times His-GU$) rescues $\Delta HisC$ homozygotes into viable adults (7). To study the phenotype of cells that contain H3^{K27R} instead of wild-type H3, we used an analogous transgene cassette with a H3^{K27R} point mutation (12 $\times His-GU^{H3-K27R}$). $\Delta HisC$ homozygotes that carry the 12 $\times His-GU^{H3-K27R}$ cassette die toward the end of embryogenesis. Their cells contain a mixture of H3 and H3^{K27R} histones, because maternally supplied wild-type H3 incorporated into chromatin before the blastoderm stage is only partially replaced by H3^{K27R} during the few cell divisions that take place before the end of embryogenesis. To analyze cells with a more complete replacement of H3 by H3^{K27R}, we generated clones of $\Delta HisC$ homozygous cells in imaginal discs of $\Delta HisC$ heterozygotes carrying 12 $\times His-GU^{H3-K27R}$ (fig. S1). $\Delta HisC$ homozygous cells stop proliferation in animals lacking a rescue transgene cassette (Fig. 1A) but are rescued into normally proliferating cells in animals carrying the wild-type 12 $\times His-GU$ or the 12 $\times His-GU^{H3-K27R}$ cassette (Fig. 1A). H3-K27me3 is undetectable in clones of H3^{K27R} cells, which suggests that most wild-type H3 has been replaced by H3^{K27R} and that the H3.3 histone variant expressed in those cells is largely absent in PRC2 substrate chromatin (Fig. 1A). We investigated whether repression of PRC2 target genes is affected in H3^{K27R} mutant cells. Like clones lacking *E(z)*, the catalytic subunit of PRC2, H3^{K27R} mutant clones also show misexpression of the Polycomb group target genes *Ultrathorax* (*Ubx*), *Abdominal-B* (*Abd-B*), *Sex combs reduced* (*Scr*), and *engrailed* (*en*) in

¹Chromatin and Chromosome Biology Research Group, Max Planck Institute of Biochemistry, Am Klopferspitz 18, 82152 Martinsried, Germany. ²Department of Molecular Developmental Biology, Max Planck Institute for Biophysical Chemistry, Am Fassberg 11, 37077 Göttingen, Germany.

*These two authors contributed equally to this work.

†To whom correspondence should be addressed. E-mail: muellerj@biochem.mpg.de (J.M.); herzig@mpiib-berlin.mpg.de (A.H.)

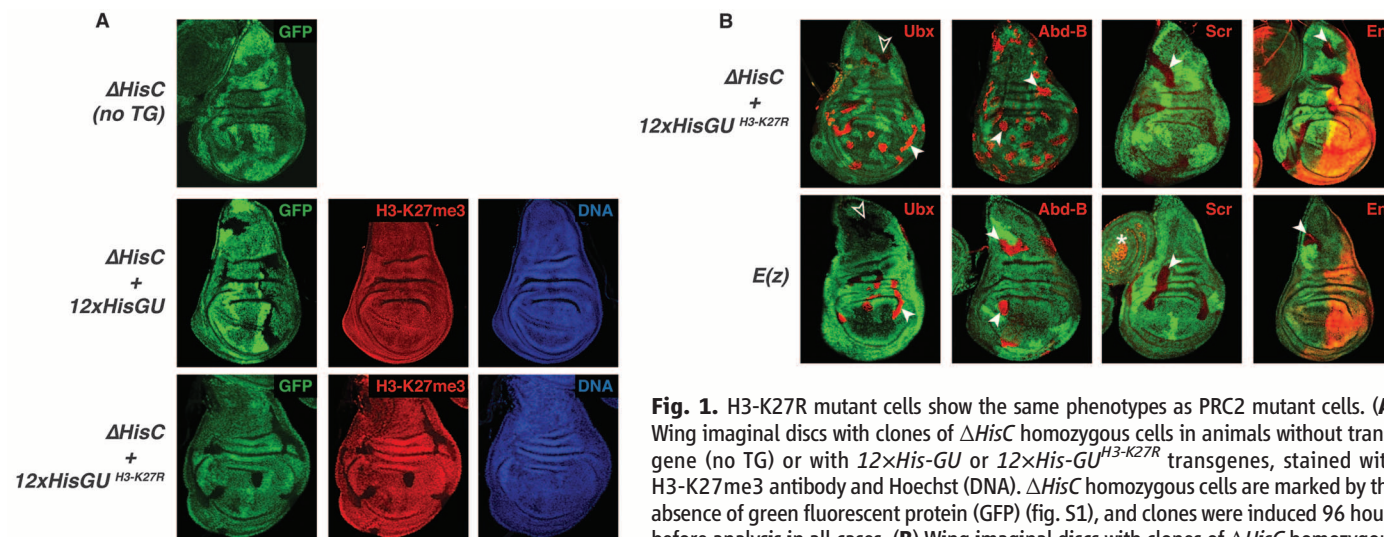
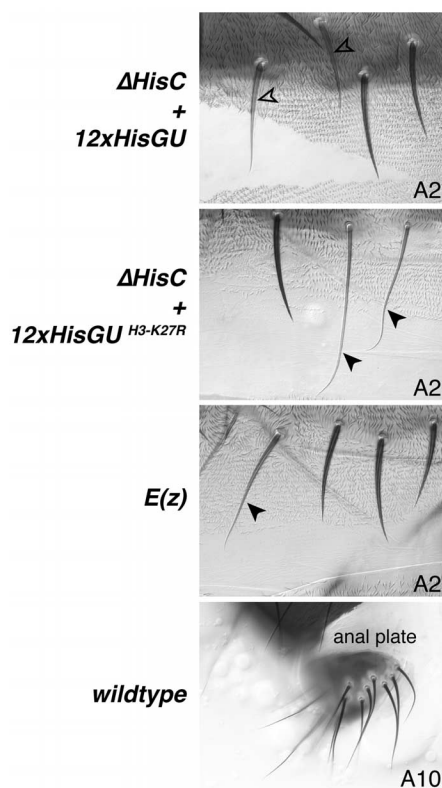


Fig. 1. H3-K27R mutant cells show the same phenotypes as PRC2 mutant cells. (A) Wing imaginal discs with clones of $\Delta HisC$ homozygous cells in animals without transgene (no TG) or with $12\times His-GU$ or $12\times His-GU^{H3-K27R}$ transgenes, stained with H3-K27me3 antibody and Hoechst (DNA). $\Delta HisC$ homozygous cells are marked by the absence of green fluorescent protein (GFP) (fig. S1), and clones were induced 96 hours before analysis in all cases. (B) Wing imaginal discs with clones of $\Delta HisC$ homozygous cells in $12\times His-GU^{H3-K27R}$ transgenics (top row) or with clones of $E(z)^{731}$ homozygous cells (bottom row), stained with antibodies against indicated proteins. Clone marking and induction as in (A). Ubx and Abd-B are misexpressed at high levels (arrowheads), Scr and En at lower levels (arrowheads); in both genotypes, not all mutant clones show misexpression (open arrowheads). Asterisk marks Scr expression in peripodial membrane cells in third leg disc.

cells (bottom row), stained with antibodies against indicated proteins. Clone marking and induction as in (A). Ubx and Abd-B are misexpressed at high levels (arrowheads), Scr and En at lower levels (arrowheads); in both genotypes, not all mutant clones show misexpression (open arrowheads). Asterisk marks Scr expression in peripodial membrane cells in third leg disc.

Fig. 2. Homeotic transformation of tissues formed by differentiated H3-K27R mutant cells. Top three panels show portions of abdominal segment A2 of adults with clones of $\Delta HisC$ homozygous cells in $12\times His-GU$ or $12\times His-GU^{H3-K27R}$ transgenics or with clones of $E(z)^{731}$ homozygous cells; in all cases, mutant cells are genetically marked with a yellow mutation (light pigmentation, fig. S1). $\Delta HisC$ $12\times His-GU^{H3-K27R}$ mutant clones show homeotic transformation into more posterior body segments; the mutant sensory bristles (arrowheads) are finer and more tapered than the neighboring wild-type bristles in A2 and resemble bristles characteristic of abdominal segment A10 in wild-type animals (bottom). In the case of $E(z)$, mutant bristles (arrowheads) are less extensively transformed, which may reflect the perdurance of $E(z)$ protein in the mutant cells. $\Delta HisC$ $12\times His-GU$ bristles (open arrowheads), shown as controls, are indistinguishable from neighboring wild-type bristles.



imaginal wing disc cells, where these genes are normally repressed (Fig. 1B). Both the levels of misexpression and the territories in the disc where each of these genes is misexpressed are very similar in $H3^{K27R}$ and $E(z)$ mutant clones (Fig. 1B). $H3^{K27R}$ and $E(z)$ mutant cells both differentiate to form epidermal structures in adult flies. However, these structures show homeotic transformations. This is illustrated by the changed morphology of

sensory bristles generated by $H3^{K27R}$ or $E(z)$ mutant cells; bristles formed by mutant cells in anterior segments (e.g., in abdominal segment A2) resemble the bristles that are characteristic for and normally only present in the most posterior body segment (Fig. 2). These segmental transformations are consistent with the observation that $H3^{K27R}$ and $E(z)$ mutant clones in anterior body segments show misexpression of posterior *HOX* genes.

In summary, these results demonstrate that cells with $H3^{K27R}$ nucleosomes reproduce the PRC2 mutant phenotype. This provides strong evidence that H3-K27 in target gene chromatin is the crucial substrate that PRC2 needs to methylate for Polycomb repression in *Drosophila*. Furthermore, the PRC2-mimic phenotype of $H3^{K27R}$ mutant cells suggests that H3-K27 acetylation does not play a major role of its own but may function only to antagonize H3-K27 methylation by PRC2. The demonstration that the H3-K27 residue has an essential function in metazoans emphasizes how important it is to resolve how PRC2 establishes, maintains, and propagates H3-K27 methylation and how this modification generates repressive chromatin.

References and Notes

1. M. D. Shahbazian, M. Grunstein, *Annu. Rev. Biochem.* **76**, 75 (2007).
2. J. Huang, S. L. Berger, *Curr. Opin. Genet. Dev.* **18**, 152 (2008).
3. R. Cao, Y. Zhang, *Curr. Opin. Genet. Dev.* **14**, 155 (2004).
4. J. A. Simon, R. E. Kingston, *Nat. Rev. Mol. Cell Biol.* **10**, 697 (2009).
5. J. Müller, P. Verrijzer, *Curr. Opin. Genet. Dev.* **19**, 150 (2009).
6. R. Margueron, D. Reinberg, *Nature* **469**, 343 (2011).
7. U. Günesdogan, H. Jäckle, A. Herzog, *EMBO Rep.* **11**, 772 (2010).

Acknowledgments: The authors are supported by the Max Planck Society and a fellowship from the Marie Curie Initial Training Network *Nucleosome4D* (A.R.P.).

Supplementary Materials

www.sciencemag.org/cgi/content/full/339/6120/698/DC1
Materials and Methods
Fig. S1
References (8–10)

11 October 2012; accepted 6 December 2012
10.1126/science.1231382

53BP1 Regulates DSB Repair Using Rif1 to Control 5' End Resection

Michal Zimmermann,^{1,2} Francisca Lottersberger,¹ Sara B. Buonomo,³ Agnel Sfeir,^{1*} Titia de Lange^{1†}

The choice between double-strand break (DSB) repair by either homology-directed repair (HDR) or nonhomologous end joining (NHEJ) is tightly regulated. Defects in this regulation can induce genome instability and cancer. 53BP1 is critical for the control of DSB repair, promoting NHEJ, and inhibiting the 5' end resection needed for HDR. Using dysfunctional telomeres and genome-wide DSBs, we identify Rif1 as the main factor used by 53BP1 to impair 5' end resection. Rif1 inhibits resection involving CtIP, BLM, and Exo1; limits accumulation of BRCA1/BARD1 complexes at sites of DNA damage; and defines one of the mechanisms by which 53BP1 causes chromosomal abnormalities in Brca1-deficient cells. These data establish Rif1 as an important contributor to the control of DSB repair by 53BP1.

The DNA damage response protein 53BP1 can influence the type of DNA repair at double-strand breaks (DSBs) (1) as seen

in immunoglobulin gene rearrangements (2–4) and in the fusion of telomeres rendered dysfunctional through the removal of the shelterin protein TRF2 (5), where 53BP1 enhances the mobility of damaged telomeres, thus potentially promoting the chance of telomere-telomere encounters. In Brca1-deficient cells, 53BP1 enhances aberrant nonhomologous end joining (NHEJ) events that create lethal radial chromosomes in response to poly(ADP-ribose) polymerase PARP1 inhibitors (PARPi) (6). In this setting, 53BP1 may favor NHEJ-mediated misrejoining by blocking the DSB resection needed for homology-directed repair (HDR)

(6, 7). 53BP1 was shown to impede 5' end resection at dysfunctional telomeres lacking all shelterin proteins and, similarly, telomeres lacking only TRF2 show evidence of 53BP1-dependent protection from resection (5, 8). Based on the finding that an allele of 53BP1 (53BP1^{28A}) lacking all potential ataxia telangiectasia mutated (ATM)/ATR and Rad3-related (ATR) kinase S/TQ target sites did not support immunoglobulin class switch recombination (CSR) and failed to generate radial chromosomes in Brca1-deficient cells (7), it appears that these functions of 53BP1 involve interacting partner(s) modulated by the S/TQ sites. One candidate 53BP1-interacting factor is Rif1, which localizes to DSBs and dysfunctional telomeres, in a manner that is dependent on ATM signaling (9–11). Rif1 was originally identified as part of the telomeric complex in budding yeast (12) and was recently shown to inhibit resection at yeast telomeres (13, 14). In contrast, mammalian Rif1 has no known function at functional telomeres but contributes to the intra-S phase checkpoint, facilitates recovery from replication stress, and affects replication timing (10, 15–17).

We introduced 53BP1^{28A} and other 53BP1 mutant alleles (7) into immortalized TRF2^{F/-} 53BP1^{-/-} mouse embryo fibroblasts (MEFs) and induced telomere dysfunction by deletion of TRF2 (Fig. 1, A and B). The results showed that the S/TQ sites were required for the accumulation of Rif1 at deprotected telomeres, whereas the GAR, BRCT, and oligomerization domains of 53BP1 were not

Fig. 1. Rif1 recruitment requires the S/TQ ATM/ATR target sites of 53BP1. (A) Detection of 53BP1 and Rif1 at dysfunctional telomeres in Cre-treated SV40 large T antigen (SV40-LT) immortalized TRF2^{F/-} 53BP1^{-/-} MEFs expressing 53BP1 mutant alleles [shown in (C)]. Indirect immunofluorescence (IF) for 53BP1 and Rif1 (red) was combined with telomeric TTAGGG fluorescence in situ hybridization (FISH) (green). Blue: 4',6'-diamidino-2-phenylindole DNA stain. (B) Quantification of 53BP1 and Rif1 telomere dysfunction-induced foci (TIFs) (21) detected as in (A). Data represent means of three experiments \pm SDs (≥ 70 cells per experiment). **, $P < 0.05$ (two-tailed paired Student's *t* test). (C) Schematic of the 53BP1 mutant alleles and the role of the N-terminal S/TQ sites in the recruitment of Rif1.

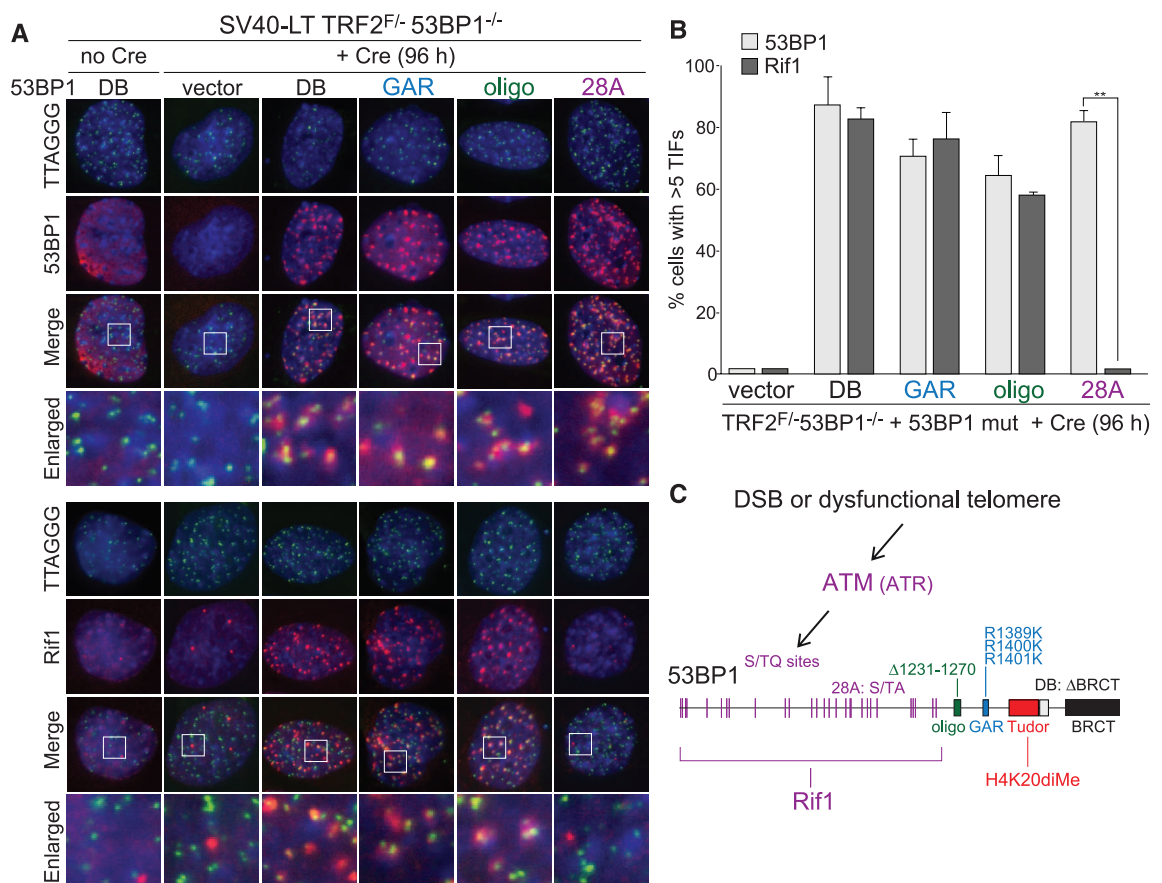


(Fig. 1, A to C, and fig. S1). The functional importance of the Rif1-53BP1 interaction was addressed using a telomere-based assay system that previously uncovered the role of 53BP1 in stimulating telomeric NHEJ and protecting telomere ends from 5' resection (5, 8). Using TRF2/Rif1 conditional double-knockout MEFs, we documented a significant reduction in the incidence and rate of telomere fusions in cells lacking Rif1 (Fig. 2, A to C, and fig. S2A). This reduced NHEJ rate was not due to changes in cell cycle progression or diminished activation of the ATM kinase pathway by the deprotected telomeres (fig. S2, B to G).

As 53BP1 increases the mobility of dysfunctional telomeres, we determined whether Rif1 contributes to this aspect of 53BP1 by live-cell imaging of mCherry fused to the 53BP1 Tudor domain, which targets this marker to dysfunctional telomeres (fig. S2H). As expected, traces of the mCherry marker demonstrated that 53BP1 deficiency reduced the mobility of dysfunctional telomeres (Fig. 2D). In contrast, absence of Rif1 did not affect the mobility of the deprotected telomeres. Thus, Rif1 is not required for the 53BP1-dependent increase in the mobility of dysfunctional telomeres.

We next determined whether Rif1 contributes to the inhibition of 5' end resection by 53BP1. When TRF2 is deleted from cells lacking 53BP1, there is a 2- to 3-fold increase in the telomeric 3' overhang signal (5) which can be detected based on annealing a telomeric oligonucleotide to native telomeric DNA (Fig. 3). As expected,

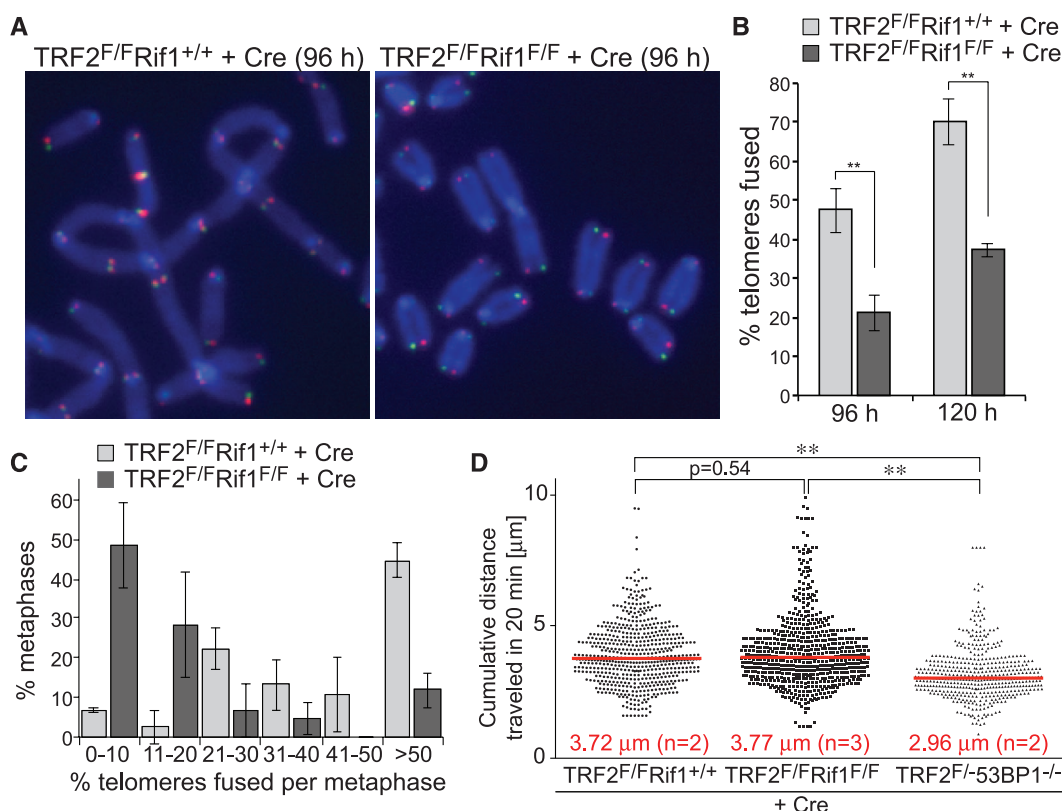
deletion of TRF2 resulted in the removal of the overhangs concomitant telomere fusion, whereas the overhang signal increased 3-fold when TRF2 was deleted from 53BP1-deficient cells in which telomeric NHEJ is rare and 5' end resection is uninhibited (Fig. 3, A and B). Deletion of TRF2 from Rif1-deficient cells also resulted in an increase in the overhang signal (Fig. 3B). However, the increase was less compared to that observed in the 53BP1-deficient cells. Because the difference might be due to the lower rate of telomere fusions in the 53BP1-deficient setting, we generated immortalized TRF2^{F/F}Lig4^{-/-}Rif1^{F/F} cells, which, owing to the absence of DNA ligase IV, have the same low telomere fusions rates as TRF2^{F/F}53BP1^{-/-} cells (5). When NHEJ was blocked, the telomeric overhang increase in the Rif1-deficient cells was the same as that which occurred in the 53BP1-deficient cells (Fig. 3, C and D). The increase in overhang signal was demonstrably due to 3' terminal sequences because the signal was removed by digestion with the *Escherichia coli* 3' exonuclease Exo1 (fig. S3A). These data suggest that Rif1 is the main factor acting downstream of 53BP1 to inhibit the resection at telomeres that lack TRF2 protection.

At telomeres that are deprived of both TRF1 and TRF2 and therefore lack all shelterin proteins, 53BP1 blocks extensive 5' end resection that involves CtIP, BLM, and Exo1 (8). To test the ability of Rif1 to inhibit resection at such shelterin-free telomeres, we generated immortalized TRF1^{F/F}TRF2^{F/F}Rif1^{F/F} MEFs. As ex-

pected, deletion of TRF1 and TRF2 resulted in frequent telomere fusions and nearly complete loss of the telomeric overhang signal when Rif1 was present (Fig. 3, E and F). When Rif1 was codeleted with TRF1 and TRF2, telomere fusions were also frequent, resulting in most telomeric restriction fragments shifting to a higher molecular weight (Fig. 3E). However, the telomeres that had not fused at the time point analyzed showed a notable increase in overhang signal (Fig. 3, E and F). This increase in the signal was diminished when cells were treated with short hairpin RNAs (shRNAs) against CtIP, BLM, or Exo1 (Fig. 3, G and H, and fig. S3, B and C). Thus, like 53BP1, Rif1 inhibits 5' end resection that involves CtIP, BLM, and Exo1.

We next asked whether Rif1 affects resection at zeocin-induced DSBs by monitoring the formation of replication protein A (RPA) foci (Fig. 4A and fig. S4A). The absence of either Rif1, 53BP1, or both did not affect zeocin-induced γ -H2AX foci or the basal level of cells containing γ -H2AX foci, which likely represent replicating cells (Fig. 4, A and B). However, in zeocin-treated cells, the absence of either Rif1 or 53BP1 resulted in a significant increase in γ -H2AX foci that colocalized with RPA (Fig. 4, A and C). When either 53BP1 or Rif1 were absent, there also was a significant increase in γ -H2AX foci containing RPA in cells not treated with zeocin, presumably reflecting a higher level of resection at stalled replication forks (Fig. 4, A and C). Examination of the RPA/ γ -H2AX foci in zeocin-treated

Fig. 2. Rif1 promotes telomeric NHEJ without affecting telomere mobility. **(A)** Metaphase chromosomes of Cre-treated SV40-LT immortalized TRF2^{F/F}Rif1^{+/+} and TRF2^{F/F}Rif1^{F/F} MEFs showing NHEJ-mediated telomere fusions detected by *chromosome orientation* FISH. Telomeres synthesized by leading-end DNA synthesis are in red; lagging-end telomeres are in green. **(B)** Quantification of telomere fusions as determined in (A) at 96 and 120 hours after Cre. Data represent means of three independent experiments \pm SDs (>3000 telomeres per experiment). **, $P < 0.01$ based on two-tailed paired Student's *t* test. **(C)** Distributions of telomere fusions per metaphase at 96 hours after Cre for experiments shown in (B). **(D)** Distribution of cumulative distances traveled by mCherry-53BP1¹²²⁰⁻¹⁷¹¹ foci in the indicated cell lines. Red lines represent medians. **, $P < 0.0001$ (two-tailed Mann-Whitney test).



Rif1/53BP1 double-knockout cells indicated that Rif1 and 53BP1 are epistatic in this regard because the induction of RPA/γ-H2AX foci in absence of 53BP1 was the same as in Rif1-deficient cells and the absence of both Rif1 and 53BP1 did not further increase the response (Fig. 4C). The simplest interpretation of these data is that Rif1 is the main factor acting downstream of 53BP1 to block 5' end resection at the zeocin-induced DSBs.

Because the 53BP1/Rif1 control affects CtIP, which is thought to be delivered by a complex containing BRCA1 (18–20), we also determined whether 53BP1 and Rif1 had an effect on the presence of the BRCA1 at zeocin-induced DSBs. Using an antibody to the constitutive BRCA1

partner BARD1, we found that absence of Rif1 or 53BP1 resulted in a significant increase in the accumulation of BRCA1 complexes at zeocin-induced DSBs (Fig. 4, E and F). Consistent with the data above, Rif1 and 53BP1 were again epistatic in this regard. The absence of 53BP1 resulted in the same phenotype as absence of Rif1, and the double knockout did not show an additional increase in the incidence of BARD1 foci (Fig. 4, E and F). The absence of Rif1 also resulted in an increase in the presence of BARD1 at dysfunctional telomeres (fig. S4, B to D).

Because 53BP1 mediates the formation of misrejoined and radial chromosomes in PARPi-treated Brca1-deficient cells, we asked to what

extent Rif1 is responsible for this effect. Cells lacking Rif1, 53BP1, or both were treated with a BRCA1 shRNA and the PARP inhibitor, and misrejoined chromosomes were quantified (Fig. 4, G and H). The data show the previously documented decrease in the frequency of chromosome misrejoining when 53BP1 is absent. Interestingly, absence of Rif1 also lowers the frequency of chromosome misrejoining, but the effect is significantly less than for 53BP1. Thus, the formation of misrejoined chromosomes in PARPi-treated Brca1-deficient cells is due to two distinct attributes of 53BP1, one of which requires Rif1 function.

These data identify Rif1 as the major factor acting downstream of 53BP1 in the control of 5'

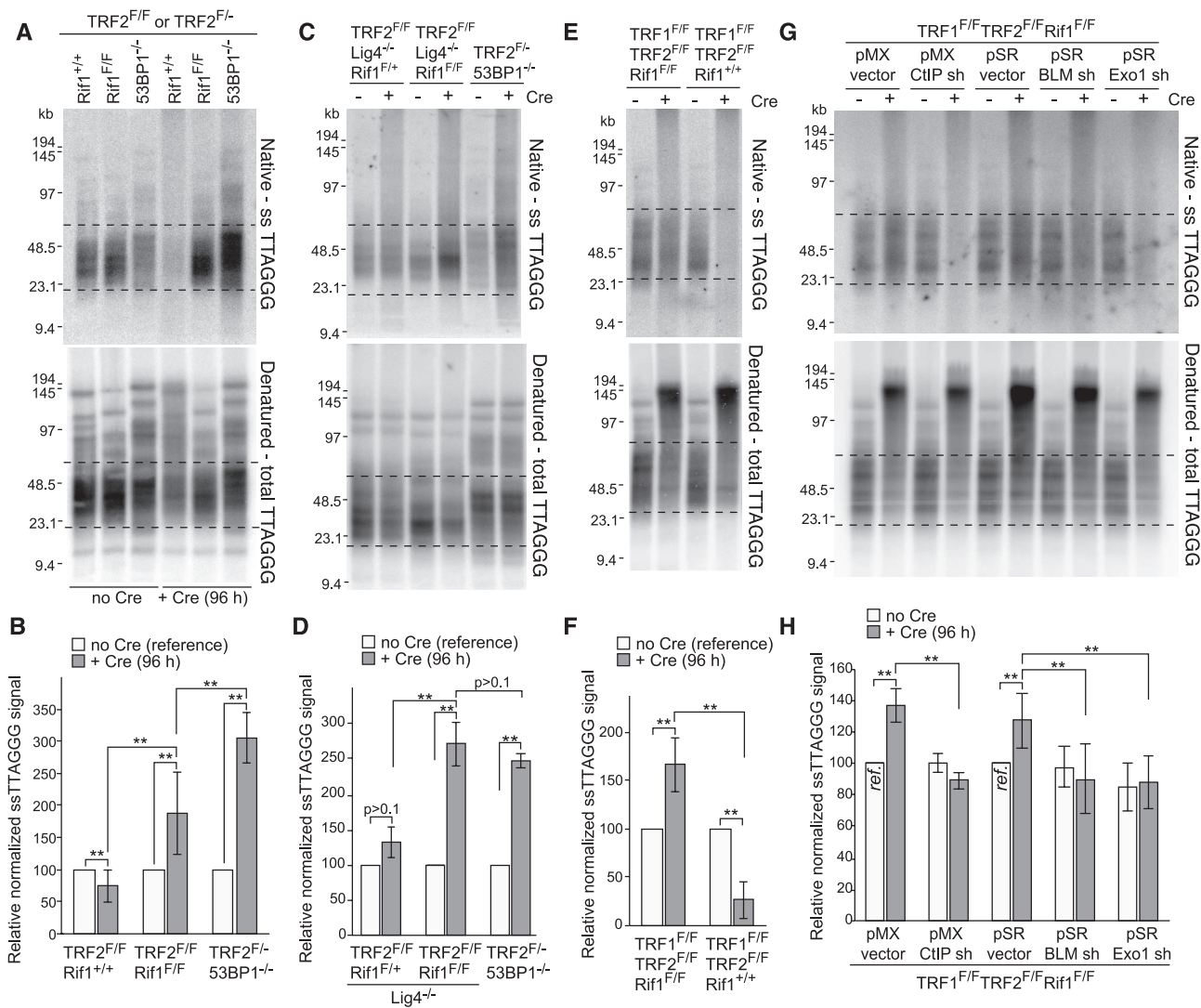


Fig. 3. Rif1 blocks 5' end resection at dysfunctional telomeres. (A) Telomeric overhang assays on TRF2^{F/F} Rif1^{+/+}, TRF2^{F/F} Rif1^{F/F} and TRF2^{F/-} 53BP1^{-/-} MEFs. Native in-gel hybridization of Mbol/Alul digested DNA with end-labeled [AACCT]₄ (top) and re-hybridization with the same probe after denaturation in situ (bottom). Dashed lines represent the bulk of free (unfused) telomeres used for quantification. (B) Quantification of overhang assays as in (A). Overhang signals in no Cre samples was set at 100%. (C and D) Overhang assays on TRF2^{F/F} Rif1^{+/+} Lig4^{-/-}, TRF2^{F/F} Rif1^{F/F} Lig4^{-/-}, and

TRF2^{F/-} 53BP1^{-/-} MEFs and quantification as in (B). (E and F) Overhang assays on TRF1^{F/F} TRF2^{F/F} Rif1^{+/+} and TRF1^{F/F} TRF2^{F/F} Rif1^{F/F} MEFs and quantification. (G and H) Overhang assays to measure dependency on CtIP, BLM, and Exo1 and quantification. Cells infected with either pMX or pSR with or without the indicated shRNAs and treated with Cre for 96 hours. Samples with empty vectors and no Cre (ref.) were used as references. Data in [(B), (D), (F), and (H)] represent means of ≥3 experiments ±SDs. **, P < 0.05 (two-tailed paired Student's t test). MEFs are SV40-LT immortalized.

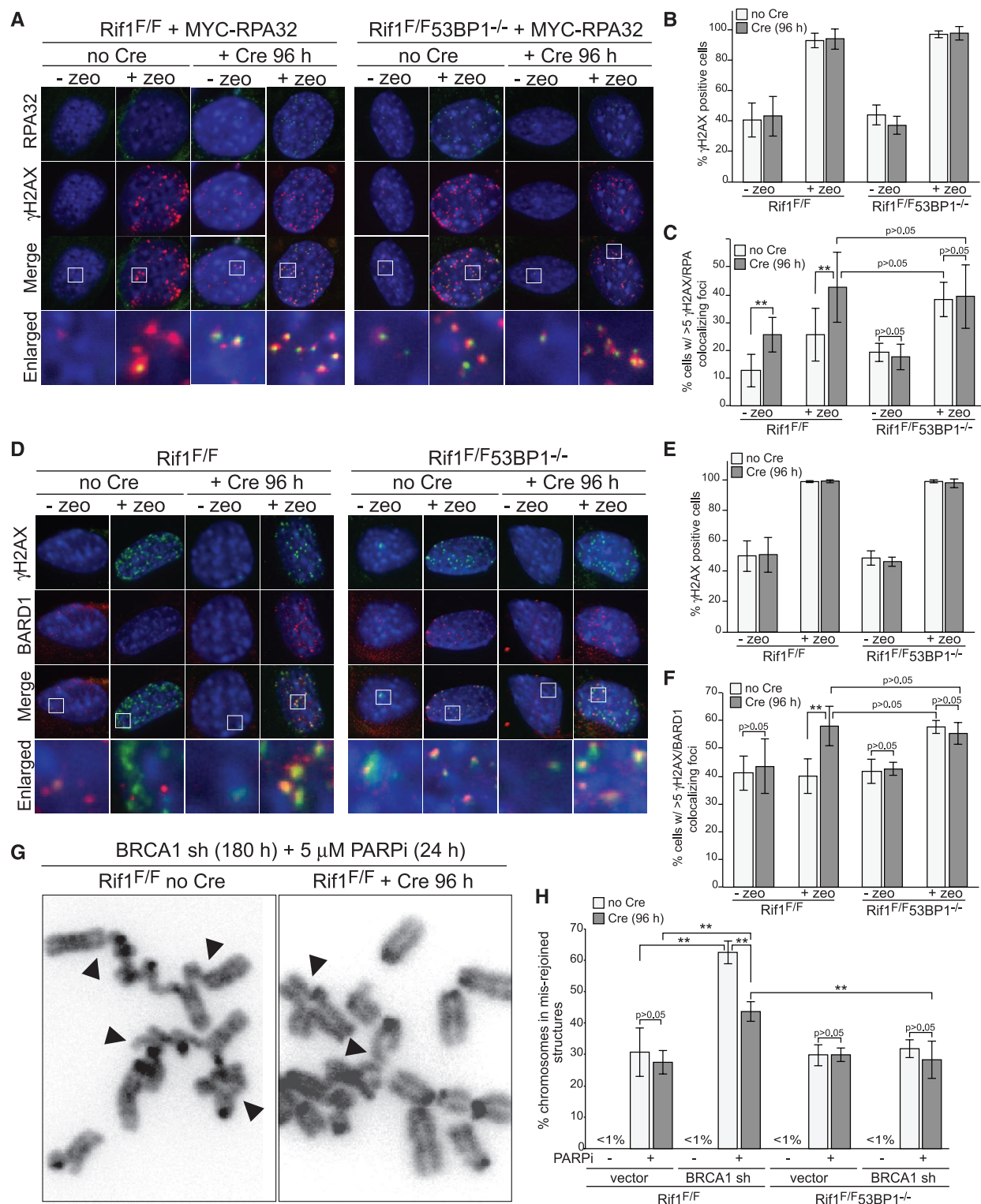


Fig. 4. Rif1 inhibits resection at DSBs and promotes radial formation. (A) IF for γ -H2AX (red) and MYC-RPA32 (green) in Cre-treated SV40-LT immortalized Rif1^{F/F} and Rif1^{F/F53BP1-/-} cells expressing MYC-RPA32 treated with zeocin (100 μ g/ml, for 1 hour; 2 hours before analysis). (B) Percentage of γ -H2AX positive cells in experiments as in (A). (C) Percentage of cells [as in (A)] scored positive when containing at least five γ -H2AX foci colocalizing with RPA. (D) IF for γ -H2AX (green) and BARD1 (red) in Rif1^{F/F} and Rif1^{F/F53BP1-/-} MEFs. Cells and treatment as

in (A). (E) Percentage of γ -H2AX-positive cells in experiments in (D). (F) Percentage of cells in (D) containing >5 BARD1/ γ -H2AX colocalizing foci. (G) Examples of misrejoined and radial chromosomes (arrowheads) in BRCA1sh/PARPi-treated Rif1^{F/F} cells with or without Cre. (H) Percentages of chromosomes that are misrejoined in the indicated genotypes and treatments. Data in (B), (C), (E), (F), and (H) are means of three to five experiments \pm SDs. **, $P < 0.05$ (two-tailed paired Student's t test).

end resection. In contrast, Rif1 does not appear to be required for the ability of 53BP1 to promote an increase in the mobility of dysfunctional telomeres. The intermediate effect of Rif1 on the fusion of dysfunctional telomeres can be explained based on these two observations. The increased resection of dysfunctional telomeres in absence of Rif1 is likely to be responsible for the mild inhibition of NHEJ. However, in the absence of 53BP1, the effect of increased resection is combined with a defect in the induction of the mobility of the dysfunctional telomeres, resulting in a more severe blockade to NHEJ. Similarly, we propose that Rif1 deletion leads to partial rescue of chromosome misrejoining in PARPi/BRCA1 shRNA-treated cells because the control of 5' end resection is only one of multiple mechanisms by which 53BP1 acts. One possibility is that the other mechanism used by 53BP1 in this context, similar to what happens at dysfunctional telomeres, involves the induction of

DSB mobility that increases the chance that DSB misrejoining occurs.

References and Notes

1. A. T. Noon, A. A. Goodarzi, *DNA Repair* **10**, 1071 (2011).
2. I. M. Ward, K. Minn, J. van Deursen, J. Chen, *Mol. Cell. Biol.* **23**, 2556 (2003).
3. J. C. Morales et al., *J. Biol. Chem.* **278**, 14971 (2003).
4. S. Difilippantonio et al., *Nature* **456**, 529 (2008).
5. N. Dimitrova, Y. C. Chen, D. L. Spector, T. de Lange, *Nature* **456**, 524 (2008).
6. S. F. Bunting et al., *Cell* **141**, 243 (2010).
7. A. Bothmer et al., *Mol. Cell* **42**, 319 (2011).
8. A. Sfeir, T. de Lange, *Science* **336**, 593 (2012).
9. L. Xu, E. H. Blackburn, *J. Cell Biol.* **167**, 819 (2004).
10. J. Silverman, H. Takai, S. B. Buonomo, F. Eisenhaber, T. de Lange, *Genes Dev.* **18**, 2108 (2004).
11. M. S. Huen et al., *Mol. Cell* **37**, 854 (2010).
12. C. F. Hardy, L. Sussel, D. Shore, *Genes Dev.* **6**, 801 (1992).
13. S. Anbalagan, D. Bonetti, G. Lucchini, M. P. Longhese, *PLoS Genet.* **7**, e1002024 (2011).
14. D. Bonetti et al., *PLoS Genet.* **6**, e1000966 (2010).
15. S. B. Buonomo, Y. Wu, D. Ferguson, T. de Lange, *J. Cell Biol.* **187**, 385 (2009).
16. D. Cornacchia et al., *EMBO J.* **31**, 3678 (2012).

17. S. Yamazaki et al., *EMBO J.* **31**, 3667 (2012).
18. A. A. Sartori et al., *Nature* **450**, 509 (2007).
19. X. Yu, L. C. Wu, A. M. Bowcock, A. Aronheim, R. Baer, *J. Biol. Chem.* **273**, 25388 (1998).
20. A. K. Wong et al., *Oncogene* **17**, 2279 (1998).
21. H. Takai, A. Smogorzewska, T. de Lange, *Curr. Biol.* **13**, 1549 (2003).

Acknowledgments: We thank D. White for expert mouse husbandry and M. Nussenzweig for providing mutant 53BP1 constructs. M.Z. was supported by a Brno Ph.D. talent fellowship and by a grant from the Czech Science Foundation to Ctírad Hofr (P205/12/0550) (see supplementary materials for detailed acknowledgement). This work was supported by a grant from the Breast Cancer Research Foundation to T.d.L. T.d.L. is an American Cancer Society Research Professor.

Supplementary Materials

www.sciencemag.org/cgi/content/full/science.1231573/DC1
Materials and Methods
Figs. S1 to S4
References (22–28)

16 October 2012; accepted 14 December 2012
Published online 10 January 2013;
10.1126/science.1231573

Regulation of Flowering by Trehalose-6-Phosphate Signaling in *Arabidopsis thaliana*

Vanessa Wahl,^{1*} Jathish Ponnu,² Armin Schlereth,¹ Stéphanie Arrivault,¹ Tobias Langenecker,² Annika Franke,¹ Regina Feil,¹ John E. Lunn,¹ Mark Stitt,¹ Markus Schmid^{2*}

The timing of the induction of flowering determines to a large extent the reproductive success of plants. Plants integrate diverse environmental and endogenous signals to ensure the timely transition from vegetative growth to flowering. Carbohydrates are thought to play a crucial role in the regulation of flowering, and trehalose-6-phosphate (T6P) has been suggested to function as a proxy for carbohydrate status in plants. The loss of *TREHALOSE-6-PHOSPHATE SYNTHASE 1* (*TPS1*) causes *Arabidopsis thaliana* to flower extremely late, even under otherwise inductive environmental conditions. This suggests that *TPS1* is required for the timely initiation of flowering. We show that the T6P pathway affects flowering both in the leaves and at the shoot meristem, and integrate *TPS1* into the existing genetic framework of flowering-time control.

The transition from vegetative to reproductive development is an important phase change in a plant's life. When timed correctly, the transition helps to ensure reproductive success and therefore has adaptive value. For this reason, plants have evolved an intricate genetic network that controls the onset of flowering in response to environmental and endogenous signals such as day length, temperature, hormonal status, and carbohydrate availability (*1*). Day length is perceived in the

leaves, where a sufficiently long day (i.e., an inductive photoperiod) leads to induction of the *FLOWERING LOCUS T* (*FT*) gene (*2–7*). The FT protein functions as a long-distance signal (florigen) that is transported to the shoot meristem, where it interacts with the bZIP transcription factor FD and triggers the formation of flowers (*8–11*).

In contrast to the detailed understanding of the photoperiod pathway, relatively little is known about the contribution of carbohydrates to the regulation of flowering (*12*). Mutations in genes of key enzymes in sugar and starch metabolism such as *HEXOKINASE1* (*HXK1*) and *PHOSPHO-GLUCOMUTASE1* (*PGM1*) have been shown to affect various aspects of development, including flowering (*13*). A particularly striking example in this respect is *TREHALOSE-6-PHOSPHATE SYNTHASE 1* (*TPS1*), which catalyzes the formation of trehalose-6-phosphate (T6P) from

glucose-6-phosphate and uridine diphosphate (UDP)–glucose (*13, 14*). T6P, which is found only in trace amounts in most plants, has been suggested to function as a signaling molecule that relays information about carbohydrate availability to other signaling pathways (*15*). In agreement with the proposed role of T6P as a central hub in carbon signaling, *TPS1* loss-of-function mutants are embryonic lethal (*16*). Expression of *TPS1* from the seed-specific *ABI3* promoter has been shown to be sufficient to rescue the embryo defect, but the resulting homozygous *tps1* *ABI3:TPS1* plants develop slowly and senesce before entering the reproductive phase (*17*). Homozygous *tps1-2* mutants have also been recovered using a chemically inducible rescue construct (*GVG:TPS1*), which enables induction of *TPS1* by dexamethasone application, allowing the *tps1-2* *GVG:TPS1* embryos to be rescued to give viable plants that can be stably maintained (*18*). The resulting *tps1-2* *GVG:TPS1* plants flower extremely late, producing infertile flowers on shoots that simultaneously arise from the shoot apical meristem (SAM) and axillary meristems, or completely fail to flower, even under inductive photoperiod. These findings indicate that *TPS1* plays a critical role in controlling the transition to flowering. However, it is currently unclear where *TPS1* is integrated into the canonical flowering-time pathways.

To better understand the molecular function of *TPS1*, we first confirmed its effect on flowering by knocking down *TPS1* expression with the use of an artificial microRNA (*35S:amiR-TPS1*; figs. S1 and S2) (*19*). This resulted in a significant 25 to 30% reduction in T6P levels (fig. S3) and a delay in flowering by more than 20 leaves (Table 1, experiment 1; fig. S4). In contrast, sucrose levels were significantly higher in *35S:amiR-TPS1* plants (fig. S4), indicating that carbohydrate availability as such was not compromised in those plants. These findings highlight

¹Department of Metabolic Networks, Max Planck Institute of Molecular Plant Physiology, Am Mühlenberg 1, 14476 Potsdam, Germany. ²Department of Molecular Biology, Max Planck Institute for Developmental Biology, Spemannstr. 35, 72076 Tübingen, Germany.

*To whom correspondence should be addressed. E-mail: vanessa.wahl@mpimp-golm.mpg.de (V.W.); maschmid@tuebingen.mpg.de (M.S.)

the importance of TPS1 activity and T6P signaling, jointly referred to as the T6P pathway, in regulating the floral transition.

To investigate whether the T6P pathway integrates into the photoperiod pathway, we next determined the diurnal changes in T6P concentration. We observed a pronounced rhythmicity in

T6P across a 72-hour time course, with maxima in T6P levels toward the end of the day (Fig. 1A), broadly following the previously reported diurnal changes of sucrose levels (15). This is exactly the time of day when the circadian and light-regulated CONSTANS (CO) protein normally induces the expression of *FT* (6, 20, 21).

Table 1. Flowering times of mutants and transgenic plants. RLN, rosette leaf number; CLN, cauline leaf number; TLN, total leaf number; *n*, number of individuals; #, identifier of individual transgenic line; NA, not applicable.

	RLN	CLN	TLN	TLN SD	TLN range	<i>n</i>
Experiment 1 (long days)						
Col-0 (wild type)	9.1	2.1	11.2	±1.0	9–14	20
35S:amiR-TPS1 #5	27.0	6.1	33.1	±2.3	30–36	20
35S:amiR-TPS1 #6	27.9	6.5	34.4	±2.9	27–43	20
CLV3:TPS1 #7	2.8	1.8	4.6	±2.1	2–9	9
CLV3:TPS1 #15	1.5	2.0	3.5	±0.6	3–4	4
CLV3:otsB #7	14.2	3.6	17.8	±1.4	16–20	10
CLV3:otsB #9	15.0	3.9	18.9	±2.0	16–23	10
Experiment 2 (long days)						
Col-0 (wild type)	10.2	1.8	12.0	±1.1	9–13	20
<i>ft-10</i>	38.1	8.1	46.2	±2.1	43–50	20
35S:amiR-TPS1 #5	29.9	7.3	37.2	±2.3	32–41	20
35S:amiR-TPS1 #6	32.5	7.2	39.7	±2.8	35–44	20
<i>ft-10</i> 35S:amiR-TPS1 #5	39.7	9.6	49.3	±1.7	46–53	20
<i>ft-10</i> 35S:amiR-TPS1 #6	40.5	9.6	50.1	±1.9	47–53	20
Experiment 3 (long days)						
Col-0 (wild type)	9.0	1.3	10.3	±1.0	9–12	20
35S:amiR-TPS1 #6	29.6	6.3	35.9	±1.9	33–40	19
35S:FT	3.8	1.2	5.0	±0.4	4–6	15
<i>SUC2:FT</i>	3.6	1.1	4.7	±0.5	4–5	15
35S:FT 35S:amiR-TPS1 #6	4	1.4	5.4	±0.5	5–6	20
<i>SUC2:FT</i> 35S:amiR-TPS1 #6	4.1	1.4	5.5	±0.5	5–6	20
Experiment 4 (short days)						
Col-0 (wild type)	58.9	3.1	62.0	±2.0	59–65	20
<i>tps1-2</i> GVG:TPS1	>100	NA	>100	NA	>100	20
Experiment 5 (short days)						
Col-0 (wild type)	54.1	9.6	63.7	±2.5	59–69	18
CLV3:TPS1 #7	24.0	5.8	29.8	±2.9	23–33	21
CLV3:TPS1 #15	37.4	8.8	46.2	±3.3	38–50	20
Experiment 6 (long days)						
Col-0 (wild type)	8.1	2.0	10.1	±0.6	9–11	20
<i>ft-10</i>	37.6	7.3	44.9	±1.9	42–48	20
CLV3:TPS1 #7	3.8	1.9	5.7	±0.7	5–7	18
CLV3:TPS1 #7 <i>ft-10</i>	13.7	2.5	16.2	±1.3	15–20	20
Experiment 7 (long days)						
Col-0 (wild type)	9.0	1.8	10.8	±1.1	9–14	20
35S:miR156	29.6	4.2	33.8	±2.6	29–38	20
35S:amiR-TPS1 #5	29.5	6.8	36.3	±1.9	30–38	20
35S:amiR-TPS1 #6	32.4	6.8	39.2	±2.1	36–42	20
35S:miR156 35S:amiR-TPS1 #5	>100	NA	>100	NA	>100	20
35S:miR156 35S:amiR-TPS1 #6	>100	NA	>100	NA	>100	20
Experiment 8 (short days)						
Col-0 (wild type)	57.1	10.5	67.6	±2.2	65–72	20
35S:miR156	97.8	4.6	102.4	±3.8	97–110	20
35S:amiR-TPS1 #6	56.3	8.4	64.7	±2.6	60–69	20
35S:miR156 35S:amiR-TPS1 #6	>120	NA	>120	NA	>120	20
Experiment 9 (long days)						
Col-0 (wild type)	10.6	2.3	12.9	±1.7	11–17	20
<i>tps1-2</i> GVG:TPS1	>80	NA	>80	NA	>80	20
35S:MIM156	2.8	4.3	7.1	±1.0	5–9	20
35S:MIM156 <i>tps1-2</i> GVG:TPS1	8.3	3.9	12.2	±1.2	10–14	20

Expression of *CO* (Fig. 1B) and that of its upstream regulator *GIGANTEA* (*GI*) (fig. S5) were unchanged in the *tps1-2* GVG:TPS1 mutant. In contrast, the induction of *FT* at the end of the long day (LD) was abolished in *tps1-2* GVG:TPS1 plants (Fig. 1C). Similarly, expression of *TWIN SISTER OF FT* (*TSF*), which has been shown to follow the same diurnal regulation and to contribute to the induction of flowering (22), was substantially reduced in *tps1-2* GVG:TPS1 plants at the end of the LD (fig. S5). Expression of *FT* and *TSF* was also substantially reduced in a developmental series in the 35S:amiR-TPS1 line (fig. S6). Furthermore, *FT* expression in *tps1-2* GVG:TPS1 plants could be significantly induced by dexamethasone application (fig. S7), confirming that the T6P pathway is required for *FT* and *TSF* expression under inductive photoperiod.

The finding that *FT* and *TSF* expression is almost completely abolished in the *tps1-2* GVG:TPS1

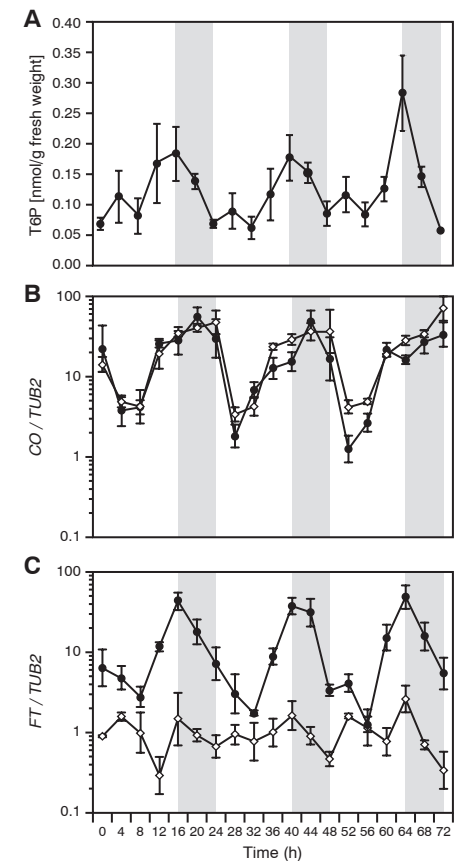


Fig. 1. Diurnal time course of T6P and flowering-time genes over 72 hours. (A) T6P levels in whole 12- to 14-day-old Col-0 rosettes. Error bars indicate SD of the mean. (B and C) Expression of *CO* (B) and *FT* (C) in 12- to 14-day-old Col-0 (solid circles) and *tps1-2* GVG:TPS1 (open diamonds) rosettes. Expression was determined by qRT-PCR using three biological replicates with three technical repetitions each and normalized to TUB2. Shaded areas indicate dark periods. Error bars indicate the upper and lower limit of the SD of the mean.

mutant and strongly attenuated in *35S:amiR-TPS1* lines explains, to a large extent, the late flowering of these genotypes. Loss of *FT* function—as, for example, in the strong T-DNA insertion mutant *ft-10*—results in delayed flowering, specifically under LD (supplementary text and table S1). Genetic analyses demonstrated that *ft-10 35S:amiR-TPS1* double mutants flowered only marginally later in LD than did *ft-10* plants (Table 1, experiment 2), indicating that the two genes act in the same pathway. Moreover, expression of *FT* from the constitutive *35S* promoter or the phloem companion cell-specific *SUC2* promoter, which has been shown by several studies to induce flowering independently of photoperiod (supplementary text and table S1), almost completely suppressed the late flowering of *35S:amiR-TPS1* (Table 1, experiment 3), confirming that the T6P pathway acts upstream of *FT* in the photoperiod pathway.

In contrast to *ft-10* mutants, which are late-flowering only under inductive LD conditions, *tps1-2 GVG:TPS1* mutants flowered late irrespective of day length (Table 1, experiment 4). This suggests that the T6P pathway also interferes with other floral signals in addition to the photoperiod pathway, and that it does so in a tissue separate from the leaves where day length is perceived. The most likely tissue for a non-leaf function of the T6P pathway is the SAM, where the different flowering-time pathways converge to regulate the expression of a small set of integrator genes, the expression of which ultimately decides whether the plant will make the transition to flowering (1).

TPS1 expression was detected by RNA in situ hybridization in the flanks of the meristem encircling the center of the SAM (Fig. 2, A to D, and fig. S8). In agreement with a proposed role of the T6P pathway in regulating flowering time at the SAM, T6P levels increased significantly during the transition to flowering in meristems of LD-grown plants (Fig. 2E) as well as in the meristems of plants in which flowering had been induced synchronously by shifting them from short day (SD) to LD (Fig. 2F). In dissected meristems of the latter, we observed a very strong correlation between T6P and sucrose levels (Fig. 2G), highlighting the role of T6P as an indicator of a plant's carbon status not only in vegetative tissues but also in the SAM.

These observations prompted us to express *TPS1* and the T6P-catabolizing enzyme trehalose-6-phosphate phosphatase, encoded by the *otsB* gene from *Escherichia coli*, in the SAM (13). Misexpression of *TPS1* from the stem cell niche-specific *CLV3* promoter (*CLV3:TPS1*) resulted in very early flowering under inductive LD as well as under noninductive SD conditions, whereas expression of *otsB* (*CLV3:otsB*) had the opposite effect (Table 1, experiments 1 and 5; Fig. 2, H to K; fig. S9). We found that the expression of *CLV3:TPS1* was sufficient to almost completely rescue the late flowering of *ft-10* mutants, demonstrating that the T6P pathway can act largely

independently of *FT* to induce flowering at the shoot meristem (Table 1, experiment 6). Taken together, these findings indicate that *TPS1* and T6P signaling are important regulators of the transition to flowering at the SAM.

To identify potential targets of the T6P pathway in the SAM, we performed a microarray analysis of dissected apices of 21-day-old SD-grown vegetative *tps1-2 GVG:TPS1* and wild-type plants (figs. S10 to S12). Transcript levels for genes known to be involved in integrating diverse flowering-time signals at the apex such as photoperiod (fig. S10), ambient temperature, prolonged periods of cold (vernalization) (fig. S11), and gibberellic acid (fig. S12) were unchanged or displayed only minor, statistically insignificant expression changes in the *tps1-2 GVG:TPS1* mutant relative to the wild type. The notable exception was *SQUAMOSA PROMOTER BINDING PROTEIN-LIKE 3* (*SPL3*), a known component of the age pathway of floral induction in *Arabidopsis thaliana* (23–26). Expression of *SPL3* was reduced by 60% in *tps1-2 GVG:TPS1* (Fig. 3E). The reduced expression of *SPL3* in *tps1-2 GVG:TPS1* was verified by quantitative reverse transcription polymerase chain reaction (qRT-PCR) on dissected meristems of 10- to 50-day-old SD-grown plants (Fig. 3F). This analysis also identified two closely related genes—*SPL4* and *SPL5* (23, 26), whose

expression was below the detection limit in the microarray experiment—as potential targets of the T6P pathway at the SAM (Fig. 3, E and F).

SPL genes have been shown to be regulated by diverse flowering signals and to form the molecular output of a pathway that regulates flowering as a function of a plant's age (25). The age-dependent induction of flowering is a fail-safe to ensure that plants eventually flower even in the absence of inductive signals. This is accomplished by the gradual reduction of miR156 levels independently of other signals, and a corresponding increase in miR156-targeted *SPL* transcripts, as plants age (25, 27). We compared mature miR156 levels at the meristem in SD-grown wild-type and *tps1-2 GVG:TPS1* plants at different times between 10 and 50 days after germination. Between 10 and 30 days after germination, the levels of the mature miR156 were consistently higher in the *tps1-2 GVG:TPS1* mutant relative to the wild type (Fig. 3G), which explains the reduced *SPL3*, *SPL4*, and *SPL5* expression observed in *tps1-2 GVG:TPS1* plants at these times (Fig. 3F). However, as the plants aged, miR156 declined to similarly low levels in both genotypes from 40 to 50 days after germination (Fig. 3G). This decrease of miR156 was accompanied by a strong increase of *SPL3*, *SPL4*, and *SPL5* transcript levels in wild-type plants.

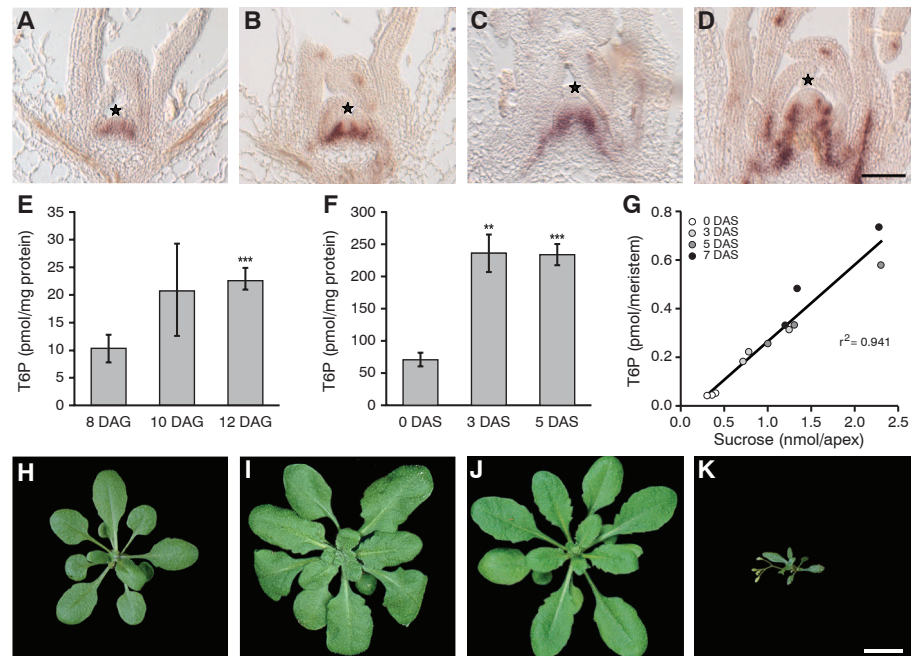


Fig. 2. *TPS1* expression and T6P concentrations in the SAM. (A to D) Detection of *TPS1* expression by RNA in situ hybridization in the SAM in LD-grown plants 6 days after germination (DAG) (A), 8 DAG (B), 10 DAG (C), and 12 DAG (D). Star indicates meristem summit. Scale bar, 100 μ m. (E and F) T6P content in dissected meristems of LD-grown Col-0 plants (E) and 30-day-old SD-grown plants shifted to LD and harvested at 0, 3, and 5 days after the shift (DAS) (F). Error bars denote SD; ** $P < 0.01$, *** $P < 0.001$ (Student's *t* test, based on four biological replicates). (G) Correlation between sucrose and T6P concentration in dissected meristems 0, 3, 5, and 7 days after shift from SD to LD. (H to K) Rosette phenotype of Col-0 (H), *35S:amiR-TPS1* #6 (I), *CLV3:otsB* #9 (J), and *CLV3:TPS1* #7 (K). Scale bar, 1 cm.

In contrast, the increase was strongly attenuated in *tps1-2 GVG:TPS1* plants (Fig. 3G).

Taken together, these results suggest that the T6P pathway controls expression of *SPL3*, *SPL4*, and *SPL5* in the SAM, in part via miR156 and in part independently of the miR156-dependent age pathway. In agreement with these findings, we observed that constitutive expression of miR156, which has been shown by several studies to delay vegetative phase transition and flowering (supplementary text and table S1), combined with down-regulation of *TPS1* (*35S:amiR-TPS1*), had an additive effect on flowering, with the double-transgenic line failing to flower in either LD or SD (Table 1, experiments 7 and 8). In addition, reducing the levels of mature miR156 by the constitutive expression of *MIM156* (28, 29), which sequesters miR156 from its targets, was sufficient to restore flowering in the *tps1-2 GVG:TPS1* mutant (Fig. 3, A to D; Table 1, experiment 9). This provides further evidence that the miR156/age pathway acts at least partially independently of the T6P pathway.

SPL proteins have also been shown to promote *FT* expression in leaves by regulating the expression of two MADS-box transcription factors, *SUPPRESSOR OF OVEREXPRESSION OF CONSTANS 1* (*SOC1*) and *FRUITFUL* (*FUL*) (25, 30). This raised the possibility that the observed repression of *FT* in *tps1-2 GVG:TPS1*

plants (Fig. 1C) was due to reduced expression of *SOC1* and *FUL*. However, expression of these two genes was not changed in the *tps1-2 GVG:TPS1* (fig. S13) and *35S:amiR-TPS1* mutant rosettes (fig. S14) before flowering, which in LD-grown wild-type plants occurs approximately 10 days after germination (fig. S4). These findings suggest that in leaves, the T6P pathway regulates *FT* largely independently of the miR156-SPL module.

Our results demonstrate that the T6P pathway regulates flowering at two sites in the plant (fig. S15). In the leaves, *TPS1* activity is required for the induction of the florigen *FT*, even under inductive photoperiod. This provides a convenient way for the plant to integrate an environmental signal (the activation of *FT* by CO in response to increasing day length in spring) with a physiological signal (the presence of high carbohydrate levels, as indicated by T6P). Together these two inputs ensure that *FT* is expressed when the conditions are optimal—that is, when day length exceeds a certain minimum and the plant has sufficient carbohydrate resources to support the energy-demanding processes of flowering and seed production. In addition, the T6P pathway affects the expression of important flowering-time and flower-patterning genes via the age pathway directly at the SAM independently of the photoperiod pathway. This might

provide a local signal to link developmental decisions in the meristem to the supply of carbohydrates. Thus, the T6P pathway acts as a signal that coordinates the induction of flowering by regulating the expression of key floral integrators in leaves and the SAM.

References and Notes

1. A. Srikanth, M. Schmid, *Cell. Mol. Life Sci.* **68**, 2013 (2011).
2. M. Abe *et al.*, *Science* **309**, 1052 (2005).
3. L. Corbesier, I. Gadisseur, G. Silvestre, A. Jacquard, G. Bernier, *Plant J.* **9**, 947 (1996).
4. I. Kardailsky *et al.*, *Science* **286**, 1962 (1999).
5. Y. Kobayashi, H. Kaya, K. Goto, M. Iwabuchi, T. Araki, *Science* **286**, 1960 (1999).
6. P. Suárez-López *et al.*, *Nature* **410**, 1116 (2001).
7. P. A. Wigge *et al.*, *Science* **309**, 1056 (2005).
8. L. Corbesier *et al.*, *Science* **316**, 1030 (2007).
9. K. E. Jaeger, P. A. Wigge, *Curr. Biol.* **17**, 1050 (2007).
10. J. Mathieu, N. Warthmann, F. Küttner, M. Schmid, *Curr. Biol.* **17**, 1055 (2007).
11. S. Tamaki, S. Matsuo, H. L. Wong, S. Yokoi, K. Shimamoto, *Science* **316**, 1033 (2007).
12. L. Corbesier, P. Lejeune, G. Bernier, *Planta* **206**, 131 (1998).
13. M. J. Paul, L. F. Primavesi, D. Jhureea, Y. Zhang, *Annu. Rev. Plant Biol.* **59**, 417 (2008).
14. J. Ponnuru, V. Wahl, M. Schmid, *Front. Plant Physiol.* **2**, 70 (2011).
15. J. E. Lunn *et al.*, *Biochem. J.* **397**, 139 (2006).
16. P. J. Eastmond *et al.*, *Plant J.* **29**, 225 (2002).
17. L. D. Gómez, A. Gilday, R. Feil, J. E. Lunn, I. A. Graham, *Plant J.* **64**, 1 (2010).
18. A. J. H. van Dijken, H. Schluepmann, S. C. Smeekeens, *Plant Physiol.* **135**, 969 (2004).
19. See supplementary materials on Science Online.
20. T. Imaizumi, T. F. Schultz, F. G. Harmon, L. A. Ho, S. A. Kay, *Science* **309**, 293 (2005).
21. F. Valverde *et al.*, *Science* **303**, 1003 (2004).
22. A. Yamaguchi, Y. Kobayashi, K. Goto, M. Abe, T. Araki, *Plant Cell Physiol.* **46**, 1175 (2005).
23. G. Cardon *et al.*, *Gene* **237**, 91 (1999).
24. G. H. Cardon, S. Höhmann, K. Nettekheim, H. Saedler, P. Huijser, *Plant J.* **12**, 367 (1997).
25. J. W. Wang, B. Czech, D. Weigel, *Cell* **138**, 738 (2009).
26. Z. Yang *et al.*, *Gene* **407**, 1 (2008).
27. G. Wu *et al.*, *Cell* **138**, 750 (2009).
28. J. M. Franco-Zorrilla *et al.*, *Nat. Genet.* **39**, 1033 (2007).
29. M. Todesco, I. Rubio-Somoza, J. Paz-Ares, D. Weigel, *PLoS Genet.* **6**, e1001031 (2010).
30. A. Yamaguchi *et al.*, *Dev. Cell* **17**, 268 (2009).

Acknowledgments: We thank C. Abel and J. Olas for help with plant work, and U. Krause for assistance with sample collection. The *tps1-2 GVG:TPS1* mutant was obtained from the Smeekens laboratory, University of Utrecht, Netherlands. Microarray data reported in this study have been deposited with EBI ArrayExpress (E-MEXP-3727). Supported by Deutsche Forschungsgemeinschaft grant SCHM-1560/6 and Priority Program 1530 (SPP1530) grant SCHM-1560/8 (M.S.), European Commission FP7 collaborative project TiMet contract 245143 (M.St.), and the Max Planck Society. The authors declare no conflict of interest.

Supplementary Materials

www.sciencemag.org/cgi/content/full/339/6120/704/DC1
Materials and Methods
Supplementary Text
Figs. S1 to S15
Tables S1 and S2
References (31–49)

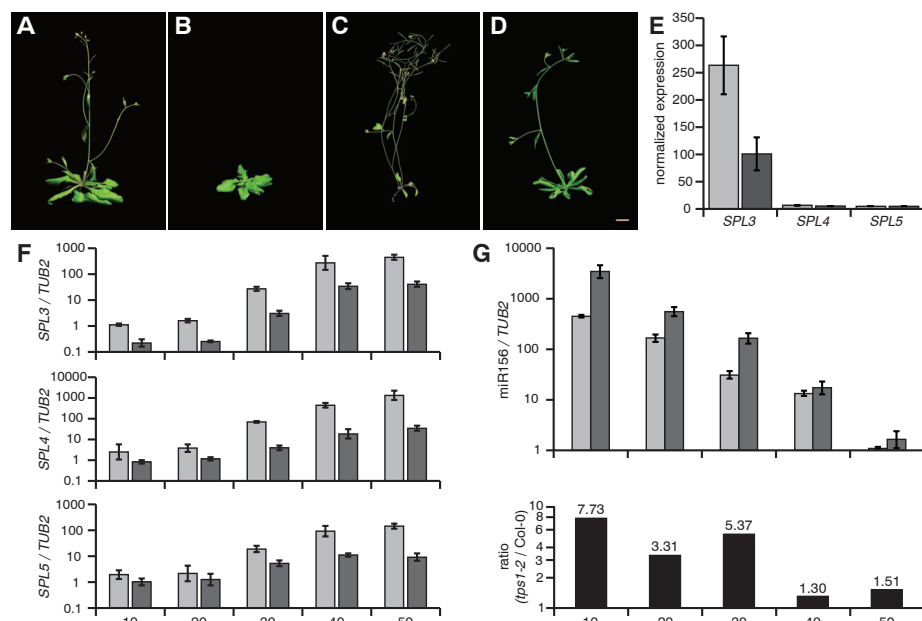


Fig. 3. SPL/miR156 module and T6P signaling. (A to D) Flowering-time phenotypes of Col-0 (A), *tps1-2 GVG:TPS1* (B), *35S:MIM156* (C), and homozygous *tps1-2 GVG:TPS1 35S:MIM156* (D) plants. Scale bar, 1 cm. (E) Expression of *SPL3*, *SPL4*, and *SPL5* in apices of 21-day-old SD-grown Col-0 (light gray) and *tps1-2 GVG:TPS1* (dark gray) as determined by microarray hybridization. Error bars indicate minimum and maximum values of two biological replicates. (F) Expression of *SPL3*, *SPL4*, and *SPL5* in SD-grown Col-0 (light gray) and *tps1-2 GVG:TPS1* (dark gray) plants 10, 20, 30, 40, and 50 days after germination. (G) Relative levels of mature miR156 as measured by qRT-PCR in apices of SD-grown Col-0 (light gray) and *tps1-2 GVG:TPS1* (dark gray) plants 10, 20, 30, 40, and 50 days after germination. Error bars in (F) and (G) denote upper and lower limit of SD of three biological replicates with three technical repetitions each.

Host-Derived Nitrate Boosts Growth of *E. coli* in the Inflamed Gut

Sebastian E. Winter,¹ Maria G. Winter,¹ Mariana N. Xavier,¹ Parameth Thiennimitr,^{1,2} Victor Poon,¹ A. Marijke Keestra,¹ Richard C. Laughlin,³ Gabriel Gomez,³ Jing Wu,³ Sara D. Lawhon,³ Ina E. Popova,⁴ Sanjai J. Parikh,⁴ L. Garry Adams,³ Renée M. Tsois,¹ Valley J. Stewart,⁵ Andreas J. Bäuml^{1*}

Changes in the microbial community structure are observed in individuals with intestinal inflammatory disorders. These changes are often characterized by a depletion of obligate anaerobic bacteria, whereas the relative abundance of facultative anaerobic Enterobacteriaceae increases. The mechanisms by which the host response shapes the microbial community structure, however, remain unknown. We show that nitrate generated as a by-product of the inflammatory response conferred a growth advantage to the commensal bacterium *Escherichia coli* in the large intestine of mice. Mice deficient in inducible nitric oxide synthase did not support the growth of *E. coli* by nitrate respiration, suggesting that the nitrate generated during inflammation was host-derived. Thus, the inflammatory host response selectively enhances the growth of commensal Enterobacteriaceae by generating electron acceptors for anaerobic respiration.

Over 90% of the cells in the human body are microbes, the majority of which reside in the large intestine, where they provide benefit to the host by stimulating the development of the immune system, supplying nutrients, and providing niche protection.

¹Department of Medical Microbiology and Immunology, School of Medicine, University of California, Davis, One Shields Avenue, Davis, CA, USA. ²Department of Microbiology, Faculty of Medicine, Chiang Mai University, Chiang Mai, Thailand. ³Department of Veterinary Pathobiology, College of Veterinary Medicine and Biomedical Sciences, Texas A&M University, College Station, TX, USA. ⁴Department of Land, Air and Water Resources, University of California, Davis, One Shields Avenue, Davis, CA, USA. ⁵Department of Microbiology, College of Biological Sciences, University of California, Davis, One Shields Avenue, Davis, CA, USA.

*To whom correspondence should be addressed. E-mail: ajbauml@ucdavis.edu

The lumen of the large bowel is thought to be primarily anaerobic, with traces of oxygen being consumed by facultative anaerobic bacteria (such as Enterobacteriaceae), which constitute a small fraction (approximately 0.1%) of the microbial community (microbiota) (1). The vast majority of microbes in the large intestine belong to the phyla Bacteroidetes (class Bacteroidia) and Firmicutes (class Clostridia), two groups of obligate anaerobic bacteria that lack the ability to respire and instead rely on the fermentation of amino acids and complex polysaccharides for growth. On the phylum level, this bacterial community structure is conserved between humans and mice (1, 2). Conditions of inflammation in the large bowel are accompanied by a microbial imbalance (dysbiosis), however, which is characterized by a marked decrease

in the representation of obligate anaerobic bacteria and an increased relative abundance of facultative anaerobic bacteria belonging to the family Enterobacteriaceae (3–12) (fig. S1, A and B).

An important component of the host inflammatory response is the generation of reactive nitrogen species (RNS) and reactive oxygen species (ROS) (fig. S1C). For example, inducible nitric oxide synthase (iNOS) is expressed at high levels during intestinal inflammation, and elevated nitric oxide (NO) concentrations are detected in the colonic luminal gas of individuals with inflammatory bowel disease (13–15). The reaction of nitric oxide radicals (NO) with superoxide radicals (O₂^{•−}) yields peroxynitrite (ONOO[−]), which can either generate nitrate (NO₃[−]) (16) or oxidize organic sulfides and tertiary amines to S-oxides and N-oxides (17, 18). Similarly, inflammation-derived ROS can generate S-oxides and N-oxides (17, 18). Unlike obligate anaerobic members of the gut microbiota, the facultative anaerobic Enterobacteriaceae can use nitrate, S-oxides, and N-oxides as terminal electron acceptors for anaerobic respiration. We thus hypothesized that colitis produces dysbiosis because highly oxidized by-products of intestinal inflammation (such as nitrate, S-oxides, and N-oxides) might enable commensal Enterobacteriaceae to edge out fermenting microbes in the gut lumen by using anaerobic respiration for energy production (fig. S1C).

Escherichia coli, a prototypic member of the Enterobacteriaceae, possesses three nitrate reductases, two S-oxygen reductases, and three N-oxygen reductases encoded by the *narGHJI*, *narZYWV*, *napFDAGHBC*, *dmsABC*, *ynfDEFGH*, *torCAD*, *torYZ*, and *yedYZ* operons, respectively (19). One common feature shared by these terminal reductases is the incorporation of an

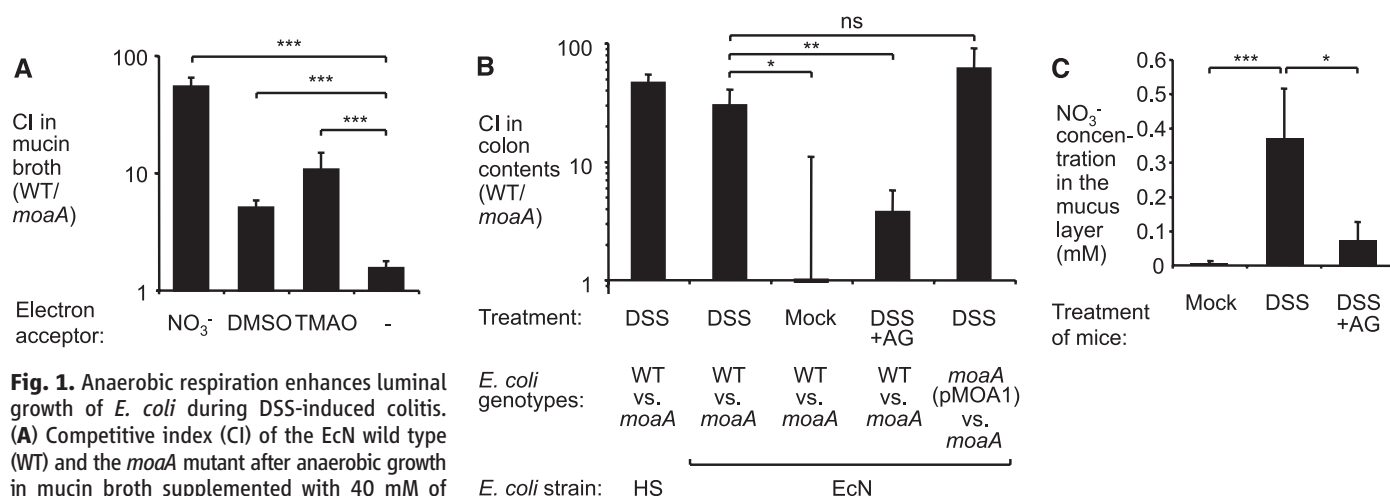


Fig. 1. Anaerobic respiration enhances luminal growth of *E. coli* during DSS-induced colitis. **(A)** Competitive index (CI) of the EcN wild type (WT) and the *moaA* mutant after anaerobic growth in mucin broth supplemented with 40 mM of the indicated electron acceptors (*n* = 3). **(B)** Mock-treated mice (Mock), DSS-treated mice (DSS), or mice treated with DSS and AG (DSS+AG) were inoculated with the indicated mixtures of *E. coli* strains, and the CI in colon contents was determined 5 days after inoculation. A plasmid (pMOA1) carrying the cloned *moaA* gene was used to complement the *moaA* mutant (*moaA*). The number of animals (*n*) is

given in fig. S3C. **(C)** Concentration of nitrate (NO₃[−]) determined in the cecal mucus layer of mock-treated mice (*n* = 4), DSS-treated mice (DSS, *n* = 3), or mice treated with DSS+AG (*n* = 4). Bars represent geometric means ± SE. **P* < 0.05, ***P* < 0.01, ****P* < 0.001; ns, not statistically significant (Student's *t* test).

essential molybdenum cofactor into the active site. To test the idea that anaerobic respiration provides a growth benefit in the inflamed intestine, we generated mutants deficient for the biosynthesis of the molybdenum cofactor (*moaA* mutants) in the *Escherichia coli* strains HS and Nissle 1917 (EcN) (fig. S2, A and B). These *moaA* mutants were anaerobically cocultured with the respective wild-type strains in mucin broth in the presence or absence of nitrate, DMSO (dimethyl S-oxide), or TMAO (trimethylamine N-oxide) (Fig. 1A and fig. S2C). Enrichment for the *E. coli* wild-type strains occurred in the presence of nitrate, DMSO, and TMAO, suggesting that anaerobic respiration can provide a growth benefit during the anaerobic growth conditions encountered in the intestinal mucus layer.

We next inoculated untreated mice (C57BL/6 mice) or mice with chemically induced colitis [induced by treatment with dextran sulfate sodium (DSS)] intragastrically with an equal mixture of EcN and its isogenic *moaA* mutant (fig. S1D). Both the wild-type strain and the *moaA* mutant colonized the intestine of mock-treated mice poorly, but similar numbers of each strain were recovered from colon contents 5 days after inoculation (Fig. 1B). This result suggested that in the absence of intestinal inflammation, anaerobic respiration did not provide a growth benefit for *E. coli*. DSS treatment induced inflammation in the colon and increased mRNA levels of proinflammatory markers in wild-type mice (fig. S3). In contrast to mock-treated mice, the EcN wild-type strain was recovered from colon contents of DSS-treated

mice in significantly higher numbers than the *moaA* mutant 5 days after inoculation. Similar results were observed when DSS-treated mice were inoculated with an equal mixture of the human commensal *E. coli* strain HS and an isogenic *moaA* mutant. Expression of *moaA* from a low-copy-number plasmid (pMOA1) in the EcN *moaA* mutant fully restored the phenotype to wild-type levels. Outgrowth of the EcN wild-type strain over the *moaA* mutant was also observed in the DSS colitis model when mice were precolonized with *E. coli* (fig. S4). These findings supported the idea that anaerobic respiration provided a growth advantage to commensal *E. coli* during intestinal inflammation.

Although ROS can be generated by several NADPH (reduced nicotinamide adenine dinucleotide phosphate) oxidases, the sole source of NO during inflammation is iNOS. To determine the contribution of RNS to the growth advantage mediated by anaerobic respiration, DSS-treated mice were treated with the iNOS inhibitor aminoguanidine hydrochloride (AG) and inoculated with a mixture of the EcN wild type and the *moaA* mutant. Consistent with the idea that RNS are a significant source for the production of terminal electron acceptors during inflammation, the growth advantage of the EcN wild type over the *moaA* mutant in the DSS-colitis model was significantly ($P < 0.01$) blunted after AG treatment (Fig. 1B). The nitrate/nitrite redox couple has a greater redox potential than the DMSO/DMS or the TMAO/TMA redox couples, which makes nitrate the preferred respiratory electron acceptor for the growth of *E. coli* under anaerobic conditions (19). Therefore, we next determined whether nitrate becomes available in the lumen of the inflamed intestine. To accomplish this objective, the concentration of nitrate was determined in the cecal mucus layer of mock-treated mice or mice with DSS-induced colitis (Fig. 1C). Whereas nitrate levels were at the limit of detection in mock-treated control mice, a significant ($P < 0.001$) increase in nitrate levels was observed in DSS-treated animals. AG treatment of mice with DSS-induced colitis significantly ($P < 0.05$) dampened nitrate production, thus supporting the hypothesis that nitrate is generated in the intestinal lumen as part of the host inflammatory response.

We next tested whether nitrate respiration bestows a growth advantage on *E. coli* wild-type isolates. To this end, we inactivated the *narG*, *napA*, and *narX* genes, which encode nitrate reductases, in the probiotic EcN. In contrast to the wild-type strain, the nitrate respiration-deficient *narG napA narX* triple mutant lacked nitrate reductase activity and was outcompeted by the wild-type strain during competitive anaerobic growth in mucin broth in the presence of nitrate (fig. S5). To determine whether nitrate respiration provides a colonization advantage in the intestine, mock-treated and DSS-treated wild-type (C57BL/6) mice were inoculated intragastrically with an equal mixture of the EcN

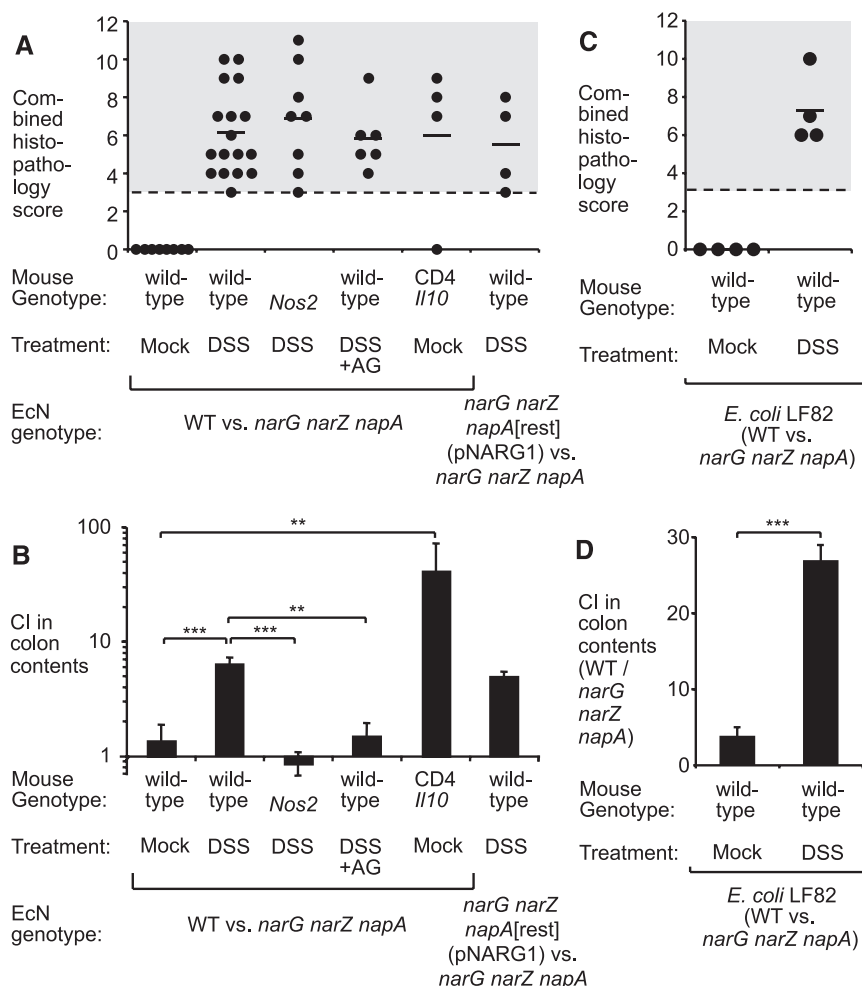


Fig. 2. Wild-type *E. coli* (WT) outcompetes a nitrate respiration-deficient mutant during colitis. Mock-treated (Mock), DSS-treated (DSS), or DSS+AG-treated wild-type mice; *Nos2*-deficient mice (*Nos2*); or mice harboring T cells deficient for the production of IL-10 (*Cd4 Il10* mice) were inoculated with the indicated mixtures of *E. coli* strains. *narG narZ napA*, *E. coli* nitrate respiration-deficient mutant. The *narG narZ napA* mutant was complemented by introducing a functional chromosomal *napA* allele and a plasmid (pNARG1) carrying the cloned *narG* gene [*narG narZ napA*(rest)(pNARG1)]. Pathological changes in the colon (A and C) and the CI recovered from colon contents (B and D) were determined 5 days after inoculation. (A) and (C) Combined histopathology score in the colon. Each dot represents data from an individual animal. Experiments were performed with EcN [(A) and (B)] or *E. coli* LF82 [(C) and (D)]. (B) and (D) Bars represent geometric means \pm SE. ** $P < 0.01$, *** $P < 0.001$ (Student's *t* test). *n* is given in (A) and (C).

wild type and a *narG napA narZ* triple mutant (Fig. 2). In the absence of inflammation (mock treatment, Fig. 2A and figs. S6 and S7), both the EcN wild type and the *narG napA narZ* triple mutant were recovered in similar numbers from colonic (Fig. 2B) and cecal contents (fig. S8A). In contrast, the EcN wild-type strain was more abundant than the *narG napA narZ* triple mutant when colitis was induced by administration of DSS. Similar results were obtained using an adherent invasive *E. coli* (AIEC) isolate (LF82) that was isolated from an inflammatory bowel disease patient (Fig. 2, C and D, and fig. S5, C and D). To test whether nitrate respiration provides a growth benefit in the absence of iNOS-dependent nitrate production, the competitive colonization experiment was repeated in DSS-treated iNOS-deficient mice (i.e., mice carrying a mutation in the *Nos2* gene) and DSS-treated wild-type mice (C57BL/6) that received AG. The severity of the colitis induced by the DSS treatment was similar among all treatment groups (Fig. 2A and fig. S7) 5 days after inoculation with *E. coli*. The EcN wild type and its nitrate respiration-deficient mutant were recovered in

equal numbers from DSS-treated iNOS-deficient mice or from DSS+AG-treated wild-type mice. Similar results were obtained using varying concentrations of DSS (fig. S9) as well as with *E. coli* strain K-12 (fig. S10). Concomitant expression of *narG* from a low-copy-number plasmid (pNARG1) and restoration of the *napA* mutation to its wild-type allele [*napA(restored)*] in the *narG narZ napA* mutant reestablished fitness in the inflamed gut to similar levels as observed with the wild-type strain (Fig. 2B and fig. S8A). Collectively, these data suggested that the reduction of host-derived nitrate by *E. coli* confers a growth advantage during gut inflammation.

To validate our findings in a second murine model of colitis, we generated mice that harbored T cells deficient for the production of the anti-inflammatory cytokine interleukin-10 (IL-10) [*Cd4 Il10* mice (*Il10^{fllox/fllox} Cd4-cre*)], a mouse strain that developed spontaneous colitis (Fig. 2A and S7) (20). After the onset of intestinal inflammation, mice were inoculated intragastrically with an equal mixture of the EcN wild type and the *narG napA narZ* triple mutant

(Fig. 2B). The nitrate respiration-proficient wild-type strain outcompeted the *narG napA narZ* mutant in the colon contents of *Cd4 Il10* mice 5 days after inoculation ($P < 0.05$). To investigate whether the growth of *E. coli* by nitrate respiration can also be observed in an unrelated animal model of intestinal inflammation, bovine ligated ileal loops were inoculated with thapsigargin, a proinflammatory compound, or mock-treated (vehicle control) (Fig. 3, A to C). At 8 hours after the inoculation of thapsigargin-treated loops with a mixture of EcN and the *narG napA narZ* mutant, significantly ($P < 0.05$) greater numbers of wild-type EcN were recovered from luminal fluid and mucus (Fig. 3D).

To determine whether nitrate respiration increases bacterial recovery from the inflamed intestine when mice are inoculated with a single *E. coli* strain, DSS-treated mice were inoculated either with the EcN wild-type strain or with the *narG napA narZ* mutant. Mice inoculated with EcN or the *narG napA narZ* mutant exhibited a similar severity of colonic inflammation (Fig. 3, E to G). The EcN wild-type strain was recovered in significantly ($P < 0.01$)

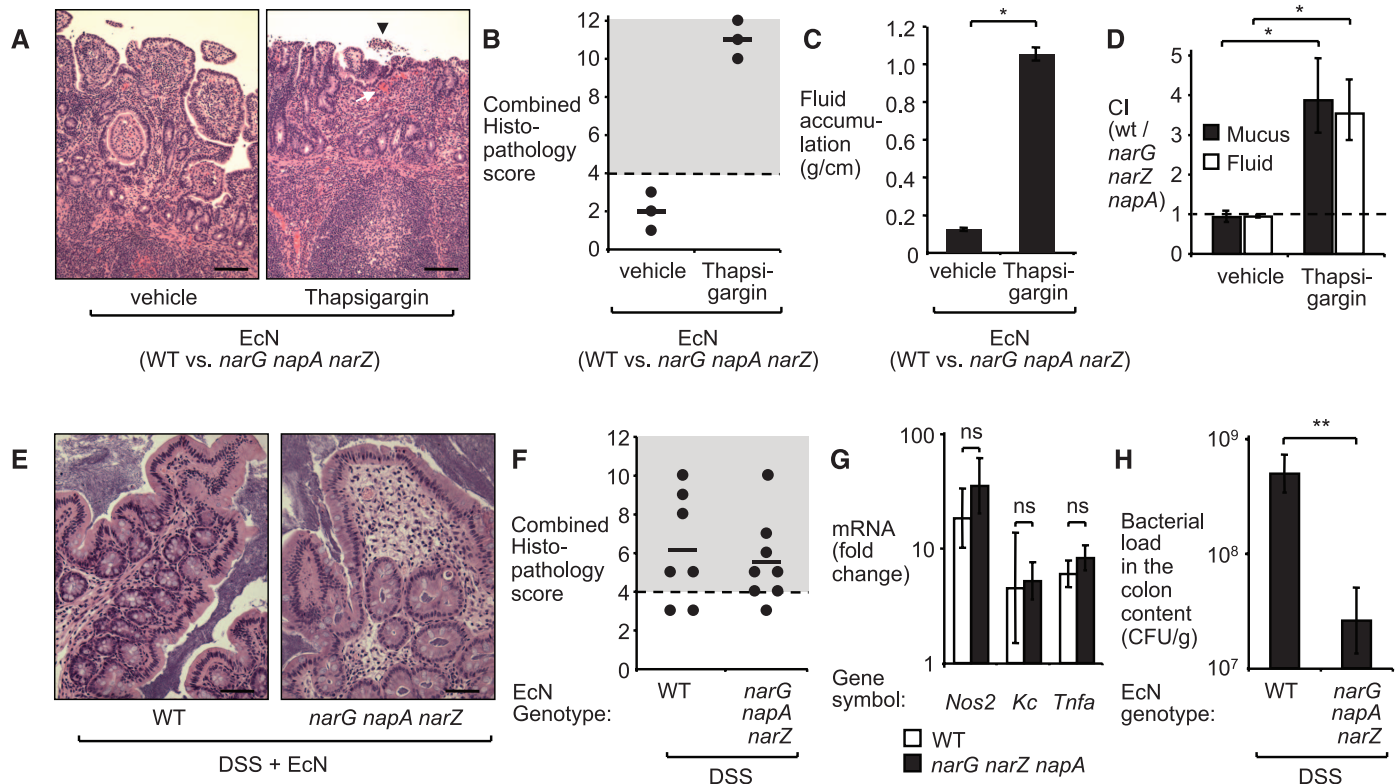


Fig. 3. Nitrate respiration enhances luminal growth of EcN during inflammation. (A to D) Bovine ligated ileal loops treated with thapsigargin or mock-treated (vehicle) were inoculated with a mixture of EcN (WT) and a nitrate respiration-deficient mutant (*narG napA narZ*). Samples were collected 8 hours after inoculation. (A) Representative hematoxylin and eosin (H&E)-stained ileal sections. Scale bar, 200 μ m. (B) Combined histopathology score in the ileum. Each dot represents data from an individual animal. (C) Fluid accumulation in ligated ileal loops. (D) CFs recovered from the luminal fluid (open bars) or mucus scrapings (solid bars). (E to H) DSS-treated mice were inoculated either with EcN (WT) or with the *narG napA narZ* mutant. Inflammation in the colon (E to G) and bacterial numbers recovered from colon contents (E) were determined 5 days after inoculation. (E) Representative H&E-stained colonic sections. Scale bar, 100 μ m. (F) Combined histopathology score in the colon. (G) Expression of *Nos2*, *Kc*, and *Tnfa* in colonic RNA samples analyzed by quantitative real-time polymerase chain reaction (fold increases over mock-treated mice). (H) Bacterial numbers [colony-forming units (CFU)] recovered from colon contents. In (C), (D), (G), and (H), bars represent geometric means \pm SE. * $P < 0.05$, ** $P < 0.01$; ns, not statistically significant (Student's *t* test). *n* is given in (B) and (F).

higher numbers from colon contents than was the nitrate respiration–deficient mutant (Fig. 3H and fig. S8B). Collectively, these data suggested that nitrate respiration conferred a marked growth advantage on commensal *E. coli* in the lumen of the inflamed gut.

The picture emerging from this study is that nitrate generated as a by-product of the host inflammatory response can be used by *E. coli*, and likely by other commensal Enterobacteriaceae, to edge out competing microbes that rely on fermentation to generate energy for growth. Obligate anaerobic microbes in the intestine compete for nutrients that are available for fermentation but cannot use nonfermentable nutrients (such as fermentation end products). The ability to degrade nonfermentable substrates probably enables *E. coli* to sidestep this competition, which explains the fitness advantage conferred by nitrate respiration in the inflamed gut. Through this mechanism, inflammation contributes to a bloom of nitrate-respiration–proficient Enterobacteriaceae, providing a plausible explanation for the dysbiosis associated with intestinal inflammation (3–12). This general principle might also influence the dynamics of host-associated

bacterial communities outside the large bowel, as nitrate respiration confers a fitness advantage in the oxygen-poor and nitrate-rich environment of the cystic fibrosis airway (21).

References and Notes

1. P. B. Eckburg *et al.*, *Science* **308**, 1635 (2005).
2. R. E. Ley *et al.*, *Proc. Natl. Acad. Sci. U.S.A.* **102**, 11070 (2005).
3. A. Krook, B. Lindström, J. Kjellander, G. Järnerot, L. Bodin, *J. Clin. Pathol.* **34**, 645 (1981).
4. M. H. Gaffner, C. D. Holdsworth, B. I. Duerden, *J. Med. Microbiol.* **35**, 238 (1991).
5. P. Seksik *et al.*, *Gut* **52**, 237 (2003).
6. U. Gophna, K. Sommerfeld, S. Gophna, W. F. Doolittle, S. J. Veldhuyzen van Zanten, *J. Clin. Microbiol.* **44**, 4136 (2006).
7. D. N. Frank *et al.*, *Proc. Natl. Acad. Sci. U.S.A.* **104**, 13780 (2007).
8. M. M. Heimesaat *et al.*, *PLoS ONE* **2**, e662 (2007).
9. C. Lupp *et al.*, *Cell Host Microbe* **2**, 119 (2007).
10. B. Stecher *et al.*, *PLoS Biol.* **5**, e244 (2007).
11. M. Barman *et al.*, *Infect. Immun.* **76**, 907 (2008).
12. W. S. Garrett *et al.*, *Cell Host Microbe* **8**, 292 (2010).
13. J. O. N. Lundberg, J. M. Lundberg, K. Alving, P. M. Hellström, *Lancet* **344**, 1673 (1994).
14. I. I. Singer *et al.*, *Gastroenterology* **111**, 871 (1996).
15. A. Enocksson, J. Lundberg, E. Weitzberg, A. Norrby-Teglund, B. Svenungsson, *Clin. Diagn. Lab. Immunol.* **11**, 250 (2004).

16. C. Szabó, H. Ischiropoulos, R. Radi, *Nat. Rev. Drug Discov.* **6**, 662 (2007).
17. C. Schöneich, *Biochim. Biophys. Acta* **1703**, 111 (2005).
18. B. Balagam, D. E. Richardson, *Inorg. Chem.* **47**, 1173 (2008).
19. R. B. Gennis, V. Stewart, in *Escherichia coli and Salmonella. Cellular and Molecular Biology*, F. C. Neidhardt *et al.*, Eds. (ASM Press, Washington, DC, 1996), vol. 1, pp. 217–261.
20. M. C. Pils *et al.*, *Inflamm. Bowel Dis.* **17**, 2038 (2011).
21. L. R. Hoffman *et al.*, *PLoS Pathog.* **6**, e1000712 (2010).

Acknowledgments: We thank W. Müller for providing *Il10^{fllox}/Cd4-cre* mice and E. Romao for technical assistance. The data reported in the manuscript are tabulated in the main paper and in the supplementary materials. This work was supported by the California Agricultural Experiment Station (I.E.P. and S.J.P.) and Public Health Service grants AI090387 (R.M.T.), AI076246 (L.G.A. and A.J.B.), and AI088122 (A.J.B.). P.T. was supported by a scholarship from the Faculty of Medicine, Chiang Mai University, Thailand.

Supplementary Materials

www.sciencemag.org/cgi/content/full/339/6120/708/DC1
Materials and Methods
Figs. S1 to S11
Tables S1 and S2
References (22–39)

7 November 2012; accepted 5 December 2012
10.1126/science.1232467

Rif1 Prevents Resection of DNA Breaks and Promotes Immunoglobulin Class Switching

Michela Di Virgilio,¹ Elsa Callen,^{3*} Arito Yamane,^{4*} Wenzhu Zhang,^{5*} Mila Jankovic,¹ Alexander D. Gitlin,¹ Niklas Feldhahn,¹ Wolfgang Resch,⁴ Thiago Y. Oliveira,^{1,6,7} Brian T. Chait,⁵ André Nussenzweig,³ Rafael Casellas,⁴ Davide F. Robbiani,¹ Michel C. Nussenzweig^{1,2†}

DNA double-strand breaks (DSBs) represent a threat to the genome because they can lead to the loss of genetic information and chromosome rearrangements. The DNA repair protein p53 binding protein 1 (53BP1) protects the genome by limiting nucleolytic processing of DSBs by a mechanism that requires its phosphorylation, but whether 53BP1 does so directly is not known. Here, we identify Rap1-interacting factor 1 (Rif1) as an ATM (ataxia-telangiectasia mutated) phosphorylation-dependent interactor of 53BP1 and show that absence of Rif1 results in 5′–3′ DNA-end resection in mice. Consistent with enhanced DNA resection, Rif1 deficiency impairs DNA repair in the G₁ and S phases of the cell cycle, interferes with class switch recombination in B lymphocytes, and leads to accumulation of chromosome DSBs.

The DNA damage response factor p53 binding protein 1 (53BP1) is a multidomain protein containing a chromatin-binding tudor domain, an oligomerization domain, tandem breast cancer 1 (BRCA1) C-terminal (BRCT) domains, and an N-terminal domain with 28 SQ/TQ potential phosphorylation sites for phosphatidylinositol 3-kinase-related kinases [PIKKs, ataxia-telangiectasia mutated (ATM)/ATM and Rad3-related/DNA-dependent protein kinase catalytic subunit (DNA-PKcs)] (1–3). 53BP1 contributes to DNA repair in several ways: This protein facilitates joining between intrachromosomal double-strand breaks (DSBs) at a distance (synapsis) (4–7), it enables heterochromatic DNA repair through relaxa-

tion of nucleosome compaction (2, 3), and it protects DNA ends from resection and thereby favors repair of DSBs that occur in G₁ phase by nonhomologous end joining (NHEJ) (4, 5, 8). Consistent with its role in DNA-end protection, 53BP1 is essential for class switch recombination (CSR) in B lymphocytes (9, 10).

Structure-function studies indicate that, besides the recruitment of 53BP1 to DNA ends, protection requires 53BP1 phosphorylation (4), but how this protective effect is mediated is unknown. To identify phosphorylation-dependent interactors of 53BP1, we applied stable isotope labeling by amino acids in cell culture (SILAC). *Tip53bp1^{-/-}* (*Tip53bp1* encodes 53BP1) B cells were

infected with retroviruses encoding a C-terminal deleted version of 53BP1 (53BP1^{DB}) or a phospho-mutant in which all 28 N-terminal potential PIKK phosphorylation sites were mutated to alanine (53BP1^{DB28A}) (4), in media containing isotopically heavy (53BP1^{DB}) or light (53BP1^{DB28A}) lysine and arginine (fig. S1, A to C) (11).

Most proteins coprecipitating with 53BP1^{DB} and 53BP1^{DB28A} displayed a H/(H + L) ratio of ~0.5 (H, heavy; L, light), which is characteristic of phospho-independent association (average of 0.57 ± 0.09, peptide count: at least four) (Fig. 1 and table S1). Many of these proteins are nonspecific contaminants, but others such as KRAB-associated protein 1 (KAP-1), dynein light chain LC8-type 1 (Dnll1), Nijmegen breakage syndrome 1 (Nbs1), and H2AX represent authentic phospho-independent 53BP1-interacting proteins (fig. S1D). Three proteins displayed an abundance ratio that was more than four standard deviations (SDs) above the mean, indicating that these proteins interact specifically

¹Laboratory of Molecular Immunology, The Rockefeller University, New York, NY 10065, USA. ²Howard Hughes Medical Institute (HHMI), The Rockefeller University, New York, NY 10065, USA. ³Laboratory of Genome Integrity and Center for Cancer Research, National Cancer Institute (NCI), National Institutes of Health (NIH), Bethesda, MD 20892, USA. ⁴Genomics and Immunity and National Institute of Arthritis and Musculoskeletal and Skin Diseases (NIAMS), NCI, NIH, Bethesda, MD 20892, USA. ⁵Laboratory of Mass Spectrometry and Gaseous Ion Chemistry, The Rockefeller University, New York, NY 10065, USA. ⁶Department of Genetics, Faculty of Medicine, University of São Paulo, Ribeirão Preto, Brazil. ⁷National Institute of Science and Technology for Stem Cells and Cell Therapy, Ribeirão Preto, Brazil.

*These authors contributed equally to this work.

†To whom correspondence should be addressed. E-mail: nussen@rockefeller.edu

with phosphorylated 53BP1: Pax interaction with transcription-activation domain protein-1 (Paxip1, or PTIP; 0.95), PTIP-associated protein 1 (Pa1; 0.97), and Rap1-interacting factor 1 (Rif1) (0.96) (Fig. 1 and figs. S1D and S2). PTIP was known to interact with 53BP1 in a phospho-dependent manner (12), whereas Pa1 and Rif1 were not.

Rif1 was originally identified in budding yeast as a protein with a key role in telomere length maintenance (13). However, in mammalian cells, Rif1 is not essential for telomere homeostasis, but has been assigned a number of different roles in maintaining genome stability, including participation in the DNA damage response (14–16), repair of S-phase DNA damage (17, 18), and regulation of origin firing during DNA replication (19, 20). However, the mechanism by which Rif1 might contribute to DNA repair and maintenance of genome stability is not known.

To confirm that Rif1 interaction with 53BP1 is dependent on phosphorylation, we performed Western blot analysis of Flag immunoprecipitates from lysates of irradiated *Trp53bp1*^{−/−} B cells infected with retroviruses encoding 53BP1^{DB} or 53BP1^{DB28A}. Whereas Dynl1, a phospho-independent 53BP1 interactor (SILAC ratio: 0.55) (fig. S1D), coimmunoprecipitated with 53BP1^{DB} and 53BP1^{DB28A} to a similar extent (Fig. 2A), only 53BP1^{DB} coimmunoprecipitated with Rif1. We conclude that the interaction between 53BP1 and Rif1 is dependent on phosphorylation of 53BP1.

Ataxia-telangiectasia mutated phosphorylates 53BP1 in response to DSBs (1, 3). To determine whether ATM induces DNA damage-dependent association between Rif1 and 53BP1, we compared irradiated and nonirradiated B cells in coimmunoprecipitation experiments. Although we detected small amounts of Rif1 in 53BP1^{DB} immunoprecipitates from unirradiated cells, this was increased by a factor of >3 after irradiation, and the increase was abrogated by treatment with the ATM inhibitor KU5933 (Fig. 2B). We conclude that Rif1 preferentially interacts with phosphorylated 53BP1 in a DNA damage- and ATM-dependent manner.

Rif1 is recruited to DNA damage foci by 53BP1 (15). To determine whether 53BP1 phosphorylation is required for Rif1 focus formation, we tested Rif1 foci in irradiated *Trp53bp1*^{−/−} immortalized mouse embryonic fibroblasts (iMEFs), which were stably transduced with either 53BP1^{DB} or 53BP1^{DB28A}. Rif1 foci were readily detected and colocalized with 53BP1^{DB} (Fig. 2C). In contrast, although 53BP1^{DB28A} formed normal-appearing foci, Rif1 foci were rare and did not colocalize with 53BP1 (Fig. 2C). Furthermore, Rif1 recruitment to ionizing radiation-induced foci (IRIF) and colocalization with 53BP1 were abrogated in ATM-deficient but not DNA-PKcs-deficient iMEFs (fig. S3) (15). We conclude that Rif1 recruitment to DNA damage response foci is dependent on ATM-mediated 53BP1 phosphorylation.

The phosphorylation of 53BP1 is essential for CSR (4). To examine the role of Rif1 in joining DSBs during CSR, we conditionally ablated Rif1 in B cells using CD19^{Cre}, which is expressed specifically in B cells (*Rif1*^{F/F}CD19^{Cre/+} mice) (fig. S4, A to C). To induce CSR, B cells were activated with lipopolysaccharide (LPS) and interleukin-4 (IL-4) in vitro, and switching to immunoglobulin G1 (IgG1) or IgG3 was measured by flow cytometry. CSR to IgG1 and IgG3 was markedly reduced in *Rif1*^{F/F}CD19^{Cre/+} B cells, but less so than in *Trp53bp1*^{−/−} controls (Fig. 3, A and B, and fig. S5). Switch junctions from *Rif1*^{F/F}CD19^{Cre/+} B cells were comparable to those from *Trp53bp1*^{−/−} and wild-type controls (fig. S6) (7), which indicates that, similar to 53BP1 deficiency, absence of Rif1 does not alter the nature of productive CSR joining events.

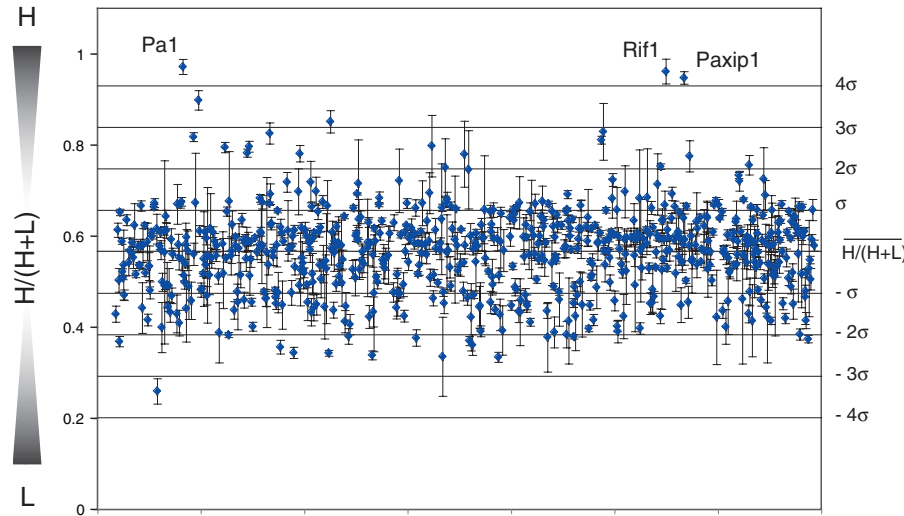


Fig. 1. Identification of phospho-dependent 53BP1 interactors. The graph shows the $H/(H + L)$ ratio distribution of proteins identified by SILAC. Error bars represent the SD of the $H/(H + L)$ mean value for all of the peptides identified for each individual protein (only proteins with at least four peptides were included). $H/(H + L)$ and σ are the mean (0.57) and SD (0.09) of the distribution, respectively.

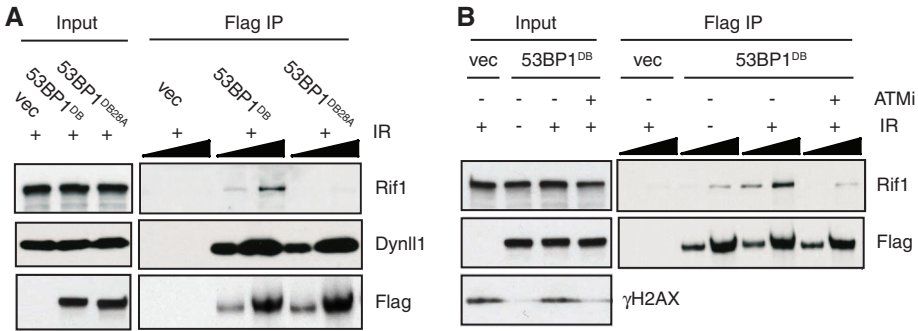


Fig. 2. Rif1 interaction with 53BP1 is dependent on phosphorylation, DNA damage, and ATM. (A) Western blot analysis of anti-Flag immunoprecipitates (IP) from irradiated (IR) *Trp53bp1*^{−/−} B lymphocytes infected with empty vector (vec), 53BP1^{DB}, or 53BP1^{DB28A} virus. Triangles indicate threefold dilution. Data are representative of two independent experiments. (B) Western blot analysis of anti-Flag immunoprecipitates from *Trp53bp1*^{−/−} B cells infected with empty vector or 53BP1^{DB}. Cells were either left untreated or irradiated [50 gray (Gy), 45-min recovery] in the presence or absence of the ATM kinase inhibitor KU5933 (ATMi). Triangles indicate threefold dilution. Data are representative of two independent experiments. (C) Immunofluorescent staining for 53BP1 (Flag) and Rif1 in irradiated *Trp53bp1*^{−/−} iMEFs reconstituted with 53BP1^{DB} or 53BP1^{DB28A} retroviruses (4). Magnification, 100x; scale bars, 5 μ m. Data are representative of two independent experiments. DAPI, 4',6-diamidino-2-phenylindole.

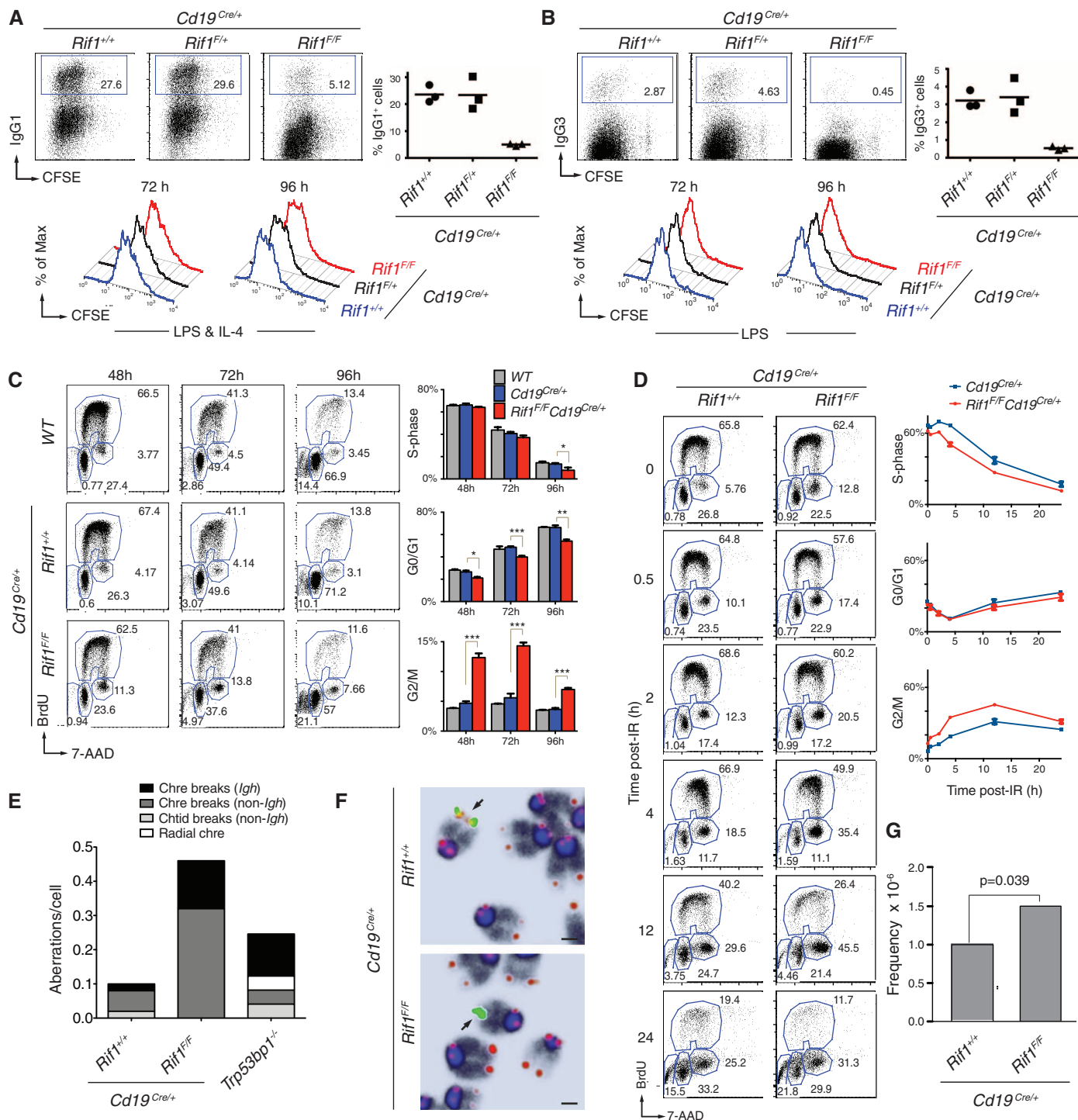


Fig. 3. *Rif1* deficiency impairs CSR and causes *Igh* and genome instability in primary B cells. (A) (Left) CSR to IgG1 96 hours after stimulation of B lymphocytes with LPS and IL-4. (Right) Summary dot plot for three independent experiments ($n =$ three mice per genotype). Mean values are: 23.6% for *Cd19^{Cre/+}*, 23.4% for *Rif1^{F/+}**Cd19^{Cre/+}*, and 5.0% for *Rif1^{F/F}**Cd19^{Cre/+}* ($P < 0.008$ with the paired Student's t test). (Bottom) B cell proliferation by carboxyfluorescein succinimidyl ester (CFSE) dilution. Data are representative of three independent experiments. (B) Same as in (A) but for CSR to IgG3 after stimulation with LPS alone. Mean values are: 3.2% for *Cd19^{Cre/+}*, 3.4% for *Rif1^{F/+}**Cd19^{Cre/+}*, and 0.5% for *Rif1^{F/F}**Cd19^{Cre/+}* ($P < 0.008$). (C) (Left) Cell cycle analysis of primary B cells after stimulation with LPS and IL-4. BrdU, 5-bromo-2'-deoxyuridine; 7-AAD, 7-amino-actinomycin D. (Right) Summary histograms for S, G₀/G₁, and G₂/M phase cells from two independent experiments ($n =$ four mice per genotype). Error bars indicate SEM.

* $0.01 < P < 0.05$, ** $0.001 < P < 0.01$, *** $P < 0.001$. WT, wild type. (D) (Left) Cell cycle analysis of LPS- and IL-4-stimulated splenocytes at the indicated times after irradiation (6 Gy). (Right) Summary graphs for S, G₀/G₁, and G₂/M phase cells from two independent experiments ($n =$ three mice per genotype). Error bars indicate SD. (E) Analysis of genomic instability in metaphases from B cell cultures. Chtid, chromatid; Chre, chromosome. Data are representative of two independent experiments ($n = 50$ metaphases analyzed per genotype per experiment). (F) Examples of *Igh*-associated aberrations in *Rif1^{F/F}**Cd19^{Cre/+}* B cells. Chromosomes were hybridized with an *Igh* *Cα* probe (green; centromeric of *Cy1*) and a telomeric sequence-specific probe (red) and were counterstained with DAPI (dark blue/black). Arrows indicate *Igh* *Cα*/telomeric signal on chromosome 12. Magnification, 63×; scale bars, 1 μm. (G) Frequency of *c-myc/Igh* translocations in activated B cells. The graph shows combined results from three mice per genotype.

A similar CSR defect was also obtained by conditionally deleting *Rif1* with 4-hydroxytamoxifen (4HT) in *Rif1^{F/F}ROSA26^{Cre-ERT2}/+* B cells (fig. S7). Finally, short hairpin RNA-mediated partial down-regulation of CtBP-interacting protein (CtIP), which interacts with *Rif1* (fig. S8C) and has been implicated in processing of DNA ends (21, 22), resulted in a very small but reproducible increase in CSR (fig. S8, A and B). Thus, *Rif1* is essential for normal CSR, and CtIP may not be the only factor that contributes to end processing in *Rif1*-deficient B cells.

Class switch recombination requires cell division, activation-induced cytidine deaminase (AID) expression, and *Igh* germline transcription (23). There are conflicting reports that *Rif1* is required for proliferation in MEFs, but not in DT40 B cells (17, 18). We found that cell division profiles of *Rif1^{F/F}Cd19^{Cre/+}* and 4HT-treated *Rif1^{F/F}ROSA26^{Cre-ERT2}/+* B cells were indistinguishable from controls (Fig. 3, A and B; and fig. S7, A, C, E, and G), indicating that *Rif1* is dispensable for B cell proliferation in vitro. Finally, AID mRNA and protein expression and *Igh* germ-

line transcription were not affected by *Rif1* deletion (fig. S4, B and D). We next examined the role of *Rif1* in cell cycle progression in primary B cells. We found no major differences in the percentage of cells in G₀/G₁ and S phases (Fig. 3C). However, the number of cells in G₂/M phase was increased approximately twofold in the absence of *Rif1* (2.64-, 2.56-, and 1.91-fold at 48, 72, and 96 hours, respectively) (Fig. 3C). We obtained similar results with the use of *Rif1^{F/F}ROSA26^{Cre-ERT2}/+* B cells treated with 4HT (fig. S7, H and I).

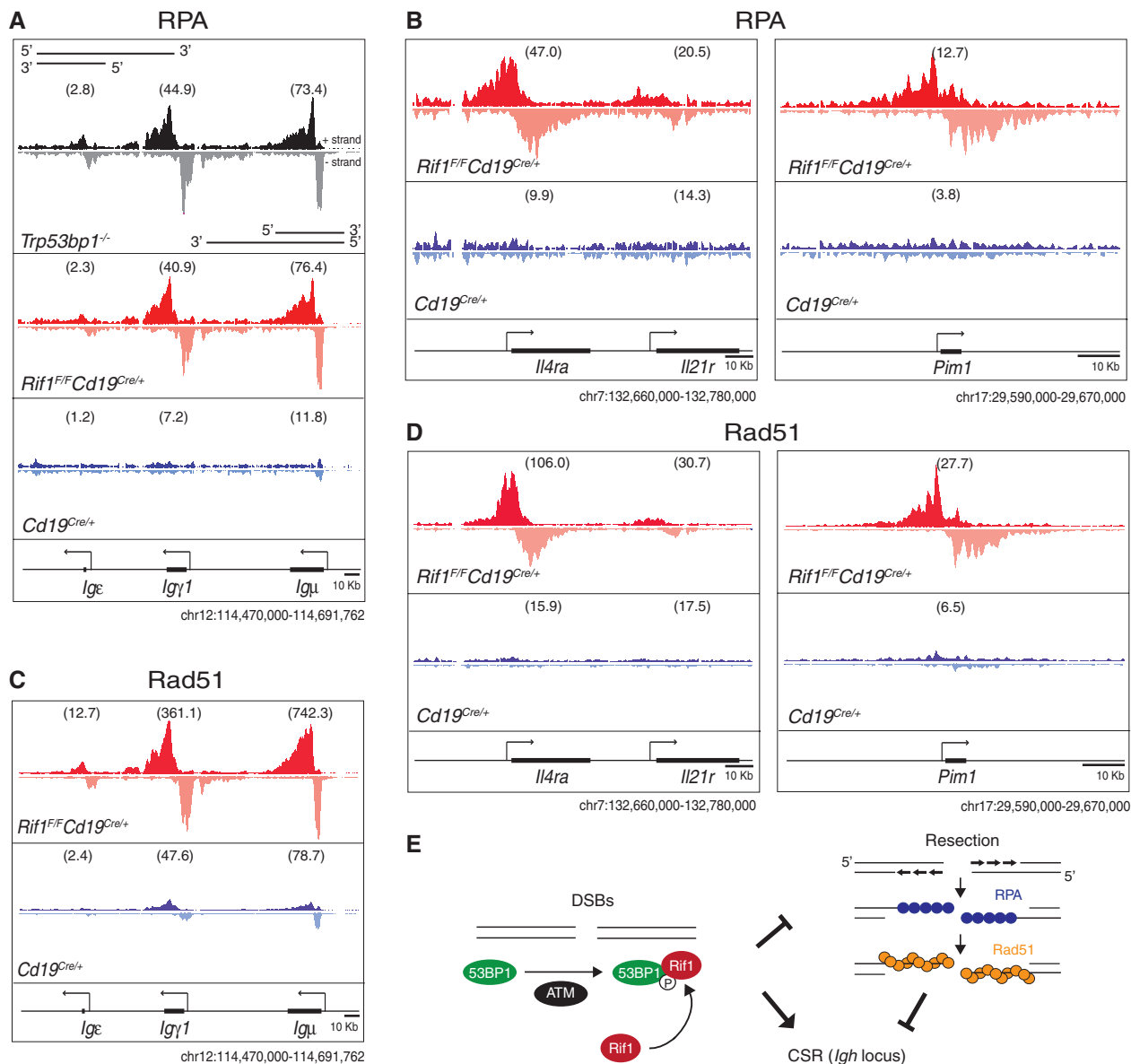


Fig. 4. *Rif1* prevents resection of DNA ends at sites of AID-induced DNA damage. (A to D) RPA and Rad51 occupancy at the *Igh* locus (A and C) and at non-*Igh* AID targets genes (B and D) in B cells activated to undergo class switching. ChIP-seq libraries were resolved into upper (+) and lower (-) DNA strands to show RPA and Rad51 association with sense and antisense strands. Within a specified genomic window, graphs have the same scale and show tag density. Deep-sequencing samples were normalized per library size, and tags per million values were calculated for

each genic region, as indicated in the supplementary materials and methods and shown in parenthesis. Data are representative of two independent experiments for RPA ChIP-seq and one for Rad51. (E) Model of *Rif1* recruitment and DNA-end protection at DSBs. DNA damage activates ATM, which phosphorylates many targets, including 53BP1. This event recruits *Rif1* to 53BP1 at the DSB, where it inhibits DNA resection. The extensive resection in the absence of *Rif1* impairs CSR at the *Igh* locus. P, phosphate.

Furthermore, irradiation increases the accumulation of *Rif1^{F/F}Cd19^{Cre/+}* B cells in G2/M phase (Fig. 3D). In addition, *Trp53bp1^{-/-}* iMEFs expressing 53BP1^{DB28A}, which did not recruit Rif1 to IRIF (Fig. 2C), exhibited delayed progression through S phase following DNA damage with accumulation of cells in G₂ phase after irradiation (fig. S9).

Accumulation of cells in G₂/M phase may reflect the persistence of unrepaired DNA damage in a fraction of Rif1-deficient cells. To investigate this possibility, we analyzed metaphase spreads from B cells dividing in response to LPS and IL-4 in vitro. These cells express AID, which produces DSBs in *Igh* and, less frequently at off-target sites throughout the genome, in the G₁ phase of the cell cycle (24–26). Chromosomal aberrations were increased in *Rif1^{F/F}Cd19^{Cre/+}* B cells compared to controls (Fig. 3E), with many localized to the *Igh* locus (Fig. 3E). Consistent with the observation that *Igh* is targeted by AID in the G₁ phase of the cell cycle, all of the *Igh* breaks were chromosome breaks (Fig. 3, E and F). Interestingly, the frequency of *c-myc/Igh* translocations is moderately increased in *Rif1^{F/F}Cd19^{Cre/+}* B cells; however, the breakpoint distribution was similar to the *Cd19^{Cre/+}* control (1.5×10^{-6} versus 1.0×10^{-6} in the control; $P = 0.039$) (Fig. 3G and fig. S10). We conclude that in the absence of Rif1, DSBs fail to be resolved efficiently in the G₁, S, or G₂ phases, which leads to increased levels of genomic instability, including chromosome breaks at *Igh* and translocations in dividing B cells.

In the absence of 53BP1, DSBs produced by AID at the *Igh* locus accumulate the single-stranded DNA-binding replication protein A complex (RPA) as a result of increased DNA-end resection (24). To determine if Rif1 is required for DNA-end protection by 53BP1, we performed RPA–chromatin immunoprecipitation followed by massive parallel sequencing (ChIP-seq) experiments on *Rif1^{F/F}Cd19^{Cre/+}* and control B cells. Ablation of Rif1 was indistinguishable from the loss of 53BP1 in that in its absence, RPA decorates the *Igh* locus asymmetrically, in a manner consistent with 5'-3' resection (Fig. 4A) (27). In addition, absence of Rif1 also results in RPA accumulation at non-*Igh* genes, such as *Il4ra* and *Pim1*, that are damaged by AID in G₁ phase (Fig. 4B) (24, 25). Rad51 is the recombinase that mediates repair of DSBs by homologous recombination in S/G₂/M phase (22). To confirm that Rif1 prevents resection that takes place in S phase, we monitored Rad51 accumulation in activated B cells by ChIP-seq. Loss of Rif1 was

indistinguishable from the loss of 53BP1 (27), in that it led to asymmetric Rad51 accumulation at sites of AID-inflicted DNA damage (Fig. 4, C and D). We conclude that in the absence of Rif1, AID-induced DSBs incurred in G₁ phase persist and undergo extensive 5'-3' DNA-end resection in S/G₂/M phase, as measured by RPA and Rad51 accumulation.

A role for Rif1 in maintenance of genome stability and protection of DNA ends against resection is consistent with its phosphorylation-dependent recruitment to the N-terminal domain of 53BP1 (4). 53BP1 facilitates DNA repair and prevents DNA-end resection during CSR. In the absence of 53BP1, AID-induced DSBs are resolved inefficiently in G₁ phase, leading to chromosome breaks, *Igh* instability, and resolution by alternative NHEJ or homologous recombination instead of classical NHEJ (4, 8, 27). Our experiments show that in the absence of Rif1, 53BP1 is insufficient to promote genomic stability or mediate efficient *Igh* repair, DNA-end protection, or CSR. Thus, these 53BP1 activities require Rif1 recruitment to the phosphorylated N terminus of 53BP1. Rif1 is likely to have additional functions beyond 53BP1, CSR, and DNA-end protection because although *Trp53bp1^{-/-}* mice are viable, Rif1 deletion is lethal (17). Indeed, Rif1 is believed to play a role in the repair of S-phase DNA damage (17, 18), as well as in the regulation of replication timing (19, 20, 28). Analogously, additional CSR factor(s) may exist downstream of 53BP1, as class switching in Rif1-deficient B cells is significantly higher than in *Trp53bp1^{-/-}*.

In summary, our data are consistent with a model in which ATM-mediated phosphorylation of 53BP1 recruits Rif1 to sites of DNA damage, where it facilitates DNA repair in part by protecting DNA ends from resection (Fig. 4E). In the absence of Rif1, DNA breaks incurred in G₁ phase fail to be repaired by NHEJ and undergo extensive 5'-3' end resection, resulting in the accumulation of chromosome breaks and genome instability.

References and Notes

1. M. M. Adams, P. B. Carpenter, *Cell Div.* **1**, 19 (2006).
2. J. Lukas, C. Lukas, J. Bartek, *Nat. Cell Biol.* **13**, 1161 (2011).
3. A. T. Noon, A. A. Goodarzi, *DNA Repair* **10**, 1071 (2011).
4. A. Bothmer et al., *Mol. Cell* **42**, 319 (2011).
5. S. Difilippantonio et al., *Nature* **456**, 529 (2008).
6. N. Dimitrova, Y. C. Chen, D. L. Spector, T. de Lange, *Nature* **456**, 524 (2008).
7. B. Reina-San-Martin, J. Chen, A. Nussenzweig, M. C. Nussenzweig, *Eur. J. Immunol.* **37**, 235 (2007).

8. A. Bothmer et al., *J. Exp. Med.* **207**, 855 (2010).
9. J. P. Manis et al., *Nat. Immunol.* **5**, 481 (2004).
10. I. M. Ward et al., *J. Cell Biol.* **165**, 459 (2004).
11. Materials and methods are available as supplementary materials on Science Online.
12. I. A. Manke, D. M. Lowery, A. Nguyen, M. B. Yaffe, *Science* **302**, 636 (2003).
13. C. F. Hardy, L. Sussel, D. Shore, *Genes Dev.* **6**, 801 (1992).
14. S. Kumar et al., *Cell Cycle* **11**, 1183 (2012).
15. J. Silverman, H. Takai, S. B. Buonomo, F. Eisenhaber, T. de Lange, *Genes Dev.* **18**, 2108 (2004).
16. L. Xu, E. H. Blackburn, *J. Cell Biol.* **167**, 819 (2004).
17. S. B. Buonomo, Y. Wu, D. Ferguson, T. de Lange, *J. Cell Biol.* **187**, 385 (2009).
18. D. Xu et al., *EMBO J.* **29**, 3140 (2010).
19. D. Cornacchia et al., *EMBO J.* **31**, 3678 (2012).
20. S. Yamazaki et al., *EMBO J.* **31**, 3667 (2012).
21. A. A. Sartori et al., *Nature* **450**, 509 (2007).
22. L. S. Symington, J. Gautier, *Annu. Rev. Genet.* **45**, 247 (2011).
23. R. Pavri, M. C. Nussenzweig, *Adv. Immunol.* **110**, 1 (2011).
24. O. Hakim et al., *Nature* **484**, 69 (2012).
25. S. Petersen et al., *Nature* **414**, 660 (2001).
26. A. Yamane et al., *Nat. Immunol.* **12**, 62 (2011).
27. A. Yamane et al., *Cell Rep.* 10.1016/j.celrep.2012.12.006 (2013).
28. M. Hayano et al., *Genes Dev.* **26**, 137 (2012).

Acknowledgments: We thank all members of the Nussenzweig laboratory for discussion, D. Bosque and T. Eisenreich for help in managing mouse colonies, A. Gazumyan for assistance with *Igh* germline and AID transcript levels analysis, and K. Yao for help with genotyping. We thank T. de Lange (The Rockefeller University, New York) for Rif1^{F/F} mice; S. Buonomo (European Molecular Biology Laboratory Mouse Biology Unit, Monterotondo, Italy) for the anti-mouse Rif1 serum #1240; G. Gutierrez (NIAMS, NIH, Bethesda, MD) for Illumina sequencing; N. Zampieri (Columbia University, New York) for assistance with immunofluorescence image processing, and M. P. Rout, J. LaCava, S. Obado, and L. Hough (The Rockefeller University) for invaluable help, discussions, and protocols for cryolysis and magnetic bead-mediated immunoprecipitation. The data presented in the manuscript are tabulated in the main text and in the supplementary materials. Sequence data shown in Fig. 4 have been deposited in the Gene Expression Omnibus database (accession number GSE42298) at www.ncbi.nlm.nih.gov/geo/. M.D.V. was a Fellow of the American Italian Cancer Foundation, and A.D.G. was supported by NIH Medical Scientist Training Program grant GM007739. This work was supported in part by NIH grants AI037526 (M.C.N.), RR022220 (B.T.C.), RR00862 (B.T.C.), and GM103314 (B.T.C.); and by the intramural program of NIAMS at the NIH (R.C.); and the intramural research program of NCI at the NIH and Center for Cancer Research (A.N. and E.C.). M.C.N. is an HHMI Investigator.

Supplementary Materials

www.sciencemag.org/cgi/content/full/science.1230624/DC1

Materials and Methods
Figs. S1 to S10
Table S1
References (29–49)

24 September 2012; accepted 16 November 2012
Published online 10 January 2013;
10.1126/science.1230624

Science

This is an abbreviated version of *Science's* Information for Authors. Complete Information for Authors is available at www.sciencemag.org/about/authors.

Science is a weekly peer-reviewed journal that publishes significant, original scientific research, plus reviews and analyses of current research and science policy. We welcome submissions from all fields of science and from any source. Competition for space in *Science* is keen, and many papers are returned without in-depth review. Priority is given to papers that reveal novel concepts of broad interest.

PEER-REVIEWED MANUSCRIPTS

Research Articles present a major scientific advance and often require additional text and figures to adequately document the findings. Articles that need more than 4500 words and 6 figures or tables will be published in full online with only an extended abstract in print. Those articles whose significance can be demonstrated in fewer words and figures will be published in full online and in print. Requests for the longer online format should provide justification for the additional presentation length. All Research Articles include an abstract, an introduction, and sections with brief subheads.

Reports present new research results of broad significance and include an abstract and introductory paragraph. Reports should have approximately 2500 words, about 30 references, and up to 4 figures or tables. Reports are published in full online and in print.

For Research Articles and Reports, other information needed to support the conclusions should be presented as supplementary materials.

Reviews (6000 words, 4 to 6 figures or tables, and up to 100 references) are now published online with an abstract in print. Reviews describe new developments of interdisciplinary significance and highlight unresolved questions and future directions. Most Reviews are solicited by the editors, but unsolicited submissions are considered occasionally.

COMMENTARY

Science's Commentary section presents analysis by scientists and other experts on issues of interest to *Science* readers.

Policy Forums (1000 or up to 2000 words) present issues at the intersection between science and society that relate to science policy.

Education Forums (1000 or up to 2000 words) present essays on science education and its practice, from preschool through postgraduate education. (Research results related to education should be submitted as a peer-reviewed manuscript.)

Books et al. (up to 1000 words) present reviews of current books, multimedia, exhibitions, and films.

Perspectives (up to 1000 words) analyze recent research developments but do not primarily discuss the author's own work. Book reviews, Education and Policy Forums, and Perspectives are frequently solicited by the editors, but unsolicited contributions will be considered.

Letters (up to 300 words) discuss material published in *Science* in the last 3 months or issues of general interest. Letters should be submitted online (www.submit2science.org) and are edited for clarity and space.

COMMENTS

Technical Comments (up to 1000 words, 2 figures or tables, and 15 references) are published online and discuss the core conclusions and/or methodology of research published in *Science* within the previous 3 months. A brief abstract is included in the Letters section of the print edition. Technical Comments should not present new data or other previously unpublished work nor be based on new findings or concepts that would not have been accessible to the authors when the target paper was written. Pertinent comments on noncentral aspects of a paper should be submitted as online comments.

Authors of Technical Comments should contact the authors of the target paper before submitting their manuscript, and should submit to *Science* the evidence of any correspondence. Technical Comments may be peer-reviewed. We hope to post accepted Technical Comments promptly online along with a formal reply from the authors of the original paper.

Online Comments. Brief online comments can be posted on papers or news stories from the full-text view on *Science* Online. Authors

Science Contact Information

Phone: (1)-202-326-6550 (USA)
(44)-1223-326500 (UK)

E-mail: science_editors@aaas.org (USA)
science@science-int.co.uk (Europe)

are identified and must agree to our terms and conditions (<http://comments.sciencemag.org/terms>).

MANUSCRIPT SELECTION

We are committed to the prompt evaluation and publication of submitted papers through our fully electronic submission and review process. Papers are assigned to a staff editor who has knowledge of the field(s) discussed in the manuscript. Most submitted papers are rated for suitability by members of the Board of Reviewing Editors (see the masthead). The editors at *Science* consider their advice in selecting papers for in-depth review. Authors of papers that are not highly rated are notified promptly, by e-mail only, within 2 weeks. Membership in AAAS is not a factor in selection.

Papers selected for in-depth review are reviewed by at least two anonymous referees. Reviewers are contacted before being sent a paper and are asked to return comments within 2 weeks. We are able to expedite the review process for papers that require rapid assessment. Papers selected for publication are edited to improve accuracy and clarity and to shorten, if necessary. Most papers are published 4 to 8 weeks after acceptance; The accepted versions of selected papers are published rapidly online in *Science* Express (www.sciencexpress.org).

Papers cannot be resubmitted over a disagreement on interest or relative merit. If a paper was rejected on the basis of serious reviewer error, resubmission may be considered. Papers submitted to *Science* but not accepted for publication may be eligible for publication in *Science Signaling* or *Science Translational Medicine*.

SUBMISSION REQUIREMENTS

Authorship. All authors must agree to be so listed and must have seen and approved the manuscript and its submission to *Science*. Any changes in authorship must be approved in writing by all the original authors. Submis-

Submitting a Manuscript or Letter

Science accepts submissions of manuscripts and letters only through our Web site: www.submit2science.org. We are not able to accept submissions by e-mail. Your submission should include a cover letter containing a statement of the paper's main point, any information needed to ensure a fair review process, and names of colleagues who have reviewed the paper for you.

PDF copies of related papers (see submission requirements) should be sent as a PDF by e-mail to science_editors@aaas.org along with your Web submission number.

sion of a paper that has not been approved by all authors will result in immediate rejection without appeal.

Prior publication. *Science* will not consider any paper or component of a paper that has been published or is under consideration elsewhere. Distribution on the Internet may be considered prior publication and may compromise the originality of the paper. Reporting the main findings of a paper in the mass media may compromise the novelty of the work and thus its appropriateness for *Science*. Please contact the editors with questions regarding these policies.

Human studies. Informed consent must have been obtained for studies on humans after the nature and possible consequences of the studies were explained. All research on humans must have approval from the author's institutional review board (IRB) or equivalent body.

Animal care. Care of experimental animals must be in accordance with the author's institutional guidelines.

Related papers. Copies of papers submitted to other journals by any of the authors that relate to the paper submitted to *Science* must be included with the submission.

Unpublished data and personal communications. Citations to unpublished data, in press papers, and personal communications cannot be used to support claims in the paper.

Dual use. Authors and reviewers are expected to notify editors if a manuscript could be considered to report dual-use research of concern. Papers identified as such will be brought to the attention of the Editor-in-Chief for further evaluation. If necessary, outside reviewers with expertise in the area will be consulted.

CONDITIONS OF ACCEPTANCE

Authorship, funding, and conflict of interest. All authors must disclose all affiliations, funding sources, and financial or management relationships related to a paper, including those that could be perceived as potential sources of bias, before acceptance. *Science* now requires all authors of accepted papers to affirm their contribution to a paper and agree to our policies on data and materials availability. The senior author from each group is required to have examined the raw data that his/her group has produced.

Data deposition. Before publication, large data sets—including but not limited to microarray data, protein or DNA sequences, and atomic coordinates and structure factors for macromolecular or chemical structures—must be deposited in an approved database, an accession number must be included in the published paper, and the deposited information must be released at the time of publication. Electron micrograph maps must also be deposited. Approved data-

Manuscript Preparation

(See www.sciencemag.org/about/authors for more information.)

Titles should be no more than 96 characters for Reports, Research Articles, and Reviews.

One-sentence summaries should be submitted for all papers.

Abstracts explain to the general reader why the research was done and why the results are important. The abstract should present, in no more than 125 words, background information to convey the context of the research, describe the results, and draw general conclusions.

Text starts with a brief introduction describing the paper's significance, which should be intelligible to readers in other disciplines. Technical terms should be defined. Symbols, abbreviations, and acronyms should be defined the first time they are used. All tables and figures should be cited in numerical order.

References and notes are numbered in the order in which they are cited, first through the text, then through the text of the references, then through the figure and table legends, and finally through the supplementary materials. Each reference should have a unique number; do not combine references or embed references in notes. Do not use *op. cit.* or *ibid.* Titles can be included in references and will appear in our online version. There should be only one reference list, containing all of the citations in the paper and in the supplementary materials.

Acknowledgments, including complete funding information; a statement indicating the

availability of data, including accession numbers; and any information related to authorship conflict of interest should be gathered into an unnumbered note at the end of the references.

Tables should be included at the end of the references and should supplement, not duplicate, the text. The first sentence of the table legend should be a brief descriptive title. Every vertical column should have a heading, consisting of a title with the unit of measure in parentheses. Units should not change within a column.

Figure legends should be double-spaced and in numerical order. The figure title should be given as the first line of the legend. No single legend should be longer than ~200 words. Nomenclature, abbreviations, symbols, and units used in a figure should match those used in the text. Units should be metric and follow SI conventions.

Supplementary materials are posted permanently on *Science* Online, are linked to the manuscript, and are freely available. Files can include materials and methods, figures, tables, and video or audio clips that are important for the integrity of the paper.

Figures should be submitted as part of the online submission or, if necessary for large files only, on a CD or DVD. No part of a figure may be selectively manipulated. When figures are assembled from multiple gels or micrographs, a line or space should indicate the border between two original images. See our online Information for Authors for information on preparing art.

bases are listed online. Large data sets with no appropriate repository must be housed as part of the supplementary materials at *Science*, or when this is not possible, on the author's Web site, provided that a copy of the data is held in escrow at *Science* to ensure availability to readers.

Data availability and materials sharing. After publication, all data and computer codes necessary to understand, assess, and extend the conclusions of the manuscript must be available to any reader of *Science*, and all reasonable requests for materials must be fulfilled. Before acceptance, *Science* must be informed of any restrictions on sharing of materials (materials transfer agreements or patents, for example) applying to materials used in the reported research.

License and access policies. Authors retain copyright but must agree to grant to *Science* an exclusive license to publish the paper in print and online. Any author whose university or institution has policies or other restrictions lim-

iting their ability to assign exclusive publication rights (such as Harvard, MIT, or Open University) must apply for a waiver or other exclusion from that policy or those restrictions. After publication, authors may post the accepted version of the paper on their personal Web site and are provided one referrer link that can be posted on a personal or institutional Web page, through which users can freely access the published paper on *Science*'s online site. *Science* allows deposition of accepted papers into repositories if mandated by funders with a release 6 months after publication and provided that a link to the final version published in *Science* is included. Original research papers are freely accessible with registration on *Science*'s Web site 12 months after publication.

Press coverage. The paper should remain a privileged document and should not be released to the press or the public before publication. Questions should be referred to the AAAS Office of Public Programs (202-326-6440).

How they contribute to society through science and technology?

“Materials and Production” Field

Contribution to the advancement of today's information society

“By developing ‘chemically amplified resist’ polymer materials which enabled the drastic miniaturization of microprocessors/memory chips and great improvement of production process”



Prof. C. Grant Willson
USA



Prof. Jean M. J. Fréchet
USA

“Biological Production and Biological Environment” Field

Contribution to the global marine environmental conservation

“By advancing marine biodiversity research and establishing the scientific basis through elucidating deep sea chemosynthetic ecosystems”



Dr. John Frederick Grassle
USA

2013 Japan Prize Laureates

This is an important element in the Japan Prize selection criteria.

The Japan Prize is awarded to scientists and engineers from around the world who are recognized as having achieved original and dramatic accomplishments that greatly enhance the progress of science and technology, thereby contributing to the peace and prosperity of mankind.



► Search for “Japan Prize” to access announcement of the 2013 laureates.
www.japanprize.jp

JAPAN PRIZE

What can RabMAbs[®] do for you?

abcam[®]
discover more

Rabbit Monoclonal Antibodies (RabMAbs) offer multiple advantages to bring you the highest quality antibody possible.



#3

Excellent for IHC

#4

High Affinity

#5

High Specificity

#6

Novel Epitopes

RabMAbs[®] consistently show higher affinity, with K_D values which can often reach the picomolar level (10^{-12} M), effectively eliminating the need for further affinity maturation (1).



Antibody affinity comparison by K_D value for a typical RabMAb vs. traditional mouse monoclonal antibodies.

1. Pope ME, *J Immunol Methods*. 2009 Feb 28;341(1-2):86-96.

Try a RabMAb and discover more at abcam.com/rabmabs-advantages

Explore the fascinating new world of QIAGEN®

Virtual showroom and application labs

Enjoy discovering innovative
sample and assay technologies
at new **QIAGEN.com**

- Experience new dimensions
- Discover fascinating innovations
- Relevant for your personal applications



Scan the code with your iPad,
or go to www.qiagen.com/qiagen-experience.

Experience



Sample & Assay Technologies

Make ends meet.



Gibson Assembly[™] Cloning Kit

New England Biolabs has revolutionized your laboratory's standard cloning methodology. The Gibson Assembly Cloning Kit combines the power of the Gibson Assembly Master Mix with NEB 5-alpha Competent *E. coli*, enabling fragment assembly and transformation in just under two hours. Save time, without sacrificing efficiency.

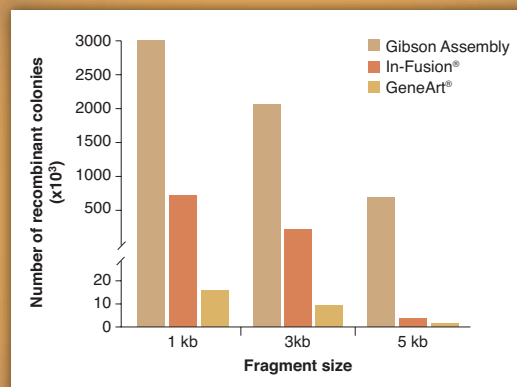
Making ends meet is now quicker and easier than ever before, with the Gibson Assembly Cloning Kit from NEB.

NEBuilder[™]
for Gibson Assembly

Visit NEBGibson.com to view the latest tutorials and to try our primer design tool.

IN-FUSION[®] is a registered trademark of Clontech Laboratories, Inc.
GENEART[®] is a registered trademark of Life Technologies, Inc.
GIBSON ASSEMBLY[™] is a trademark of Synthetic Genomics, Inc.

Gibson Assembly Cloning Kit provides robust transformation efficiencies



Assembly reactions containing 25 ng of linear pUC19 vector and 0.04 pmol of each fragment were performed following individual suppliers' recommended protocols and using the competent cells provided with the kit. The total number of recombinant colonies was calculated per 25 ng of linear pUC19 vector added to the assembly reaction.



SYNTHETIC GENOMICS[®]

Some components of this product are manufactured by New England Biolabs, Inc. under license from Synthetic Genomics, Inc.

Little Genius



BLItz brilliantly packs the power of Dip and Read™ label-free analysis into a personal assay system. Give BLItz a drop of your sample and it does the rest!

- Protein presence/absence in seconds
- Binding kinetics assays at your bench
- Protein quantitation in seconds
- Develop immunoassays in minutes
- Easily analyze crude samples

Cleverly priced under \$20K so you can have your own little genius.

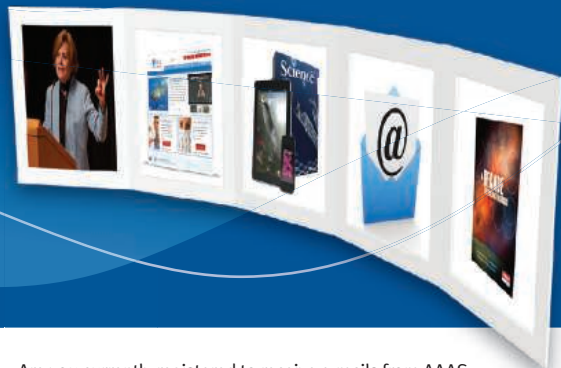
Want to try BLItz in your lab? Visit BlitzMeNow.com or call 855.BLITZ.ME.

fortéBIO®
A Division of **Pall Life Sciences**

PALL® Life Sciences

STAY INFORMED! STAY CONNECTED!

Get more from your
AAAS membership



Are you currently registered to receive e-mails from AAAS and *Science*? E-mail is the primary way that AAAS communicates with our members about AAAS programs, new member benefits, invitations to special events, and, of course, the latest news and research being published in *Science*.

Sign up today to ensure that you are getting the most out of your membership and *Science* subscription.* To get started visit: promo.aaas.org/stayconnected. You'll need your AAAS Member number. Find it above your name on your *Science* mailing label.

Don't miss a thing. Sign up for e-mail communications from AAAS today!



*AAAS follows CAN-SPAM and European Safe Harbor guidelines for protecting your privacy. We will never sell your e-mail address and you can opt-out of receiving e-mails at any time.

LAMBDA DG-4/DG-5 PLUS

High Speed
Wavelength Switcher

This complete illumination system with improved digital servo technology allows 30% greater light output and switching times of up to 0.5msec. The unique optical design uses modern interference filters, providing integral blocking characteristics 1000-times better than typical monochromators.



FEATURES

- Complete system for wavelength switching
- Switches in 0.5msec
- Integral shuttering
- Integral neutral density filtering
- Two outputs for monitoring filter position
- Turbo blanking
- Video sync pulsed ring buffer

SUTTER INSTRUMENT

PHONE: 415.883.0128 | FAX: 415.883.0572
EMAIL: INFO@SUTTER.COM | WWW.SUTTER.COM



Recommend
Science Classic
to your institution's library.
[ScienceOnline.org/
recommend](http://ScienceOnline.org/recommend)

Science Classic

Digital Archives of *Science*
1880–1996

Fully integrated with *Science Online*
(1997–Current Issue)



ScienceClassic.org



CARBON DIOXIDE SENSOR

A new carbon dioxide (CO₂) sensor combines precise and reliable determination of dissolved CO₂, with the performance benefits of Intelligent Sensor Management. The new InPro 5000i is a fully sterilizable and autoclavable in-line CO₂ sensor. The sensor's membrane provides an excellent barrier against volatile organic acids, ensuring errorless measurement. The InPro 5000i's modular design makes maintenance and spare part replacement fast and convenient. The ideal housing for the sensor is the retractable InTrac 797 as its integrated flushing chamber allows easy sensor calibration and cleaning, even during a running fermentation. The InPro 5000i is the latest member of the Intelligent Sensor Management (ISM) family of sensors and transmitters. ISM is a digital platform for analytical measurement solutions. ISM's predictive diagnostic tools constantly monitor the InPro 5000i's "health" so that it can be easily determined if the sensor can be safely used for the next fermentation run.

METTLER TOLEDO

For info: 800-638-8537 | www.mt.com/CO2

LARGE-WELL MICROPLATES

Offering 24 high-volume (3.1 mL) wells in an industry standard 96-well plate footprint, the Krystal 24 provides a large surface area per well, enabling unmatched cell growth. Constructed in ultrapure grade polystyrene, Krystal 24 microplates are tissue-culture treated to ensure optimal cell growth and attachment. Precisely manufactured to ANSI/SLAS microplate dimensions, the microplates are fully compatible with all commercially available plate readers, robotic sample processors, and automated liquid handling systems. The plate edges and lids are designed to reduce evaporation, and the raised well rims reduce the risk of cross contamination. The unique Krystal 24 design also provides the convenience of direct measurements on bottom reading spectrophotometers and inverted microscopes. For sensitive fluorescence measurements, the black Krystal 24 plate provides the all-absorbing background needed to minimize background interference. The opaque white Krystal 24 plate maximizes reflectivity enabling even weakly emitting luminescence assays to be routinely undertaken.

PORVAIR SCIENCES

For info: +44-(0)-1372-824290 | www.porvair-sciences.com

FRESH HUMAN PANCREATIC ISLETS

The new Clonetics Fresh Human Pancreatic Islets possess a guaranteed quality with each batch tested for quantity (total IEQ), viability, purity, and sterility. They can be used in a variety of research areas including islet cell transplantation, insulin production, cell metabolism, immunosuppression, and other metabolic disorders. Some of the major challenges within diabetes research are the acquisition and availability of high-quality islet cells. Researchers now have easy access to islets to support research in long-term islet grafting survival, prevention of islet rejection, and prevention of adverse effects from immunosuppressive drugs.

LONZA BIOSCIENCE

For info: +41-(0)-61-316-81-11 | www.lonza.com

CELL METABOLISM ANALYZER

The Seahorse XFe Extracellular Flux Analyzer measures the two major energy pathways of the cell—mitochondrial respiration and glycolysis—in a microplate, in real-time. The XFe Analyzer and stress test kits have standardized the measurements of mitochondrial dysfunction and glycolysis, enabling scientists to better understand the connection between physiological traits of cells with genomic and proteomic data. The XFe Analyzer and stress test kits are the gold standard platform for metabolic assays in neuroscience. The XFe Analyzer is able to identify mitochondrial dysfunction and subtle changes in neuronal cell metabolism before the development of observable neurodegeneration. The XFe Analyzer sets a universal standard for acquiring and reporting cell metabolism data. It enables cloud-based sharing of the elements and protocols of metabolic experiments, affording new users and experts the opportunity to collaborate and accelerate their research.

SEAHORSE BIOSCIENCE

For info: 800-671-0633 | www.seahorsebio.com

COOLED SPECIMEN CLAMP

The Cool Cut specimen clamp maintains block temperature for more consistent, better quality sections. Paraffin wax continues to be the most popular tissue-embedding medium, due to its low cost and ease of use, facilitating long-term storage of the embedded tissue blocks. To promote good ribbon generation, the paraffin block needs to be sufficiently hard to enable the sections to be cut on the microtome. This is routinely achieved by placing the paraffin blocks on ice, cooling both the tissue and the wax to a similar consistency and swelling the tissue to make it easier to section. As the block heats up, however, the paraffin softens and expands, resulting in corrugation and variations in the consistency of the sections, rendering some unsuitable for use. The Cool Cut Clamp is a peltier-cooled specimen clamp, which helps to address this issue by maintaining the paraffin block at a suitable temperature for sectioning for a prolonged period.

THERMO FISHER SCIENTIFIC

For info: 800-522-7270 | www.thermoscientific.com/pathology

Electronically submit your new product description or product literature information! Go to www.sciencemag.org/products/newproducts.dtl for more information. Newly offered instrumentation, apparatus, and laboratory materials of interest to researchers in all disciplines in academic, industrial, and governmental organizations are featured in this space. Emphasis is given to purpose, chief characteristics, and availability of products and materials. Endorsement by *Science* or AAAS of any products or materials mentioned is not implied. Additional information may be obtained from the manufacturer or supplier.

WEBINAR

Microscopy in Focus

The Art and Science of Image Quality

THURSDAY, MARCH 7, 2013

9 a.m. UK, 10 a.m. CET, 5 p.m. China,
6 p.m. Japan, 4 a.m. Eastern US

An on-demand recording will be available
soon after the live event.

Register now at webinar.sciencemag.org!

REGISTER NOW!

webinar.sciencemag.org

High-resolution microscopy has become a widespread and ubiquitous technology in most life science laboratories and high-quality images have become an essential part of many publications. Technology such as confocality can enhance image contrast by eliminating out of focus light, but this is often at the expense of signal intensity and increased phototoxicity. In this webinar, our experts will discuss the benefits and challenges of confocality, compare and contrast it with other technologies such as deconvolution, and provide advice on which technology is best for which application.

During this webinar, our viewers will:

- Obtain an overview of confocal microscopy and its application in basic research
- Learn about technologies such as deconvolution, which can help to preserve maximum light input and provide better image quality
- Receive advice on best practices for obtaining the best quality images, regardless of the technique used
- Have their questions answered live by our respected thought leaders!

SPEAKERS

Jason Swedlow, Ph.D.

University of Dundee
Dundee, Scotland



John Murray, M.D., Ph.D.

Indiana University
Bloomington, IN



Paul C. Goodwin, M.Sc

GE Healthcare
Issaquah, WA



Sponsored by



Brought to you by the
Science/AAAS Custom
Publishing Office



Illuminate Cancer Biology

The complexity of cancer systems biology requires innovative tools for interrogating the signaling pathways responsible for oncological transformation.

Promega's integrated tools for reporter gene analysis assure biologically relevant results in cancer research.

FuGENE® HD

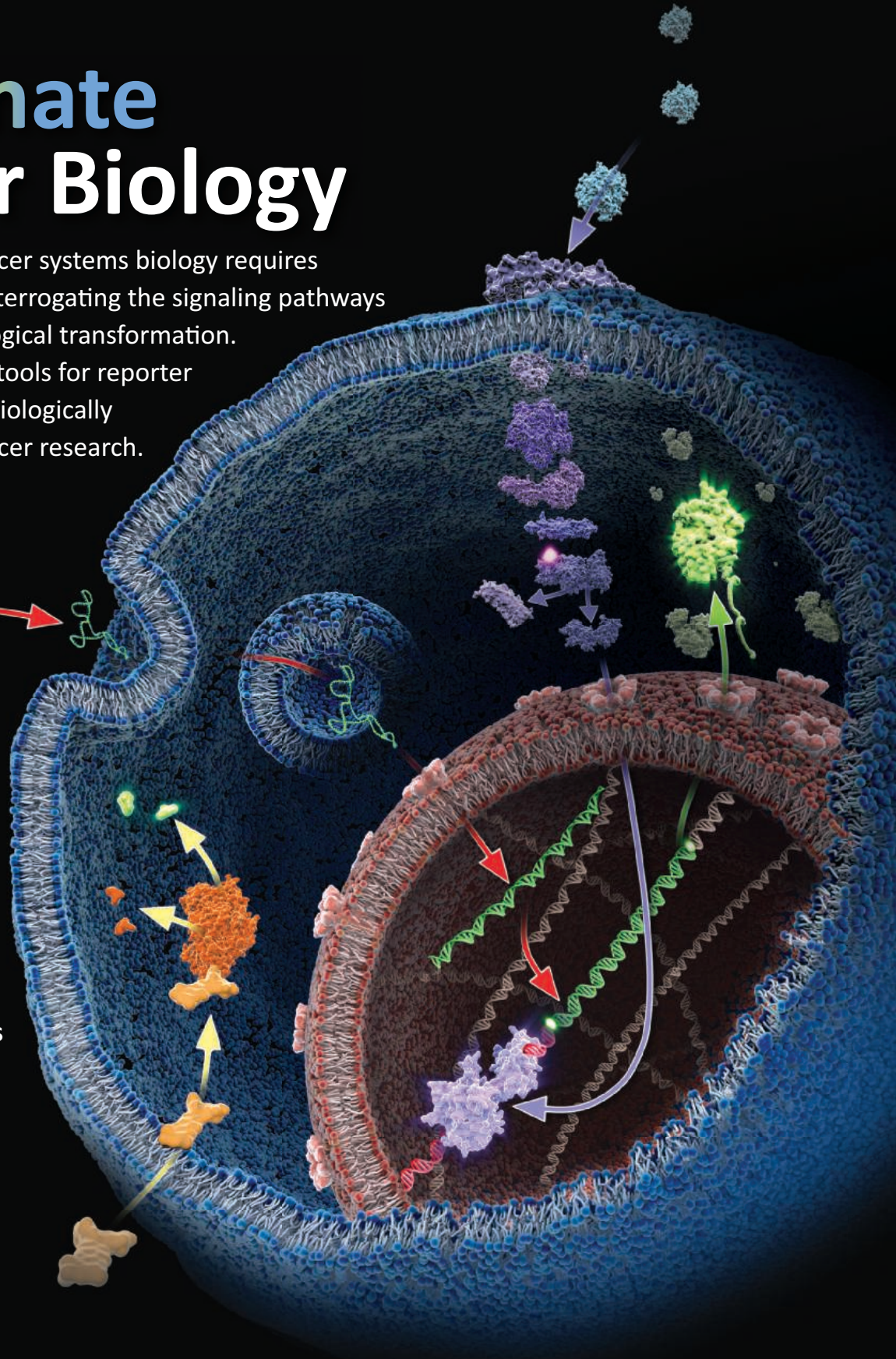
The next generation transfection reagent, effective on almost every cell type with virtually no cell toxicity

ONE-Glo™ + Tox

Multiplexed reporter gene analysis with off-target toxicity detection in the same well

New! NanoLuc™ and pGL4 Tox Vectors

Introducing NanoLuc - the brightest, smallest, luciferase available - plus a new line of pGL4 response element vectors for mapping oncological pathways



Promega

To get a *FREE* sample of any one of these reagents, visit:

www.promega.com/pathwaybiology

There's only one

Science



Science Careers Advertising

For full advertising details, go to ScienceCareers.org and click For Employers, or call one of our representatives.

Tracy Holmes

Worldwide Associate Director
Science Careers
Phone: +44 (0) 1223 326525

THE AMERICAS

E-mail: advertise@sciencecareers.org
Fax: 202-289-6742

Tina Burks

East Coast/West Coast/South America
Phone: 202-326-6577

Allyson Rosen

Midwest/Canada/Corporate
Phone: 202-326-6578

Marci Gallun

Sales Administrator
Phone: 202-326-6582

Online Job Posting Questions

Phone: 202-312-6375

EUROPE / INDIA / AUSTRALIA / NEW ZEALAND / REST OF WORLD

E-mail: ads@science-int.co.uk
Fax: +44 (0) 1223 326532

Lucy Nelson

Phone: +44 (0)1223 326527

Kelly Grace

Phone: +44 (0) 1223 326528

JAPAN

Yuri Kobayashi

Phone: +81-(0)90-9110-1719
E-mail: ykobayas@aaaas.org

CHINA / KOREA / SINGAPORE / TAIWAN / THAILAND

Ruolei Wu

Phone: +86-1367-1015-294
E-mail: rwu@aaaas.org

All ads submitted for publication must comply with applicable U.S. and non-U.S. laws. *Science* reserves the right to refuse any advertisement at its sole discretion for any reason, including without limitation for offensive language or inappropriate content, and all advertising is subject to publisher approval. *Science* encourages our readers to alert us to any ads that they feel may be discriminatory or offensive.

Science Careers

From the journal *Science*



ScienceCareers.org

FACULTY OF VETERINARY MEDICINE



Postdoctoral Research Scholarships

The University of Calgary is a leading Canadian university located in the nation's most enterprising city. Named a cultural capital of Canada and one of the best places to live in the world, Calgary enjoys more days of sunshine than any other major Canadian city and is less than an hour's drive from the majestic Rocky Mountains. The Faculty of Veterinary Medicine at the University of Calgary (UCVM) is unique amongst veterinary colleges world-wide in sharing the Health Sciences Centre with the Faculty of Medicine, ensuring and fostering interaction and collaboration between animal and human health researchers and professionals.

The Faculty of Veterinary Medicine invites applications for five new postdoctoral scholars:

Characterization of adult human dermal stem cells and bioprocess development to improve wound-healing.

Supervisor: Dr. Jeff Biernaskie — ucalgary.ca/biernaskie

Population genomic approaches to investigate drug resistance in parasitic helminths.

Supervisor: Dr. John Gilleard — ucalgary.ca/jsgilleard

Animal sentinels of health effects from exposure to oil- and gas-related contaminants in Alberta.

Supervisor: Dr. Judit Smits — vet.ucalgary.ca/profiles/judit-smits

Control of chronic pain following brain injury.

Supervisor: Dr. Patrick Whelan — ucalgary.ca/whelanlab

Investigating the biochemistries of antigen processing.

Supervisor: Dr. Robin Yates — ucalgary.ca/yateslab

Applicants should clearly specify the project to which they are applying and submit a curriculum vitae, a letter of application outlining research experiences and aspirations, and the names and contact information for at least three referees to ucvmpds@ucalgary.ca.

Consideration of applications will continue until the position until the positions are filled between now and March 30, 2013.

ucalgary.ca/careers



The University of Calgary is a leading Canadian university located in the nation's most enterprising city. The university has a clear strategic direction to become one of Canada's top five universities by 2016, where research and innovative teaching and learning go hand in hand, and where we fully engage the communities we both serve and lead. This strategy is called *Eyes High*, inspired by the university's Gaelic motto, which translates as 'I will lift up my eyes.'



UNIVERSITY OF
CAMBRIDGE

A world of opportunities

www.cam.ac.uk/jobs/

The Herchel Smith Professorship of Molecular Genetics

The Board of Electors to the Herchel Smith Professorship of Molecular Genetics invite applications for this Professorship from persons whose work falls within the general field of the Professorship to take up appointment by 1 September 2013.

Candidates will have an outstanding research record of international stature in Molecular Genetics and the vision, leadership, experience and enthusiasm to build on current strengths in maintaining and developing a leading research presence.

The annual pensionable stipend for a professor is on a scale from £65,435 to £132,860 with the possibility of market supplementation where appropriate. Standard professorial duties include teaching and research, examining, supervision and administration. The Professor will be based in central Cambridge.

Further information is available at: www.admin.cam.ac.uk/offices/academic/secretary/professorships/ or contact the Academic Secretary, University Offices, The Old Schools, Cambridge, CB2 1TT, (email: ibise@admin.cam.ac.uk), to whom a letter of application should be sent, together with details of current and future research plans, a curriculum vitae, a publications list and form CHRIS/6 (parts 1 and 3 only) with details of three referees, so as to reach him no later than 12 March 2013.

Informal enquiries may be made to the convenor of the Board of Electors, Professor Anne Ferguson-Smith +44 (0)1223 (3)33834 or email afsmith@mole.bio.cam.ac.uk

The University is committed to Equality of Opportunity.



Opportunities for YOUNG GROUP LEADERS in Biomedical Research at the Spanish National Centre for Cardiovascular Research CNIC, Madrid - Spain

The CNIC is dedicated to excellence in cardiovascular research and to translating new knowledge into real improvements in clinical practice.

The scientific project of the centre has been structured in three areas:

- Cardiovascular Development and Repair Department (CDR)
- Vascular Biology and Inflammation Department (VBI)
- Epidemiology, Atherothrombosis and Imaging Department (EAI)

To be eligible, candidates must:

- Hold a PhD/ MD degree
- Demonstrate a minimum of three years' postdoctoral/post MD experience in centres of international reference
- Candidates must not have resided or carried out their main activity in Spain for more than twelve months in the last three years

The CNIC can offer you:

- A 3-year contract
- An internationally competitive salary
- Contribution to research and training
- State of the art infrastructure and latest generation of technological equipment
- Scientific-technical support and complementary training

Deadline for submission of proposals: 04 April 2013.

CNIC is an inclusive, equal opportunity employer, irrespective of nationality, ethnic origin, gender, marital or parental status, sexual orientation, creed, disability, age or political belief. Confidentiality is guaranteed throughout the selection process and all current regulations relating to the protection of personal data will be strictly adhered to.

For further information and applications, please, visit www.cnic.es



Faculty Positions in Immunology/Inflammation/Infectious Diseases University of Utah School of Medicine, Salt Lake City

The University of Utah's Department of Pathology announces new faculty positions for basic and translational scientists with disease-focused basic and translational research programs in Immunology, Inflammation, and/or Infectious Diseases. The successful candidates will be expected to establish a vigorous research program that fosters institutional collaborations in disease-focused research. The ideal candidates must have a MD, PhD, or DVM degree and research track record that supports the establishment of an independent research program that complements ongoing research at the institution. Faculty rank will be commensurate with experience and appointments will include competitive start-up packages. Interested candidates should submit electronically to <http://utah.peopleadmin.com/postings/21307> a curriculum vitae, a brief cover letter and the names and addresses of three references and description of anticipated research direction. More information at www.path.utah.edu/recruiting or you may contact Allison Boyer, allison.boyer@path.utah.edu

As a patient-focused organization, The University of Utah Health Sciences exists to enhance the health and well-being of people through patient care, research and education. Success in this mission requires a culture of collaboration, excellence, leadership, and respect. The Health Sciences Center seeks faculty and staff who are committed to the values of compassion, collaboration, innovation, responsibility, diversity, integrity, quality and trust that are integral to our mission.

The University of Utah values candidates who have experience working in settings with students from diverse backgrounds, and possess a [strong or demonstrated] commitment to improving access to higher education for historically underrepresented students.

The University of Utah is an Equal Opportunity/Affirmative Action Employer and Educator. Minorities, women, and persons with disabilities are strongly encouraged to apply. Veterans preference. Reasonable accommodations provided. For additional information: <http://www.regulations.utah.edu/humanResources/5-106.html>.



INDEPENDENT RESEARCH FELLOWSHIPS

The John Innes Centre (JIC), Norwich, UK is a world leading centre of excellence in plant and microbial sciences based on the Norwich Research Park.

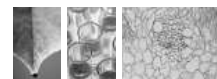
We are inviting applications from outstanding researchers who either hold, or wish to apply for Independent Research Fellowships, to attend a Conference at the JIC on 29/30 April 2013. At the meeting you will be able to present a talk about your proposed area of research and to discuss your proposals, the development of your group and your future career plans in depth with senior JIC Scientists.

After the Conference we will select and mentor outstanding candidates in writing Fellowship applications and/or offer the opportunity to move existing Fellowships to the JIC.

Further details and particulars can be found at:
<http://www.jic.ac.uk/corporate/fellows.htm>

Please email a two page summary of your research plan, a copy of your CV and arrange for three letters of recommendation to be emailed to dawn.rivett@nbi.ac.uk by Friday 15th March 2013.

The John Innes Centre is a registered charity (No. 223852) grant-aided by the Biotechnology and Biological Sciences Research Council and is an Equal Opportunities Employer.





UNIVERSITÉ DE GENÈVE

The Faculty of Medicine of the University of Geneva is seeking to fill a position of:

ASSOCIATE or ASSISTANT PROFESSOR
in the Section of fundamental medicine
(host-pathogens interactions)

CHARGE: This full-time position will involve undergraduate and postgraduate teaching in host-pathogens interactions, preferably in virology, as well as supervising Masters' and doctoral theses. The incumbent will undertake research in this area at the highest national and international levels and secure external funding. He/She will also take up administrative and organizational duties within the Department of microbiology and molecular medicine and the Faculty of Medicine.

The incumbent is also expected to show the capacity to carry out a transversal mission through strong collaboration with partner services.

REQUIREMENTS:

- Doctorate of Medicine (MD) , PhD or equivalent degree
- Full postgraduate training in microbiology is an advantage.
- Previous teaching and independent research experience.
- Publications in leading international journals.
- Good knowledge of French within two years.

STARTING DATE: October 1st, 2013 or according to agreement.

Mandatory online registration before
March 22nd , 2013 at: <http://www.unige.ch/academ> + paper application to be sent to:

The Dean of the Faculty of Medicine
CMU, 1 rue Michel-Servet
1211 Genève 4 – Switzerland

More information: sylvia.deraemy@unige.ch

Women are encouraged to apply

PRIZES



The Alberta Prion Research Institute is calling for nominations of junior researchers for the APRI International Young Researcher Prize.

NOMINATION DEADLINE
IS MARCH 15

\$25,000 Prize

WINNER WILL SPEAK AT
PRION 2013, MAY 26-29
BANFF, ALBERTA, CANADA
PRION2013.CA



**Alberta
Innovates
Bio
Solutions**

FOR MORE INFORMATION, VISIT:
prioninstitute.ca/APRI-IYRP

THE UNIVERSITY OF HONG KONG



Founded in 1911, The University of Hong Kong is committed to the highest international standards of excellence in teaching and research, and has been at the international forefront of academic scholarship for many years. The University has a comprehensive range of study programmes and research disciplines spread across 10 faculties and about 100 sub-divisions of studies and learning. There are over 23,400 undergraduate and postgraduate students coming from 50 countries, and more than 1,800 members of academic and academic-related staff, many of whom are internationally renowned.

School of Biological Sciences

Applications are invited for the following tenure-track appointments in the School of Biological Sciences, from as soon as possible:

- (1) **Professor/Associate Professor/Assistant Professor in Food Science** (Ref.: 201300064)
- (2) **Associate Professor/Assistant Professor in Molecular Toxicology/Food Toxicology** (Ref.: 201300065)

The positions are first offered on a three-year fixed-term basis, with the possibility of renewal and with consideration for tenure during the second fixed-term contract. For exceptionally outstanding candidates, appointments can be made with tenure. Current strategic research areas of the School include: Food Safety and Food for Health, Endocrinology, Ecology, and Plant Evolution and Adaptation. Further information about the School can be obtained at <http://www.biosch.hku.hk/>.

For post (1), candidates with a strong publication record in any area of food science and technology are encouraged to apply, although preference will be given to those with expertise in food safety, food toxicology, food microbiology, food processing/engineering and product development/sensory science. The appointee must be able to contribute strongly to the strategic research area of food safety and food for health in the School. He/She should be able to teach a broad spectrum of courses within the general area of food science. Applicants who have responded to the previous advertisement (Ref.: 201101146) need not re-apply.

For post (2), applicants should have a strong publication record in Molecular Toxicology and/or Food Toxicology, and be able to contribute to at least one of the strategic research areas of the School. The appointee is expected to teach courses related to food toxicology, food safety, environmental toxicology and molecular toxicology. Applicants who have responded to the previous advertisement (Ref.: 201101147) need not re-apply.

A globally competitive remuneration package commensurate with the appointee's qualifications and experience will be offered. The appointments will attract a contract-end gratuity and University contribution to a retirement benefits scheme, totalling up to 15% of basic salary, as well as leave, and medical benefits. Housing benefits will be provided as applicable. At current rates, salaries tax does not exceed 15% of gross income.

For enquiries of the existing research activities and the specific job requirements, please write to Professor Rudolf Wu, Director of the School of Biological Sciences (e-mail: rudolfwu@hku.hk). Interested applicants should submit a completed application form, together with a full C.V., a research plan, and a statement on teaching philosophy to scsbs@hku.hk. Please indicate clearly which level they wish to be considered for and the reference number in the subject of the e-mail.

Application forms (341/1111) can be obtained at <http://www.hku.hk/apptunit/form-ext.doc>. Further particulars can be obtained at <http://jobs.hku.hk/>. **Closes April 30, 2013.** The University thanks applicants for their interest, but advises that only shortlisted applicants will be notified of the application result.

The University is an equal opportunity employer and is committed to a No-Smoking Policy

PENN STATE



Tenure-Track Faculty Positions Assistant/Associate/Full Professor Cluster Hire in CyberScience: Computational Biology The Pennsylvania State University

This search is part of a Penn State CyberScience Cluster Hire in Computation and Data- Enabled Science and Engineering (see <http://www.ics.psu.edu/hire.html>). Penn State has embarked on a transformative cluster hiring initiative in cyberscience (computation- and data-enabled science and engineering), coordinating multiple faculty appointments across colleges to develop new functional capabilities centered on data, models and simulation for deeper insights into critical problems in science and engineering. We seek outstanding faculty who can work across disciplines and in a team to advance algorithms, software and theory to exploit "Big Data" and "Big Simulations" for scientific discovery in a variety of disciplines. Multiple positions at any academic rank are available.

As part of this initiative, several departments in the Eberly College of Science are conducting a combined search emphasizing computational biology. Participating departments are Biochemistry and Molecular Biology, Biology, Statistics, Mathematics and Physics. Our goal is to appoint outstanding faculty utilizing large-scale computation and data-intensive methods and interdisciplinary approaches to advance functional genomics, evolutionary biology, population genomics, genotype-phenotype relationships, biological networks, bioinformatics, and other areas of biology.

Applications should be submitted as a single pdf document via email to **Traci Shimmel** (tshimmel@psu.edu). Document should include the letter of application, CV, a brief description of research plans, and contact information of three referees. **PLEASE REFERENCE JOB NUMBER 38704.**

Review of applications will begin immediately and continue until positions are filled.

Employment will require successful completion of background check(s) in accordance with University policies.

Penn State is committed to Affirmative Action, Equal Opportunity and the diversity of its workforce.



Established Investigators in Metabolism

The new Department of Integrative Biology and Physiology at the University of Minnesota Medical School seeks outstanding faculty candidates in integrative biology and physiology of metabolism and related fields of diabetes/obesity at the Associate or Full Professor levels. Substantial resources including leading a focused junior faculty cluster hires for program development and new state-of-the-art research buildings are committed to this effort: <http://www.abc.umn.edu/research/bdd/>. Successful candidates will have an established and innovative research program that embraces biological complexity from molecular building blocks to the living organism. Applicants must have a strong record of research accomplishments, as documented by publications in leading peer-reviewed journals. A commitment to excellence in teaching is essential. An outstanding record of extramural funding with a multiple grant portfolio is required. Minimum requirements are a PhD, MD or MD/PhD with tenure at an academic research institution. Additional information about the department: <http://physiology.med.umn.edu/>. Information on the vibrant Twin Cities community and Minnesota's acclaimed high quality of life: <http://www1.umn.edu/wishyouwerehere/>. **Nominations are appreciated: Dr. Randi Lundell** rmlunde@umn.edu. Applicants please apply on-line (http://www1.umn.edu/ohr/employment/requisition_number_#179062); submit cover letter, curriculum vitae, statement of programmatic and research goals and reference letters to this web address).

The University of Minnesota is an Equal Opportunity Educator and Employer.



Chair, Department of Neurobiology and Director of the Kavli Institute for Neuroscience Yale University School of Medicine

Yale University School of Medicine announces a search for Chair of the Department of Neurobiology and Director of the Kavli Institute for Neuroscience at Yale. The Department of Neurobiology, which was founded by Pasko Rakic in 1978, and the Kavli Institute, which began in 2003, play a key role in Yale's broader neuroscience community. The successful candidate will be expected to possess an outstanding academic record in research and education, together with demonstrated leadership ability. He/she must meet the requirements for appointment as a Full Professor at Yale. Interested candidates should send a curriculum vitae and bibliography, a brief statement of programmatic interests and goals, and a list of professional references prior to **March 15, 2013** either electronically (to charlene.bloch@yale.edu) or by mail to:

Pietro DeCamilli

**Chair, Neurobiology Search Committee
c/o Charlene Bloch**

**Yale University School of Medicine,
CNRR Program**

**295 Congress Ave, BCMM 436D
PO Box 9812**

New Haven, CT 06519-1418

*Yale University is an Equal Opportunity,
Affirmative Action Employer. Minorities and
women are encouraged to apply.*



NORTHWESTERN UNIVERSITY

Senior Faculty Position in Virology Department of Microbiology-Immunology Northwestern University Feinberg School of Medicine

A tenured or tenure track position is open for a full-time faculty researcher at the Associate Professor or Full Professor level studying aspects of Virology. Areas of particular interest include viral pathogenesis, entry, egress, assembly, host-pathogen interactions and immune evasion.

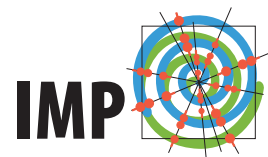
All applicants should have substantial peer-reviewed publications that demonstrate the ability to perform cutting edge research. Candidates should also have substantial research productivity, a history of grant support and academic service, and an interest in teaching graduate and medical students. Starting date is negotiable.

Application materials will be reviewed as received, but to receive full consideration, should be received by **April 1, 2013**. Please send a complete CV and the name and contact information of at least three references by email to: seniorvirologist@northwestern.edu.

Northwestern University is an Affirmative Action, Equal Opportunity Employer. Women and minorities are encouraged to apply. Hiring is contingent upon eligibility to work in the United States.

SCIENTIFIC DIRECTOR

Research Institute of Molecular Pathology (IMP), Vienna



The IMP is a basic research center sponsored primarily by the pharmaceutical company Boehringer Ingelheim (www.imp.ac.at). The IMP develops its own independent research program with the main goal to conduct outstanding basic research in the life sciences. The IMP together with the Institute of Molecular Biotechnology of the Austrian Academy of Sciences (IMBA) and several biomedical institutes of the Vienna University constitutes the Vienna Biocenter, which shares common activities including an active PhD program and scientific infrastructure. The IMP is presently organized into 17 research groups with a scientific staff of approx. 200, which have free access to excellent core-funded services including a state-of-the-art animal facility. The language spoken at the institute is English.

The Scientific Director should be an active world leader in her/his own scientific area with broad scientific interests. She/he takes responsibility for the scientific concept of the institute, first and foremost through the recruitment of excellent faculty members. The management burden is limited in this middle-sized institute as the director is supported by an administrative director and experienced staff.

Applications should be addressed to the chair of the search committee:

Tom Rapoport (Harvard Medical School)
c/o Christopher Robinson
IMP, Dr. Bohr-Gasse 7, A-1030 Vienna
e-mail: robinson@imp.ac.at



Canada Excellence Research Chair Green Chemistry and Green Chemicals

McGill University seeks an internationally recognized leader in Green Chemistry to fill the Canada Excellence Research Chair (CERC) in Green Chemistry and Green Chemicals. The CERC program awards world-renowned researchers and their teams \$10 million over seven years to establish ambitious research programs at Canadian universities (<http://www.cerc.gc.ca/hp-pa-eng.shtml>).

The CERC in Green Chemistry and Green Chemicals will hold a PhD or equivalent degree and an established record of independent research in chemical sciences, at an internationally-recognized level. Research activities sought might include, but are not limited to, catalyst discovery and application to synthesis, synthesis and application of new materials and/or solvents, biocatalysis, and catalysis applied to energy conversion. In addition to developing a highly competitive research program at McGill, the incumbent will be expected to participate in teaching at the undergraduate and/or graduate student level as well as administrative work to support these activities. Applications, including curriculum vitae, a statement of research and teaching interests, and the names of three referees should be sent to R. B. Lennox, Chair, Department of Chemistry, McGill University (Bruce.Lennox@McGill.ca). Applications will be considered starting February 1, 2013.

McGill University is committed to diversity and equity in employment. It welcomes applications from Aboriginal persons, persons with disabilities, ethnic minorities, persons of minority sexual orientation or gender identity, visible minorities, women, and others who may contribute to further diversification. All qualified candidates are encouraged to apply; however, in accordance with Canadian immigration requirements, Canadians and permanent residents will be given priority.



The Vienna Center for Quantum Science and Technology (VCQ) invites applications for the

Vienna Quantum Fellowships

These Fellowships in Experimental or Theoretical Quantum Science will be awarded both on the PhD- and the postdoc-level on the basis of an international competition. The appointments are for a three-year duration. Postdoctoral Fellowships carry a competitive annual salary, and offer an annual research expense fund. PhD Fellowships will participate in the Vienna graduate program CoQuS.

The Vienna Quantum Fellowship program has been established with the support from the Austrian Ministry of Science and Research to offer young scientists the best possible opportunity to develop their talents in the environment of the Vienna Center for Quantum Science and Technology (VCQ).

The VCQ faculty provides a broad variety of research opportunities in the areas of Experimental and Theoretical Quantum Science (see <http://vcq.quantum.at>):

- Matter-wave interferometry and quantum atom optics
- Micro- and nanoscale quantum optics and quantum optomechanics
- Microoptics and novel quantum states of light
- Cold atoms and degenerate quantum gases
- Many-body quantum physics and quantum simulations
- Entanglement-based quantum communication on Earth and via satellites
- Quantum information and foundations of physics

Information about how to apply and the required application material can be obtained from <http://vcq.quantum.at>

Deadline for the application is **April 28, 2013**. Fellowship candidates will automatically be considered for other available postdoctoral positions in their fields of interest.



There's only one

DR. SHIRLEY MALCOM



To Dr. Shirley Malcom, born and raised in the segregated South more than 65 years ago, a career based on her studies in science seemed even less likely than the launch of the Soviet's Sputnik. But with Sputnik's success, the Space Race officially started and, in an instant, brought a laser-like focus to science education and ways to deliver a proper response. Not long after, Dr. Malcom entered the picture.

Although black schools at the time received fewer dollars per student and did not have sufficient resources to maintain their labs at a level equivalent to the white schools, Dr. Malcom found her way to the University of Washington where she succeeded in obtaining a B.S. in spite of the difficulties of being an African American woman in the field of science. From there she went on to earn a Ph.D. in ecology from Penn State and held a faculty position at the University of North Carolina, Wilmington.

Dr. Malcom has served at the AAAS in multiple capacities, and is presently Head of the Directorate for Education and Human Resources Programs. Nominated by President Clinton to the National Science Board, she also held a position on his Committee of Advisors on Science and Technology. She is currently a member of the Caltech Board of Trustees, a Regent of Morgan State University, and co-chair of the Gender Advisory Board of the UN Commission on Science and Technology for Development. She has held numerous other positions of distinction and is the principal author of *The Double Bind: The Price of Being a Minority Woman in Science*.

Of her active career in science, Dr. Malcom says, "I guess I have become a poster child for taking one's science background and using that in many other ways: we ask questions; we try to understand what we find; we consider what evidence we would need to confirm or refute hypotheses. And that happens in whatever setting one finds oneself."

At *Science* we are here to help you in your own scientific career with expert career advice, forums, job postings, and more — all for free. Visit *Science* today at ScienceCareers.org.



AAAS

For your career in science, there's only one **Science**

ScienceCareers.org

COURSE

INTERDISCIPLINARY SUMMER COURSE

Biophysics and Computation in Neurons and Networks

Directors: David W. Tank and Michael Berry
Princeton Neuroscience Institute

Course Date: June 16 – July 13, 2013

Location: Princeton University

Application Deadline: April 1, 2013

Application Forms: bcnn.princeton.edu

This course, supported by the Burroughs Wellcome Fund, targets students with training in the physical sciences, mathematics or engineering who seek an introduction to the concepts and research methodologies of modern neuroscience. No previous training in biology is required. Topics covered will range from cellular biophysics to systems neuroscience, including particularly imaging methods for the study of single neurons, networks of neurons and human brain dynamics during execution of behavioral computations. The course will be unique in its focus on neural dynamics at several scales of complexity – cells, circuits, intact brains – and the combination of didactic lectures and laboratory exercises, including cellular biophysics, synaptic interactions and plasticity in neuronal networks, and fMRI imaging of targeted brain regions in human subjects. The capstone of this course will be one-week student-designed research projects integrating concepts and methodologies encountered during the initial formal lectures and laboratory exercises. Course work will include morning lectures and tutorials and laboratory exercises selected to complement and extend the themes presented in morning lectures.



POSITIONS OPEN



Systems Agronomist

The Institute of Agriculture and Natural Resources at the University of Nebraska, with support from the Robert B. Daugherty Water for Food Institute (DWFI) is accepting applications for a Systems Agronomist a 70% research, 30% extension, 12-month, tenure-leading or tenured appointment at the Assistant, Associate, or Full Professor rank. Housed in the Department of Agronomy and Horticulture, this is a key contributing position to development of the DWFI, providing leadership as the agronomic center of a cluster of faculty members to define and address compelling issues in the use of water in Nebraska's agriculture with focus on efficiency of water use and decreasing the yield gap of major crops and cropping systems in variable and changing climates.

The successful candidate is expected to collaborate on multi-disciplinary research in the development of sustainable cropping systems for corn, soybean and other crops resulting in improved input use efficiency, reduced greenhouse gas emissions, and higher yields through closure of the exploitable yield gap; to maintain a vigorous program supported through external grants and contracts; publish research results in peer-reviewed journals and present results at professional meetings; advise graduate students; develop education programs to serve a diverse clientele including producers, government agencies, crop consultants, businesses and University of Nebraska extension educators; contribute to crop production and environmental extension action team efforts; provide leadership to extension education programming teams on the use of crop models and decision support tools with a focus on improving water and nutrient use efficiency in Nebraska; and communicate research results through a variety of channels to key stakeholders and clientele groups.

Requires Ph.D. degree or Ph.D. in place by date of hire, in agronomy or closely related field. Rank and tenure will be based on experience and credentials of the successful applicant.

To view complete position details and to apply, go to: <http://employment.unl.edu> and search for requisition #F130036. Complete the Faculty Academic Administrative Information Form. Attach a letter of application, an overview of research and extension experience and interests, and a curriculum vitae. Arrange for 3 letters of reference to be emailed to: cwendt1@unl.edu. Review of applications will begin on **March 15, 2013** and continue until the position is filled or the search is closed.

The University of Nebraska has an active National Science Foundation ADVANCE gender equity program, and is committed to a pluralistic campus community through affirmative action, equal opportunity, work-life balance, and dual careers.

COURSE

Santa Barbara Advanced School of Quantitative Biology

2013 Summer Research Course @ UCSB

Presented by KITP & CNSI

New Approaches to Morphogenesis: Live Imaging and Quantitative Modeling

July 22 - August 24, 2013

For information and to apply visit:

www.kitp.ucsb.edu/qbio

**Application deadline:
February 28, 2013**

$$\frac{dU_{ij}}{dt} = kD_i F_j (1 + \alpha U_{ij}) - \gamma U_{ij} (1 + \beta U_{ij})$$



ANNOUNCEMENTS

Analyze Evolution in Action

The Virtual Stickleback Evolution Lab



Explore evolutionary patterns with your students by analyzing body structures of modern and fossil fish. Available free online for tablets and computers.

BioInteractive.org/Science



POSITIONS OPEN



NEW JERSEY MEDICAL SCHOOL
UNIVERSITY HOSPITAL
CANCER CENTER
University of Medicine & Dentistry of New Jersey

INTERDISCIPLINARY TRAINING PROGRAM IN CANCER RESEARCH

Postdoctoral positions are available from an NCI-sponsored Interdisciplinary Cancer Training Grant for Ph.D., MD, or M.D.-Ph.D. recipients who seek training in basic or translational cancer research. Preference will be given to new postdoctoral graduates or those who anticipate degrees by July 1, 2013. Faculty mentors have primary appointments in both basic and clinical departments, and many are located in the newly constructed New Jersey Medical School-University Hospital Cancer Center ([website: http://njmsuhcc.umdnj.edu/home/](http://njmsuhcc.umdnj.edu/home/)). The Cancer Center is located within the New York Metropolitan area and contains three research floors, a 20,000 square foot mouse barrier facility, and extensive in-house Core facilities. While the principal training mechanism of this program is through mentored research with outstanding faculty, a key element of this program is a structured exposure to cancer clinical care through a unique "shadowing program". A detailed program description, list of participating faculty, and application information, can be found at [website: http://njmsuhcc.umdnj.edu/home/index.php/training-program-faculty-mentors.html](http://njmsuhcc.umdnj.edu/home/index.php/training-program-faculty-mentors.html). Salary support will be for two to three years for qualified applicants who must be training grant eligible (*U.S. citizen or permanent resident*). For additional information contact, **Dr. Harvey Ozer**, Program Director at **telephone: 973-972-3557**, or to **e-mail: ozerhl@umdnj.edu**.

ASSISTANT PROFESSOR Utah State University

The Department of Chemistry and Biochemistry at Utah State University (USU) invites applications for a tenure-track position at the Assistant Professor level in the area of biochemistry who will participate in the Chemical Biology program beginning fall 2013. The successful candidate will have a research program that complements at least one departmental focus area (i.e., macromolecular structure and function and/or eukaryotic biochemistry), the technical infrastructure within the department, and should also allow the candidate to interact with researchers in the biological sciences from other USU departments and colleges. Applicants must have earned a Ph.D. in Chemistry, Biochemistry, Biology, or a related field; postdoctoral experience is required. The position requires the development of an externally funded research program as well as teaching at the undergraduate and graduate levels. Applicants should submit curriculum vitae, a concise description of future research projects, a description of how the research to be pursued complements existing research focus areas and technical infrastructure in the Department, a description of teaching experience and preferred teaching area(s), and the names and e-mail addresses of three references. Apply online at [website: http://jobs.usu.edu](http://jobs.usu.edu) (053398). Evaluation of applicants is ongoing; posting will remain open until position is filled. For more information please visit our [website: http://www.usu.edu/science/htm/chemical-biology](http://www.usu.edu/science/htm/chemical-biology).

Utah State University, located in Logan, Utah, is an Equal Opportunity/Affirmative Action Employer committed to assembling a diverse faculty. Women and members of minority groups are strongly encouraged to apply.

Help employers find you.
Post your resume/cv.
www.ScienceCareers.org

POSITIONS OPEN

POSTDOCTORAL POSITIONS in The Enzyme Function Initiative

The Enzyme Function Initiative (EFI; [website: http://enzymeefunction.org/](http://enzymeefunction.org/)) was established in 2010 with a Glue Grant from NIGMS/NIH (U54GM093342). The goal is to develop a sequence/structure-based strategy for facilitating assignment of in vitro enzymatic and in vivo metabolic/physiological functions of unknown enzymes discovered in genome projects, a crucial limitation in genomic biology. This is being accomplished by integrating bioinformatics, structural biology, and computation with enzymology, genetics, and metabolomics. The EFI consists of five Scientific Cores that provide essential intellectual, computational, and experimental infrastructure for functional predictions, which are tested by Bridging Projects that focus on functionally diverse enzyme superfamilies.

Postdoctoral positions are available in microbiology with focus on phenotypic analyses of knockout/overexpression mutants and transcriptomics and on mass spectrometry-based metabolomics. Due to the collaborative and multidisciplinary environment, the EFI provides an opportunity to receive training in several areas. For example, those with a primary interest in microbial genetics can receive training in bioinformatics or in metabolomics.

To apply and/or for more detailed information, please contact **Professor John Cronan** (e-mail: jcronan@uiuc.edu).

FACULTY POSITION in Marine Biogeochemistry

Stony Brook University's School of Marine and Atmospheric Sciences (SoMAS) invites applications for a tenure-track faculty position in Marine Biogeochemistry, to begin as early as fall 2013. The position will be filled at the **ASSISTANT PROFESSOR** level. Review of applications will begin March 1, 2013, but applications will be considered until the position is filled. Candidates are expected to interact with and augment existing activities in biogeochemistry at SoMAS. The successful candidate is expected to carry out an independent research program, attract external grant support for independent and collaborative projects, support and foster the development of graduate students, contribute to teaching activities at both the graduate and undergraduate levels, and participate in School and University service. Application instructions and procedures, as well as further information about this position, can be found at [website: http://www.somas.stonybrook.edu/about/empopps.html](http://www.somas.stonybrook.edu/about/empopps.html) (Ref #F-7743-13-01). *Stony Brook University/SUNY is an Affirmative Action/Equal Opportunity Educator and Employer.*

Stop
searching
for a job;
start your
career today.

Science Careers

From the journal *Science*



www.ScienceCareers.org



Nontraditional Careers: Opportunities Away From the Bench Webinar

Want to learn more about exciting and rewarding careers outside of academic/industrial research? View a roundtable discussion that looks at the various career options open to scientists and strategies you can use to pursue a nonresearch career.

**Now Available
On Demand**
www.sciencecareers.org/webinar

Produced by the
Science/AAAS Business Office.

Science Careers

From the journal *Science*

